Nanoparticle-assisted Enhanced Oil Recovery

Zhongliang Hu

Submitted in accordance with the requirements for the degree of

Doctor of Philosophy

The University of Leeds

School of Chemical and Process Engineering

July, 2017

The candidate confirms that the work submitted is his own, except where work which has formed part of jointly-authored publications has been included. The contribution of the candidate and the other authors to this work has been explicitly indicated below. The candidate confirms that appropriate credit has been given within the thesis where reference has been made to the work of others.

In Chapter 3, Dr Ghulam Raza synthesised the TiO_2 nanoparticle, and did the TEM characterization. In Chapter 4, Dr. Ehsan Nourafkan undertook the surfactant (XOF-25S + EA) preparation and characterization, and then prepared TiO_2 NPs coated with surfactant. He also helped do part of the characterization, including electrophoretic mobility and zeta potential, for five different types of rock samples. Using COD method to determine the surfactant concentration was also proposed and conducted by Dr. Ehsan. In Chapter 5, the microemulsion stabilized by *in-situ* synthesized iron oxide nanoparticle (IONP) was prepared by Dr. Ehsan Nourafkan.

Acknowledgements

First and foremost, I would like to extend my deepest gratitude to my supervisor, Prof. Dongsheng Wen, for his endless guidance and support through these years, for funding my studies at University of Leeds, and for the guidance on career development. Stepping close to him can always let me feel a kind of positive energy. The regular gatherings and invitations to his place also made the entire process enjoyable.

I also would like to extend my appreciation to Prof. Paul Glover, for his support in experiment facilities, papers correction and useful suggestion at every stage of this PhD study. Thanks to Dr. Ghulam Raza, Dr. Ehsan Nourafkan and Dr. Hui Gao for their support in materials and discussion during experiments. Dr. Raza also showed me the flooding system developed in his PhD which gave me lots of inspirations for the development of a packed core flooding system. Apart from providing materials, Dr. Ehsan and Dr. Hui contributed to sample characterization and data analysis. Also special thanks to several MSc students, Siddeequah Azmi, Phillip Nwufoh and Maje Haruna, for helping set up the flooding facilities and conduct core flooding experiments.

I also would like to thank Dr. Carlos Grattoni, who is always kind and helpful when I approach him with my question, and who helped me characterize and clean the rock samples. Thanks to the technicians: Mr. Antony Windross and Dr. Ms. Jane-Marie Stocks from School of Earth and Environment, Peter Dawson and Dr. Susanne Patel and other technicians from School of Chemical and Process Engineering, for their generous support on facilities and manufacturing.

Thanks to a few PhD students: Dr. Mahoulo Ahouansou, Dr. Mathieu Lasfargues, and Dr. Jabbar Gardy for their help on equipment training and advices. Also special thanks to all the colleagues who are staying in the same office with me. Talking with

you guys has broaden my horizon, laughing and sometime even singing together are good times and sweet memories during the PhD journey.

Finally, I would like to say an eternal thank you to my parents, who have been giving support and COURAGE throughout my life.

At the end of polishing this thesis, I am deeply missing my girlfriend, Dr. Hui Gao, who is now doing a postdoc in Hong Kong. We have engaged after 10-year love marathon, which is obviously the most golden age in our lives. There are so many good moments in the past to be engraved, and I believe we can fight together to create a happy home and bright future. Thank you for accompanying me.

Abstract

Considering low recovery rate and techniques uncertainties faced by traditional enhanced oil recovery (EOR) techniques, especially the methods of chemical and engineered water flooding, this thesis develops emerging nanotechnologies for EOR applications. Five areas were studied ranging from water flooding, surfactant flooding, microemulsion flooding, polymer flooding to nanoparticle mobility studies.

Firstly, rutile ellipsoid TiO_2 nanoparticles (NPs) were synthesised and stabilised by tri-sodium citrate dihydrate for brine flooding in water-wet Berea sandstone cores. The results showed that the oil recovery depended on NPs concentration and volume injected: 10 ppm TiO_2 had the highest total oil recovery while 500 ppm had the highest increment recovery after the breakthrough. The EOR effects were attributed to the log-jamming effects and probably wettability change towards water wetting.

Following this, nanoparticles were proposed as surfactant carrier to address the issue of excess adsorption of surfactants during a chemical EOR process. The adsorption of surfactants blend of 25% anionic alkylaryl sulfonates (XOF-25S) and 75% alcohol ethoxylated was found being reduced by commercial TiO_2 nanoparticle in dolomite and silica cores. The surfactant concentration was determined by chemical oxidation demand (COD) method. Surfactant adsorption in rock grain matrix was found to have a direct relationship with the nanoparticle retention.

To address the problems associated with conventional microemulsion flooding, *in-situ* synthesised iron oxide NPs were proposed to stabilize the oil-in-water microemulsion texture, prevent surfactant from detaching from the interface and forming viscous phase in produced oil, and mobilize more oil as increasing the particle concentration. Core flooding experiments showed the promise of the nanoparticle-engineered microemulsion.

To address the polymer degradation issue at high temperature during a traditional polymer-flooding, SiO_2 NPs were used to improve the salt-tolerance, rheological properties and thermal stability of hydrolysed polyacrylamide (HPAM), as well as its EOR potential. The EOR experiments at 50 ^oC showed that the oil recovery was increased to 69.6% with 0.5 wt% HPAM seeded with 0.6 wt% SiO_2 NPs, compared to a plain brine flooding efficiency of 56.2%.

Finally, the migration properties of nanoparticles were investigated in columns packed with glass beads, saturated with brine at various salinities up to API standard. The luminescent carbon particles were used and a nearly full breakthrough behaviour (100% of C/C_0) was observed even in API brine for 5-nm carbon dots. Controversially, the breakthrough behaviour was discounted in calcite limestone matrix. The good thermal stability and mobility enable the carbon dots act as reservoir sensor in sandstone rock, and detection of the saturation degree of hydrocarbon in sandstone core was demonstrated.

The work conducted in the thesis showed the great promise of nanoparticles for EOR applications at the laboratorial scale, and future work shall be planned at large scales.

Keywords: nanoparticles, enhanced oil recovery, microemulsion, surfactant, polymer, particle migration, nanoparticle sensor

Table of Contents

List of Tables

List of Figures

List of Abbreviations

API	American Petroleum Institute
BET	Brunauer–Emmett–Teller
BF	Brine Flooding
BSF	Brine with Stabiliser Flooding
BTC	Breakthrough Curve
CAC	Critical Association Concentration
CDs	Carbon Dots
CFT	Clean Bed Filtration Theory
CLSM	Confocal Laser Scanning Microscopy
CMC	Critical Micelle Concentration
CNC	Critical Nanoparticle Concentration
CNT	Carbon Nanotube
COD	Chemical Oxygen Demand
COR	Cumulative Oil Recovery
CSC	Critical Salt Concentration
CTAB	Cetyltrimethylammonium Bromide
DLS	Dynamic Light Scatting
DLVO	Derjaguin-Landau-Verwey-Overbeek
DPR	Disproportionate Permeability Reduction
E_{COR}	Cumulative Oil Recovery Efficiency
E_{EOR}	EOR efficiency
E_{IOR}	Increased Oil Recovery Efficiency
EA	Ethoxylated Alcohol

EDX	Energy-dispersive X-ray spectroscopy
EM	electromagnetic
EOR	Enhanced Oil Recovery
FTIR	Fourier-transform infrared spectroscopy
HPAM	Partially Hydrolyzed Polyacrylamide
HPLC	high performance liquid chromatography
IFT	Interfacial Tension (N/m)
IO	Iron Oxide
IONP	Iron Oxide Nanoparticle
ME	Microemulsion
MEIN	Microemulsion Stabilized by Iron Oxide Nanoparticle
MICP	Mercury Intrusion Capillary Pressure
NF	Nanofluid Flooding
NP	Nanoparticle
OOIP	Original Oil In Place
PEG	Polyethylene Glycol
PV	Pore Volume
PVP	Polyvinylpyrrolidone
R&D	Research & Development
SAGD	Steam Assisted Gravity Drainage
SCD	Sodium Citrate Dihydrate
SDP	Structural Disjoining Pressure
SDS	Sodium Dodecyl Sulphate
SEM	Scanning Electron Microscopes
SRFA	Suwannee River Fulvic Acid

TEM	Transmission Electron Microscope
UV-Vis	Ultraviolet–visible
XOF-25S	Sulfonic acid of Alkylate H250 (C14 – C30)
G'	Storage Modulus (Pa)
G''	Loss Modulus (Pa)
$\tan\delta$	Damping factor
η^*	Complex Viscosity (Pa·s)
ω	Angular Frequency (rad/s)

Chapter 1

Introduction

1.1 Global concerns

Global energy consumption is set to increase drastically over the coming decades, with most of this demand being met by fossil fuels . The U.S. Energy Information Administration (EIA) released the <International Energy Outlook Report> in 2017 that suggested energy use in all other end-use sectors would group more quickly from 2015 to 2040 [1]. Even though the report highlights the fastest growing energy resources are renewable and nuclear, with consumption increasing by an average 2.3%/year and 1.5%/year over that period, respectively., Although consumption of nonfossil fuels is projected to grow faster than fossil fuels, Fossil fuels (including liquid fuel, natural gas and coal) are still predicted to supply around 77% of world energy consumption through to 2040. Among them, natural gas will show a strong growing rate at 1.4% /year, while petroleum and other liquid fuel will increase by 0.7%/year and still remain the largest source of energy, despite of that their share of the world energy consumption slightly declining from 33% in 2015 to 31% in 2040 (Figure 1-1).

However, the era of finding “easy oil” is coming to an end, and future supply will become more reliant on fossil fuels produced from non-conventional reservoirs and from enhanced oil recovery (EOR) processes. It is estimated that the average oil recovery rate from mature oilfields around the world is typically 20%- 40% of the

original oil in place (OOIP) [2]. Therefore, techniques that can improve reservoir characterisation and enhance oil recovery are crucial in finding a solution to the challenge of meeting the ever-growing energy demand.

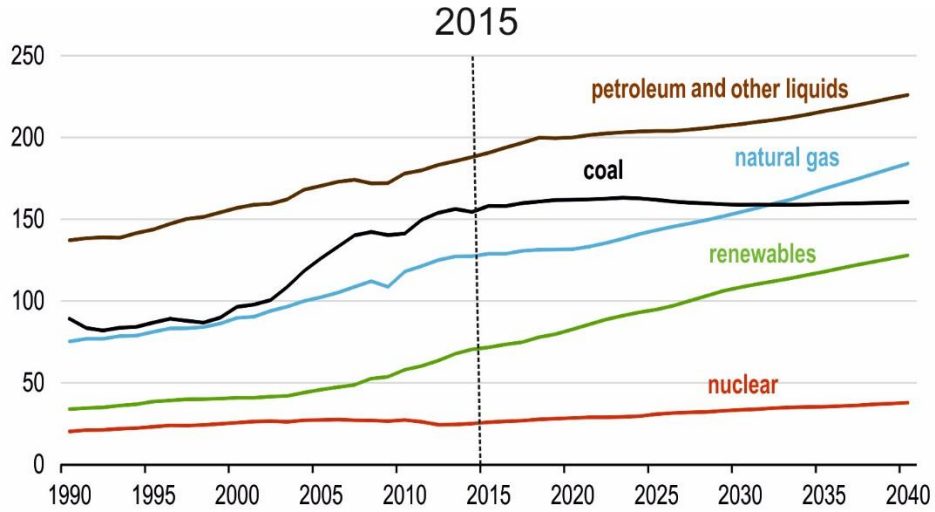

Figure 1-1. World energy consumption by energy source predicted by EIA in 2017 , 1990-2040 (quadrillion British thermal units) [1].

1.2 Oil recovery methods

Primary oil recovery refers to the process of extracting hydrocarbon either via the natural rise (such as gas drive, water drive and gravity drainage) to the surface of the reservoir or via pump jacks and other artificial lift equipment. The hydrocarbon can be derived by a differential pressure flowing toward the well and up to surface, because the reservoir pressure is considerably higher than the bottom hole pressure inside the wellbore [3]. However, because driving mechanism for primary oil recovery is different and the reservoir pressure declines naturally because of production, the oil recovery efficiencies through primary method are various and normally not high [4].

Water flooding is usually considered as the most commonly used secondary oil recovery method, where water is injected into the oil reservoir to support pore pressure in the reservoir and thereby stimulate production [4]. This method is typically can

mobilize an additional 30% of the oil reserves, though the figure could be more or less depending on the oil and of the rock surrounding it. However, water flooding still has several limitation, such as compatibility of the planned injected water with the reservoir's connate water, interaction of the injected water with the reservoir rock [5]. Especially, it is not efficient for heavy and extra-heavy oil recovery due to the huge viscosity difference between water and oils, leading to low sweep efficiency [6].

Rather than simply trying to force the oil up to the surface, as did the previous two methods, enhanced oil recovery seeks to alter the properties of displacing fluids, hydrocarbon, and even the oil reservoir to make it more conducive to extraction [7].

1.3 Current enhanced oil recovery processes

Currently EOR techniques including thermal, gas-injection, chemical methods, engineered water flooding and others have been used in physical situations where primary and secondary oil recovery method is inefficient (Figure 1-2).

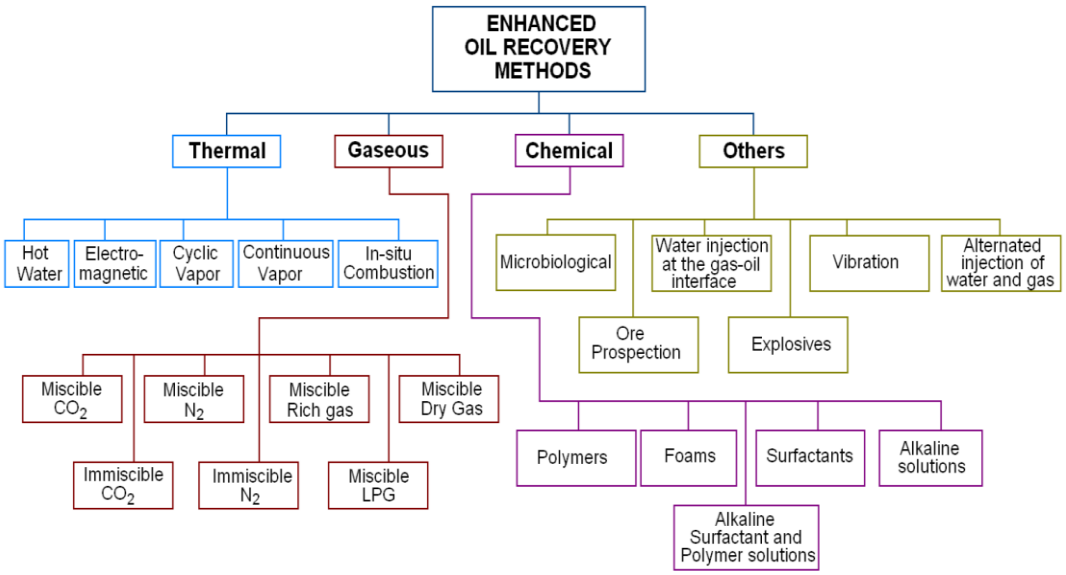

Figure 1-2. Classification of current EOR methods [8, 9].

Gas injection, as shown in Figure 1-3, which uses gases such as natural gas, nitrogen, or carbon dioxide (CO_2), accounts for nearly 60% of EOR production in the United

States [10]. Among them, CO_2 is most commonly used for miscible displacement because it is less expensive than liquefied petroleum gas and has reliable source from the fossil fuel power plant [11]. Gas injection or miscible flooding is presently the most commonly-used approach in EOR. Miscible flooding is referring to introduce miscible gases into the reservoir, to maintain reservoir pressure and improve oil displacement efficiency by reducing the interfacial tension between oil and water.

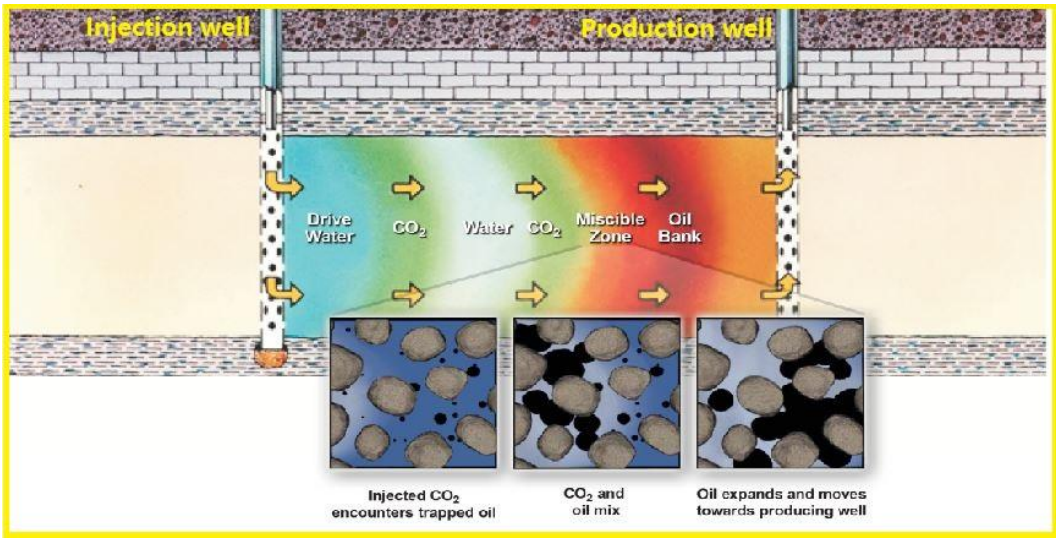

Figure 1-3. Cross-section illustrating how carbon dioxide and water can be used to flush residual oil from a subsurface rock formation between wells [11].

Thermal injection accounts for 40% of EOR production in the United States, with most of it occurring in California [12]. In this approach, various methods are used to heat the crude oil in the formation to reduce its viscosity and/or vaporize part of the oil and thus decrease the mobility ratio, including Cyclic steam stimulation (CSS), steam flooding, fire flooding (in-situ combustion), and steam assisted gravity drainage (SAGD) [13]. Those processes, in most cases, have to be cyclical to ensure success of thermal injection (Figure 1-4). Thermal method are applicable for oil reservoir with high oil saturation and porosity. For these processes, heat from the fire reduces oil viscosity and helps vaporize reservoir water to steam. The steam, hot water, combustion gas and a bank of distilled solvent all act to drive oil in front of the fire toward production wells.

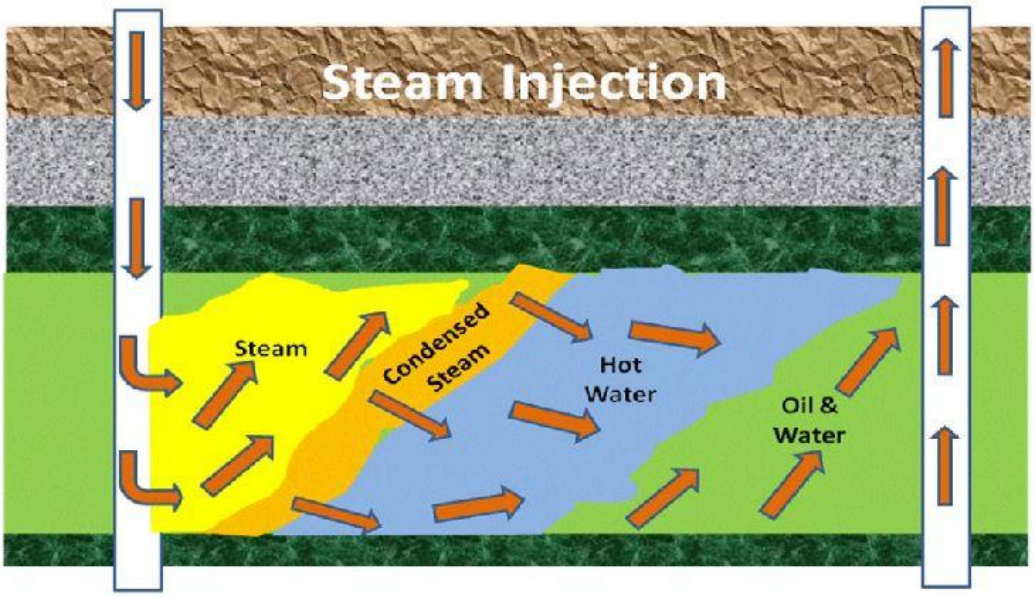

Figure 1-4. Cross-section illustrating how the hot steam can be used to heat and flush residual oil from a subsurface rock formation between wells [14].

Chemical methods involve a process that injecting of chemical formulation, such as surfactant, polymer, alkaline, foams, emulsion slug, alkaline-surfactant-polymer mixture formulation, and emulsion-polymer formulation, to reduce the mobility ratio between displacing fluid and hydrocarbon, and/or to increase the capillary number by reducing the IFT between oil and water phases [15, 16]. The theory relating to chemical EOR can be referred to Section 1.4, while current popular EOR manners practiced worldwide in chemical methods are discussed separately below.

- Surfactants, either *in-situ* formulated from the original crude oil or carried by the injected brine in the process of flooding, can accumulate at the oil/water interface and lower the IFT between crude oil and water, and consequently mobilizes the oil trapped by capillary force after water flooding process [17-24]. Ideally, the surfactant is required to remain water-soluble at elevated temperature and ionic strength, capable to generate ultralow IFT and have low adsorption on reservoir rock (better economic feasibility). The viscosity for surfactant solution is usually not high enough to reduce

the mobility ratio, therefore it has to be used in parallel with polymer flooding, as shown in Figure 1-5.

- Polymer is usually employed in a small quantity to thicken the displacing water. The primary purpose of polymer is to control the mobility ratio. Polymer can reduce the mobility ratio by increasing the viscosity of displacing phase and by causing disproportionate permeability reduction (DPR). The effect of DPR refers to the phenomena whereby many water-soluble polymers and polymer gel reduce the permeability of water flow to a much greater extent than for oil/ gas flow. Among several mechanisms proposed to interpret the DPR effect, pathway segregation and polymer absorption are believed as the dominant mechanisms for DPR when polymer solution are used [25-29]. However, polymer cannot reduce the IFT efficiently. It is usually applied coupled with surfactants.

- Alkaline flooding refers to adding alkali into the injection fluids. The mechanism of alkaline flooding is complex, which contains emulsification with entrainment, emulsification with entrapment, emulsification with coalescence, wettability reversal, wettability gradients, oil-phase swelling, disruption of rigid films, and low IFT [30, 31]. Different mechanisms could be attributed to chemical properties of the crude oil and the reservoir rock. However, most of research agree that acidic components in the crude oil are the most important factors for alkali flooding.

- Alkaline-surfactant-polymer (ASP) flooding is a kind of flooding strategy combining surfactant flooding, polymer flooding and alkaline flooding [32-34]. It is primarily proposed to reduce the amount of surfactant required through the formation and sequestering divalent cation and *in-situ* generation of synergetic surfactant with alkaline in oil reservoir [35, 36].

The synergic effects of those chemicals can recover large amount of water flood residual oil by decreasing IFT which contributes to an increased capillary number and

consequently a higher microscopic efficiency (as explained in Section 1.4), and reducing the water/oil mobility ratio which renders a macroscopic sweep efficiency. The reduction in IFT is introduced by a synergistic interaction of added surfactant and *in-situ* generated soaps by alkali reacting with naturally occurring organic acid in the crude oil [37-39]; while polymer is used for increasing viscosity. ASP method can significantly reduce the amount of surfactant required to recovery oil. Typically ASP formulations involves 0.2 PV of 1% surfactant and 0.5% alkali, chased by 0.3 PV or more of a solution containing 1000 ppm polymer. It is typically followed by a freshwater injection to optimize chemicals recovery and then chasing flood with drive water (Figure 1-5). [40]

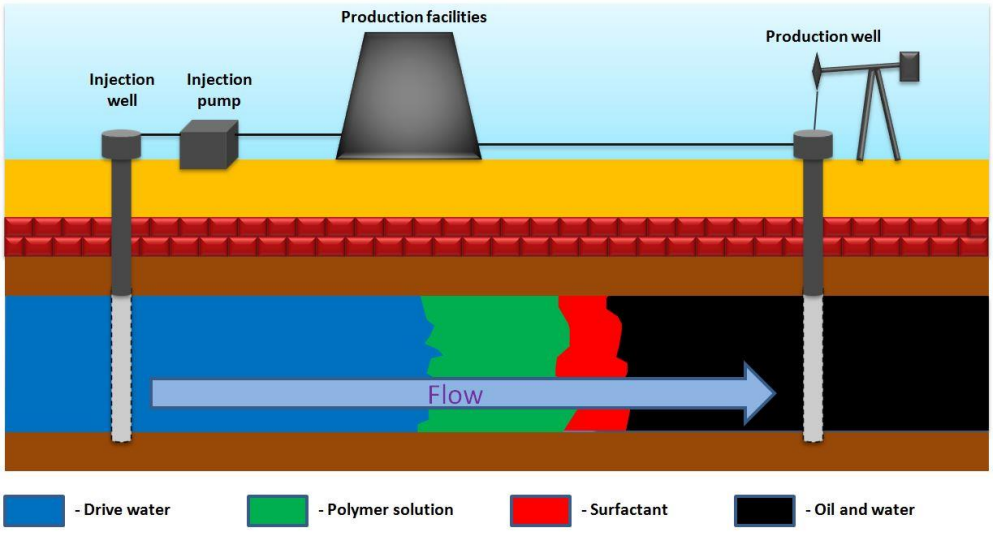

Figure 1-5. Schematic of polymer/surfactant flooding [40].

Engineered water flooding usually refers to tuning the ionic composition of the injecting brine, and it is more popularly known as 'low salinity water flooding' and in different publications it is referred to 'Designer Water Flood' by Shell [41], 'Advanced Ion Management (AIMSM)' by ExxonMobil [42], 'Low Salinity Water Flood (LoSal™)' by BP [43] and 'Smart Water Flooding' by several authors in recently published articles [44]. The wettability alteration by ionic activity on the rock surface is identified as the main mechanism behind oil recovery improved by low salinity water

flooding, which has obtained greater support compared to other possible mechanisms. However, other mechanisms such as IFT reduction, electric double layer expansion, and rock dissolution are also found to contribute in releasing trapped oil in laboratory investigations [45]. Other engineered water flooding includes adding nanoparticle to the displacing fluids to mobilize more oil. However, the mechanisms behind nanoparticle enhanced oil recovery are still controversial as reviewed in Section 2.3.

1.4 Theory of enhanced oil recovery

1.4.1 Overall oil recovery efficiency

Based on the material balance of oil reservoir, the overall oil recovery efficiency (E_{OR}) can be calculated as equation 1-1:

$$E_{OR} = \frac{N_c}{OOIP} \qquad \text{Equation 1-1}$$

Where, N_c is the volume of accumulate oil recovered via flooding processes, OOIP is the Original Oil in Place, which usually shows the total oil content of an oil reservoir.

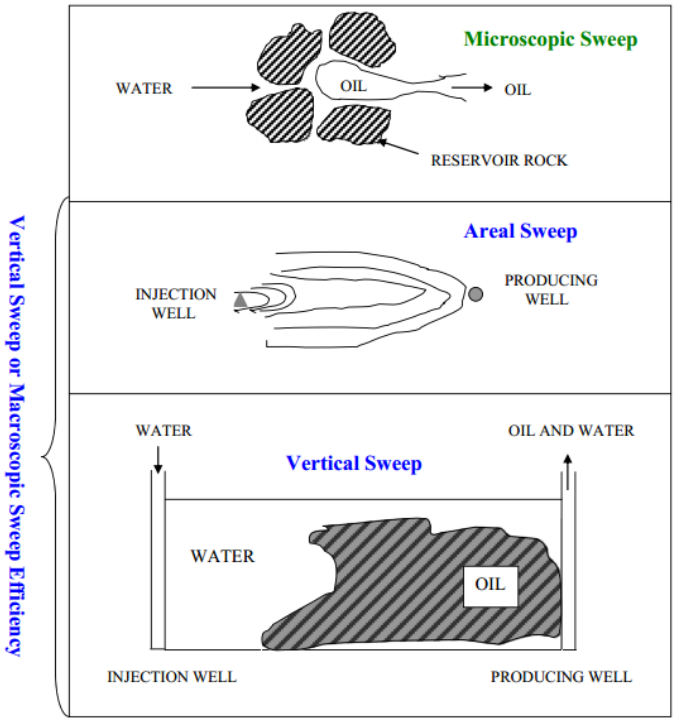

Figure 1-6. Schematic of macroscopic and microscopic efficiency [8, 46].

It is defined that the overall E_{OR} (equation 1-2) is affected by macroscopic or volumetric sweep efficiency (E_{ma}) which indicates the effectiveness of the displacing fluids to sweep the oil zone volumetrically, and the microscopic displacement efficiency (E_{mi}) which is a measure of the effectiveness to mobilized the oil trapped in pore space by capillary force [29, 47], shown in Figure 1-6.

$$E_{OR} = E_{ma}E_{mi} = E_a E_v E_{mi} \qquad \text{Equation 1-2}$$

Where, E_a is the areal displacement efficiency, E_v is vertical displacement efficiency.

1.4.2 Factors controlling macroscopic sweep efficiency

The macroscopic displacing efficiency (E_{ma}) is principally affected by geological heterogeneity in the reservoir, which affects the spatial distribution of porosity and permeability. The channels or layers with high permeability (often named as 'thief zones') allow water flow preferentially through these zones, bypassing the oil contained in the portion of reservoir with low permeability (Figure 1-7), resulting in an early water breakthrough and reduced E_{OR}.

The effect of geological heterogeneity is intensified when injecting a displacing fluid with a large viscosity contrast with oil. The effect of heterogeneity on oil recovery can be characterized by the mobility ratio, for instance gas is injected instead of water for oil recovery [48-51]. The mobility ratio is generally defined as the mobility of the displacing phase divided by the mobility of the displaced phase, which can be expressed by equation 1-3 [52]:

$$M = \frac{k_{rw}}{\mu_w} / \frac{k_{ro}}{\mu_o} = (\frac{k_{rw}}{k_{ro}})(\frac{\mu_o}{\mu_w}) \qquad \text{Equation 1-3}$$

where k_r usually refers to relative permeability, μ refers to dynamic viscosity, the subscript *w* represents displacing phase (usually water), and the subscript *o* is for the displaced phase (usually oil). The ratio shows the mobility of the injecting fluid to that

of the oil phase, and the effect is dependent on the relative permeability and the viscosity ratio.

Unfavourable mobility usually occurs when the value is greater than 1, and water is moving forward in a finger-like front. Whereas, a favourable mobility usually happens when there is a large viscosity contrast between the displacing fluid and displaced oil phase, which more likely to result in a piston-like displacement of oil from the injection well to the production well, as shown in Figure 1-7.

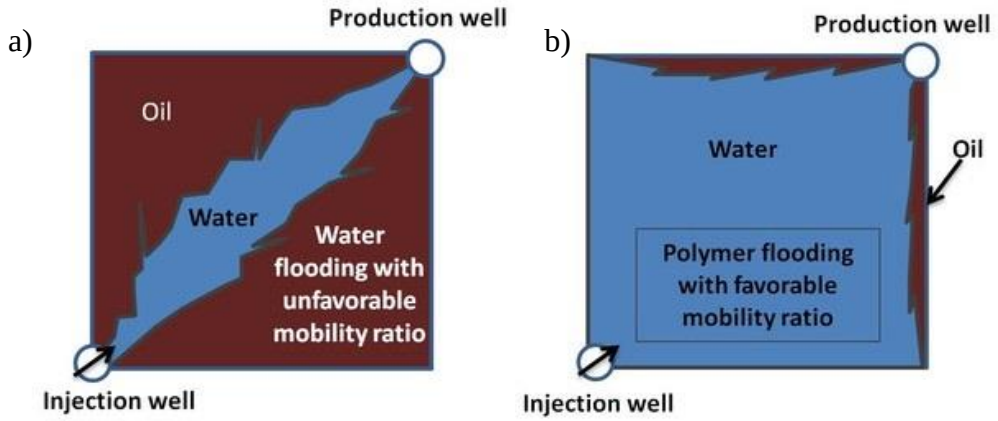

Figure 1-7. (a) Flooding with poor mobility control; (b) Flooding with good mobility control.

Viscosity control, like adding polymer to increase the viscosity of displacing phase or reducing the viscosity of oil phase by thermal method like steam-assisted gravity drainage (SAGD), is regarded as main way to achieve a favourable mobility. Moreover, achieving good mobility control in combination with other mechanisms including low interfacial tension (IFT) or wettability alteration is also essential for any successful EOR.

1.4.3 Factors controlling microscopic sweep efficiency

In water-wetting reservoirs, the typical microscopic displacement efficiency (E_{mi}) from water flood is 70% or less, this is mainly because the oil is trapped in pore space by capillary force, and is also contributed to relative permeability properties of the rock

[2]. The latter usually determines the mobility of water and oil when flowing through the pore space.

In water-wetting reservoirs, the capillary forces can be overcome by viscous force or gravity force. The competition between capillary force and viscous force is governed by the dimensionless Capillary Number C_a (equation 1-4):

$$C_a = \frac{\mu_i \times \vartheta}{\sigma} \qquad \text{Equation 1-4}$$

where μ_i is the dynamic viscosity of injected fluid (Pa·s), ϑ is Darcy's velocity (m/s), σ is the interfacial tension (N/m). In the circumstance of low capillary number (usually in the order of 10^{-7} - 10^{-6}), flow in porous media is dominated by capillary forces, and capillary trapping is likely to happen. Therefore, to increase oil recovery, either the viscosity of brine should be increased significantly or the o/w IFT should be brought down to ultra-low level (< 10^{-3} mN/m) [53]. For high capillary number, the trapped oil will be mobilized because the capillary forces are negligible compared to the viscous forces.

The relative importance of capillary force and gravity force can be characterized by normalized bond number N_b (equation 1-5) [54]*:*

$$N_b = \frac{\Delta\rho g k_a k_{rw}}{\sigma \cos\theta} \qquad \text{Equation 1-5}$$

where $\Delta\rho$ is the density difference between oil and water, g is gravity acceleration, k_a is the absolute permeability, k_{rw} is the relative permeability of water phase, θ is the contact angle of wetting phase on the rock. Total trapping number N_t (equation 1-6) is derived from the combined effect of capillary and bond number:

$$N_t = C_a + N_b \qquad \text{Equation 1-6}$$

It should be noticed that the oil recovery affected by capillary forces differs fundamentally between non-fractural and fractural reservoirs. In a non-fractured reservoir, Lowering the w/o IFT and consequently reducing the capillary fore is

necessary to mobilized the large volume of residual oil trapped in pore space after water flooding. While in fractured reservoir, spontaneous imbibition of water due to strong capillary force is essential to achieve a high recovery efficiency [55].

1.5 Challenge faced by current EOR technologies

Although thermal method has been commercially used in heavy oil reservoirs in Canada, Brazil, China and USA, etc., it is facing big economic and environmental challenges. The use of steam for all steam-based injection methods, means an intensive energy consumption as well as large CO_2 emission ascribed to the steam generation from methane, increasing both the economic and environmental costs. The used water brings issues such as the handling of large volumes of liquids, and extra dehydration facility for oil and water separation [13]. The application of SAGD, specifically, is restricted by a series of geological and geometric factors, including sufficient reservoir thickness, high horizontal and vertical reservoir homogeneity for the formation of uniform steam chamber, and good permeability to enable the efficient flow of the fluids [56, 57].

While, issues related to gas flooding include segregation, viscous figuring, the concern of long-term CO_2 sequestration in oil reservoir, and stable source of CO_2 gas [10, 13].

Since 1970s, the US department of Energy conducted several pilot trials to evaluate the potential of surfactant/polymer flooding for enhanced oil recovery. Unfortunately the results are generally disappointing. Most oil recovered are generally less than 5% compared with water flooding, regardless of the chemical flooding technologies (surfactant/water, surfactant/polymer, surfactant/CO_2, foam, and surfactants/thermal recovery) [58]. However, some controversary information can be found from the review of Olajire et al. [8]: the earliest field testing of ASP flooding at West Kiehl, Wyoming had reached 26% OOIP with an additional price cost of less than $2.00 per incremental

barrel, over the next 2.5 years after its start. Another ASP pilot test, a Minnesula field located contiguous to the Kiehl field, increased recovery by 28% of OOIP (1,143,000 bbls) and incremental costs were estimated at 2.42 $/bbl. Other chemical oil recovery recordings include 21% OOIP for Cypress, 24% OOIP for Bridgeport, and 17% for Tanner filed.

In China, chemical flooding has been studied and tested for more than 20 years though with several pilots of different scales and there have been 13 field cases (pilots and commercial scale) reported. Among them, five are from Daqing and most of the cases are in small scale operations, and all in sandstone reservoirs. A tertiary pilot application of the ASP process initiated in Sept.1994 in the west central area of Daqing oilfield has increased the average pilot area oil production rate from 36.7 to 91.5 m3/d, and decrease the water cut from 82.7 to 59.7% [8].

ASP flooding is still facing some major challenges in produced fluid handling on its way to commercial application, such as selecting chemicals, large chemical quantities required, scaling of the well bore equipment, and surfactant precipitation, etc.[8]

With today's technology, Alkali-Polymer (AP) and Alkali-Surfactant-Polymer (ASP) floods are applicable to sandstone reservoirs only. However, surfactant-polymer (SP) seems to be a feasible recovery process in both carbonate (e.g., Midland Farm Unit, Texas) and sandstone reservoirs. Actually, surfactant injection is the only chemical method used recently as a well stimulation and wettability modification of carbonate reservoirs. In addition, chemical EOR methods are not expected to make an important contribution in oil production from carbonate reservoirs during the next one or two decades. However, chemically based gas and water shut-off strategies (e.g., gels and foams) will continue to contribute optimizing water, gas or WAG projects in carbonate reservoirs in the near future [59].

1.5.1 High cost for developing new surfactant

In selecting chemicals for an ASP flood, it is necessary to consider availability, quantities required, cost, performance, and logistics. All of these factors are critical due to the large quantities usually required to flood one field, which can run into the hundreds of millions of pounds [8].

Prior to the filed implementation of this technique, the research and development (R&D) of new EOR surfactant is usually expensive and takes long operation cycles, because key process parameters need to be optimized through a series of test procedures. Extensive screening test methods have been developed to minimize the cost and evaluated the potential increment recovery factor of the tested surfactant compositions [60-63]. R&D of new surfactants for EOR purposes should consider surfactant properties, reservoir rock wettability, brine salinity, and reservoir temperature and pressure, adsorption properties under static and dynamic condition and displacement studies under reservoir conditions [8, 13].

Generally, surfactant is composed of a hydrophobic group (non-polar and oil-soluble) and a hydrophilic group (polar and water-soluble). The non-polar group is usually hydrocarbon chain with 8-18 carbon atoms, which is may or may not branched, whereas the polar group is normally constituted by charged moieties. Based on the type of polar group, surfactant can be categorized into four groups: anionic surfactant containing negatively charged hydrophilic group (e.g. carboxylate (COO^-), sulphate (SO_4^{2-}), sulfonate (SO_3^{2-}), cationic surfactant bearing positive charge (e.g. cetyl ammonium bromide ($C_{16}H_{33}(CH_3)Br$), Laurylamine hydrochloride ($CH_3(CH_2)_{11}NH_3^+Cl^-$)), non-ionic surfactant whose polar groups in hydrophilic part is soluble in water regardless of no obvious charge overall (e.g. Polyoxyethylene alcohol $C_nH_{2n+1}(OCH_2CH_2)_mOH$, n=8-18, m=3-15), and zwitterionic surfactant having both positive and negative charge

(e.g. $RNH_2CH_2COO^-$ (long chain amino acid), $C_{17}H_{37}NSO_3$ (alkyldimethylpropanesultaine)) [64].

R&D of new class of polymer is also technically difficult or economically unfavourable due to very limited types of polymer to date. Presently there are two sets of polymer for enhancing oil recovery: synthetic polymers and biopolymers [63]. The most utilized polymers today are the synthetic and partially HPAM (hydrolysed polyacrylamide), the modified natural polymers and the biological polysaccharide, xanthan [64,65]. The natural polymers and their derivatives include HEC (hydroxyl ethyl cellulose), guar gum and sodium carboxymethyl cellulose, carboxyethoxyhydroxyethylcellulose.

1.5.2 High concentration required

The economics of surfactant EOR at the oil field site is usually determined by a bundle of parameters such as the cost of surface facilities, displacing fluids, and requirement of additional well drilling, royalty, taxes, and most significantly the price of oil [65]. However, the cost for surfactant, which includes the primary investment to purchase surfactant and the cost of tailoring surfactant needed to replace the surfactant absorbed in oil reservoir, is usually half or more of the total project cost [66, 67]. Therefore, surfactant flooding at lower surfactant concentration can reduce the overall cost significantly.

However, it is reported that the ionic surfactant should be implemented at the concentration above critical micelle concentration (CMC), and even for non-ionic molecular the surfactant should be used at the concentration around CMC [68]. At CMC concentration, surfactants tend to form micelles and all additional-added surfactants also form micelles. Considering the large scale of oil reservoir, large amount of surfactant is needed to formulate displacing fluid.

Surfactant flooding usually carried out in three forms: micellar, microemulsion and ASP, but many of them are used at concentration, as seen from the literature review below. For example of surfactant flooding in micellar, Bourrel et al. [69] reported that the O/W micellar contain 4-12% surfactant (also has 1-6% alcohol, 2-50% hydrocarbon, and 40-90% water), and the W/O micelles consist of 5-12% surfactant (also composed of 1-4% alcohol, 35-80% hydrocarbon, and 10-55% water).

Microemulsion is another type of surfactant flooding, which is also not commercially possible, because it usually constitutes of 2-6% surfactant and 1-5% cosolvent (alcohol) [70-72]. Flaaten et al. [73] used 2 wt% total surfactant concentration including 0.5 to 2 wt% co-solvent. Bera et al.[74] prepared the microemulsion with non-ionic surfactants (Tergitol 15-S-5, Tergitol 15-S-7 and Tergitol 15-S-9) at concentration of 0.4 wt% which is around their CMC. Even for ASP flooding, which is proposed to reduce the amount of surfactant required through the formation and sequestering of divalent cations and in-situ generation of synergetic surfactant with alkali in oil reservoir [35, 36], the concentration of surfactants used in pilot tests is usually 0.1-0.5% [75, 76], which is still higher considering the large amount of fluids required.

Research indicates that surfactant mixtures are more efficient to reduce IFT than a single surfactant. For example, Rosen [53] believed that surfactant with branched/multi hydrophobic chain, or a surfactant mixture can generate ultra-low IFT. The mixture of Aerosol TR and Aerosol OT at ratio of 1:8 can reach ultralow IFT value in all decane, dodecane, and tetra-decane, even at surfactant concentration lower than 0.06 wt%.

1.5.3 Retention in porous media

Retention of surfactant/polymer in the porous media (i.e. reservoir rock) is the main contribution to surfactant loss in chemical EOR processes. Retention is a term that

covers all the mechanisms inducing the concentration of surfactant/polymer in the bulk fluids when they propagate in the porous media.

1.5.3.1 Theory for surfactant/polymer adsorption

Investigation of surfactant adsorption is an old subject that usually based on the difference of surfactant concentration in solution before and after flowing through the rock. In general the adsorption of surfactant onto a solid surface is attributed to several forces including: electrostatic force, chemical interaction (covalent bonding), non-polar lateral interactions, hydrophobic interaction between the hydrocarbon chains and hydrophobic sites on the solid, hydrogen bonding, solvation, and desolvation energy [77]. The total adsorption is usually the integrated result of some or all of the forces above [78].

An adsorption isotherm is usually applied to indicate the depletion of surfactant due to adsorption. The adsorption isotherm for *ionic* surfactant absorbing onto a opposite charged surface, which is called 'Somasundaran–Fuerstenau' isotherm [78], can be subdivided into four regions when plotted on a log-log scale, as shown in Figure 1-8, which shows an example that the adsorption of sodium dodecyl sulfate on alumina [79]. The region I happens at low surfactant concentration and is due to the electrostatic interaction between the individual isolated charged surfactant species and solid surface. The adsorption isotherm is governed by Gouy–Chapman equation with a unity slope when the ionic strength is constant. In Region II, surfactant began to aggregate upon reaching a threshold concentration, and form solloids because of the lateral interactions between the adsorbed species. Under the accumulating results of lateral interaction and the still-active electrostatic interaction, the adsorption density soars up sharply. As increasing the surfactant concentration in Region III, the solid surface will be electrically neutralized by the surfactant ions. Thus lateral interaction is only the driving

force for surfactant adsorption, leading to a reduced slope. In Region IV, the surfactant concentration approaching CMC, any further increase in the concentration just give rise to the micellization in bulk solution, instead of changing the adsorption density.

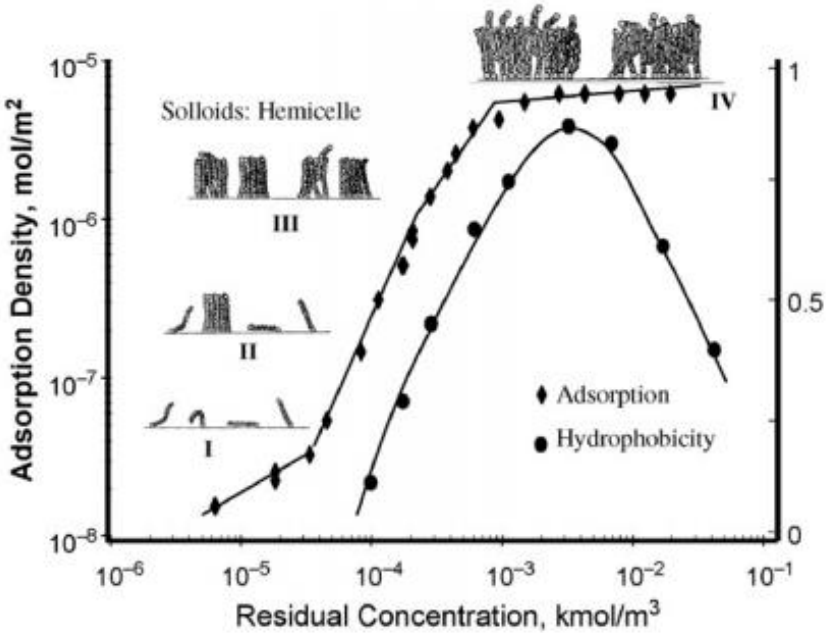

Figure 1-8. Isotherm for ionic surfactant adsorption on the opposite charged solid surface [71].

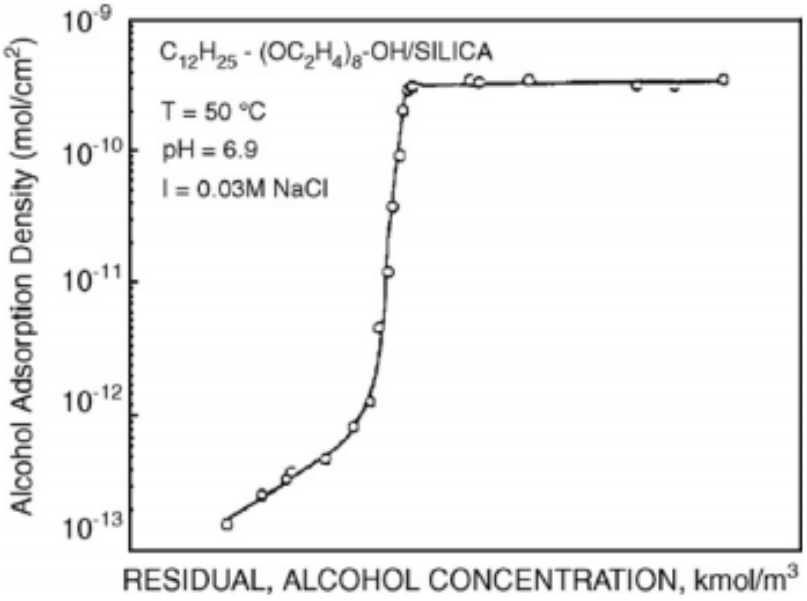

Figure 1-9. Non-ionic surfactant adsorption on solid surface [80].

While the for the non-ionic surfactant, the adsorption is usually reversible with little hysteresis (Figure 1-9). As the electrostatic attraction is not operative, the adsorption density is several orders of magnitude lower than that for ionic surfactant.

For the anionic-nonionic surfactant mixture, they usually synergistically absorb on the solid surface, which is attributed to the hydrophobic interaction between the two surfactants as well as the reduction of electrostatic repulsion between the anionic head groups which are shielded from each other by the nonionic surfactant molecules [81]. The initial electrostatic interaction provides sufficient hydrophobic site for hemimicellar type adsorption of nonionic species.

1.5.3.2 Review of surfactant retention

Many researchers have investigated the effects of different physico-chemical properties of solution, such as pH [18, 68], temperature and ionic strength on the retention of surfactant [22].

Higher salinity can compress the electrical double layer of the hydrophilic group of a surfactant that decreases the functional group's electrostatic repulsion in the adsorbed layer of rock. As a result, the adsorption of ionic surfactant typically increases with an increase of salt concentration [27]. Considering the phase behaviour of microemulsion, the Winsor III microemulsion at optimum salinity is favourable because the oil-microemulsion and water-microemulsion interfaces have equal and low IFT. When the salinity is higher than the optimum value, the surfactant can be trapped in the residual microemulsion in Type II conditions because the greater water-microemulsion IFT reducing oil mobilization. In contrast, salinity less than the optimal lower water-microemulsion IFT which can keep surfactant trapped in a lower phase microemulsion and increasing oil-microemulsion IFT [73]. Therefore, design stable surfactant system in saline aqueous environment and reducing surfactant retention are very important in

any chemical flood, since the soft water may be unavailable and soften the very hard, high salinity formation brine in the reservoir can be experience [73]. Fortunately, research in this area has achieved a lot by using surfactant mixture, and selecting high-performance surfactant.

Liu et al. [82] has shown that surfactant mixtures are aqueous stable at higher electrolytes and divalent cation concentrations. Flaaten et al. [73] conducted phase behaviour experiments for the microemulsion mixed by two high-performance surfactants: Petrostep®S1 (C_{16-17}- 7PO- SO_4^{2-}) and Petrostep®S2 (C_{15-18}IOS). Even in high salinity, the emulsion showed a good performance. Through core flooding and high performance liquid chromatography (HPLC) analysis, the surfactant mixture showed high oil recovery and low surfactant retention in a hard, saline environment without the need for a pre-flooding.

Bo et al. [83] showed the potential of utilizing Gemini surfactants in harsh reservoir conditions for EOR applications. Gemini surfactant molecules have excellent aqueous stability even in high salinity and properties that can lower maximum adsorption densities more than the conventional single chain surfactants.

Through phase behaviour, Ko *et al.* [83] found that D-type (branched) surfactant requires lower concentration to reach CMC, and both surfactants broke the emulsion phase at a salinity of 5 wt% NaCl.

Temperature and pressure also influences the adsorption of surfactant on reservoir rock surface. Bera et al. [22] illustrated that the adsorption capacity of surfactant decreases with the increase of temperature, which was due to the viscosity reduction that increased the rate of diffusion of the adsorbed surfactants molecule inside pores. Moreover temperature would change the adsorption capacity of the rock surface, depending on whether the adsorption process is exothermic or endothermic.

1.5.3.3 Review of polymer retention

The amount of polymer absorbed depends on the nature of the polymer and the rock surface. Retention of polymer mostly consists of polymer adsorption. Sometimes it may involve mechanical entrapment of polymer macromolecules in porous media, and to some extent hydrodynamically trapped polymer molecules in stagnant zones [8]. Zitha et al. [84] examined the influence of polymer concentration and permeability on the retention of high molecular weight non-ionic polyacrylamide (PAAm) during flow in granular porous media. Park et al. [85] found that concentration-induced polymer adsorption caused non-proportionally enhanced oil recovery with increase in polymer concentration below 1000 ppm, and decrease above 1000 ppm.

The retention mechanism for several common polymers, hydrolyzed polyacrylamide (HPAM) and polyacrylamide (PAM), in porous media have been known to some extent [86-88]. However, even though the viscosity and flooding properties of hydrophobically associating polyacrylamide (HAPAM) has been reported in several recent studies [86, 89], there is still insufficient study regarding their behaviour of retention in porous media. There could be large difference retention behaviour between HAPAM and PAM, due to the existence of hydrophobic associative groups on HAPAM backbone [90]. The research by Lu et al. [90] shows that the dynamic and static retention of PAM was smaller than that of HAPAM correspondingly. For both the HAPAM and PAM, the static retention was higher than dynamic retention.

1.5.4 Chemical degradation

1.5.4.1 surfactant degradation

Another type of chemical loss could be the degradation of surfactant/polymer in reservoir. Karnanda et al.[91] explained that most of the surfactant solutions have a cloud point temperature beyond which the surfactant becomes ineffective and drops out

of the aqueous solution, and the solution becomes cloudy and measuring the IFT or other parameters become almost impossible. Surfactant phase separation at high temperature could lead to the reduction of surfactant concentration in aqueous phase, thus exhibiting poor performance to reduce IFT. Most of the experiments in the literature indicate that temperatures above 120 °C results in either degradation or precipitation of most of the surfactant.[92]

1.5.4.2 Polymer degradation

Many of polymers typically also suffer from degradation in reservoir environment, resulting in precipitation and chemical degradation at high salinities and temperature . For instance, weak polyelectrolytes, poly (acrylic acid) (PAA), is water-soluble with the presence of 1 M NaCl at relatively high temperatures but tend to precipitate when divalent cation Ca^{2+} is introduced at room temperature [93-95].

Partially hydrolyzed polyacrylamides (HPAM) is widely used as a polymer additive for mobility control in oil reservoirs, and it has been tested at the field scale [86, 96, 97]. However, it has been found that there are a few problems hindering the successful application of HPAM for EOR applications, notably the polymer degradation issue under high temperature and high salinity conditions [98].

As most of the reservoirs that requires EOR have high temperatures, for example the temperature in Shengli oilfield in china is above 85 °C [99], and there are thousands of oil and gas well with temperature up to 120 °C [100], HAPM would experience a serious viscosity reduction under such temperatures, which would be caused by the impairment of hydrophobic effects due to the increased mobility of the polymer chains and the resultant loss of inter-chain liaisons and increased copolymer solubility [101-103].

Another problem is the poor salt resistance of HPAM in hot oil reservoirs. The salinity in a real oil field are usually high, for example, the API brine contains 8 wt%

NaCl and 2 wt% $CaCl_2$ (i.e., 1.8 M total ionic strength) [104], and the salinity of Shengli oilfield in China is usually higher than 30,000 $mg \cdot L^{-1}$ in which the total amount of Ca^{2+} and Mg^{2+} exceeds 800 $mg \cdot L^{-1}$. For temperature above 60 °C, the acrylamide groups within the HPAM polymer would experience a hydrolysis process to form acrylate [98] or carboxylic [105] groups. The final hydrolysed anionic polyelectrolytes are sensitive to the presence of inorganic salt (especially divalent cations such as Ca^{2+} and Mg^{2+}), which is commonly present in oil reservoirs. If the degree of hydrolysis become too high, HPAM polymer tends to precipitate due to the complexes formed between the polymer and divalent cations [106]. In addition, the shielding of the mutual repulsions between carboxylic groups along the HPAM skeleton leads to the decrease of hydrodynamic volume, resulting in a viscosity reduction [107-109]. It has been shown that the higher salt concentration always corresponds to a lower temperature limit for the applicability of HPAM for EOR applications [110].

1.6 Research Motivation

Nanotechnology is a science regarding the manipulation of matter in an atomic, molecular, or supramolecular scale, involving very small structures in the 1 nm to 100 nm range. Nanoparticles are therefore of great interest to the oil and gas sector at the moment for a variety of reasons, mainly due to their small size, large surface/volume ratio, modifiable surface, transportation abilities for other materials, and customizable migration properties.

Recently, nanoparticles (NPs) has been proposed as a potential material to improve reservoir characterization and to increase oil production [111-113]. Compared to conventional chemicals applied in oil/gas reservoirs, nanoparticles (NPs) possesses several advantages. It is thought that the small size of particles (< 100 nm) would allow them to pass through pore throats of a reservoir rock and be delivered to the parts of the

pore network where they can make an active and significant difference in some way. The addition or deposition of different nanoparticles could modify the displacing fluid effective properties such as viscosity [114-116], IFT [117, 118], and dielectric properties [119], change the permeability of the rock matrix [120], or alter the rock surface wettability [118, 121]. In addition, the size-dependent properties (i.e., optical, magnetic, electrical, thermo-physical and interfacial properties) of NPs can be used as sensitive down-hole sensors to target locations that are inaccessible by conventional methods [113, 122, 123].

Because of low EOR efficiency and techniques uncertainties faced by chemical EOR and engineered water flooding, as reviewed in Section 1.5, particular attention is given to engineered water flooding and chemical EOR in my serial studies in this thesis. The main motivations are included below:

- Waterflooding is not usually regarded as EOR process unless it is combined with some other flooding methods. Here we will use nanoparticle to modify the water flooding as EOR process, in the meantime explore the possible mechanism associated with NPs-assisted water flooding.

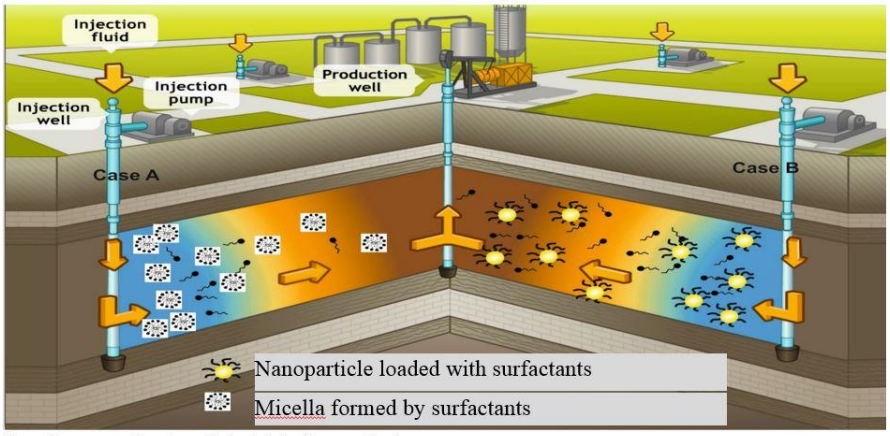

Case A: conventional surfactant injection method;
Case B: enhanced surfactant delivery by using nanoparticle, nanoemulsion, encapsulated surfactant, etc. and triggered release of surfactant when contacting with oil phase, or approaching the area in interest.

Figure 1-10. Enhanced surfactant delivery for improving the efficiency of surfactant flooding process. Picture is adapted from Ref. [124]

- Reduce the retention of surfactant in porous matrixes. Instead of inventing novel surfactant, the usage of present surfactant can be improved to reduce the adsorption, precipitation and phase changes in reservoir rock (Figure 1-10).
- Add nanoparticle in emulsion to stabilize the structure and increase its viscosity;
- Investigate whether the nanoparticle can improve the polymer's thermal and salinity tolerance in the reservoir environment;
- Nanoparticle transport behavior in reservoir environment is related to its majority of the applications, thus investigating the particle transport behavior in reservoir environment is necessary.

1.7 Thesis outline

The layout of this thesis is shown in Figure 1-11.

Chapter One: Introduce the industry-related background information and basic theories of enhanced oil recovery . A comprehensive review of the challenges associated with current EOR is done is this chapter.

Chapter Two: Literature review of nanoparticles for enhanced oil recovery application and the proposed mechanisms found in current literatures. Two main common issues related to EOR, namely nanoparticle stability and mobility in reservoir, are also clarified in this chapter

Chapter Three: This chapter studies the EOR potential through core flooding experiment by using TiO_2 nanoparticle and examines the current mechanisms proposed in literature to explain the observed EOR effects. As nanoparticle is stabilized by surfactant which would also contribute to the oil recovery, this chapter is also to identify the contributions from the stabilizer and the nanoparticles, and discuss the possible oil recovery mechanisms applicable in the nanoparticle-assisted recovery process.

Chapter four: This chapter is to demonstrate the concept of using engineered nanoparticle as carrier to reduce the surface retention in porous media and thus as an alternative way to improve surfactant flooding efficiency instead of inventing new category of surfactant. The retention property of surfactant coupling with TiO_2 NPs was investigated in five different types of reservoir rock, to evaluate the influence of substrate on surfactant retention.

Chapter Five: in this chapter the iron oxide NPs were synthesized in the oil-in-water (o/w) microemulsion by an *in-situ* method which is distinguished to the pre-fabricated method. The joint network composed of nanoparticle and surfactant are thought to strengthen the texture of o/w emulsion shell, to improve the viscosity of microemulsion, and to prevent the surfactant from detaching with the interface, thus improve microemulsion's core flooding performance.

Chapter Six: In this chapter, HPAM solution seeded by SiO_2 nanoparticle as crosslinker were prepared, and the rheological properties of hybrids were investigated under high temperature. The impact of various nanoparticle loadings, temperatures, aging time and electrolyte concentrations on the rheological behaviour were investigated. The dynamic viscosity and viscoelastic properties were also checked to clarify the contribution of NPs on the improvement of polymer rheological properties.

Chapter Seven: carbon dots (CDs) was found in this chapter to have a good transport ability in glass column packed with micro glass beads, regardless of the influence of nanoparticle concentration and ionic strength. As the CDs are strongly hydrophilic, their good mobility were applied to detect the oil saturation.

Chapter Eight: Main conclusions and suggestions for future work are provided here.

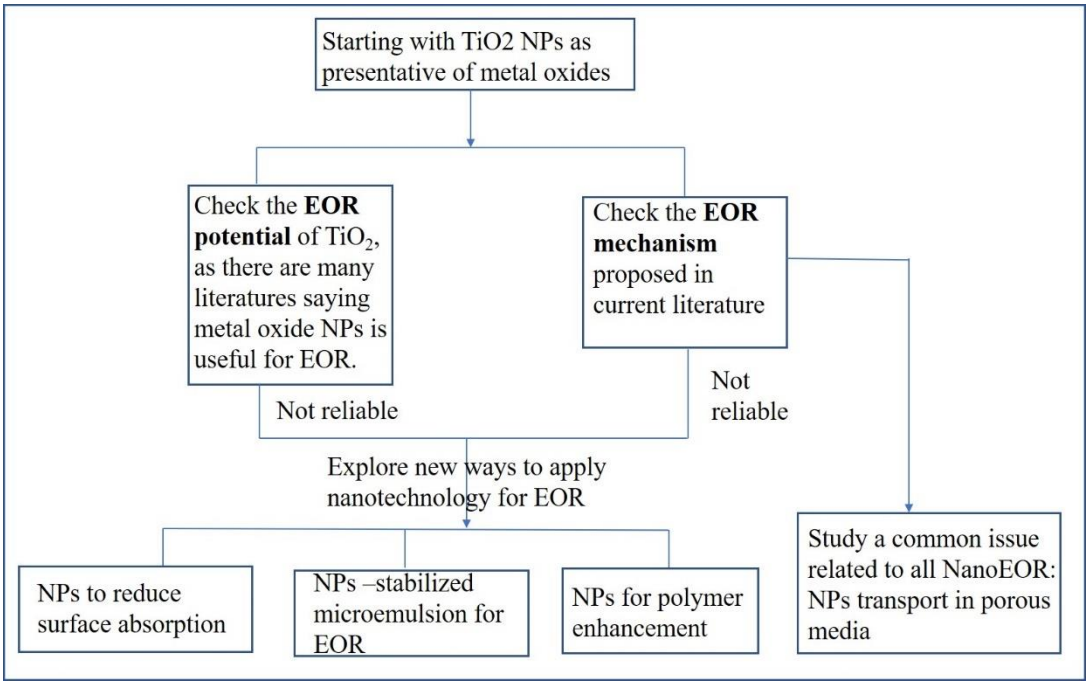

Figure 1-11. Layout of the thesis

Chapter 2

Literature review

2.1 Nanoparticle for upstream hydrocarbon exploration

The use of NPs for upstream industry has received intensive attention since 2008, when an internationally recognized research organization, Advanced Energy Consortium (AEC), was founded by the University of Texas at Austin's Bureau of Economic Geology, to achieve transformational understanding of subsurface oil and natural gas reservoir through the deployment of unique micro- and nano- sensor [125]. Since then, much work has been conducted and can be generally categorized as (see Table 2-1), (i) the development of 'contrast-agent' type of NPs to improve the detection limitation of seismic and electromagnetic (EM) techniques and to provide better reservoir characterization [122, 123, 126]; (ii) the use of NPs as property modifiers, i.e., to alter rock wettability and IFT at the oil/water interface in order to increase oil recovery rate [117, 118, 121, 127]; (iii) the use of NPs for conformance control such as nanoparticle-stabilized emulsions, and gelation materials to block easy flow paths [128, 129]; (iv) the use of NPs as additive to develop smart drilling fluids by optimizing its properties like yield stress, viscosity, gel strength, fluids loss, and filter cake surface morphology [130-133]. Nanoparticle for EOR application will be described specifically in Section 2.2.

Table 2-1. Challenges faced by the oil and gas industry and solutions that nanotechnology offers

Industry Challenge		**Nanotechnology Resolution**
Reduced downtime and better component lifetime	Drilling bit lifetime	Anti-wear coatings
	Pipe and tanker corrosion	Anti-corrosion coatings
	Gas hydrate formation	Dendrimers
	Marine fouling	Anti-fouling coatings
	Fines migration	Nanoparticle adsorption of and removal of fines
Filtration and separation of oil emulsions before downstream	Gas separation	Nanoporous membranes
	Toxic metal removal	
	Oil water separation	
Improvement of catalysts lifespans and operating efficiencies	Nanocatalysts	
Heavy oil displacement and recovery	In-situ nanocatalysts	
Recovery of vast amount of residual oil left in reservoirs	Nanoparticles-modified drilling muds	
	Nanosensors for reservoir characterisation	
	Nanoparticles dispersions in surfactant flooding	

2.2 Nanoparticles for enhanced oil recovery application

Following an explosion of hype and speculation, use of nanoparticles for chemical EOR is beginning to see some advances. However, it has to be admitted that the research in this field is just at the beginning. Most of the studies are at the laboratory scale [134] and many contradictory results have been reported, especially regarding the effect of nanoparticles on EOR. For instance, Hendraningrat et al. [135] showed that the

maximum oil recovery was increased by 14.29% of OOIP by using SiO_2 nanoparticles, whereas Bayat et al. [112] observed only a 2% increase over OOIP for enhanced oil recovery using SiO_2 nanoparticles.

2.2.1 Nanoparticles-assisted water flooding

In the past few years, there had been extensive research about using naked nanoparticles or functionalized nanoparticle for enhanced oil recovery. However, the investigations, ranging from what type of particle is good for EOR, what concentration is beneficial, through to the mechanism of nano EOR and to what extent the nanoparticles can increase the oil recovery, are far from conclusive and definite. Some conflicting results are review below.

Bayat et al. [112] applied Al_2O_3 (40 nm, 60 m^2/g), TiO_2 (10- 30 nm, 50-100 m^2/g), SiO_2 (20 nm, 160 m^2/g) at low concentration of 0.005 wt% as the agent for enhanced oil recovery in intermediate limestone at various temperature. They found that Al_2O_3 had the better ability to reduce capillary force and the lowest tendency to be adsorped in porous media, which is followed by TiO_2. Core flooding experiments show that both Al_2O_3 and TiO_2 showed better results in EOR compared to SiO_2 at all temperatures. Similar to Bayat et al's research, Ehtesabi et al. [136] found the 0.01% anatase TiO_2 NPs solution could recover 80% of the oil after injecting two pore volumes at optimum conditions at optimum conditions, while water recovered only 49%. The mechanism is attributed to wettability change towards water wet.

However, silica NPs is the most widely used nanoparticle in the literature for EOR applications. Counter to Bayat's research, Safari et al. [137] aged the carbonate core in the lipophobic-hydrophilic polysilicon nanoparticles with concentration ranging from 0 to 0.5 wt% for 20 days. The experiments show that increasing nanoparticle concentration caused a reduction in the contact angle, for oil depositing on carbonate

cores, from initial contact angle of 87°. There were no oil recovery experiments in this study. Roustaei et al. [117] used the partially hydrophobic fumed silica (AEROSIL R 816) in water-wet sandstone for flooding experiments, yielding up to 25.43% oil recovery. The research carried out by Li et al. [118] showed that hydrophilic silica NPs can reduce the IFT between the oil and water phase, thus releasing the oil trapped by capillary force, and resulting in an increase in recovery of about 4-5% compared to brine flooding. Maghzi et al. [138] found that the ultimate efficiency for silica nanofluid (0.1 wt%) flooding increased by a factor of 8.7% in comparison to distilled water flooding. Hendraningrat et al. [135] employed hydrophilic silica at three concentrations of 0.01, 0.05 and 0.1 wt%, and observed that IFT decreases as nanofluid concentration increases and that indicates a potential for EOR. The displacement efficiency was as high as 14.29%. Similar work conducted by Li et al. [118] in glass micromodel flooding system, showed that injecting hydrophilic silica NPs (0.01, 0.05 and 0.1 wt%) at 7 nm into sandstone (300 -400 mD) after brine flooding can increase the oil recovery about 4-5% compared with brine flooding. The mechanism is attributed to the reduced IFT and tailoring of the wettability of solid surface towards more water wet. Maghzi et al. [138] found that the ultimate efficiency for silica nanofluid (0.1 wt%) flooding increased by a factor of 8.7% in comparison to distilled water flooding. This increment in oil recovery was raised to 26% by increasing silica NPs weight percent from 0.1 wt% to 3.0 wt%.

With the advancement in nanosciences, some researchers have investigated the use of other metal oxides NPs and proven their ability as EOR agents and their advantages over SiO_2 NPs. Ehtesabi et al. [127, 136] found that anatase TiO_2 NPs in low concentration (0.01%) could recover ultimate 80% of the OOIP after injecting two pore volumes at optimum conditions on a laboratory scale, while water flood only recovered 49% of oil. Meanwhile, Haroun et al. [139] proposed a new EOR method, called

electrokinetics (EK)-assisted nanofluid flooding. They compared the ultimate oil recovery performances of several NPs (Fe_2O_3, CuO and NiO) flooding, immediately after the waterflooding stage with or without the assisstance of EK (direct current voltage of about 2 V/cm) in the carbonate cores from Abu Dhabi reservoirs, and found that CuO produced better results than Fe_2O_3 and NiO due to exhibiting both higher density and electrical conductivity.

Luo et al. [140] are the first to present the tertiary oil recovery experiments by using graphene-based Janus amphiphilic nanosheets at a low concentration at 0.005 wt% and 0.01 wt%. The result from core flooding measurements showed that the oil enhancement efficiency is 15.2%. The enhanced oil recovery is attributed to several mechanisms (Figure 2-1): (i) the accumulation of nanosheets at the oil–water interface, (ii) the appearance of climbing films, and (iii) the generation of elastic interfacial films may be responsible for the high oil recovery efficiency.

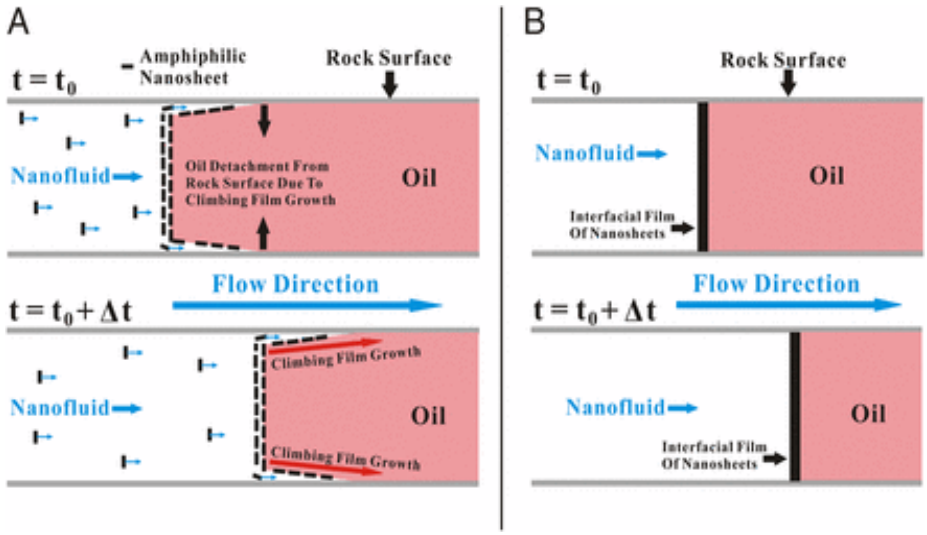

Figure 2-1. Schematic illustration of oil displacement mechanisms. (*A*) Climbing film encapsulation mechanism for water-wet surface. (*B*) Slug-like displacement mechanism. The figure is taken from [140].

In conclusion, research using non-functionalized nanoparticles for EOR is sometimes controversary in terms of the parameters such as nanoparticle type,

concentration, EOR effects and mechanisms. The reason behind this could be due to conflicting EOR mechanism, and nanoparticle dispersibility/mobility problems in harsh reservoir environments (high temperature, high pressure, high salinity, existence of oil phase and porous media), and most experiments were done in the lab, as would be reviewed in Section 2.4. One approch to improve the dispersibility of nanoparticles and tailor their properties for EOR application is to covalently attach surfactant or polymers to the nanoparticle surface, which is regarded as nanoparticle-assisted surfactant or polymer flooding in the lieterature review below.

2.2.2 NPs as surfactant carrier

One of the critical issues in enhanced oil recovery is the loss of surfactants due to their adsorption on reservoir rocks [20, 141]. Adsorption of surfactant in reservoir rock would increase the quantity of surfactant needed, resulting in a lower economic viability. Moreover, surfactant loss by adsorption impairs the reduction of oil/water IFT, leading to decrease of EOR efficiency [9].

In the oil reservoir, the adsorption isotherm depends, to a large extent, on the type of surfactant used, and the morphology and mineralogy of reservoir rock. It is also determined by the presence of other surfactants/polymers/alcohols [142], pH, the type and strength of electrolytes in formation water[143]. For example, the adsorption of an anionic surfactant system blended by nonylphenyl-6-ethoxy-sulfonate (6EOS) and dodecyl-benzene-sulfonate (DDBS) was studied by Fjelde et al. [68] using static (in kaolinite) and long-term dynamic adsorption (in North Sea reservoir core). Both cases showed that a selective adsorption takes place from the dual system until the most stable micelles was obtained and the adsorption of DDBS is remarkable higher than that for 6EOS. Alhassawi et al. [67] studied the adsorption of Sodium dodecyl sulfate (SDS) in free- and complex- state on solid surface mixed by sandstone, oil shale, and kaolinite.

The results show that without complexing with β-cyclodextrin, the adsorption of SDS was 64–76% higher when inclusion in a complex case. Curbelo et al. [142] investigated the adsorption of two non-ionic surfactants in sandstone cores with different ethoxylation degrees. The results show that ENP95 with a smaller ethoxylation degree of 9.5 has a higher adsorption than ENP150 with a higher ethoxylation degree of 15. ShamsiJazeyi et al. [20] examined the competition adsorption between anionic surfactant blend (constituting Neodol-67 and IOS15-18) and sodium polyacrylate on dolomite, and found that sodium polyacrylate with molecular weight above a critical value can reduce the surfactant adsorption significantly, while the adsorption of sodium polyacrylate was not influenced. According to Bera et al.'s research [22], the anionic (SDS) and non-ionic surfactant (Tergitol 15-S-7) showed higher adsorption efficiency on clean sand particle at low pH, but the cationic surfactant (CTAB) show the opposite trend. Increasing salinity facilitates the adsorption of SDS on the clean sand particle.

Nanoparticles (NPs) have been widely used for controlled drug delivery in the nanomedcine field [144-149]. Due to tailoring or potentially-better mobility of nanoparticle in porous media, the ability of nanoparticles as a carrier for surfactants/polymers in porous media is one of the emerging implementations of nanotechnology for enhanced oil recovery processes [19, 20, 150].

However, research in this concept, taking nanoparticle as surfactant/polymer carrier for controlled delivery, is just at the emerging phase. Zargartalebi et al. [19] showed that the adsorption of surfactant on rock surface was generally reduced in the presence of nanoparticles. Liborio De Avila et al. [150] also evaluated the usage of polystyrene nanoparticles as surfactant carriers able to pass through the porous media to deliver surfactant at the water/oil interface. They concluded that nanoparticles coated with nonylphenol ethoxylate were successful to reduce the water/oil interfacial tension and had potential to be used as surfactant carriers for EOR. Yu et al. [151] found that

particles stabilized by polystyrene sulfonate-alt-maleic acid show a good adsorption tendency at the oil/water interface but low adsorption at the rock surface (~0.02 mg/m^2), which could contribute to less surfactant adsorption at the solid surface. In summary, due to the small number publications in this field, studying the nanoparticle as surfactant carrier and reducing surfactant adsorption on rock surface is far from conclusive and sufficient to justify the concept, due to the limitations now described below:

Previous research lack investigation of the effects of different type of reservoir rock on nanoparticle as a carrier for controlled surfactant delivery. It has been long recognized that the rock surface energy and surface chemistry could significantly affect the behaviour of surfactant adsorption and NPs retention [152-154]. Careful characterization of the rock surface is fundamental to understand the particles effects on the wettability, the adhesion force and the behaviour of pore-scale flow [133, 155]. Consequently, it is still unclear if NPs can work as an effective surfactant carrier for enhance oil recovery applications in all types of reservoir rock.

In addition, there is not any information or discussion about retention of NPs inside porous media and its effect on surfactant delivery in porous media. Conversely, most research to date is emphasising how the presence of surfactant affects the transport behaviour of NPs in porous media [156-160], instead of focusing on the concept of using nanoparticles to facilitate surfactant delivery in porous media.

2.2.3 NPs-assisted microemulsion flooding

Surfactant flooding has being commercially used at pilot scale for enhanced oil recovery after primary and secondary recovery particularly in USA and China [161]. In surfactant flooding, adsorption of amphiphilic surfactant at the oil/water interface reduces the IFT and consequently reduces the fluids capillary force and mobilizes the oil trapped after waterflood process. However, surfactant is usually not sufficient to

increase the viscosity of displacing fluids, hence polymers are usually needed in surfactant slug to increase the viscosity of the injected fluids. The efficiency of surfactant EOR also drops due to the impairment of IFT reduction between residual water and crude oil caused by elevated temperature, unfavourable salinity and surfactant adsorption in oil reservoir [20], which would ultimately reduce the economic availability of this technic.

2.2.3.1 Microemulsion for enhanced oil recovery

Compared to surfactant flooding, microemulsions have been used as potential candidates for chemical EOR, because of its higher ability to generate ultra-low IFT [161] and higher viscosity than general surfactant solutions [16]. As a consequence, the additional recovery in the case of microemulsion flooding is higher than surfactant flooding [16]. A successful microemulsion flood pilot test has been completed by Exxon in a watered-out portion of the Weiler sand, Loudon Field, Fayette County, Illinois, USA [161]. In 1963 Marathon Oil Company also used microemulsion flooding, known as the Maraflood process, to displace petroleum from reservoir rocks for the first time [9]. Afterwards numerous studies have been under taken to assess the properties of microemulsions, especially viscosity, surface tension and resistivity in EOR [16].

However, the oil-in-water emulsion stabilized by traditional surfactant, or polymer, can be degraded or deformed gradually in the oil reservoir by the surrounding high temperature and high salinity [129, 162], and the mobility control by this surfactant-stabilized emulsion is usually not sufficient to some extent [129].

2.2.3.2 Phase behaviour of microemulsion

Phase behavior screening helps robust evaluation of favorable microemulsion formulations. Winsor [163] first described the phase behavior of microemulsions, which include four general types of phase equilibria:

- Winsor I: the surfactant is preferentially soluble in water and oil-in-water (o/w) microemulsions form. The surfactant-rich water phase coexists with the oil phase where surfactant is only present as monomers at small concentration.
- Winsor II: the surfactant is mainly in the oil phase and water-in-oil (w/o) microemulsions form. The surfactant-rich oil phase coexists with the surfactant-poor aqueous phase (Winsor II).
- Winsor III: a three-phase system where a surfactant-rich middle-phase (microemulsion) coexists with both excess water and oil surfactant-poor phases. It contains almost all of the surfactants in the system. Therefore, it has ultra-low interfacial tension. Middle-phase microemulsion is also called type III, or Winsor type III. This microemulsion is crucial in enhanced oil recovery. Therefore, the favourite composition of a microemulsion for enhanced oil recovery is Winsor type III [16].
- Type IV: a single-phase (isotropic) micellar solution, that forms upon addition of a sufficient quantity of amphiphile (surfactant plus alcohol).

Depending on surfactant type and sample environment, types I, II, III or IV form preferentially, the dominant type being related to the molecular arrangement at the interface. As illustrated in Figure 2-2, phase transitions are brought about by increasing either electrolyte concentration (in the case of ionic surfactants) or temperature (for non-ionics). Table 2-2 summarizes the qualitative changes in phase behaviour of anionic surfactants when formulation variables are modified [22].

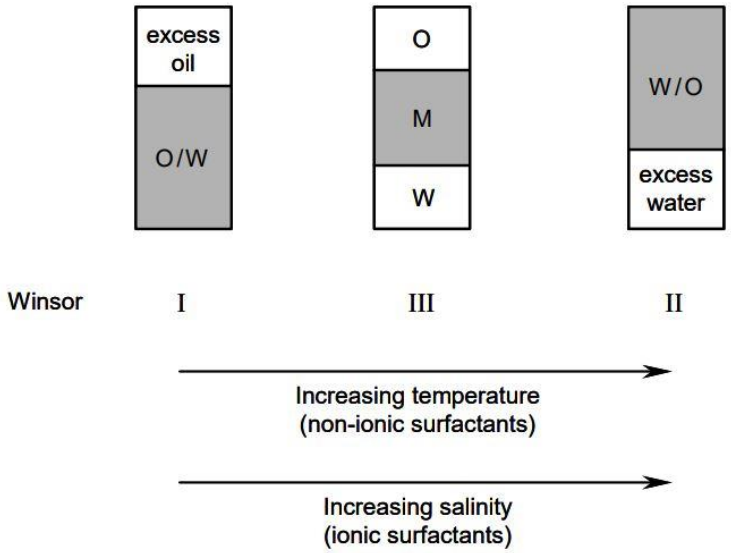

Figure 2-2. Winsor classification and phase sequence of microemulsions encountered as temperature or salinity is scanned for non-ionic and ionic surfactant respectively. Most of the surfactant resides in the shaded area. In the three-phase system the middle-phase microemulsion (M) is in equilibrium with both excess oil (O) and water (W).

Table 2-2. Qualitative effect of several variables on the observed phase behaviour of anionic surfactants. Taken from Ref. [164].

Scanned variables (increase)	Ternary diagram transition
Salinity	I ⌫III ⌫II
Oil: Alkane carbon number	II ⌫III ⌫I
Alcohol: low molecular weight	I ⌫III ⌫II
Alcohol: high molecular weight	I ⌫III ⌫II
Surfactant: lipophilic chain length	I ⌫III ⌫II
Temperature	II ⌫III ⌫I

2.2.3.3 Nanoparticle-assisted microemulsion for flooding

Nanoparticles are very active and energetic materials with a high tendency to form nanotextured surfaces in combination with surfactants, resulting in a significant change in the interfacial properties of the system . Nanoparticles can also be used to stabilize emulsion and beyond that NPs-stabilized or co-stabilized emulsion has several advantages over sole surfactant(s)-stabilized emulsion.

Firstly, nanoparticles can stabilize microemulsion at a low concentration. Zhang et al. [165] found that stable toluene-in-water emulsions can be formed both at 24 °C and 55 °C, with nanoparticle silica concentration only higher than 0.2 wt%. Pei et al. [129] presented that emulsion stabilized by 0.1 wt% CTAB and various concentration of silica NPs (NP20) ranging from 0.01 wt% to 0.50 wt% remain stable over the tested period of 60 days, and even the smallest concentration of 0.01 wt% gave the best equilibrium stability.

Secondly, microemulsions stabilized by nanoparticles have better temperature tolerance, higher viscoelastic properties and enhanced surface viscoelasticity. Sun et al. [166] found that the half-life time of SiO_2/SDS foam was increased significantly compared to SDS foam. The long-standing shape of SiO_2/SDS foam revealed the increased viscoelasticity due to the adsorption of SiO_2 at the interface preventing the foam interfacial layer from deforming. Zhang et al.[167] also presented that NPs can induce highly stable emulsion by being irreversibly attached at the o/w interface and forming a nanoparticle monolayer. Their experiments show that extremely stable toluene/water and water/toluene emulsions, as well as stable CO_2-in-water[167], can be made when silica NPs' concentration is 0.5 wt% or higher. Zaid et al. [168] found that the emulsion which is created by adsorption of surfactant coated NPs at the O/W interface had a higher viscosity than its original components, thus adding another mechanism to oil recovery by controlling the W/O mobility ratio.

Thirdly, addition of nanoparticle can facilitate the mobility control for heavy oil recovery. Through phase behaviour and rheology tests, Pei at al. [129] found that adding nanoparticles in the system of surfactant-stabilized emulsion can not only improve the emulsion stability, but also the bulk viscosity. The coreflooding experiments further confirmed that, co-stabilized by NPs and surfactants, emulsion showed a remarkably higher oil recovery efficiency than that without nanoparticles, because NPs thicken the

mobility of emulsion thus improve the sweep efficiency which is observed in the microchannel. Esmaeilzadeh et al. [169] found that adding negatively charged ZrO_2 NPs considerably increased the surface activities for all of the investigated surfactant: SDS, CTAB and LA7 and decrease the IFT, which is beneficial for mobilizing oil at the microscale.

Last, but not the least, nanoparticles can improve the economic viability by reducing surfactant usage and retention in reservoir rocks [19, 170, 171]. According to Zaid et al. [168], introducing particles led to *in-situ* emulsification even when the surfactant concentration was lower than the CMC. which led to the conclusion that reducing IFT is not necessary for higher oil recovery efficiency. Yang et al. [172] explained that an increase of surface tension or IFT between surfactant coated nanoparticles and air/oil phase may be caused by the decrease in the free surfacnt molecules present in the solution due to the surfactant adsorption on the surface of the nanoparticles.

2.2.4 NP-assisted polymer flooding

The most utilized polymers today are synthetic and partially hydrolysed polyacrylamide (HPAM), the modified natural polymers and the biological polysaccharide, xanthan [173, 174]. HPAM has attracted a great deal of attention in the petroleum industry over the last a few decades, ranging from the treatment of waste water produced from oil extraction [175], low-grade oil sand ore processing [176] to EOR [177, 178].

To alleviate the problems mentioned above in Section 1.5.4, a few strategies have been applied to improve the performance of HPAM during flooding, which can be categorised as: mobility control, copolymerization, and forming organic /inorganic nanocomposites. For example, research [179, 180] showed that by forming polymers with low-enough mobility, the freshwater polymer bank could displace the oil and brine

ahead of it with the minimum mixing in high salinity reservoirs. Various functional groups such as the sulfoacid group, annular material, and hydrophobic monomers have been introduced into PAM for copolymerization [181, 182]. The copolymerized acrylamide with a monomer group 2-acrylamide-2-methylpropane sulphonic acid (AMPS) showed similar properties to that for HPAM [98].

However, as reviewed in Section1.5, polymer flooding is usually hindered by material retention and thermal and salt degradation in oil reservoir, and the cost to develop and test novel polymers is usually high. Adding properly-selected inorganic nanoparticles into polymer solutions can reinforce the intermolecular hydrophobic associations by forming polymer/inorganic nanocomposite hydrogels, and improve the rheological behaviour of polymer solutions. It is expected that the hybridization of appropriate nanoparticles with a polymer could improve its bulk mechanical, and the thermal properties by strengthening the network structure of polymers. To date, main inorganic constituents that have drawn attention including clay minerals [183-185], layered double hydroxides (LDHs) [186-188], CNTs [189] and graphene oxide (GO) [190, 191] and metal oxide nanoparticles [192], etc.

Parizad et al. [193] added SnO_2 NPs into xanthan gum in order to improve the water-based drilling fluids' performance. It was found that electrical conductivity and thermal conductivity were increased by 30% and 15%, respectively. Research by Kennedy et al. [194] showed that adding 10% NPs in xanthan gum gave rise to enhanced viscosity and viscoelastic moduli. Moreover, ramping temperature from 25 °C to 85 °C, the complex modulus for solution of Xanthan gum containing 10% SiO_2 was relatively constant, indicating that nanoparticles counteracted the effect of temperature on the material properties.

The dispersion of SiO_2 nanoparticles into a HPAM to form HPAM/silica nanocomposite hydrogel has been recently investigated. Bhardwaj et al. [192] reported

that synthesised PAM-SiO_2 nanocomposites showed improved thermo-resistance and high thermal stability behaviours. Maghzi et al. [195] showed that the viscosity of PAM was increased by introducing SiO_2 nanoparticles and the oil recovery efficiency was also 10% higher during a polymer flooding process.

It shall be noted that most of these studies were either focused on the temperature effect or the salinity effect, and experiments were performed in a limited range with insufficient understanding of NPs loading on the variation of NPs/polymer hybrids, and how the polymer entanglement structure is changed with adding nanoparticles. The long term behaviour of the formed nanocomposites (i.e., up to a few weeks) under reservoir-like conditions is also little understood.

2.2.5 NPs for reservoir characterization

2.2.5.1 The limitation of traditional reservoir probing methods

One overriding problem for successful water flooding or tertiary exploration is related to the probing and mapping subsurface reservoirs that cannot be seen. However, in practice there are many assumptions, involving a bench of parameters like reservoir geometry, fluid properties, reservoir depth, lithology and rock properties, hydrocarbon saturation, etc., made by reservoir engineer in the modelling of a large volume of formation [251]. Taking the carbonate reservoirs, which contain 50-60% of the world's oil and gas reserves [252], as an example, many low-matrix-porosity carbonate reservoirs are productive because permeability is controlled by fractures and faults. Understanding basic fracture properties is critical in reducing geological risk and therefore reducing well costs and increasing oil recovery.

Lowering probes into boreholes is one of the traditional ways to acquire information from the oil reservoir, but the information is insufficient by being sourced from a single 6-inch hole [253]. Images obtained through seismography, on the other hand, is another

way to map the reservoir. However, it gives too broad a view due to their imaging quality and resolution inadequacies [251, 254]. For example, in carbonate rock formation, fractures having apertures that are measured in millimetres, or geobodies only centimetres across, allow fluids moving at several Darcies, and by-pass matrixed oil. These kind of dimensions cannot be detected by seismic devices and data from logging is handicapped by insufficient resulting data. Subsequently, the fault lines drawn on reservoir structure maps cannot depict an actual permeability pathway. Furthermore, a solid understanding of the regional stress-strain regimes is needed in order to filter out fracture swarms which may not be contributing to premature fluid breakthroughs. Even combing these two ways together, does not enable for the mapping of these high-permeable fractures or geobodies.

Techniques using natural tracers and isotopes, as well as various artificial tracers, are now contributing to obtain the flow pattern, velocity field and well continuity, and the data can also be used to upgrade a reservoir model. For example, the combination of partitioning tracer and conservative tracer was used to estimate non-aqueous-phase liquid (NAPL) in porous media [255, 256]. Adding well-specific DNA-based tracer to the hydraulic fracturing fluid, enable determination whether connectivity exists between drilling sites and ground or drinking water, thus reducing the issue of uncertainty in liability and improving information on well maintenance [257].

However, current tracers suffer from some limitations. The dye and radioactive chemical tracers can be helpful locally, but generally do not reveal the actual pathway that is taken by the host fluid from the entry well to the detection well [50]. DNA tracers is the lack of stability in environments with low pH or abundant microbiotic activity [257]. Molecular tracers, due to their small size, tend to diffuse into the small pores of a matrix (as compared with larger tracers), and thus take longer periods of time to travel

between the injection well and the production well. Additionally, adsorption of the molecular tracers can also be a factor, requiring the injection of much larger quantities.

2.2.5.2 Concept of nanosensor for reservoir characterization

Recently, injection of NPs has been proposed as a potential means to improve both reservoir characterization and understanding of oil displacement mechanism [39, 41, 50, 258, 259], as shown in Figure 2-3. Similar to DNA-tracers, the intrinsic information-coding capacity (particle type, shape, coating, etc.) allows discrimination between two or more particle tracers coming from different sources or released at different times. Particle with good mobility can also be used as carrier to transport cargo which can be

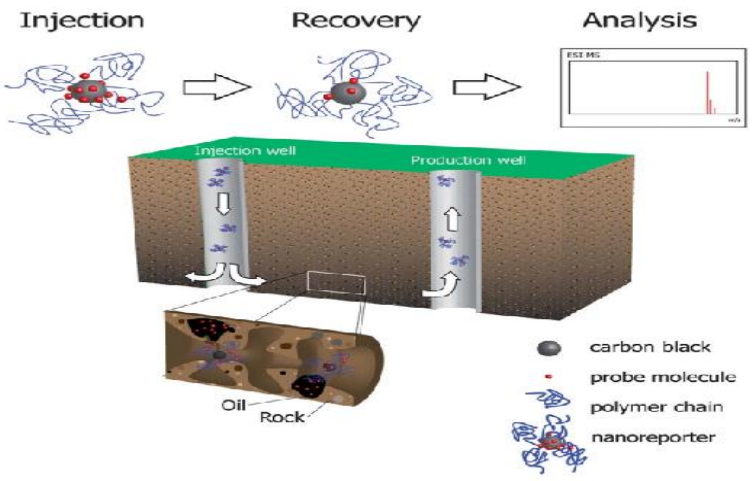

Figure 2-3. Schematic diagram of subsurface oil detection by nanoreporters. Nanoreporters transport probe molecules through downhole rocks followed by selectively releasing them when the rock contains oil. The interrogation of the nanoreporter at the production well will give quantitative information of the oil content based upon the amount of the probe molecule remaining on the nanoreporter. Picture taken from [122].

changed by subsurface environment, or released to the NAPL. The capabilities of nanoparticles might also become limitless if compositing special functionalization,

responsive to reservoir temperature [260-265], pressure [263], chemical (e.g. H_2S [51], oil [50], water, gas and mineral type), selective to rock porosity and permeability [266], and responsive to ultrasound or ultra-violet [229, 230] and magnetic field [267, 268]. It can be expected that the use of certain nano-based agents may soon lead to the development and deployment of sensing and intervention devices that can help delineate the water-flood front, identify bypassed oil, and map super permeability zones in-situ in the underground.

2.2.5.3 The challenge for successful nanosensors

However, due to the often encountered hostile and extreme reservoir conditions, the first challenge should be addressed is how to synthesis proper nanoparticles that are able to withstand high temperature, high pressure and salinity, which are encountered commonly in oil reservoir. Secondly, the transport behaviour of these novel particles should be investigated sufficiently. Nanoparticles are expected to have significantly different transport behaviour in porous media compared with organic molecular because of their more rigid structure [196].

One of the current attempts to address these challenges described above is by injecting carbon nanoparticles through wellbores into one of the phases in the reservoir. For example, Berlin et al. [197] selected oxidized carbon black (OCB) as core and sequestered a polyvinyl alcohol (PVA) shell. This carbon based nanoparticle, PVA-OCB, displayed good stability and transport ability in the field rocks and selective release of hydrophobic compounds when contacting with hydrocarbon, but it suffered from stability problem at higher temperature (70 °C) and in positively charged dolomite rocks. To address these problems, Hwang et al.[122] chose PVA with appropriate molecular weight to keep the PVA-OCB NPs stable in high temperature, and also switched the NPs core from OCB to a carboxyl group-functionalized carbon black

(fCB) to improve its migration behaviour in various porous media. Other alternative carbon materials have been evaluated to transport in subsurface environment include graphene oxide nanoparticles [156, 198, 199], water-dispersed aggregation of fullerene (C60) [196, 200], carbon nanotubes [201-203], to name but a few. But a vital problem associated with these materials is that it is difficult to detect the particle at low concentration, and none of those applications are targeted for reservoir-like environments, which is quite different to the normal subsurface.

With only a few studies that can be found, using luminescent particles for reservoir characterization is rarely reported, nor their migration behaviour in porous media. Wang et al. [204] investigated the retention behaviour of CdSe quantum dots coated with polyacrylic acid-octylamine (PAA-OA). Kini et al. [205] demonstrated the stability and transport properties of CdSe QDs at high ionic strength and elevated temperature in Berea sandstone core, which is targeting for the application of oil exploration. It should be paid special attention that these sort of QDs are usually high-toxic and contaminate for the environment. Moreover, it is hard to separate these from the crude oil.

2.3 Nano-enhanced oil recovery mechanisms

Multiple possible mechanisms have been proposed to explain the effect of nanoparticles on EOR, including: (i) viscosity increase for mobility control [89], (ii) substrate wettability change [117, 118, 121, 127], (iii) the effect of structural disjoining pressure [127, 206, 207], (iv) the reduction of the displacing fluid/oil IFT [117, 118, 208, 209], and (v) the so-called log-jamming effect [111, 210]. However none of them have been found to provide sufficient explanation for all of the observed EOR enhancements. For instance, for the structural disjoining pressure to be effective, a very high nanoparticle concentration is required (>30% by volume [211]). Consequently, it

is difficult to invoke this mechanism to explain the results of most published work because these have utilized very small particle concentrations (i.e., in the ppm range).

2.3.1 Wettability alteration

Wettability is the term used to describe the relative adhesion of two fluids to a solid surface. Giraldo et al. [212] showed that wettability plays an important role in oil recovery processes and reservoir productivity. It is a major factor controlling capillary pressure, the flow and spatial distribution of fluids (relative permeability and saturation) in porous media. Currently, there are three main experimental methods that are commonly used by researchers for wettability measurement: the contact angle method, the Amott test and the core displacement test. Among them, the contact angle method is the most universal used approach to determine wettability (Figure 2-4).

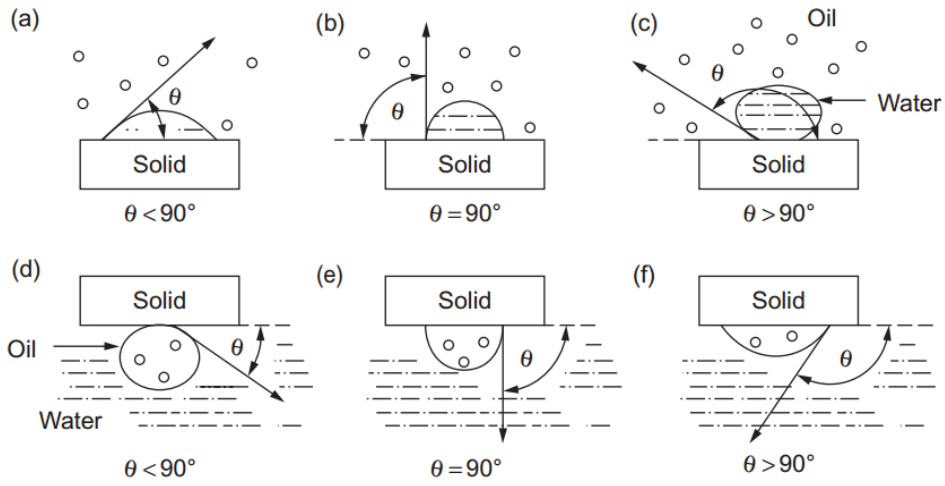

Figure 2-4. Measurement of contact angles for water-oil systems; (a-c) show measurements using a drop of water surrounded by oil, wettability changing from water wet to oil wet, and (d-f) show drops of oil surrounded by water, wettability changing from water wet to oil wet.

2.3.1.1 Towards water wetting or oil wetting?

The nanoparticles depsition on the surface of reservoir rock could change its wettability. However, controverse exists among literature regarding whether the

wettability alteration towards water wet or oil wet is beneficial for EOR. Karimi et al. [121] proved that ZrO_2 nanoparticles suspension can change carbonate system from oil-wetting to water-wetting by formation of composite surfaces, as a result of nanoparticles being adsorbed onto the solid surfaces. Theoretical models presented that the wettability was being tuned by altering area fractions of the nanostructure, partition coefficient of the materials forming nanostructures, and surface roughness. It should be noted that the wettability may be changed by adsorption of surfactant which is not considered in the theoretic analysis. Ehtesabi et al. [127] studied the contact angle of porous media component before and after core flooding. They found TiO_2 deposition reduces the contact angle of water droplet from 125 ± 3° to 90± 3°, which is regarded as the main reason for enhanced oil recovery. Bayat et al. [112] applied Al_2O_3, TiO_2, SiO_2 as the agent for enhanced oil recovery in inter-mediate limestone at various temperature. They concluded that the intermediate-wet limestone sample was changed to water-wet through NPs adsorption, and as a result, the reduction of capillary force is the dominant factor for EOR. Similar results of tuning the substrate wettability towards more water-wetting for recovering more oil is observed by Ref. [137]

However, the wettabillity alteration towards water wet is not always beneficial for oil recovery. Onye et al. [213] concluded that neutral and hydrophobic nanoparticles are good for EOR in water-wet rock, because in this kind of rock hydrophilic particle yeild poor recovery fators by switching already water wet rocks to strongly water wet. Sometimes, even the wettability changing towards oil wet is helpful to mobilized more oil. Roustaei et al. [117] used the partially hydrophobic fumed silica (AEROSIL R 816) in water-wet sandstone for flooding experiments, resulting in oil recovery increased by 25.43% and 14.55% for two samples injection. The mechanism was attributed to significant reduction of IFT and rock wettability changing from water wet toward oil-

wet in a light oil reservoir. However, in this research, they did not clarify the contribution between these two mechanisms.

2.3.1.2 The reason of wettability change triggered by NPs

Some researchers try to analyse the reasons why the NPs can result in wettability alteration of rock surfaces by examining the microscopic morphology change after deposition with the nanoparticles. For example, Karimi et al. [121] and Al-Anssari et al. [214] proved that NPs adsorbed on calcite forming nano textured surfaces, and thus change the surface free energy, as shown in Figure 2-5 and Figure 2-6.

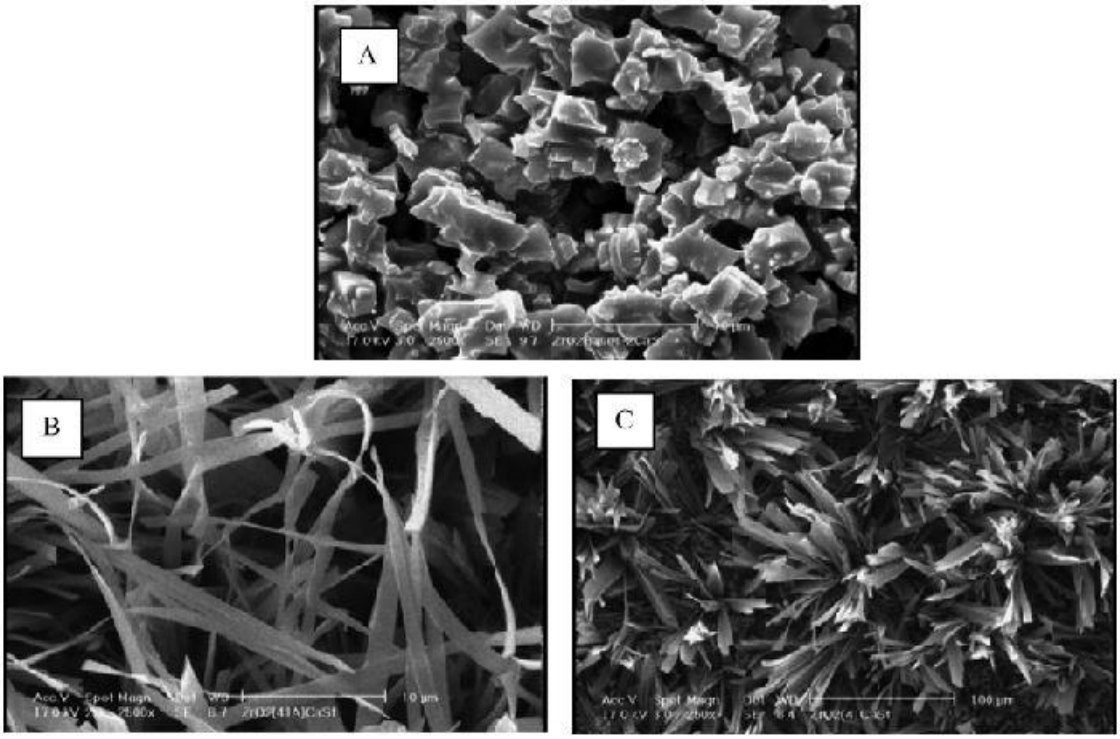

Figure 2-5. SEM images of an oil-wet carbonate rock aged in (A) Tween 80 + Span 85 + glycerin + LA2 and 0% ZrO_2 NPs, (B) Tween 80 + Span 85 + glycerin + LA2 + 0.05 g/ml ZrO_2 nanoparticle, and (C) Tween 80 + Span 85 + glycerin + LA2 + 0.1 g/ml ZrO_2 nanoparticle. Figure is taken from [121].

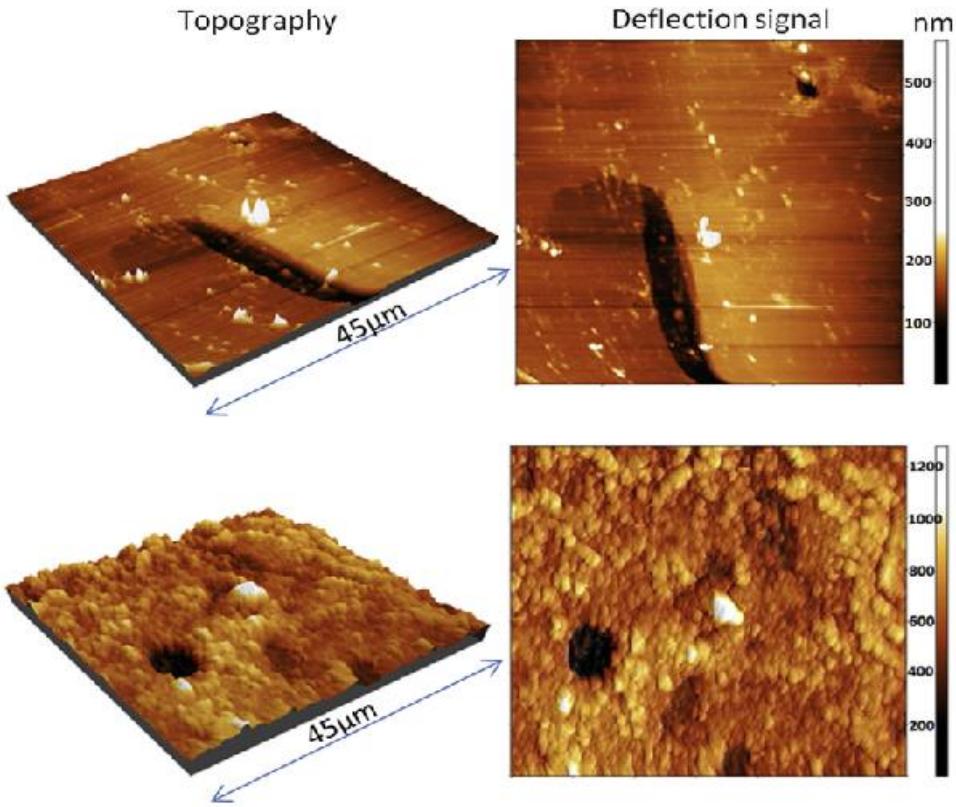

Figure 2-6. Atomic force microscopy images of a calcite surface used in the experiments before (upper image) and after (lower image) nano-modification. The RMS surface roughness before nano-modification was 32 nm, which is very smooth. After nanofluid treatment (0.5 wt% SiO_2 in 10 wt% NaCl brine for 4 h) the RMS surface roughness increased to 1300 nm. Different colours refer to variations in height (black: 0 nm, white: peak height = 640 nm [upper image], 1300 nm [lower image]) [214].

2.3.2 Structural Disjoining pressure

The structural disjoining pressure (SDP) effect was proposed by Wasan & Nikolov [206]. The SDP is different from the conventional disjoining pressure, which is a result of the London-Van der Waals force that has a short range. It has been demonstrated that the structural disjoining force is generated from the ordering of nanoparticles in a confined wedge (structuring) and the influence can extend to a film depth of a few nanoparticle diameters (long range) [206]. The origin of the structural disjoining pressure is due to the confinement of the particles in the film region as opposed to their

greater freedom of location in the bulk liquid. The layering arrangement of the particles gives rise to an excess pressure in the film, the structural disjoining pressure, which has an oscillatory decay profile with the film thickness (Figure 2-7). A result of such a structure force is that nanofluids could exhibit a good spreading capability in confined spaces. Such forces have been observed (i) to be able to change the macroscopic contact angle of a liquid droplet [215-217], (ii) to stabilize liquid films [218], and (iii) to lift an oil droplet from a wall in an aqueous solution [207, 219-223].

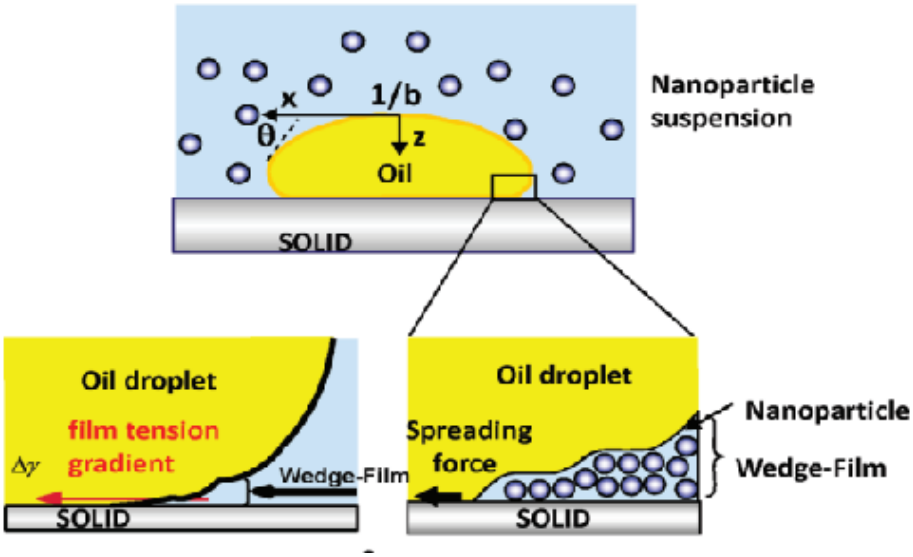

Figure 2-7. Nanoparticle structuring in the wedge-film resulting in structural disjoining pressure gradient/film tension gradient at the wedge vertex. Figure is taken from [219].

2.3.3 Interfacial tension reduction

IFT is one of the main parameters used to determine fluids' distribution and movement in porous media. As the EOR theory reviewed in Section 1.4, lowering the w/o IFT and consequently reducing the capillary fore is necessary to mobilized the large volume of residual oil trapped in pore space after water flooding. Nanoparticles have been considered as a potential agent to reduce IFT, which is one of the main mechanisms for Nano-enhanced oil recovery (NanoEOR).

Hendraningrat et al. [135, 209, 224] measured the IFT between synthetic oil and nanofluids by the pendant drop method. The results showed that adding NPs into brine reduced the IFT from 14.7 mN/m to 9.3 mN/m. In addition, increasing nanofluid concentration from 0.01 wt% to 0.05 wt% decreased the IFT from 9.3 mN/m to 5.2 mN/m. Therefore, IFT is sensitive to nanofluid concentration, and decreases as nanofluid concentration increases. Li et al. [118] and Parvazdavani et al. [120] also carried out similar experiments to study the effect of SiO_2 NPs on IFT, and they believed that SiO_2 NPs have more impact on IFT reduction than wettability alteration.

However, some research shows that the presence of nanoparticles is mainly for alterating surface activity or facilidating the formation of the emulsification process, reducing IFT is not the main contribution for EOR. For example, in the research from Esmaeilzadeh et al. [169], as increasing the concentration of ZrO_2 NPs coated by CTAB or LA7, the IFT of n-heptane /water and air/water systems did not change obviously under various surfactant concentrations. However, ZrO_2 NPs can alter the surface activity of SDS molecules at both n-heptane /water and air/water interfaces. It means in some cases surfactant-coated NPs can influence the IFT, but depending on the surfactant type.

Zaid et al. [168] found that the size of ZnO naoparticle affected the potential of oil recovery via inducing an emulsification process *in-situ,* because a cloudy solution was observed during the tests, which indicated the occurance of an emulsification procees. The larger particles gave a higher increase of oil recovery, and Al_2O_3-SG-1100 nanofluid could mobilize more oil even through it has smaller particles than ZnO-RM nanofluid. They also concluded that ultra-low IFT is not necessary to create spontaneous emulsification in a dielectric nanofluid flooding. Bai et al. [225] also acquired a same conclusion with Zaid et al., that emulsification plays a more important role for enhanced

oil recovery compared with IFT, although a relatively low IFT is required for the occurrence of emulsification.

2.3.4 Mobility control

The mobility ratio is generally defined as the mobility of the displacing phase divided by the mobility of the displaced phase, which can be expressed by

$$M = \frac{k_{rw}}{\mu_w} / \frac{k_{ro}}{\mu_o} = (\frac{k_{rw}}{k_{ro}})(\frac{\mu_w}{\mu_o})$$

Where k_r usually refers to relative permeability, μ refers to viscosity, the subscript '*w'* represents displacing phase (usually water), the subscript 'o' is for displaced phase (usually oil). The ratio shows the capability of the injecting fluid to that of the oil phase, and the effect is dependent on the relative permeability and the viscosity ratio. Good mobility control is obtained when the viscosity of the injected fluid is higher than the viscosity of the oil in the reservoir and can lead to a piston-like displacement of the oil from the injection well to the production well.

A method for achieving high viscosities of the injected phases and good mobility control is through generation of foams and emulsions, which can form in the presence of surfactants or nanoparticles. Unlike surfactants, nanoparticles have the advantage that they can irreversibly adsorb to a liquid-liquid or gas-liquid interface, forming very stable foams and emulsions. However, bare nanoparticles may be too hydrophobic or hydrophilic for stabilizing an interface. NPs should be tailored by coating with surfactant or polymer for a specific interface and application [226].

Another method is for waterflood mobility control by using nanoparticles, where a low-viscosity nanomaterial is co-injected with the waterflood and will travel through the highest permeability regions (Figure 2-8)**.** Activated by designed triggers, the payload system will burst to release expandable polymers and crosslinkers to create a

plug, diverting water to less-permeable areas of the reservoir resulting in increased sweep efficiency in waterflood applications.

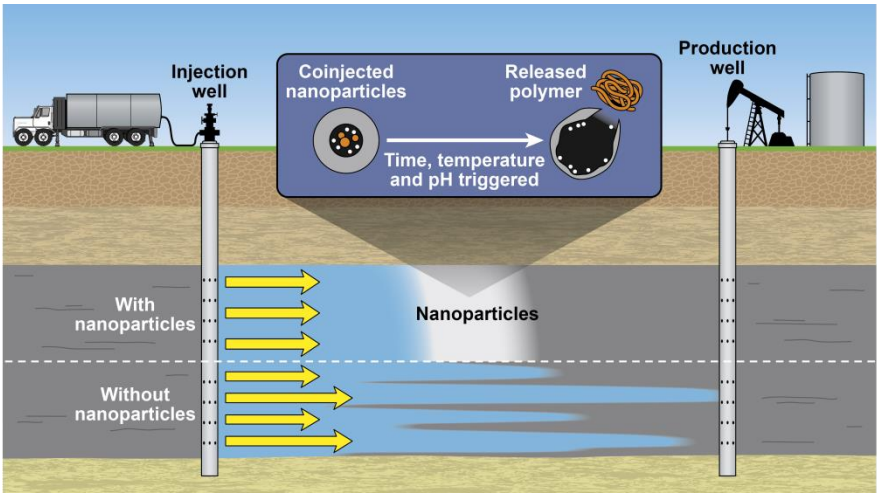

Figure 2-8. Early payload delivery concept with nano-enhanced water-flow blocker to mitigate undesirable water flow through high-permeability zones.

2.3.5 Pore Channels Plugging

Pore channel plugging can be caused by two mechanisms: mechanical entrapment and log-jamming [111]. Mechanical entrapment occurs because the diameter of injected components is larger than pore channels that they flow through, while the log-jamming is plugging of pore channels that are larger than each NP.

When a nanofluid flows from pores to throats, the narrowing of flow area and the differential pressure will lead to a velocity increase of the nanofluid. The small H_2O molecules will flow faster than the NPs causing accumulation of NPs at the entrance of the pore throats (Figure 2-9). NPs accumulation and blockage of small pore throats due to log-jamming leads to the pressure building up in the adjacent pore throat, forcing out the oil trapped. Once the oil is freed, the surrounding pressure drops and the plugging gradually disappears and the NPs start to flow with the water.[111, 210] Hendraningrat et al [227] observed the log-jamming effect during single-phase flooding water-wet Berea sandstone, through differential pressure and microscopic visualization.

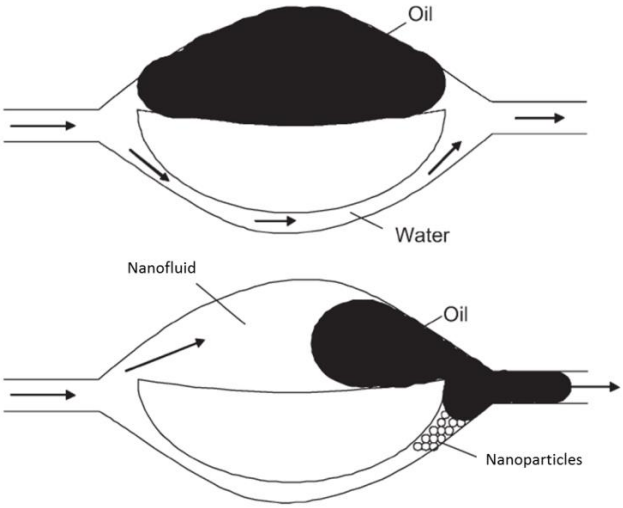

Figure 2-9. Schematic of pore channel plugging caused by log-jamming [111].

2.3.6 Other mechanisms

The mechanism for NanoEOR depends on the flooding methods including bare NPs flooding, NPs coated with surfactant/polymer, NPs as cross linker to strengthen the polymer networking, NPs-stabilized emulsion and foams, etc., also change with oil type, reservoir rock, salinity of displacing fluids. There are some other mechanisms including preventing asphaltene precipitation [228-230], nanocatalysts [231], and the appearance of climbing films [140].

2.4 Difficulties for Nano-enhanced oil recovery

2.4.1 Nanoparticle stability in harsh environment

The nanoparticles are most commonly dispersed in the base fluid with little or no ionic strength, under room temperature and pressure. Unfortunately, the conditions in oil reservoir is quite different with those in the laboratory. The subsurface reservoir usually has high salinities (ionic Strength 3.77 M in API brine) and elevated temperatures (up to 150 °C), which presents technical challenges, such as aggregation as well as excessive nanoparticle adsorption on mineral surfaces, due to the compression

of electrical double layer and stronger Brownian motion [232-234]. Therefore, fabrication of suitable nanoparticles that can be stable in reservoir-like environments is essential for successfully application.

Another concern is that the stability of nanoparticles will affect the properties of injection fluids, like viscosity, IFT with oil phase, density, etc., which is essential for successful EOR. Learning from the experience of nanofluids [235-239], the displacing fluid property modification will be significantly affected by the choice of nanoparticle material, particle concentration, morphology and stability in saline water. However, in all references involved in Section 2.2.1, the stability of NPs in synthetic brine with high ionic strength was not paid enough attention and little information regarding NPs stability can be found.

The literature review below will reach to the latest research on nanoparticle stability affected by electrolyte, surfactant and temperature, which are the main influencing factors encountered in oil reservoirs.

2.4.1.1 Effect of electrolyte types and strength

Metin et al. [240] studied the stability of silica dispersion without surfactant, specifically focusing on how the critical salt concentration (CSC) for different salts, namely NaCl, $CaCl_2$, $BaCl_2$ and $MeCl_2$, affects the stability of a silica dispersion. Divalent cations Mg^{2+}, Ca^{2+} and Ba^{2+} are more effective in destabilizing silica nanoparticle dispersion than the monovalent cation Na^+. The CSC for Na^+, which is 1.5% just after fabrication, is about 100 times more than for Mg^{2+}, Ca^{2+} and Ba^{2+}. Moreover, Mg^{2+} is the most effective in destabilizing the silica particles. The CSC is independent of silica concentration, and can be lowered at high temperature.

According to Agarwal et al. [241], kerosene as a non-polar fluid is less responsive to charged particles and thus electrostatic stabilization was not found to be effective in

kerosene based nanofluids. On the other hand, steric stabilization, works well in a non-polar medium like kerosene, where the surfactant chains keep nanoparticles apart, effectively due to higher osmotic pressure build-up between the hydrocarbon chains of surfactant.

Ehtesabi et al. [127] applied anatase and amorphous TiO_2 nanoparticles in sandstone for enhanced oil recovery. They checked the nanoparticle stability in 10,000 ppm NaCl after 24 h and 48 h, and concluded that nanofluid can be stabilized at least 24 h, which is enough for the EOR application.

Results from French et al. [242] show that 4-5 nm titanium dioxide particles readily form stable aggregates with an average diameter of 50-60 nm at pH ~4.5 in a NaCl suspension adjusted to an ionic strength of 0.0045 M, further lead to the formation of micron-sized aggregates within 15 min by increasing the ionic strength to 0.0165 M. At all other pH values tested (5.8-8.2), micron-sized aggregates form in less than 5 min, even at low ionic strength (0.0084-0.0099 M with NaCl). It is also observed that the aggregation is more easily to be introduced in the presence of divalent cations such as Ca^{2+}.

Solovitch et al. [243] acquired similar results in terms of ionic strength, namely, at low electrolyte concentration (10^{-2} M), the size of NP reached around 500 nm in 20 min. In addition, the aggregation rate measured at pH 5 was always higher than that obtained at pH 8 and maximum in both cases at 1 M.

Bouhaik et al. [244] focused on the modelling of stability of TiO_2 nanoparticles based on Derjaguin-Landau-Verwey-Overbeek (DLVO) theory with only three adjustable parameters (the minimum separation distance between NPs, the Hamaker constant, and the effective interaction radius of the particle). Their model predicted very well the stability ratios of TiO_2 NPs measured at different pH values and over a broad range of ionic strengths (KCl aqueous solution).

2.4.1.2 Stabilization by surfactant/polymer

Extensive research have been under taken by using an NP stabilizer to overcome particle aggregation in reservoir-like environment with high temperature and high pressure, but with limited success [245]. The NP stabilizer, like surfactant and polymer, can physically introduce a steric repulsion force, which fill the vacancy of electrostatic repulsion between particles because of the charge screening at high ionic strength. However, surfactant is not always a good NP stabilizer at high ionic strength and high temperature. At high temperature, the bonding between nanoparticles and surfactant can be damaged [246, 247]. On the contrary, polymeric stabilizers have the potential to prevent NP flocculation if the pure polymer does not undergo phase separation, and can provide sufficient steric and electrosteric stabilization.

According to a review paper from Ghadimi et al. [247], popular surfactants that have been used to stabilize nanoparticle can be listed as sodium dodecyl sulphate (SDS), sodium dodecylbenzenesulfonate (SDBS), salt and oleic acid, cetyltrimethylammoniumbromide (CTAB), dodecyl trimethylammonium bromide (DTAB) and sodium octanoate (SOCT), hexadecyltrimethylammoniumbromide (HCTAB), polyvinylpyrrolidone (PVP) and gum arabic. Choosing the right surfactant is important to stabilize nanoparticles.

Hwang et al. [248, 249] added SDS in fullerene and multi-wall carbon nanotube (MWCNT) nanofluids, which improved the stability of nanoparticles in aqueous suspensions. The result could be explained that the hydrophobic surfaces of MWCNTs and fullerene are modified hydrophilically and that the repulsion forces between the suspended particles increase due to an increase of zeta potential. Jiang et al. [250] formulated stable homogeneous dispersions of carbon nanotubes (CNTs) using SDS as the dispersant. The study showed that after 150 h, no precipitation is found for

CNT/SDS dispersions, exhibiting an extreme stability. But this experiment was done under the room temperature.

A polymer coating that imparts the steric repulsion (main), electrostatic or electro-steric (minor) stability is another important way to ensure nanoparticle remain unaggregated. Weak polyelectrolytes, such as poly(acrylic acid), poly(vinylpyridine) and poly- (styrenesulfonate) provide moderate stability, but can be susceptible to changes in ionic strength, and elevated temperatures [154, 251-254]. High ionic strengths lead to charge screening, whereas elevated temperatures disrupt favourable hydrogen bonding; both leading to reduced polymeric hydration, and eventually nanoparticle flocculation. Especially, divalent ions are known to be problematic, because they sharply reduce polymeric hydration via specific ion complexation [255].

The most promising approaches to date have relied on strongly anionic polysulfonates that are known to remain moderately hydrated at high ionic strengths. Highly acidic sulfonated polymers exhibit low Ca^{2+} binding affinities and remain soluble even at high temperatures, especially those containing high levels of polystyrene sulfonate (PSS) or 2- acrylamido-2-methylpropanesulfonate (PAMPS) (25-27 in [245]). Bagaria et al. [245] reported an amine functionalized iron oxide core (for reservoir imaging) modified by the covalent attachment of an anionic polymer of 2-acrylamido-2-methylpropanesulfonate (AMPS) via multiple acrylic acid sites. In a different approach, Hwang et al. [122] reported a carbon black nanoreporter to which a light sulfonated poly(vinyl alcohol) was covalently conjugated via ester linkages. This particle can survive in API brine at 100 °C. Following that research, they grafted PVA(2k) with 2000 g/mol molecular weight onto the carboxyl-functionalized carbon black (CB) core by condensation of the hydroxyl groups of the PVA with the carboxyl groups through a *N,N′*-dicyclohexylcarbodiimide (DCC) coupling reaction [123].

Bagaria et al. [104] report a rare example of steric stabilization of iron oxide nanoparticles grafted with poly(2-acrylamido-2-methylpropanesulfonate-co-acrylic acid) (poly- (AMPS-co-AA)) that not only display colloidal stability in standard API brine (8% NaCl + 2% $CaCl_2$ by weight) at 90 °C for 1 month but also resist undesirable adsorption on silica surfaces (0.4% monolayer NPs).

Table 2-3: Summary of nanofluid fabrication and stability

Investigator	NPs	Base fluid	Surfactant & pH	Fabrication method	Characterization method	Stability
Hwang et al. [256]	Carbon black (CB), 40 nm, initial 0.5 wt%,	Deionized water (DW)	SDS, 1 wt%.		SEM, Electrophoretic light scattering (ELS)	
Hwang et al. [256]	Ag, 35 nm, initial 0.5 wt%,	silicon oil (DC-704, Dow Corning Inc.)	Oleic acid, 1 wt%.		SEM, Electrophoretic light scattering (ELS)	
	Au, 1.65 nm Spherical	toluene	N/A	Directly by chemical reaction method		thermal conductivity and thermal diffusivity did not change over 48 h for the nanofluids at lower volume fractions. (not sure it is for all of the four samples or just for CNF)
(Zhang et al. [257]) TREIBER et al. [258] Wang et al. [259]	Al_2O_3, 20 nm Spherical	DW	N/A	Sonic		thermal conductivity and thermal diffusivity did not change over a period of 48 h for the nanofluids at lower volume fractions. (not sure it is for all of the four samples or just for CNF)
	TiO_2, 40 nm Spherical	DW	N/A	Sonic		
	CuO, 33 nm spherical	DW	N	Sonic		
	CNF average length 10 μm and diameter 150 nm	DW	SDS 1.5 mass%	Sonic		
	Cu, average 25 nm, spherical or near spherical, 0.05 wt%	DW	SDBS	stirred thoroughly and ultrasonicated for at last 15min		
Zhu et al. [260]	Al_2O_3, 100 m^2/g, 15–50 nm, 3965 Kg/m^3	DW	SDBS	stirred thoroughly and ultrasonicated for at last 15min		
LotfizadehDehkordi et al. [261]	Al_2O_3, average size of 13 nm, concentrations range from 0.01 up to 1 vol%,	Ethylene glycol/water (mass ratio, 60:40)	anionic dispersant, mass ratio of SDBS/alumina NPs of 1:1	Sonication	XRD: crystalline structures and purity of the alumina NPs.	

Table 2-3 continued

Investigator	NPs	Base fluid	Surfactant & pH	Fabrication method	Characterization method	Stability
Esmaeilzadeh et al. [262] Agarwal et al. [241]	ZrO_2 0.001, 0.01 and 0.05 g of ZrO_2 per 100 mL H_2O	DW & n-heptane	SDS, concentration: 0.001, 0.01, 0.1, 1, and 5 times of CMC	Ultrasonic		stable for several hours
	ZrO_2 0.001, 0.01 and 0.05 g of ZrO_2 per 100 mL H_2O Al_2O_3, 13 nm and 50 nm	DW, n-heptane, kerosene	C12TAB, concentration: 0.001, 0.01, 0.1, 1, and 5 times of CMC	Ultrasonic Ultrasonicate 30 min for 0.05% to 3 h for 1%	Pendant drop technique for Liquid–liquid IFTs; Kruss-Nr.2215 Tensiometer for Liquid–vapor surface tensions; Zetasizer; Brookfield LVDV-II digital viscometer;	stable for several hours volume fraction less than 0.2% were very stable (more than 10 days)
			LA7, Kimyagaran Emrooz, Concentration: 0.001, 0.01, 0.1, 1, and 5 times of CMC			
			Oleic acid (optimum volume ratio (0.3) of oleic acid to alumina particle)			
Kole and Dey [263, 264]	Al_2O_3, <50 nm, volume fraction between 0.001 and 0.015	Engine coolant (halfand-half mixture of propylene glycol and water)	oleic acid	Ultrasonication for 3h, homogenized for 1 h by magnetic force agitation		be stable for more than 80 days
Maghzi et al. [265]	SiO_2, 14 nm, 200 m^2/g, 0.048 g/m^3	Water	Polyacrylamide powders, Concentration (0.5 g polymer to 0.5 g silica NPs and 499 g distilled water).	Polymer in water; Homogenizer for 48 hours at 100 rpm Ultrasonication for 1 h, then stir for 48 hours after adding surfactant	Brookfield DV-III Ultra rheometer,	placed one month in a closed transparent bottle far from degrading factors such as light and heat, no precipitation and significant colour alteration in sample detected.
Amraei et al. [266]	SiO_2, 2-5nm,	water or paraffin	Tween 80, Span 80, Lauric alcohol-3EO, CTAB, SDS and K-Laurate Detail in original paper	stir		

2.4.2 NPs mobility in long distance

In terms of particle for reservoir application, especially for reservoir diagnosis, they should has the ability to be transported a desired distance from the injection well. This means the particles should exhibit little retention in sedimentary rock and minimal formation damage [243]. However, there is little report regarding particle which has a breakthrough ability as high as 100% as reported.

2.5 Conclusion

As many of current investigations are using metal oxides nanoparticle for enhanced oil recovery, research in this thesis starts with TiO_2 NPs, a typical metal oxides nanoparticle, to examine the current proposed EOR mechanisms which are reviewed in Section 2.3. This work will also involve investigation on nanofluid stabilization in high salinity water and characterization.

Following this trial study, the work in this thesis will explore more potential ways to apply the nanotechnology for enhanced oil recovery, such as nanoparticle as carrier to reduce the surfactant retention in reservoir rock and nanoparticle to stabilize the structure of microemulsion, in order to address the problem reviewed in Section 2.2.

Nanoparticle transport in porous media which is essential for the coreflooding experiment will also be investigated to address the problem reviewed in Section 2.4.

Idea of the layout of this thesis has also been illustrated in Figure 1-11.

Chapter 3

TiO2 nanoparticle-assisted water-flooding in Berea sandstones

3.1 Introduction

Traditionally, many EOR techniques target the oil remaining after waterflooding. Waterflooding is generally not considered an EOR method unless it is combined with some other flooding methods. In this Chapter, we examined the EOR potential for TiO_2 NP engineered waterflooding, and the mechanisms behind it.

It has been noted that some stabilizers (either surfactants or dispersants) were generally used to stabilize NPs in water or brine, but their characterization and effects on recovery have seldom been considered [156, 204]. These stabilizers alone could affect significantly effective reservoir properties especially viscosity and interfacial tension (IFT) [24, 267], and hence have an EOR effect. Consequently it is unclear if the observed effect has been due to the stabilizers, the NPs, or a combination of both.

A systematic study of the effect of rutile TiO_2 NPs assisted EOR in a sandstone rock is reported in this work. To address the current limitations discussed in Chapter 2, both rock samples and nanomaterials were carefully characterized, including nanoparticle stability in fluids of different salinity. Individual experiments were performed by core-flooding with brine alone (BF), brine with stabilizer (BSF), and with a stabilized suspension of nanofluids in brine (i.e., brine + stabilizer +NPs) flooding (NF) to clearly

identify the contributions from the stabilizer and the NPs. The nanoparticle concentrations before and after flooding experiments were determined, and the effects of stabilizer and nanoparticle concentration on the mobility and EOR effect during the secondary water flooding were assessed, as well as an in-depth discussion of the possible mechanisms.

3.2 Nanoparticle preparation and Characterisation

3.2.1 Raw Materials

Synthetic brine (nominally 0.1 M NaCl in deionized water, laboratory grade) was used as the formation liquid and the base fluid for dispersing nanoparticles in all experiments. The density of brine was measured as 1.000024±0.001171 g/mL, pH 6.72±0.2 and dynamic viscosity 0.89±0.01 mPa·s at 25 °C. The oil phase was High Viscosity Index (HVI) hydraulic 60 mineral oil, a highly refined mineral oil that consists of saturated aliphatic and alicyclic hydrocarbons, which has a density of 0.868 g/mL and a dynamic viscosity of 42.75±0.16 mPa·s at 25 °C. The oil is less volatile and consequently has physical properties that are more stable than oils of greater volatility, allowing more reliable data to be produced over longer experiments.

There is the potential for confusing concentration of the suspension brine with concentration of NPs in the brine. Consequently, throughout this work we have used the protocol that we use only the word ‘salinity’ to describe the strength of the brine in which the NPs are suspended and reserve the word ‘concentration’ to denote the amount of NPs per volume of suspension solution.

Titanium dioxide (TiO_2) NPs were synthesized from titanium (III) chloride ($TiCl_3$) precursors (Sigma Aldrich, UK) using a hydrothermal reaction. Various stabilizers including tri-sodium citrate dihydrate (SCD, Fisher Scientific), sodium dodecyl sulfate

(SDS, Fisher Scientific), polyvinylpyrrolidone (PVP, Fluka, Switzerland), polyethylene glycol 2000 (PEG, Schuchardt, Germany), cetyltrimethylammonium bromide (CTAB, Fisher Scientific), Triton-100 (Sigma Aldrich) and Suwannee river fulvic acid (SRFA, IHSS, USA) were used to stabilize NPs in the brine.

3.2.2 Nanoparticle fabrication

In a typical synthesis, 4.17 mL of 1.5 M $TiCl_3$ was added to 250 mL of agitated distilled water. The pH of the system was adjusted to 3.8±0.2 at room temperature by using NaOH and HCl. The solution was stirred by a magnetic stirrer at room temperature overnight for rutile phase synthesis. After the synthesis, extensive dialysis was performed to remove impurities from the NP dispersion.

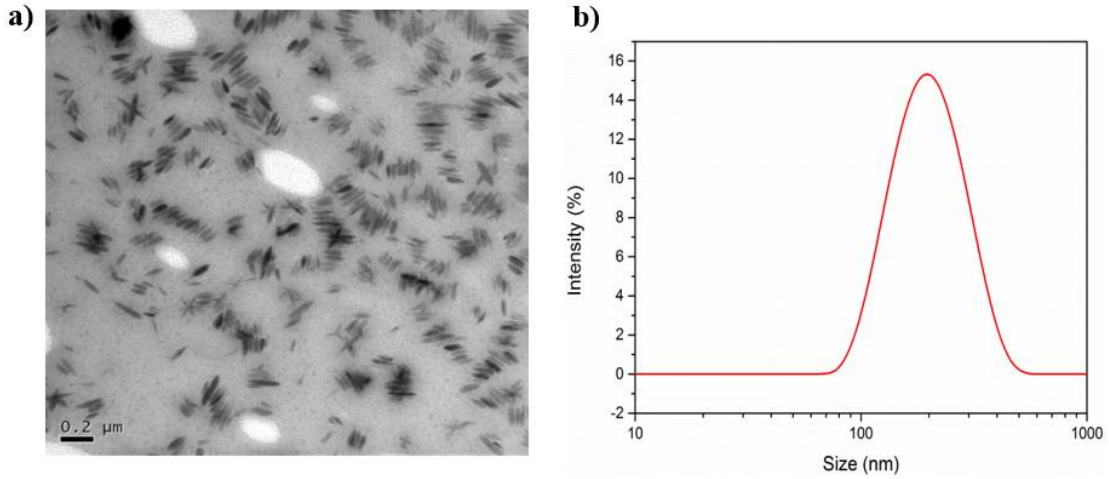

Figure 3-1. (a) TEM images for rutile anatase TiO_2 NPs, and (b) particle size spectrum from the Dynamic Light Scattering (DLS) method.

The morphology of the synthesized particles was examined using a transmission electron microscope (TEM, FEI Tecnai TF20), as shown in Figure 3-1 (a). The synthesized NPs were in cylindrical shape, with a diameter of approximately 150±20 nm and aspect ratio in the range 7-9. The specific surface area of rutile nanoparticle was determined at 85.3 ± 20 m^2/g (Acorn Area^{TM}, XiGo Nanotools Corporate). The hydrodynamic particle size distribution in 0.1 M NaCl solution (Figure 3-1 (b)) was measured using a Malvern Nanosizer, based on the dynamic light scattering (DLS)

method, which shows a distribution between 80-400 nm peaking at 207.7±14.4 nm. The zeta potential of the dispersion was measured as -32.0±1.04 mV.

3.2.3 Viscosity

The viscosity was being measured by Anton Paar MCR 301. A cone-plate module (Figure 3-2) is applied for the measurement, in which the shear rate does not depend on radial distance. The diameter for the cone, namely the measure system (CP50), is 50 mm, and the gap between these two plates is pre-set by the manufacture at standard value of 0.098 mm, leading to a desired sample volume of 0.67 mL. Actually, plate-plate measure system (PP50) is also available, but the calibration test with it was not convincing and determining a proper gap which can provide accurate data was difficult to achieve [268] hence it was not employed in our measurement. The shear rate was being changed from 100 s^{-1} to 1000 s^{-1}.

$$\gamma(r) = \frac{\Omega}{\alpha}$$

While, Ω is the angular velocity and the α is angle. This equation means when using core-plate geometry, the influence of radius on the viscosity can be removed.

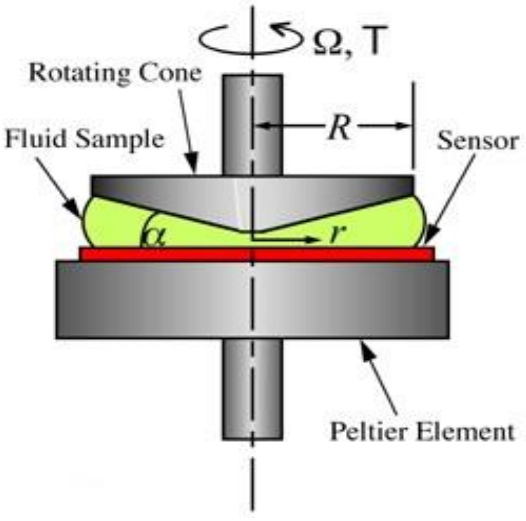

Figure 3-2. Schematic diagram of core-plate measure system.

The machine is calibrated by the standard oil regularly or after occasional reparation for the purpose of maintenance (Figure 3-3), and before each time of measurement, de-ionized water whose (dynamic) viscosity is already-known (0.89 mPa·s) under the room temperature is used for checking the accuracy (Figure 3-4).

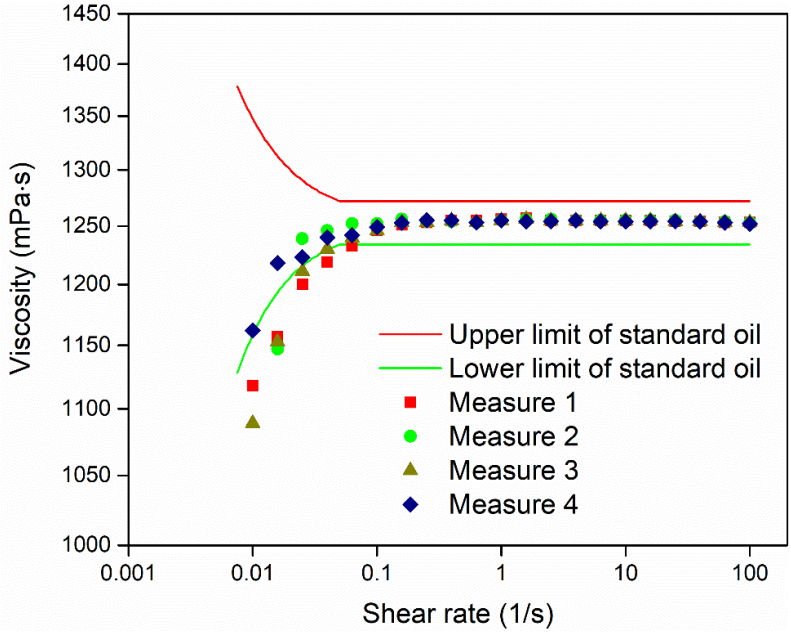

Figure 3-3. Standard oil viscosity for the rheometer calibration by using CC27 'Cup and Bob' geometry.

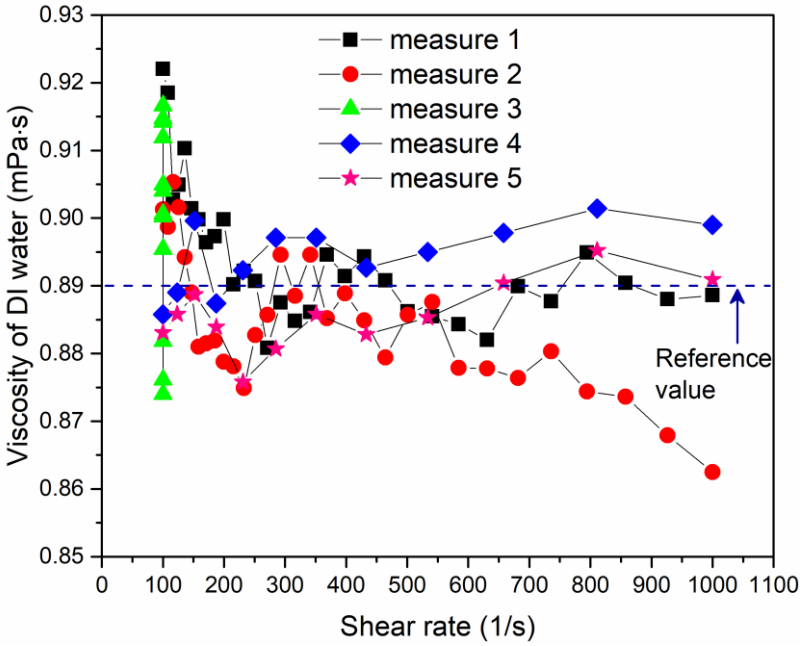

Figure 3-4. Measure the viscosity of De-ionized water before each formal measurement.

3.2.4 Interfacial tension (IFT)

There are several popular methods for measuring IFT, including Pendant drop, Wilhelmy plate, Du Nouy ring and Spinning Drop method. In general, interface tension of 10^{-2}-10^{-1} mN/m is referred to as low interface tension, and that of lower than 10^{-2} mN/m as ultra-low interface tension. The Pendent drop method is usually valid for IFT higher than 0.5 mN/m, but not for low/ultralow IFT. For ultralow IFT it can be measured by spinning drop method, which refers to use a rotating horizontal tube containing a dense fluid in which a drop of less dense sample is placed. Starting to deform into an elongated shape, the elongation stops when the interfacial force is balanced with the centrifugal force [63].

For pendant drop method, the shape of a drop of liquid hanging from a syringe tip is determined from the balance of forces that include the surface tension of that liquid. The surface or IFT at the liquid interface can be related to the drop shape through the following equation:

$$\gamma = \frac{\Delta\rho \cdot G \cdot R_0^2}{\beta}$$

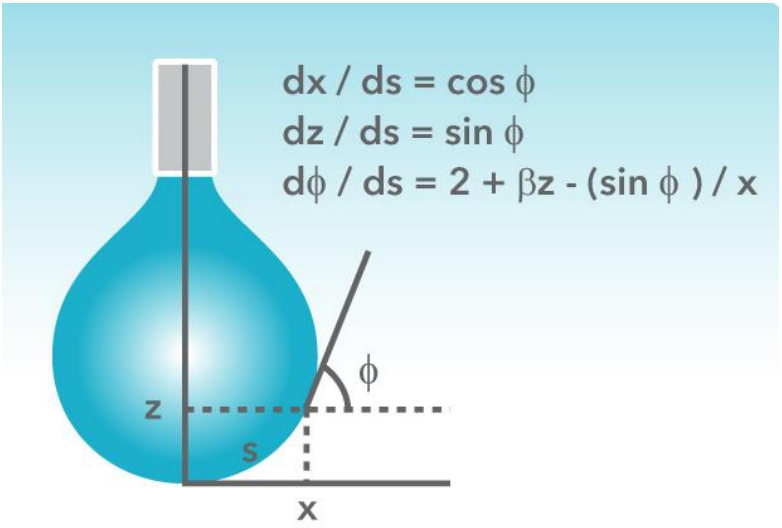

Figure 3-5. Shape factor calculation in Pendent drop method. Figure and equations are taken from Technex website [269].

Where: γ is the surface tension; $\Delta\rho$ is difference in density between fluids at interface; G is the gravitational constant; R_0 is the radius of drop curvature at apex; β is shape factor which is determined by Figure 3-5 and its equations.

3.2.5 Morphology

By using a focused electronic beam to scan the surface of specimens and collecting emitted secondary electrons from the sample which are excited by primary focused electrons, the scanning electron microscopes (SEM) allows imaging surfaces of the samples, and thusly investigating the roughness, quality and the "visual" appearance of the samples. Conventionally, SEM relies on electron interactions at the surface, therefore in order to avoid accumulation of the electrostatic charges at the sample surfaces, specimens should be conductive. Nonconductive specimens can be coated with an ultrathin gold or carbon layer (nanometers thick) either by low-vacuum sputter coating or by high-vacuum evaporation.

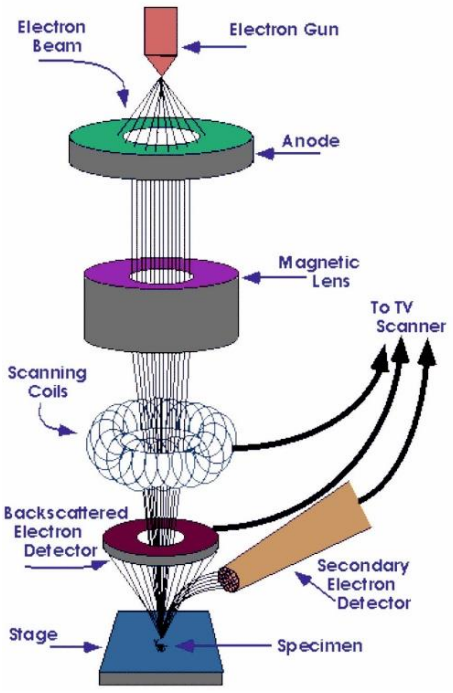

Figure 3-6. Schematic diagram of FEI Quanta 650 FEG-ESEM scanning electron microscope [270].

In this thesis, the morphologies of all rock samples were observed by SEM (FEI Quanta 650 FEG-ESEM). Images of the employed SEM instrument used in this work and its schematic diagram is presented in Figure 3-6.

3.2.6 Concentration

Ultraviolet-Visible (UV-Vis) spectrophotometer can be used to determine the NPs concentration by the light absorbed or reflected by the sample. This technique can also be used for acquiring the absorption or reflection spectrum of the substances based on Beer-Lambert law (Equation 3-1) [126]. The Beer-Lambert law states that the absorbance intensity is proportional to the concentration of absorbing species in the solution and the path length.

$$\mathrm{A} = \log_{10} \frac{I_0}{I} = \varepsilon l c \qquad \text{Equation 3-1}$$

Where A is the measured absorbance, ε is a wavelength-dependent molar absorptivity coefficient when working in concentration units of molarity, b is the path length, and c is the analyte concentration.

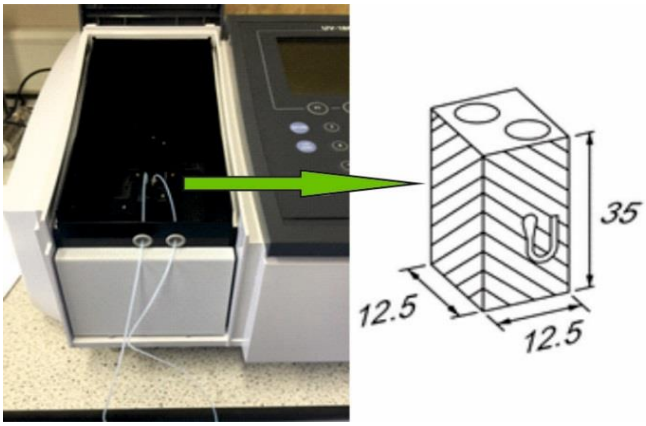

Figure 3-7. Flow cell for UV-Vis spectrophotometer for the experiments conducted in this thesis.

In this study, an UV-Visible spectrophotometer (UV 1800, Shimadzu) was employed to measure the absorption spectrum (in ‘spectrum’ mode), and particle concentration in both static (in ‘quantitative’ option) and dynamic (in ‘kinetic’

option) modes. For dynamic mode, a quartz flow cell was applied to allow the fluids passing through, as shown in Figure 3-7.

Before measuring the concentration of unknown samples in section 3.5.5, the calibration curve was generated for each concentration at a proper wavelength which was selected to make sure the maximum absorbance is not out of range (Figure 3-8).

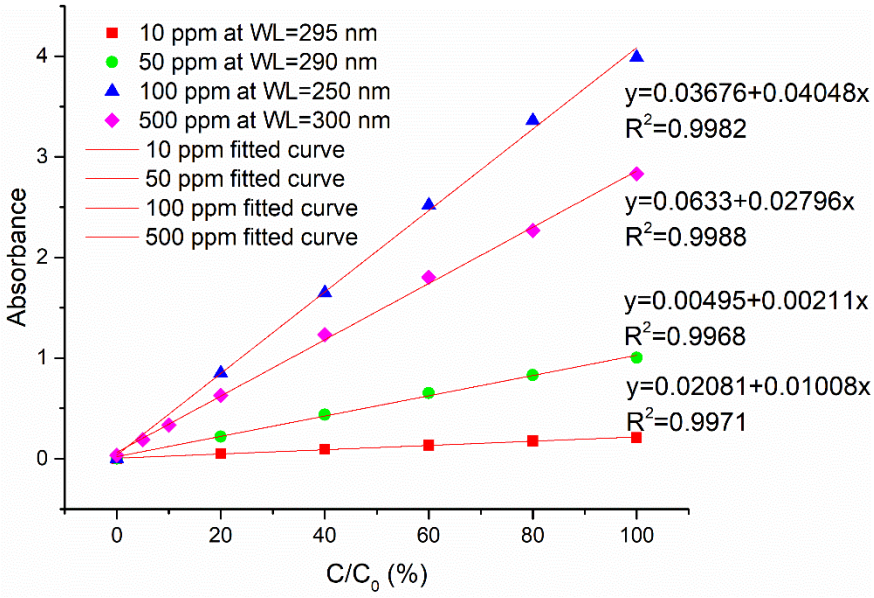

Figure 3-8. The calibration profile to determine the concentration of TiO_2 nanofluid collected in Section 3.5.5.

3.3 Core sample preparation and characterisation

3.3.1 Berea sandstone

Berea sandstone (Figure 3-9) is a commonly used clastic reservoir analogue within the hydrocarbon industry. Consequently, its behavior is well-known with regard to an extremely wide range of parameters and characteristics. Berea sandstone is a moderately porous ($\emptyset \sim 0.18 – 0.25$) sandstone with a high permeability ($k \sim 100$ - 1000 mD, 9.87×10^{-14} - 9.87×10^{-13} m^2). It is isotropic and homogeneous, and is composed of well-sorted sub-rounded grains in the range 70 – 400 µm. The grains are predominantly

quartz (85 to 90%) and feldspar (3 to 6%) and are cemented by quartz, dolomite (1 to 2%), clays (6 to 8%), and trace amounts of iron sulphides [224].

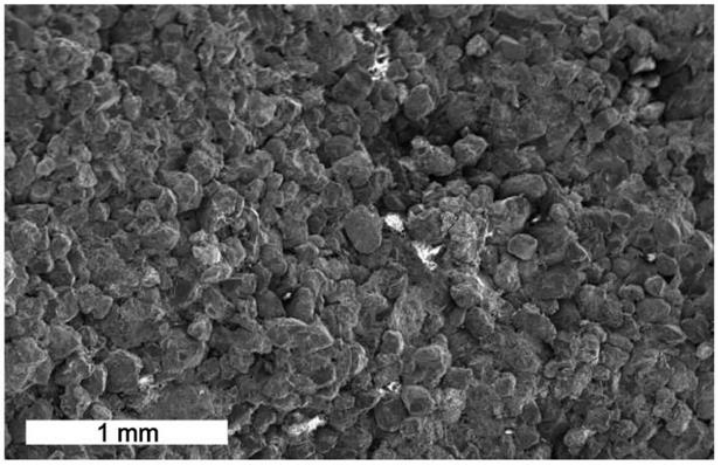

Figure 3-9. Scanning electron microscope image of a broken surface of the Berea sandstone clearly showing well-sorted sub-rounded grains and a homogeneous and isotropic microstructure.

3.3.2 Porosity

The helium porosimeter employed to measure the porosity of cores is working based on Boyle's law. The helium gas in the reference cell isothermally expands into a sample cell. After expansion, the resultant equilibrium pressure is measured. Helium has advantages over other gases because: (1) its small molecules rapidly penetrated small pores, (2) it is inert and does not adsorb on rock surfaces as air may do, (3) helium can be considered as an ideal gas (i.e., z = 1.0) for pressures and temperatures usually employed in the test, and (4) helium has a high diffusivity and therefore affords a useful means for determining porosity of low permeability rocks.

The schematic diagram of the Helium porosimeter apparatus is shown in Figure 3-10. Before putting the rock in the core holder, volumes of V_1 and V_2 need to be acquired through standard steel billets. Then keep the exhaust and connection valve closed, open the fill-in valve until the pressure in reference cylinder get P_1 (around 100 psi) and then close this valve; Keep the fill-in and exhaust valve close, open the connection valve to

build an equilibrium pressure P_2 in the volume system, which is corresponding to the sum of V_1 and V_2, subtracting the volume of grain V_{grain}.. The relationship can be illustrated by the Equation 3-2 below:

$$(V_1 + V_2 - V_{grain})P_2 = V_1 P_1 \qquad \text{Equation 3-2}$$

Calibrate the porosimeter after each 5 times measurements.

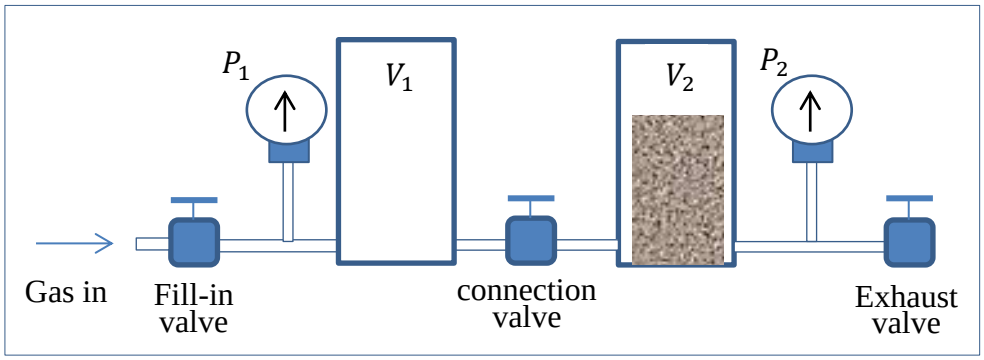

Figure 3-10. Schematic diagram of porosimeter

The porosity, Archimedes saturation weight and dry weight were measured after each cycle of cleaning in order to verify that the cleaned rocks (the cleaning method is described in Section 3.3.7) had similar properties to those of their native state. The dry core weight was measured after 2 days drying in an oven at 70°C. The porosity was determined by both helium pycnometry and Archimedes (buoyancy) methods. For the Archimedes method, the rock samples have to be fully saturated by brine with known density in a vacuum desiccator for 4 hours to make sure they were 100% saturated. The pore volume, grain volume, grain density can be calculated from the recorded dry, saturated and suspended masses, as shown in Table 1. As expected, the Archimedes porosity was slightly smaller than the helium porosity, due to the size, polarity and large molecular weight of water compared to helium. All four cores had similar porosities and pore volume. However there is a moderate variation of the permeability, ranging from 99-195 mD.

Table 3-1. Basic rock properties

No.	Length (mm)	Diameter (mm)	Archimedes method					Helium Porosity (%)	Permeability (mD)
			Bulk Volume (mL)	Pore Volume (mL)	Porosity (%)	Grain Volume (mL)	Grain Density (g/mL)		
SZ1	65.030	38.018	72.96	13.46	19±0	59.52	2.61±0	21.20±0	150.92±0.39
SZ2	64.749	37.922	72.52	13.42	18±0	59.10	2.58±0	21.08±0	138.46±0.80
SZ3	65.470	37.886	73.56	13.40	18±0	60.16	2.66±0	20.82±0	98.73±0.59
SZ4	66.109	37.884	74.26	13.84	19±0	60.43	2.61±0	21.01±0	195.46±0.56

3.3.3 Permeability

Permeability indicates the ability of oil reservoir to allow petroleum liquid passing through its interconnected pores, which is dependet on effective porosity. The permeability is affected by rock grain size, grain shape, grain size distribution (sorting), grain packing, and the degree of consolidation and cementation (Table 2). It is also affected by clay minerals present, especially when fresh water is present. Some clay, particularly smectites and montmorillonites, swell in fresh water and can completely block pore spaces. The permeability can be calculated by using the following Darcy's law.

$$v = -\frac{k}{\mu}\frac{dp}{dx} \qquad \text{Equation 3-3}$$

where: v is apparent fluid flow velocity (cm/s); k is the permeability of the porous rock (D); μ is the viscosity of the flowing fluid (cP), dp/dx is the pressure gradient in the flow direction (atm/cm); and x is the distance in the direction of flow (cm).

The key to acquire a correct absolute water permeability is to get a reliable pressure drop when brine is flowing through the core plug. Before permeability measurement, the dried rocks was saturated in a deaerator for at least 4 hours. Then, the differential pressure was acquired (red line in Figure 3-11) by introducing a back pressure (BP) of 200 psi for around 40 minutes, then removing the back pressure control, and recording

the pressure drop when increasing the injection flow rate at steps of 30, 60, 120, 240 and 480 mL/min, and brought down in the reverse trend.

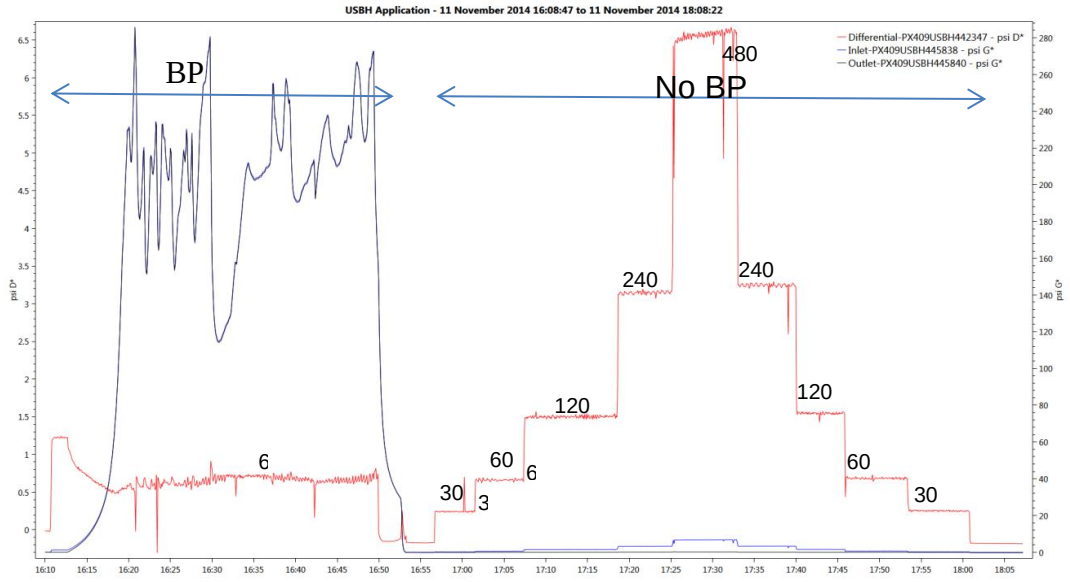

Figure 3-11. Pressure files saved in the format generated by pressure transducer software.

3.3.4 Wettability

The contact angle and IFTs were measured using a KSV CAM 200 optical contact angle and surface tension tensiometer. It uses a high speed CCD camera to record drop shape, then fits the Young-Laplace equation to the drop image for calculation of surface or IFTs, as described in Section 0.

3.3.5 Capillary pressure and pore size distribution

Because mercury cannot wet most subsurface and not spontaneously penetrate fine pores by capillary action, it can only be forced into fine pores by applying an external pressure. Figure 3-12 is the schematic diagram of mercury porosity measurement.

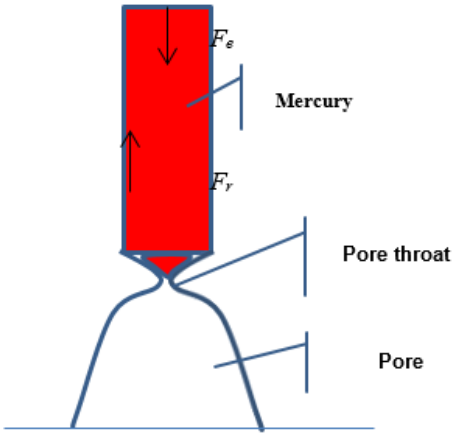

Figure 3-12. Schematic diagram of mercury porosity

The resisting force (F_r) is proportional to the diameter of pore throat (D), the surface tension of mercury and the cosine of contact angle (θ), thus it can be calculated as:

$$F_r = \pi D\gamma \cos\theta$$

The external force can be calculated as:

$$F_r = PA = 2P\pi D$$

When the resisting force is just overcome, the external force should be equal to the resisting force. Thus, the diameter of pore throat (D) can be calculated as:

$$D = -4\gamma \cos\theta / P$$

This equation is called the Washburn equation. By measuring the volume of mercury that intrudes into porous media for each pressure, the volume of pores in the corresponding size class is known. The surface tension of the mercury is usually 480 dyne/cm and θ is the contact angle between mercury and the pore wall, usually taken as 140º. Monitoring mercury volume intruded as a function of pressure permits the generation of pore size/volume distributions from the Washburn equation.

Mercury Intrusion Capillary Pressure (MICP) was used to determine the pore size distribution. The measurements were conducted on a small piece of Berea sandstone, representing an off-cut from the core plugs used in the flooding experiments. The porosity was 19.7%, similar to the helium pycnometry values shown in Figure 3-1. The

specific pores area from MICP measurements was 1.01 m^2/g. It can be concluded from Figure 3-13 that 88% of pore throat diameter centralized in 0.6-36.2 µm range, providing a mean diameter of 14.09 µm, with 6% pore throat diameter was below 227 nm. This size is very close to the hydrodynamic diameter of the rutile ellipsoids nanoparticles, which implies that some pore throats would be blocked by the nanoparticles.

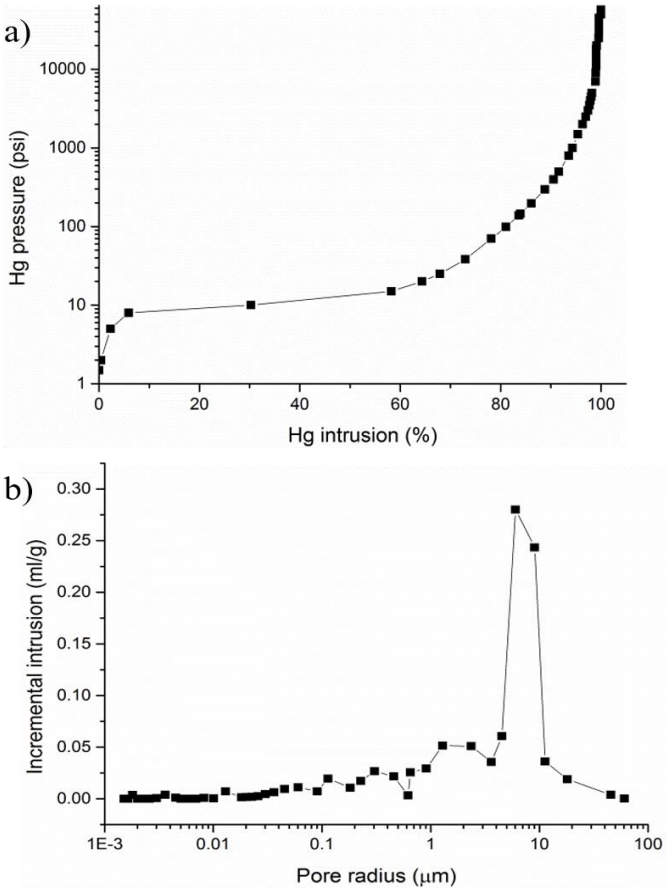

Figure 3-13. A Berea sandstone core sample (SZ13) characterisation by MICP. (a) Mercury injection capillary pressure curve showing the pressure (*y*-axis) required to effect a change in mercury saturation in the sample (*x*-axis). (b) Inverted pore throat radius spectrum showing a well-defined characteristic pore throat size of 7 – 10 µm.

3.3.6 Morphology and mineralogy

An examination of the morphology of grains and pores in the core samples, as well as an elemental analysis were carried out using scanning electron microscope (SEM,

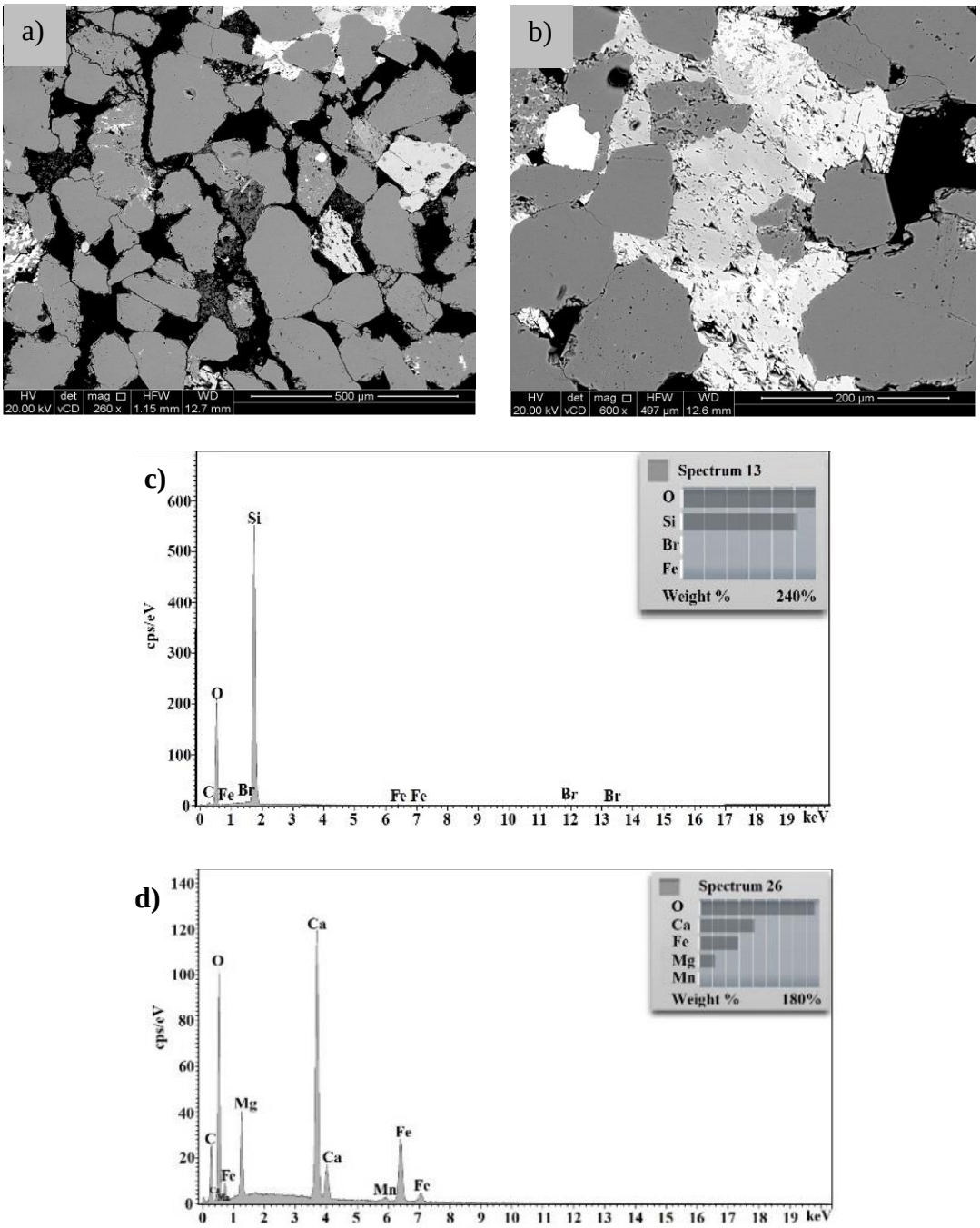

Figure 3-14. (a) SEM of the Berea sandstone with pores shown in black, silica grains in light gray and feldspar in white; (b) higher magnification SEM image of feldspar and porosity between silica grains; (c) EDX spectrum of sand grain showing peaks only for silicon and oxygen; (d) EDX analysis of feldspars.

FEI Quanta 650 FEG-ESEM) and integrated energy-dispersive X-ray spectroscopy (EDX, Oxford X-max 80 SDD) with INCA 350 software. It can be seen from Figure

3-14 that the majority of the pore sizes were above several micrometers, while confirming that the grains were composed of silica with minor contributions from clays (calcium, iron and aluminum).

3.3.7 Core samples cleaning

A group of water-wet Berea sandstones with permeability ranging from 98.73 mD to 195.46 mD were selected as core plugs in this study. All cores were cleaned by the Soxhlet Extractor method (Figure 3-15) before initial flooding and between each subsequent cycle of flooding. This cleaning procedure used dichloromethane (DCM, or methylene chloride) as the solvent, which is immiscible with water and has a boiling point of 40.1 °C. This cleaning process would typically last 7 to 10 days in order to ensure that solvent has extracted all possible oil from the core. After cleaning, the restored core sample was oven dried at 70 °C for 2 days to allow it return to its native condition.

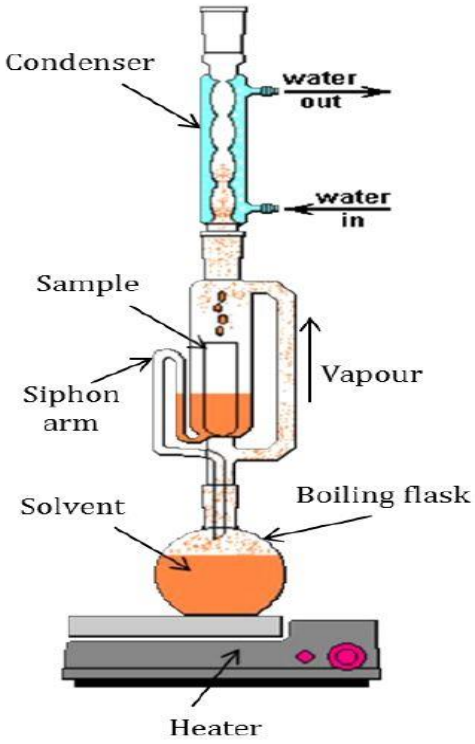

Figure 3-15. Schematic diagram of a Soxhlet Extractor

3.4 Core flooding experiments

3.4.1 Setup description

A flooding system was set up to reveal the nanoparticle-assisted water potential for EOR, and Figure 3-16 shows the integrated experimental instruments and Figure 3-17 shows the schematic view of the core-flooding setup. A Hassler type of core holder, in which the core was loaded, was located vertically and supported by a customized stand. Fluid was injected through the core-holder vertically upwards. Inside the holder, the core was enclosed in an elastic rubber sleeve, upon which was applied a radial overburden pressure of 1500 psi over the rock sample. This pressure was introduced by injecting pressure oil by the high pressure hydraulic hand pump (P142, ENERPAC). An inlet and outlet port in each end plug allowed upstream and downstream flow lines and pressure transducers to be attached. A back-pressure regulator was used to raise the pore pressure inside the core during brine saturation stage, to ensure that gas bubble are completely removed from the core-flooding system at the start of the experiment.

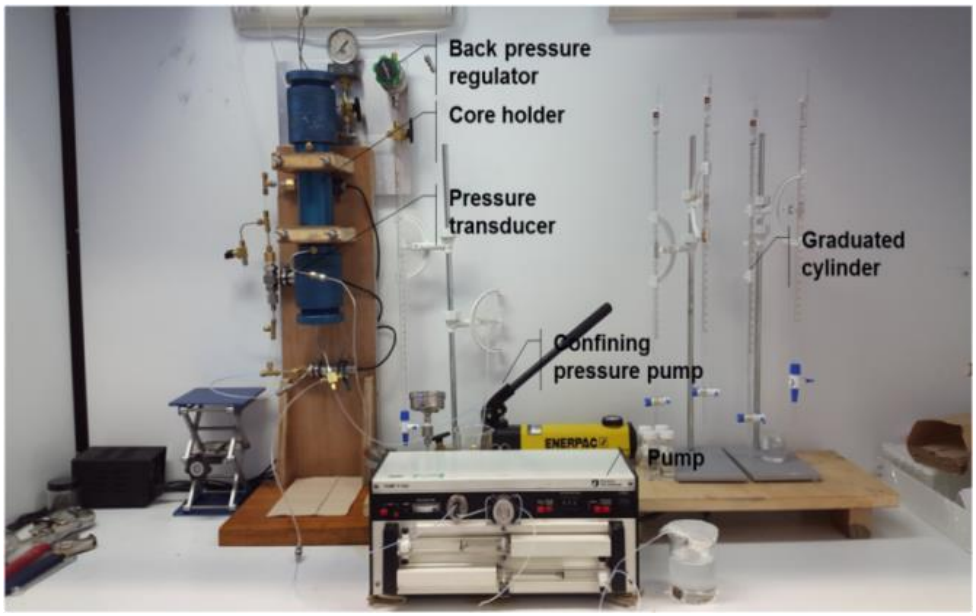

Figure 3-16. Core-flooding experiment setup

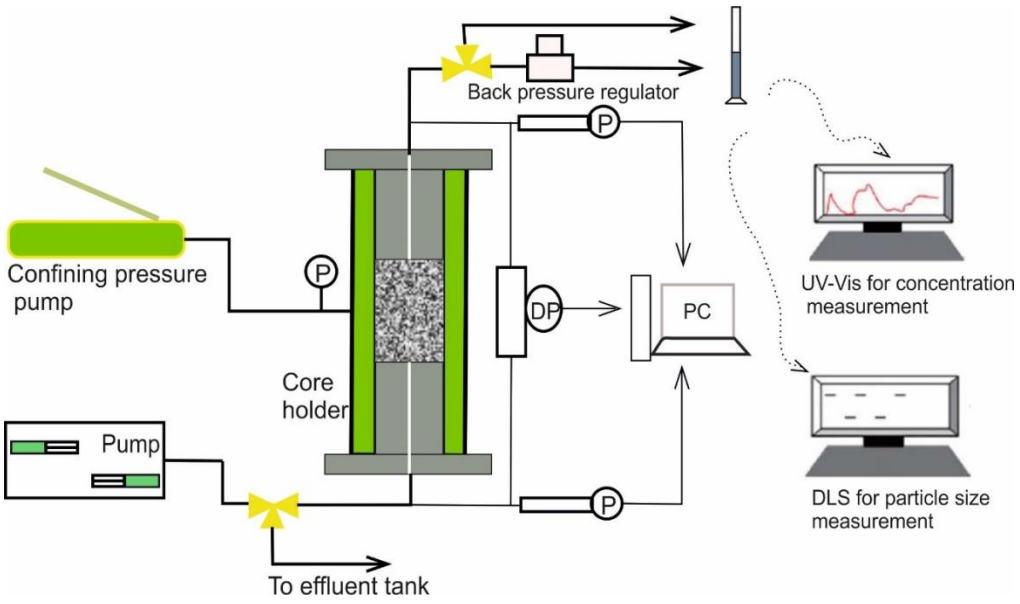

Figure 3-17. Schematic flow diagram for the flooding system

3.4.2 Formal Coreflooding procedure

To clarify the effect of potential influence of stabilizers, three cycles of water-flooding tests were conducted (Figure 3-18). The experiments of each cycle included four stages:

- Brine saturation at a flow rate of 2 mL/min for 6 pore volumes (PV);
- High Viscosity Index (HVI) 60 Oil saturation at a flow rate of 17 mL/min until an 'irreducible' water saturation of S_{wi} =25% was achieved;
- Flooding stage at flow rate of 0.5 mL/min for 3 PV.
- Core cleaning and ready for the next cycle.

This simulates secondary flooding of the reservoir.

Each set of experiments began with a water-flooding with only the synthetic brine (BF) followed by a water-flood with the synthetic brine and the nanoparticle stabilizer but no nanoparticles (BSF), and finally nanoflooding using the synthetic brine, stabilizer and different concentrations of nanoparticles (NF). The cores were cleaned as discussed earlier between each water-flooding cycle.

During each flooding experiment, graduated cylinders marked in 0.1 mL divisions were used to collect the effluent liquid in order to determine the volume of oil and water. During NF experiment, effluent samples were collected manually during the flooding process and a total of 15-19 effluent samples of 1.5 mL each were collected. The nanoparticle size distribution of the effluents was determined off-line by the DLS device, and UV-Vis spectroscopy (introduced in) was used to measure the particle concentration. The determination of concentration was based on the comparison of the effluent absorbance against an established calibration curve between the absorbance and nanoparticle concentration. The concentration of nanoparticle suspension entering cores, C_o, and the concentration of sample collected, C, were applied to generate breakthrough curves of C/C_o as a function of pore volumes passing through the porous medium. Detailed sample characterization was conducted for nanofluids after the flooding experiments.

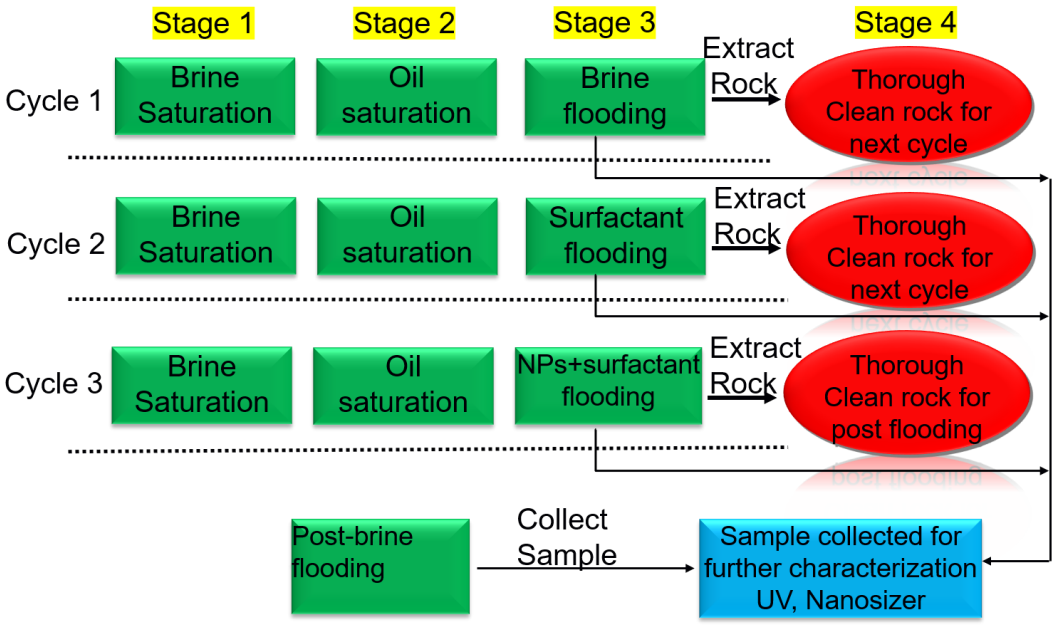

Figure 3-18. Core-flooding procedure to examine the oil recovery potential of brine, stabilizer and nanoparticles.

3.5 Results and discussion

3.5.1 Nanofluid stability

For any practical application, nanoparticles have to be stabilized properly in the presence of various ions similar to the composition of brine. The stabilization mechanism could be either steric [271], electrostatic [272] or a combination of both. Many researchers have reported that nanoparticle cannot be stabilized easily in high salinity water [240-244], especially when the ionic strength exceeds the critical salt concentration (CSC) [240]. The presence of ions, especially divalent cations such as Mg^{2+}, Ca^{2+} and Ba^{2+}, [242], could significantly reduce the stability due to the compression of the electric double layer [234, 273].

The agglomeration kinetics of TiO_2 under the influence of a number of stabilizers mentioned above were assessed in 0.1 M and 1 M NaCl concentrations in order to determine the right stabilizing agent. In this exercise, the TiO_2 nanoparticle concentration was 500 ppm and the pH was adjusted at 6.8±0.3 when gentle magnetic stirring was applied. All surfactant concentration was fixed at 0.3 wt% relative to water content except SRFA whose concentration was 100 ppm. The main results are given in Figure 3-19. Regardless of the stabilizer, an increase in the brine salinity clearly increases particle size (Figure 3-19a). SCD showed the best performance in terms of particle size and was chosen for the following further experiments.

The particle size and zeta potential evolution of four SCD-stabilized nanofluids of different concentrations from 10 ppm to 500 ppm in a 0.1 M NaCl brine were measured over a two week period following their fabrication, as shown in Figure 3-19b. There was a slight increase in size for almost all concentrations, but always remaining lower than 240 nm after two weeks. Absolute values of zeta potential often saw sharp decreases in the first 4 days, becoming more stable during the remainder of the two

week period, at around -27±3 mV for the 50, 100 and 500 ppm concentration samples, and below -18 mV for the 10 ppm sample. Extrapolation implies that the low concentration sample would become stable at about -14±3 mV after about 3 weeks.

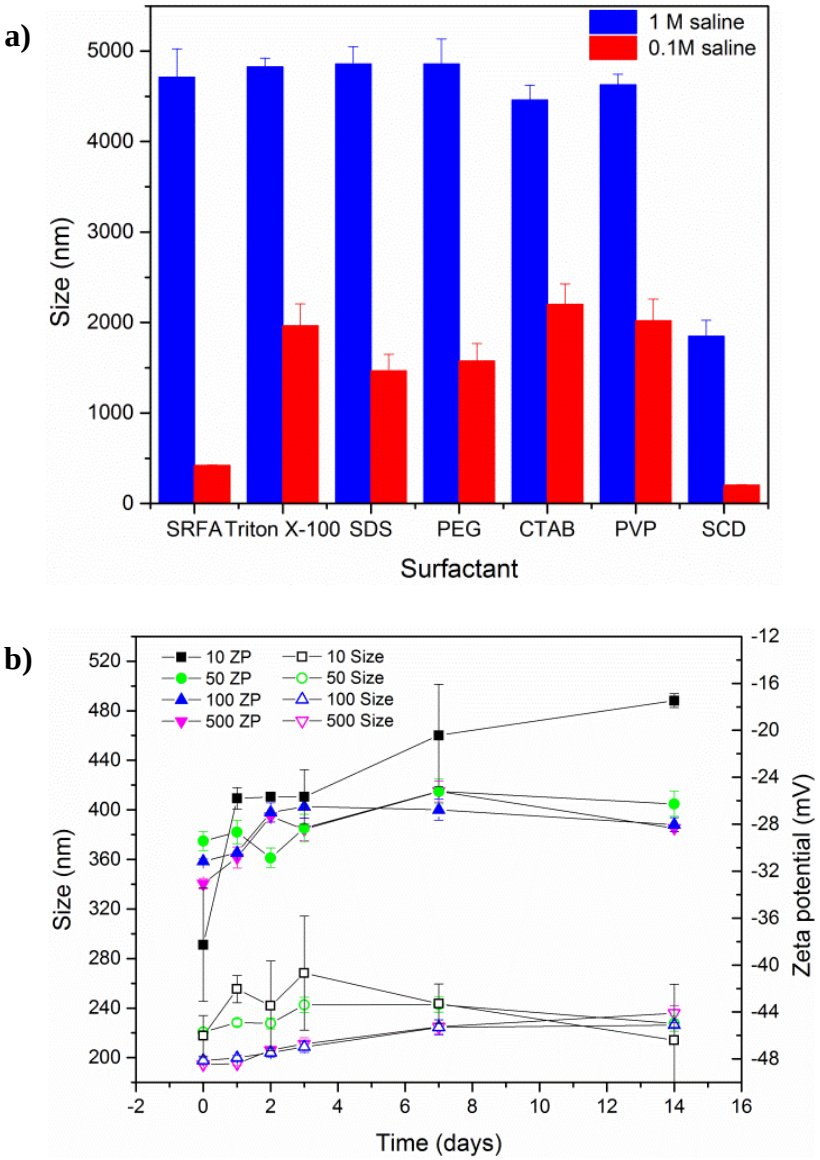

Figure 3-19. Stability of TiO_2 nanoparticles (rutile ellipsoids), (a) average particle size comparison for different stabilizers and two brine salinities (0.1 M and 1 M NaCl), and (b) temporal behaviour of the average particle size (open symbols) and zeta potential (solid symbols) for four different TiO_2 nanoparticle concentrations (10, 50, 100 and 500 ppm) in a 0.1 M NaCl brine solution stabilized by SCD)

3.5.2 Fluid properties

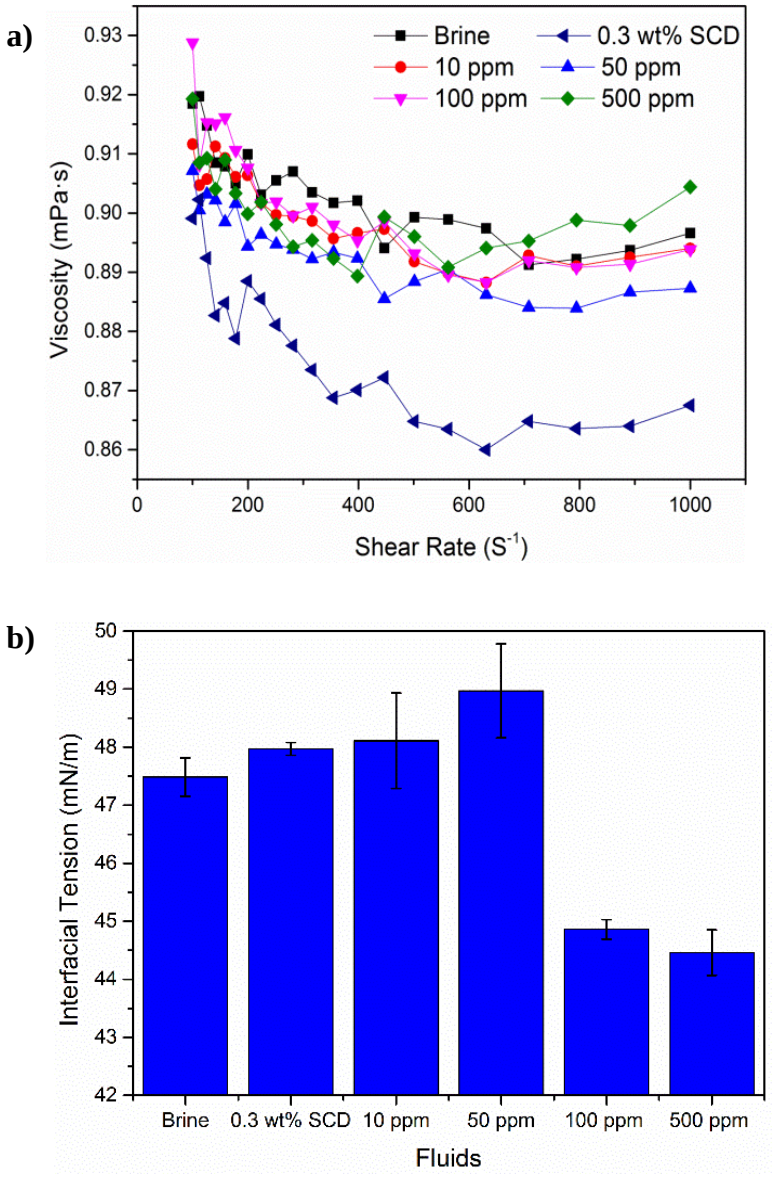

Figure 3-20. (a) Dynamic viscosity, and (b) IFT of the 0.1 M brine alone, the 0.1 M brine with 0.3%wt SCD stabilizer, and the stabilized brine with 10, 50, 100 and 500 ppm of TiO_2 nanoparticles.

The dynamic viscosities of the base fluid (brine), base fluid with stabilizer and all four nanofluids are shown in Figure 3-20a. The dynamic viscosity for the High Viscosity Index (HVI) mineral oil was also measured at 41.2 mPa·s. This relatively high dynamic viscosity is beneficial, reducing the irreducible water saturation S_{wi} to 25% in a water-wetting rock.

The introduction of the stabilizer (SCD) alone reduced the viscosity significantly, but the effective viscosity returned to almost the level of the initial brine after the inclusion of nanoparticles. The effect of particle concentration on the effective dynamic viscosity was therefore small due to the low particle concentration.

The addition of SCD alone slightly increased the IFT of brine, as shown in Figure 3-20b, reaching about 47.97±0.11 mN/m for an SCD concentration of 0.3 wt%. The variation of IFT of nanofluids was also small, having a maximum value of 48.97±0.81 mN/m at 50 ppm and a minimum of 44.46±0.39 mN/m at 500 ppm.

3.5.3 Rock property changes

The absolute permeability and helium porosity were measured after each flooding cycle to track whether the rock itself was damaged or modified by the core-flooding processes. The results are summarized in Figure 3-21, which show that the change of porosity from core-flood to core-flood was small for all rock samples, with the largest variation in the range of 2% for sample SZ2. Nearly constant porosity was observed for both samples SZ3 and SZ4 during different stages of the flooding.

The permeability experienced a drop after the BF and BSF flooding, but the change was small after the NF flooding Figure 3-21b. This suggests that the stabilizer used may have a deteriorating effect on the permeability. Some stabilizers may partially remain inside the rock during the flooding and reduce the permeability value. The nanoparticle alone may not cause the reduction in the permeability, and instead samples SZ2 and SZ4 showed that the permeability are slightly increased after the NF flooding, suggesting perhaps that some stabilizer was removed during the NF flooding phase. This clearly shows the importance of proper selection of stabilizers. As the porosities and absolute permeabilities for all rocks after NF flooding were very close to those after

BSF flooding, two of the cleaned rocks (SZ1 and SZ2) were selected for 5 ppm and 20 ppm NF flooding respectively.

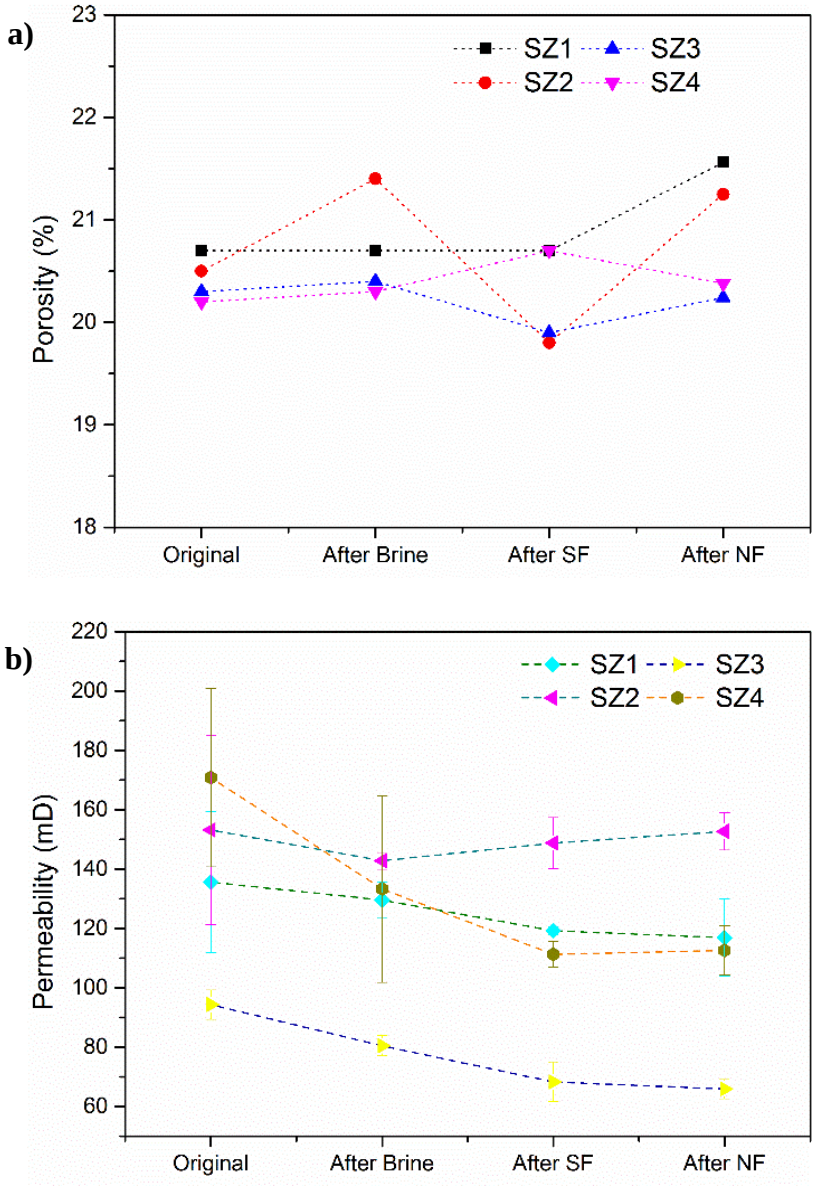

Figure 3-21. Variations of (a) sample helium porosity, and (b) sample permeability for original core samples, and for restored cores after core-flooding with brine (After Brine), brine and stabiliser (After SF) and nano-flooding (After NF).

3.5.4 Core-flooding results

While we measured the oil and brine production regularly during each core-flooding (as shown in Figure 3-22), we paid particular attention to the cumulative oil production, and hence the oil saturation at three main interest points: break-through (BT) saturation,

saturation at 1PV, and ultimate saturation. The former value showed the practical oil amount when the breakthrough occurs, whereas the last one showed the maximum amount of oil that can be recovered for a given flooding. In the experiments, the breakthrough was identified when the first drop of water was produced at the downstream of the core by removing the delay caused by dead volume. It was observed that additional oil recovery becomes small after about 1 PV and the cumulative oil recovery (COR) was calculated at 3.2 PV, by which time no more oil could be collected for another 20 minutes.

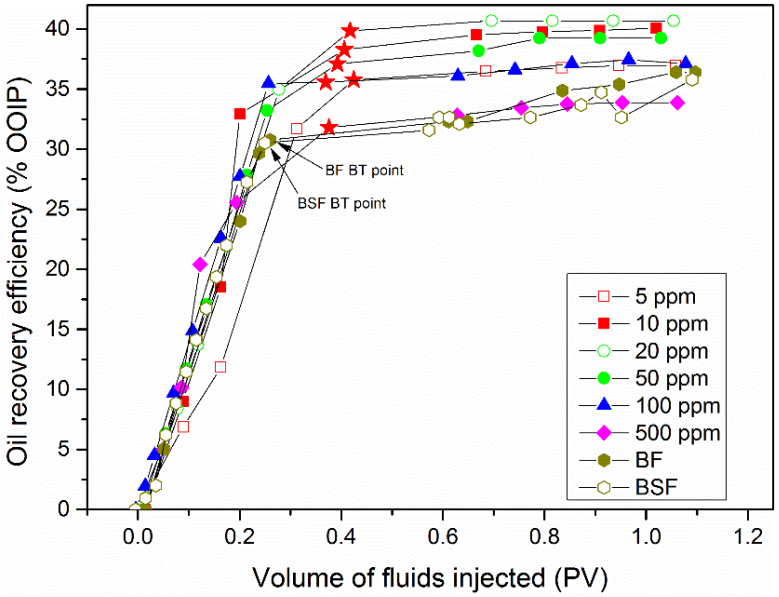

Figure 3-22. Examples of the volume of oil recovered from 0 to 1 PV expressed as a percentage of the initial oil saturation. The stabiliser is 0.3 wt% SCD, and data is given for synthetic brine (BF), synthetic brine with stabiliser (BSF) and for synthetic brine, stabiliser and six different concentrations of TiO_2 nanoparticles. The breakthrough points are marked by red five-pointed stars.

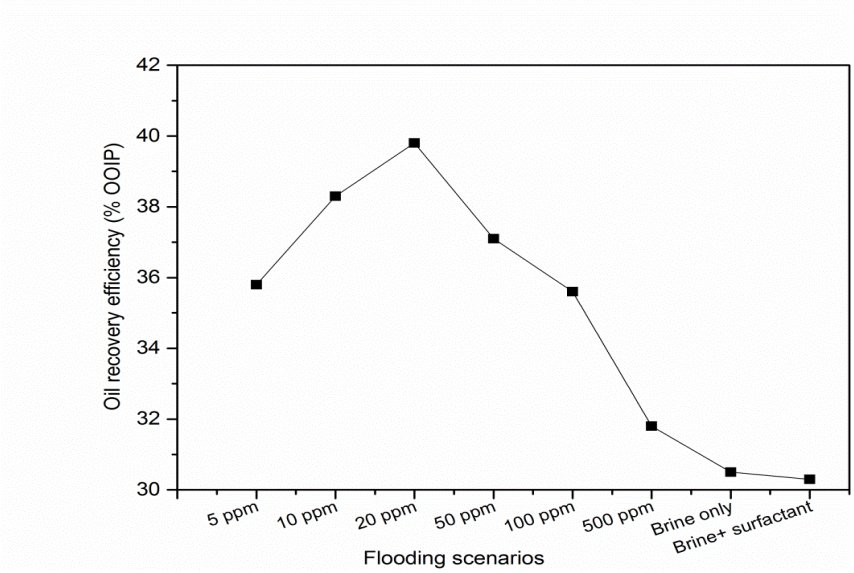

Figure 3-23. Oil recovery at breakthrough expressed as a percentage of the initial oil saturation for synthetic brine (BF), synthetic brine with stabiliser /surfactant (BSF) and for synthetic brine, stabiliser and six different concentrations of TiO_2 nanoparticles. The stabiliser (labelled as surfactant here) is 0.3 wt% SCD.

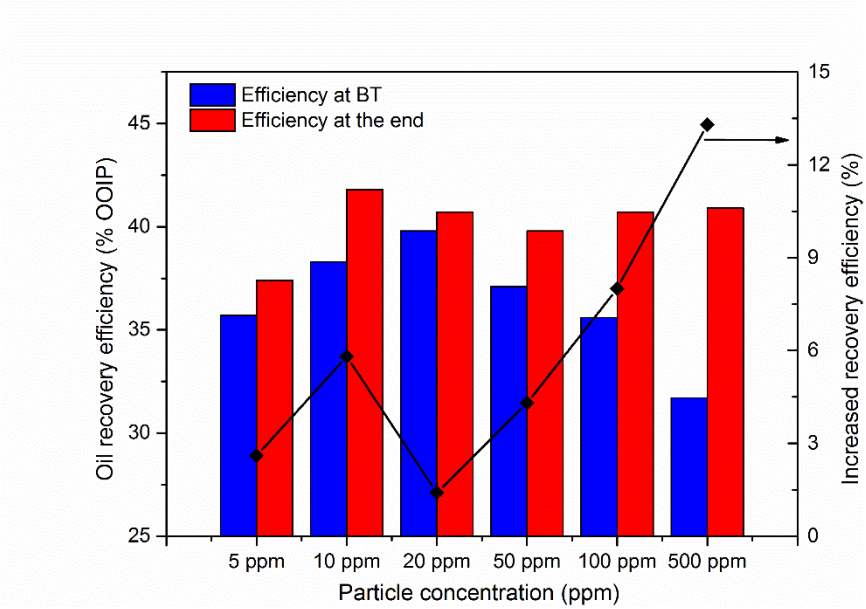

Figure 3-24. COR at breakthrough (blue bars) and at the end of flooding (red bars) expressed as a percentage of the initial oil saturation for six different concentrations of TiO_2 nanoparticles, together with the amount of oil produced after breakthrough (solid diamonds and lines) expressed as a percentage of the oil in place at breakthrough. The stabiliser is 0.3 wt% SCD.

Figure 3-22 shows that there was a rapid recovery of oil immediately following the fluid injection and before oil breakthrough. In this part of the core-flood the aqueous fluid pushes the oil out of the sample in a quasi-piston-like displacement process, and the oil recovery increases approximately linearly with the volume of injected displacing fluids. This linear increase in oil production ends after the injection of about 0.4 PV, when brine breakthrough occurs.

The cumulative oil recovery at breakthrough is shown in Figure 3-22. The BT point was observed at about 0.25 PV for the brine only (BF) and brine with stabiliser floods (BSF), and in the range of 0.35 to 0.45 for TiO_2 nanofluid flooding (NF) with different concentrations of nanoparticles. Brine only flooding resulted in an average of 30.3% recovery of the oil originally in place (OOIP), and a similar value (i.e., 30.5%) was found for flooding with a mixture of brine and stabiliser (BSF). This shows that the influence of the 0.3 wt% SCD stabilizer on the oil recovery was negligible in this work. However it should be noted that this is not a universal conclusion. Other stabilizers especially some designed surfactants, could affect the oil recovery rate significantly, and their effects shall be identified appropriately in any experiments to illustrate the nanoparticle effect. Figure 3-23 clearly shows that adding TiO_2 nanoparticle can increase the oil recovery rate significantly but in a non-linear manner. At lower particle concentrations, the oil recovery rate increases with the increase of particle concentration, reaching a peak value at about 20 ppm, after which it starts to decline. About 35.8% of the oil originally in place was recovered at the lowest concentration of nanoparticles tested, i.e. 5 ppm, compared to the use of brine alone (30.3%). The best oil recovery of those scenarios tested was about 39.8% of OOIP, which occurred for a nanoparticle concentration of 20 ppm. This represents nearly a 31.4% increase in oil recovery compared to water-flooding with plain synthetic brine or brine with stabiliser but no nanoparticles. However, further increase of particle concentration resulted in a

decrease in the enhancement of oil recovery compared to the plain brine and brine with stabilizer cases. For a nanoparticle flooding with a concentration of 500 ppm, an oil recovery of only 31.8% of OOIP was achieved at the breakthrough, representing only 4.95% enhancement of oil recovery over flooding with brine or brine with stabilizers but no nanoparticles. Detailed discussions are in the below section.

The COR at the end of the experiment is shown together with that at breakthrough in Figure 3-24. The general dependence of the COR on particle concentration was found to be similar to that at breakthrough, but the peak value occurred for a 10 ppm nanofluid, with a total oil recovery of 43.75% of OOIP, representing a 44.39% increase on the BF scenario.

Unlike the breakthrough case, there was no substantial decrease in total COR at the end of the experiment for nanofluids with concentrations greater than 20 ppm because these fluids progressively exhibited a large post-breakthrough production of oil. Despite having the lowest recovery at breakthrough, the 500 ppm nanofluids achieved a COR at the end of the experiment of 40.9% of OOIP, second only to the total recovery of the 10 ppm nanofluid. The 500 ppm nanofluid mobilized an additional 13.3% of the oil in place at breakthrough point. We have attributed the mechanism for post-breakthrough enhancement of oil production to ‘log-jamming’ of some pores with nanoparticles which then forces oil to be produced from adjunct pores where it was previously trapped. This mechanism is discussed in the following sections.

3.5.5 Nanoparticle migration behaviour during flooding

3.5.5.1 Pressure profiles among different flooding cycles

Examples of three differential pressure profiles that were measured during different stages of flooding are shown in Figure 3-25. The nanoparticle concentration in this figure is 500 ppm and occurs in the data represented by blue triangles. The behaviour

indicated in the figure suggests that a log-jamming effect [111, 210] may be significant in the core-flood with the 500 ppm nanofluid.

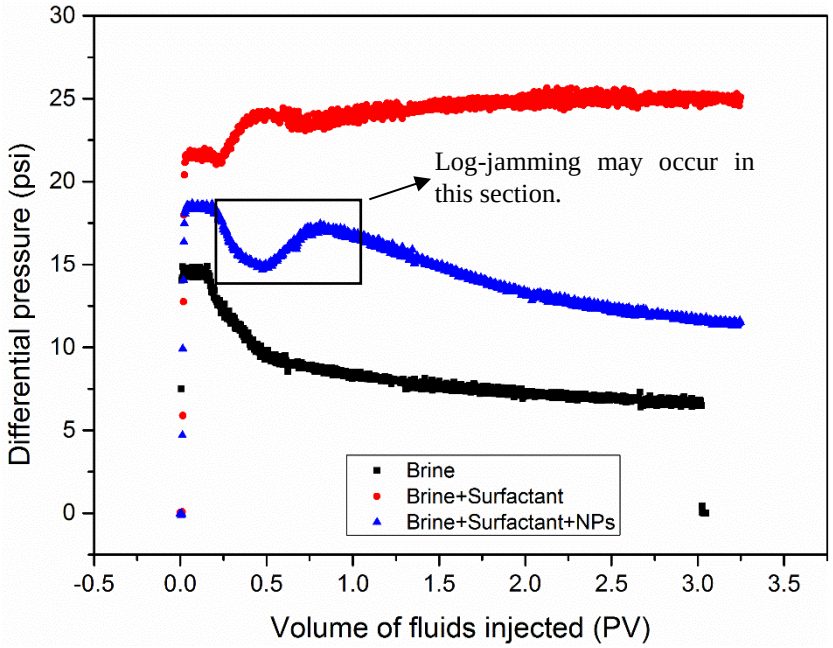

Figure 3-25. Pressure profiles for brine (0.1 M NaCl, black points), brine with stabiliser/surfactant (red points) and a 500 ppm TiO_2 nanofluid (blue points) flooding on core SZ4. The pressures should the same at the start, at which time there is still oil to be introduced by the leading dead-volume. The differential pressure offsets between each of the flooding profiles is caused by small permeability differences between flooding cycles as shown in Figure 3-21).

The increased pressure for the nanofluid suggests that a portion of the nanoparticles became temporarily stuck in the core, reducing the permeability, and increasing the pressure. Subsequent decrease of pressure may be caused by the un-blockage of the jammed particles. It was thought that the accumulation of nanoparticle at the entrance of pore throats would produce a higher pressure at the adjunct pore channel, in which the oil trapped would be mobilized. Similar observations were reported by previous research [111, 210]. The presence of oil phase may promote the jamming effect as the nanoparticles were diffused to the oil-water interfaces and were confined there. The enriching of particle concentration at the oil/water interface has been identified by a few

prior studies [274-276], where it is concluded that the nanoparticles tend to stay at the oil/water interface and the energy (ΔG) required to detach the nanoparticle from the interface is high, as long as the particle is not completely water-wet or oil-wet. More analysis can be found in Section 5.5.1.

3.5.5.2 Nanoparticle breakthrough behaviour

Ultra-violet spectrophotometer measurements have been used to monitor the amount of nanoparticles transported through the core samples. The measurements in Figure 3-26 show that nanoparticle transport is strongly dependent on the nanoparticle concentration. The outlet to inlet concentration ratio, C/C_o, generally decreases with increasing particle concentration. For example, for a 10 ppm nanoparticle concentration, breakthrough was achieved quickly with C/C_o approaching unity at 0.43 PV just as the first drop of nanofluid emerged from the core. The 50 ppm nanoparticle sample showed a similar early breakthrough at 0.39 PV but with a reduced concentration of nanoparticles in the emerging fluid (C/C_o =0.7), implying that up to 30% of the injected nanoparticles are remaining within the core. At higher nanofluid concentrations (100 ppm and 500 ppm) the concentration of nanoparticles in the breakthrough fluid is even less (C/C_o =0.65 and C/C_o =0.18, respectively) with most of the injected nanoparticles remaining inside the core (Figure 3-26). The peak concentration for the 500 ppm nanofluid flood was reached at 1.69 PV, and the maximum transport ability stayed below 20% (i.e., C/C_o <0.2).

Each flooding experiment was followed by an injection of a further 4 PV of plain synthetic brine (0.1 M NaCl) in order to check if the particles were strongly stuck inside the rock. This brine post-flooding process was conducted after the end of the nanofluid flooding at 3.2 PV for all experiments. The results (i.e., right-most part of Figure 3-26) show that significant amount of NPs can be cleaned out from the cores immediately

following the brine flooding. However after another about 3 PV, no more nanoparticles can be driven out, suggesting that some nanoparticles remain trapped in the cores. Further calculation shows that, for the highest concentration (500 ppm) flooding, 19.66 mg of nanoparticles in total (87.2% of the total injected amount) were deposited in the rock during nanofluid flooding and remained trapped there, which corresponds to about 17.15 mg of TiO_2 nanoparticle per square meter of grain surface, which represents an coverage of 0.92% of the rock's internal surface area if it is assumed that the nanoparticles are deposited as a monolayer (Table 3-2).

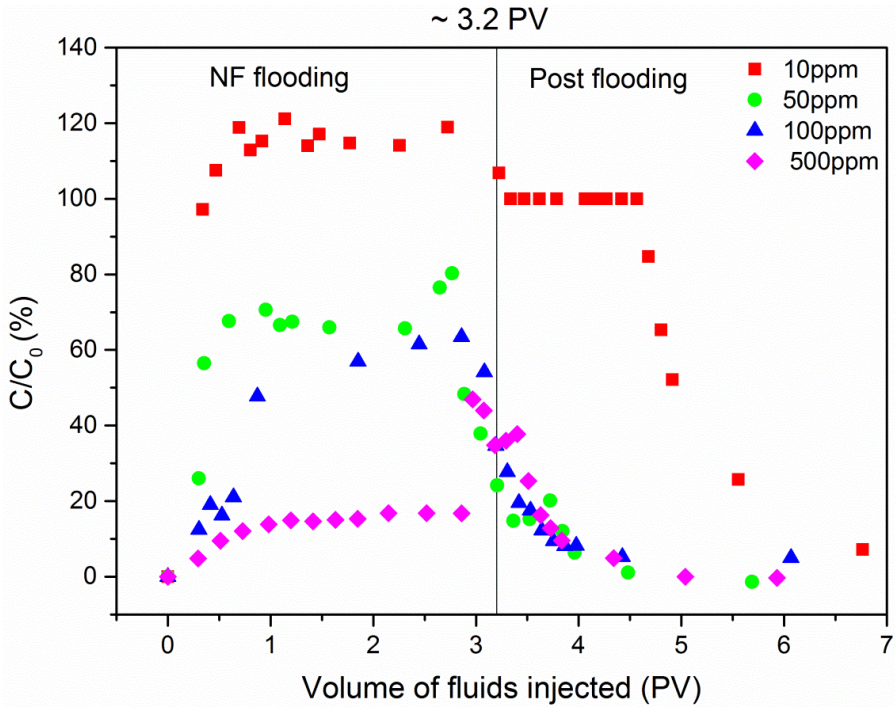

Figure 3-26. Particle breakthrough ability during flooding with four different concentrations of TiO_2 nanofluid and subsequent post-flooding with synthetic brine. C_0 is the concentration of initial fluids before NF flooding.

Fine particle migration in porous medium is an area of extensive research interest [196, 277]. It is known that the mobility of particles is affected by four main mechanisms; (i) blockage, (ii) adsorption, (iii) straining, and (iv) gravity sedimentation. The adsorption effect would be small in this study because our nanoparticles are negatively charged, and the zeta potential of Berea sandstone is negative at high ionic

strength [278] and the range of pHs encountered in these experiments and in hydrocarbon reservoirs [234, 279, 280]. The gravity sedimentation effect is also expected to be small due to short residence time of particles in the core and the effect of Brownian motion.

Table 3-2. Nanoparticle retained in core samples during nanofluid flooding.

Core No.	NP conc. (ppm)	Total NP mass (mg)	NP mass retained in core (mg)	NP retained in core (%)	Total internal pore surface area (m^2)	Mean retained NP trapping density (mg/m^2)	Mean area of internal pre surface coated (%)
SZ1	10	0.375	-0.133	NA	154.73	NA	NA
SZ2	50	1.685	0.776	46.0	152.58	0.005	0.08
SZ3	100	3.786	2.248	59.4	157.26	0.014	0.22
SZ4	500	19.659	17.152	87.2	158.32	0.108	0.92

In this work, it appears that the particle migration was affected mostly by pore-throat blockage and straining (i.e., a log-jamming effect), as well as the presence of the oil phase. The blockage effect is highly dependent on the particle concentration [281]. This is supported by pore size analysis of the Berea sandstone (Figure 3-13 and Figure 3-14), the latter of which shows that around 6% of pore throats are under 220 nm when subjected to quantitative image analysis, i.e., less than the hydrodynamic diameter of nanoparticle (Figure 3-1b). These relative dimensions suggest strongly that the blockage could take place, especially when the fluid contains high concentrations of nanoparticles. Consequently, log-jamming of high concentrations of nanoparticles is consistent not only with the relative dimensions of the pores and nanoparticles themselves, but also with the data shown in Figure 3-25 and Figure 3-26, making it an important factor influencing particle migration and implying that high nanoparticle concentrations should be avoided in nanoEOR.

In order to examine the NP migration behaviour without the presence of oil, 100 ppm nanofluids were injected into Berea sandstone directly after brine saturation. The

comparative results (Figure 3-27) show that the nanoparticles present a faster breakthrough in the presence of oil. Significant amount of nanoparticles were detected at the exit of the core sample at about 0.8 PV in the presence of oil, but their presence was delayed to about 1.5 PV in the absence of the oil phase. The Berea sandstone used in this work is strongly water-wet. Consequently, the water phase occupies the pore spaces close to the grain surfaces and the oil phase occupies discrete drops or connected ganglia in the centre of pores, which are continuous through pore throats when they are sufficiently wide and can modify the electrical and hydraulic connectedness of the fluids in the pores [282].

The transport of the nanoparticles is confined to the aqueous phase because the rutile ellipsoids TiO_2 nanoparticles used in this work are water-wet. The early breakthrough for the transport of nanoparticles in the presence of oil exhibited in Figure 3-27 occurs because the nanoparticles are confined to be transported in the water phase that initially occupies only a fraction of the pore volume. Consequently any given volume of injected nanofluids, expressed in pore volumes, will displace more than its apparent volume of water phase and hence apparently travelling through the core more efficiently. That same nanofluid is also displacing oil, which is produced, so that the injection of nanofluids becomes apparently less and less effective as the nanoflooding progresses, explaining why the data for the displacement in the presence of oil appears to start effectively with a breakthrough at about 0.5 PV, but becomes less efficient after about 1.4 PV. By contrast, in the absence of an oil phase the nanofluids have the entire pore volume to travel through during the entire injection process. The breakthrough is consequently delayed until about 1.2 PV.

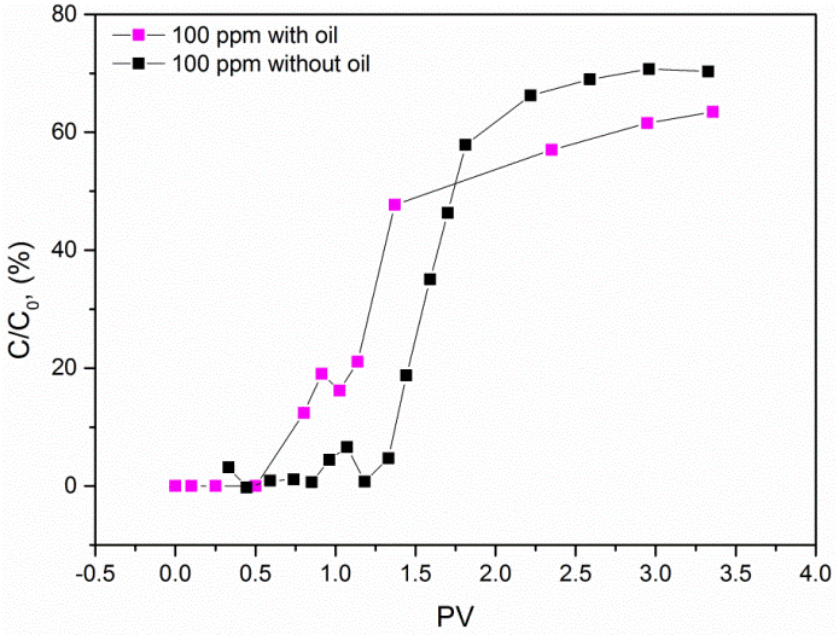

Figure 3-27. Nanoparticle transport during core-flooding with a 100 ppm table TiO_2 nanofluid with and without presence of oil. The ratio of the concentration of nanoparticles at the outlet to that of the inlet (C/C_o) is shown as a function of pore volumes of nanofluid injected.

3.5.5.3 Particle size distribution

The particle size distribution of the effluent samples was examined by the dynamic light scattering (DLS) method. It was interesting to observe that the hydrodynamic size of nanoparticle showed a bimodal distribution, which has also been reported by Ehtesabi et al. [126]. Consequently, although the size distribution of the injected samples show a range of about 100 nm to 400 nm (Figure 2b), the effluent shows a population of nanoparticles in the range 10 nm to 100 nm and a larger group, ranging from about 100 nm to 400 nm. It is clear that passage through the rock has effectively separated the two size fractions.

The peak particle sizes of the two modes and a measurement of their ranges at different flooding volumes are shown in Figure 3-28. It is interesting to note that the smaller and larger fractions of nanoparticle occur in the effluent, but the middle range

does not. This implies that it is the nanoparticles of intermediate size that become trapped in the cores. This implies that the choice of nanoparticle size is a critical one for designing an efficient nanoEOR process.

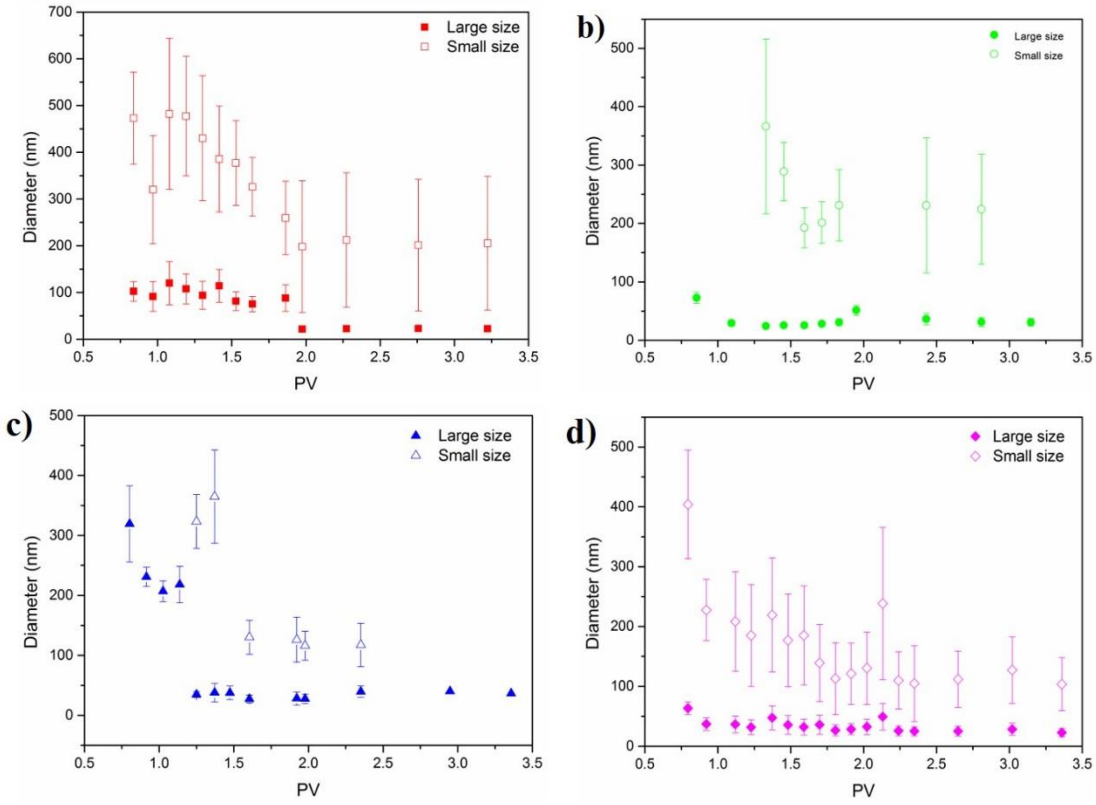

Figure 3-28. Effluent nanoparticle size distributions for nanofluid core-flooding with different nanoparticle concentrations; (a) 10 ppm, (b) 50 ppm, (c) 100 ppm, (d) 500 ppm.

As discussed above, a few particle migration mechanisms were responsible for the particle mobility, and among those, the log-jamming effect could form large loose agglomerates, responsible for the forming of the large particle population. It is also interesting to note that for all nanoparticle flooding scenarios, the particle size for the larger population of nanoparticles decreased from around 300 nm to around 100 nm as the flood progressed Figure 3-28.

3.6 NanoEOR mechanisms

The results so far clearly show that well-stabilized nanofluids can increase oil recovery, and that the effect is strongly dependent on the nanoparticle concentration. At nearly 33% increase of oil recovery at breakthrough, this method has gone beyond our initial expectation. As reviewed briefly in the introduction section, many potential mechanisms have been proposed for the nanoparticle enhancement of oil recovery, but none is well-accepted as yet.

We have seen in Section 3.5 that log-jamming is likely happen after breakthrough, especially for high nanoparticle concentrations, such as 100ppm and 500 ppm in this research, and this may contribute to enhancement of oil recovery. We will examine other mechanisms in depth in this section.

3.6.1 The effect of mobility ratio modification

The value of *M* was larger than unity in this work, indicating a higher water mobility than that of the oil. Under these conditions the displacing fluid (brine, brine and stabiliser and nanofluids) would invade the rock through a non-uniform front, resulting in an early breakthrough, which is supported by Figure 3-22. Clearly reducing the mobility ratio could lead to a higher oil recovery. Figure 3-20a shows that the effective viscosity of the nanofluid was almost independent of nanoparticle concentration within the 5 ppm to 500 ppm range used in this work. However, the produced oil (Figure 3-29) shows a small reduction in viscosity, which is attribute to contamination by nanoparticles. It is still unclear about the effect of nanoparticles on relative permeability curves. There have been a few limited studies which show that the inclusion of different nanoparticles could affect the relative permeability ratio significantly [120] and this modification might be through the modification of the wettability of the rock by the deposition of nanoparticles, as will be discussed later.

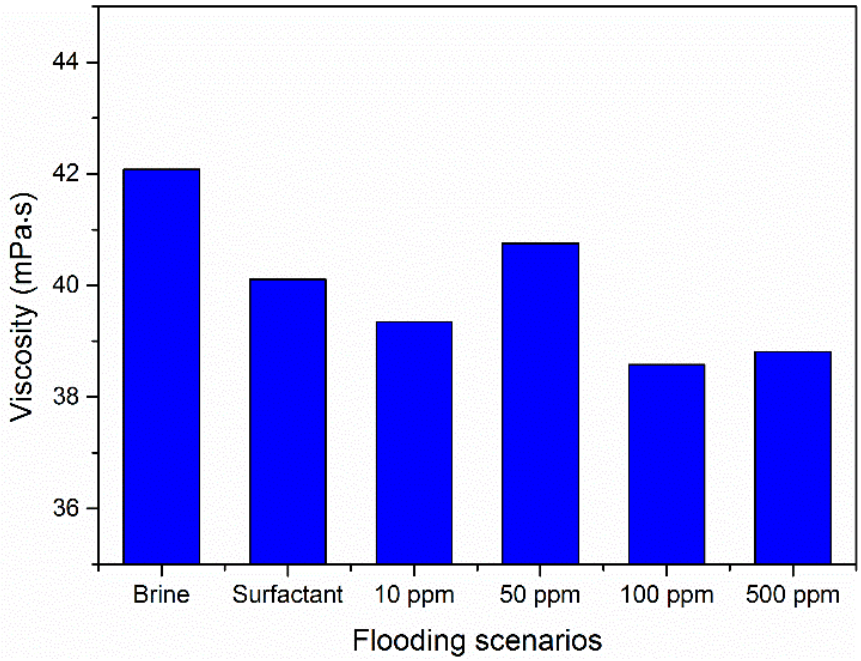

Figure 3-29. Viscosity of produced oil for synthetic brine (BF), synthetic brine with stabiliser/surfactant (BSF) and for synthetic brine, stabiliser and four different concentrations of TiO_2 nanoparticles.

3.6.2 The capillary effect

One of the proposed mechanisms for nanoEOR requires that nanoparticles reduce the oil/water IFT and consequently improve the oil recovery [117, 118, 209, 283]. We have already shown that the influence of nanoparticles on the dynamic viscosity and IFT are small in this work (as shown in Figure 3-20). The calculated Capillary Number is of the order of 10^{-7}, which is too small to increase oil recovery by freeing residual oil. Jeong suggested that the capillary number should be of the order of 10^{-5} or higher in order to produce a significant enhancement of oil recovery [284]. Clearly the influence of the capillary effect was not, therefore, responsible for the observed nanoEOR effect.

3.6.3 The structural disjoining pressure effect

As shown by Ref. [207], the SDP could be important for mobilising individual oil droplets. However as suggested earlier, the droplet form of oil was unlikely in the

current experiments. In addition there are two major concerns for such an approach, namely, the concentration effect and the transient effect [211]. The modelling results of SDP show that the increase in wettability with concentration is non-linear and it only becomes important at high particle volume concentrations (i.e., >20%) [207, 219, 222]. However most of nanoEOR experiments reported were based on very dilute nanofluids with typical concentrations of below 1% in weight. The structural disjoining pressure may not be that important although nanoparticles have a tendency to migrate into the microlayer to form ordered solid-like layers. Of note though, with the increase of local concentration, the increased viscous effect could become important and should be considered as well. Another concern is that the modeling was based on the steady state, and only the equilibrium shape of the meniscus under the action of an oscillatory structural disjoining pressure was calculated. Such a model could be only valid during the flooding if the oil displacement time is much longer than that of forming ordered nanoparticle layers.

3.6.4 The surface wettability effect

Nanoparticle deposition and subsequent rock surface wettability modification has been proposed by a few researchers in order to explain the nanoEOR effect. For example, Li et al.[118] found that nanoparticles can change an already water-wet rock surface to a more water-wet surface, while Karimi et al.[121] found that an oil-wet rock surface can be made to be strongly water-wet by ZrO_2 nanoparticles, leading to a considerable amount of oil recovery.

By contrast, Roustaei et al. [117] have argued that changing the rock surface towards oil-wet could change the role of the capillary force from a barrier to a driving force, which would be beneficial for oil recovery. Several authors [127, 213, 283] have proposed that the main mechanism for nanoEOR is wettability change of rock surface

from either water or oil wet to neutral wettability. In our experiments the Berea sandstone were water-wet, but measurements in Figure 3-30 have indicated that saturation of the sandstone with increasing concentrations of nanoparticles can change it to have an even higher wetness to water, contributing to an increase in the recovery factor.

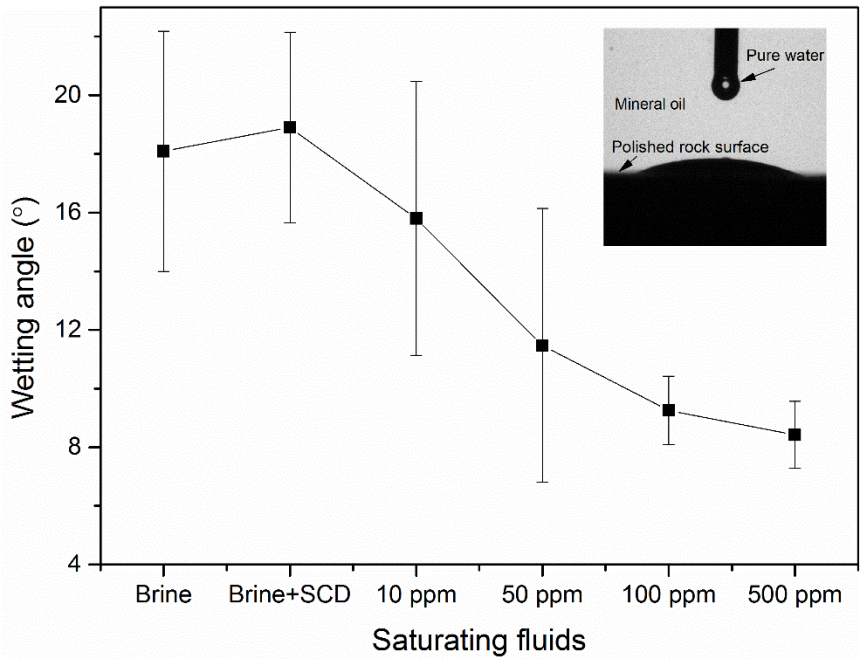

Figure 3-30. Evolution of the wetting angle to pure water of Berea sandstone immersed in mineral oil and pre-saturated with varying concentrations of TiO_2 nanoparticles, with only one drop photograph as an inset.

3.6.5 Possible reasons for observed EOR effect

Having examined the known possible mechanisms that could cause the enhancement of oil recovery concomitant upon core-flooding with nanofluids that is observed in this work, it can be said that mobility control, log-jamming and wettability changes may all have a role to play. However, it is difficult to quantify the exact contribution of each. Additional experiments are currently being carried out in order to clarify the contribution of each mechanism.

3.7 Conclusions

A systematic study of the effect of rutile TiO_2 nanoparticle assisted brine flooding was conducted in this work. Comprehensive characterization of the rock sample and nanomaterials before and after the flooding was carried out. The relative EOR contributions from the stabilizer and the nanoparticles have been identified. The effect of using different concentrations of TiO_2 nanoparticles has also been studied. Finally, the known possible mechanisms of nanoparticle-assisted secondary flooding have been examined. The main conclusions of the research may be summarized in the following points:

- Tri-sodium citrate dihydrate (SCD), was found to have non-negligible influences on the effective properties of brine, which were returned to approximately those of the plain synthetic brine by the addition of nanoparticles.
- Small concentrations provided higher enhancement of oil production at breakthrough, with a 20 ppm concentration providing an enhancement of 39.8% of OOIP compared to a value of 30.3% for water-flooding with plain synthetic brine. Whereas an oil recovery of only 31.8% of OOIP was achieved at breakthrough for 500 ppm.
- The best total cumulative recovery occurred for a 10 ppm nanofluid, with a total oil recovery of 43.75% of OOIP, representing a 44.39% increase on the plain water-flooding scenario.
- Post-breakthrough oil production was better for larger concentrations of nanoparticles. At the end of the flood, the 500 ppm nanofluid mobilized an additional 10.9% of the original oil in place after breakthrough, which was partially attributed to a log-jamming effect.
- The concentration of particles trapped in the core after flooding increased with

the increase of particle concentrations. Some of these nanoparticles could be removed from the core by subsequent flooding with plain synthetic brine, while some crossed into the oil phase, lowering its viscosity marginally.

- Different to the original mono particle size distribution, the effluent showed a bimodal distribution, and varied during the flood, which suggested that particles underwent a complicated morphology change process during the core flooding process.
- The wettability study shows that the water-wet Berea sandstone used in this work became progressively more water-wet by saturation with fluids with increasing concentrations of nanoparticles.
- An analysis of the possible mechanisms for the enhanced oil recovery due to nanoparticles suggested that while the exact causes are unknown at present, the EOR effect in our experiments occurs through a combination of mobility ratio modification, rock wettability modification and log-jamming effect.

Chapter 4

TiO_2 nanoparticles to reduce surfactant adsorption in porous medias

4.1 Introduction

From the literature review in Chapter 2, delivering surfactant by NPs in porous media is a new concept with just small number publications to date. To further justify this concept, this work aims to answer two basic questions: i) whether NPs can act as a carrier for surfactant delivery in all common porous media, and ii) what is the relationship between nanoparticle migration and surfactant retention in porous media. In this Chapter, a blend of commercial anionic alkylaryl sulfonates and nonionic alcohol ethoxylated surfactants was used to form microemulsions and the optimum salinity for emulsion fabrication determined. A comprehensive collection of reservoir rocks including calcite, dolomite, sandstone, black and red limestones, were used and characterized. The effect of TiO_2 nanoparticles on the delivery of surfactant blend, including the adsorption and transport in saturated porous media with different rock grain matrix was then investigated, as well as the adsorption mechanisms.

4.2 Materials

4.2.1 Rock and surfactant samples

Analytical grade materials including n-hexane, sodium chloride, propyl alcohol and

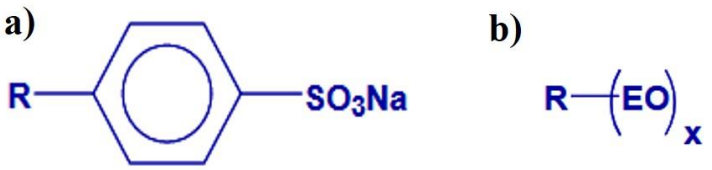

Figure 4-1. Molecular structure for (a) Alkylaryl Sulfonates XOF-25S , and (b) The co-surfactant Alcohol Ethoxylated. Taken from Ref. [145]

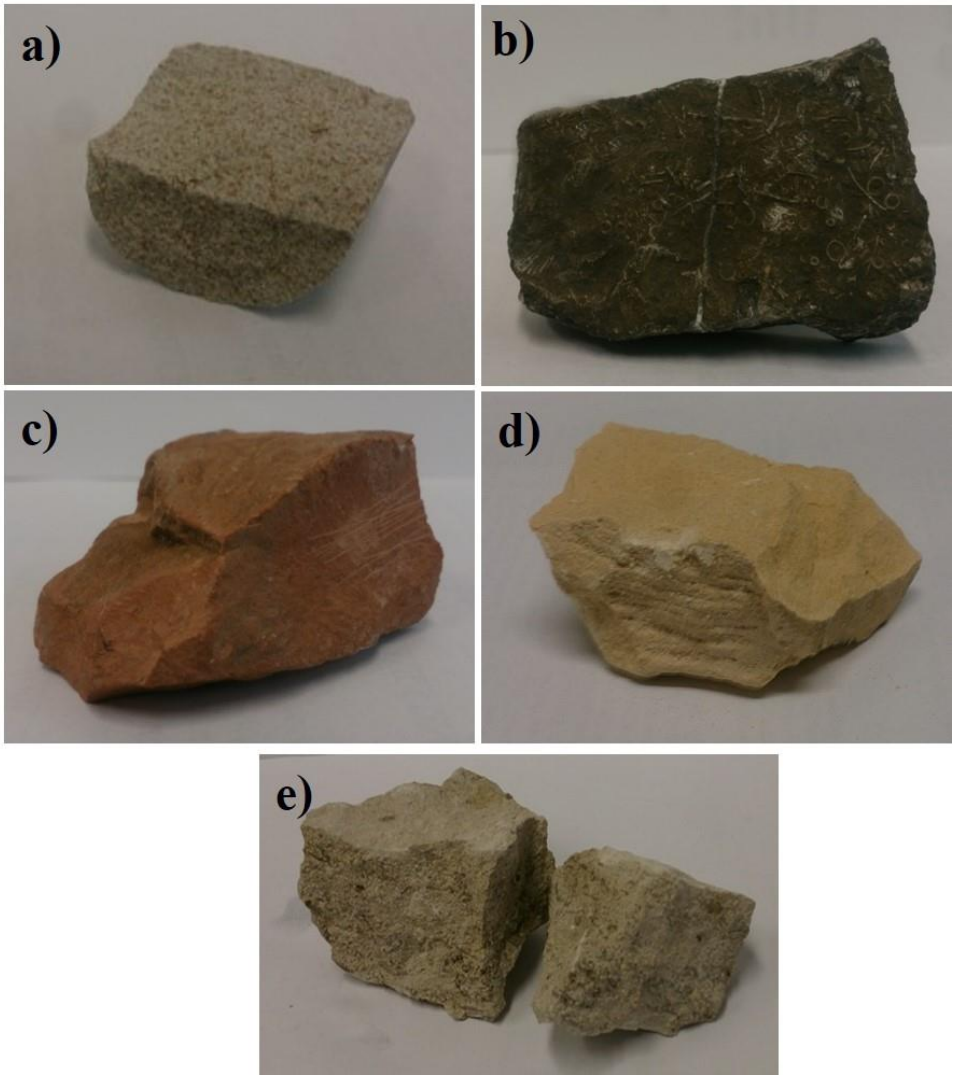

Figure 4-2. A collection of rocks: (a) silica, (b) black limestone, (c) red limestone, (d) dolomite and (e) calcite.

Titanium (IV) oxide NPs (P25, 21 nm primary particle size (TEM), ⩾99.5% trace metals basis, Sigma-Aldrich) were purchased from Sigma-Aldrich. The anionic alkylaryl sulfonates (XOF-25S, Sulfonic acid of Alkylate H250 (C14 – C30)) was

provided by Huntsman Corportion and its molecular structure is shown in Figure 4-1a. The nonionic alcohol ethoxylated (EA, C12-13/7EO) was purchased from Mistral chemical company, and its molecular structure is shown in Figure 4-1b.

Five different reservoir rocks (Figure 4-2) were crushed and sieved (ASTM Standard Testing Sieves, Retsch Ltd) to obtain small grains with relative homogeneous size distribution between 250 μm and 425 μm. Then 10 g of grain samples were packed into glass tubes (I.D. = 2.44 cm, packing length=2.1 cm) to generate unconsolidated packing columns for core flooding tests. To prevent particles from being flushed out from the packing column, a PTFE filter membrane from Millipore (pore size of 10 μm) was placed at both ends of the column.

4.2.2 TiO_2 NPs coated with surfactant

TiO_2 NPs were selected in this study as carrier to facilitate surfactant delivery in porous media, because it had been used as assistant agent for water flooding in Chapter 3, and also been widely investigated for enhance oil recovery application by other researchers [127, 285, 286]. TiO_2 suspensions were prepared by dispersing 0.002 g/mL of TiO_2 into aqueous solution containing 0.003 g/mL surfactant blend at optimum salinity (4 wt%) and optimum composition (25% XOF-25S plus 75% EA), as determined in Section 4.4. The NP suspensions were mixed using a sonic dismembrator (Model 705, Fisher scientific Ltd.) running at an amplitude of 25% for 15 minutes prior to each dynamic adsorption test. The zeta potential of TiO_2 NPs was measured as -10.1 mV by Malvern Nanosizer, based on the dynamic light scattering (DLS) method. Figure 4-3b shows the hydrodynamic size distribution of TiO_2 NPs in surfactant solution, with an average size of 147 nm.

4.2.3 FTIR analysis

The particle coated with surfactant was separated from the 20 mL bulk suspension by being centrifuged at 10,000 rpm for 30 min (Thermo Scientific megafuge 16R). The settled particles were collected and washed with 5 mL de-ionized water and dried in oven at 40 ºC for 48 hours. FTIR was employed for analysing TiO_2 NPs before and after coated with surfactants. Figure 4-4 shows the FTIR spectra of pure surfactants, pure TiO_2 NP and dried TiO_2 NP collected as sedimentation from centrifuge.

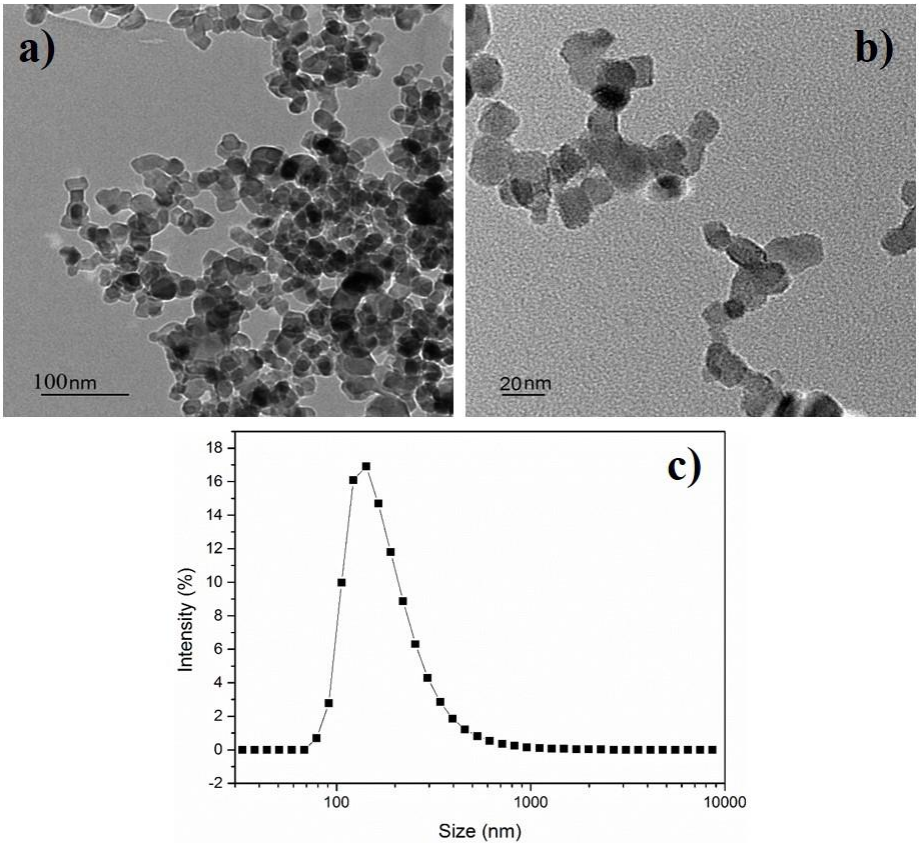

Figure 4-3. (a) TEM images of TiO_2 NPs; (b) Hydrodynamic size distribution of TiO_2 NPs in surfactant solution.

The absorption band at 1180 cm^{-1} for XOF 25S and functionalized NPs corresponds to the stretching vibrations of SO_3 group. The broad intense absorption in the range of 600-900 cm^{-1} for pure TiO_2 is associated with the vibrations of the bonds Ti-O and Ti-O-Ti [287]. The vibrations observed in the 855, 946 and 1096 cm^{-1} for EA are attributed to the stretches of C-O-C bond in ethoxylated group of EA [288, 289]. A strong

absorption peak is also found at 3400 cm^{-1} for EA, attributing to the O–H bending vibration. For pure TiO_2 NP and functionalized TiO_2 NP in aqueous phase, the absorption peak at 1600 cm^{-1} is attributed to the H-O-H stretching vibrations of water. The intensity of the peak at 3400 cm^{-1} significantly decreases for functionalized TiO_2 NPs compared to the pure one, which strongly evidences the decline of the surface hydroxyl number after the modification of NPs with surfactant.

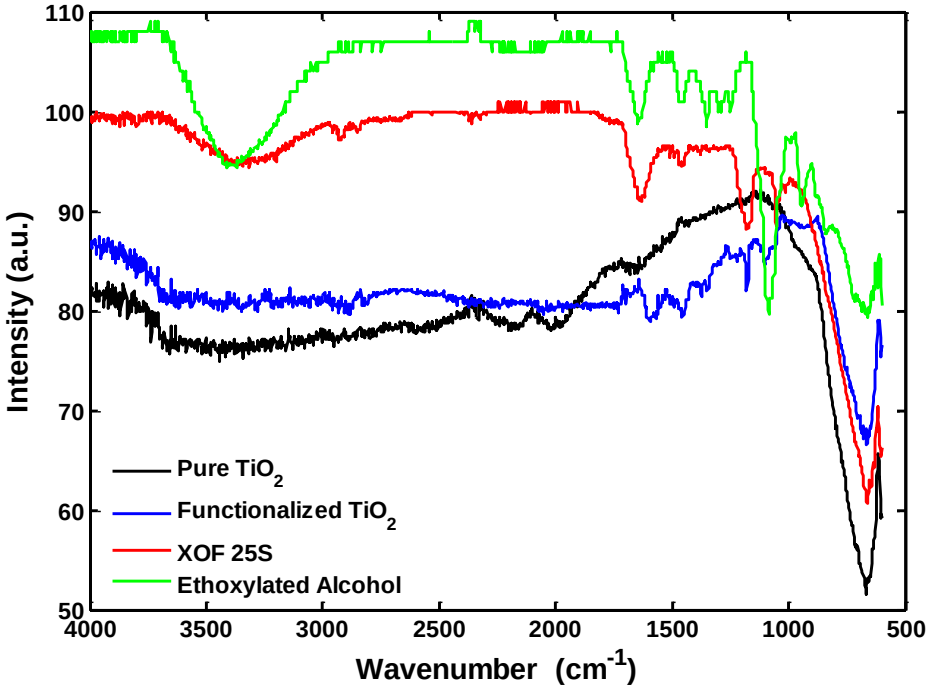

Figure 4-4. FTIR spectra of pure surfactants, pure TiO_2 and sediment TiO_2 NP.

4.3 Core sample preparation and characterization

The bulk rock samples were crushed into small grains and sieved into the size ranging from 425 μm to 600 μm. The grain morphology and mineralogy were analysed by SEM and EDS, as described in Sections 3.2.5 and 3.3.6. The wettability was determined by optical contact angle meter on the polished rock chunk surface. BET method was employed to determine the specific surface area of the rock powder by using

Micromeritics TriStar 3000 system. Their surface roughness was characterized by NPFLEX 3D from Bruker company.

4.3.1 Morphology and element analysis

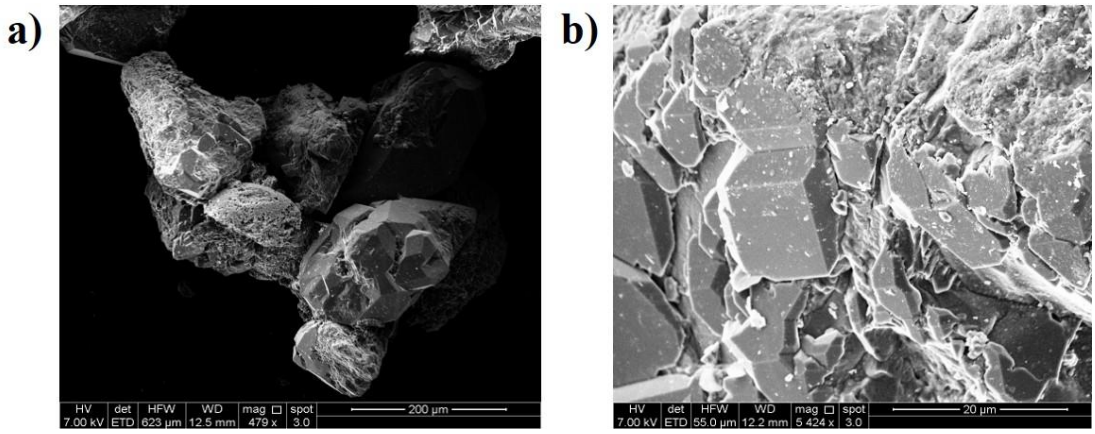

Figure 4-5. SEM photos of crushed sandstone grain: (a) in low resolution; (b) in high resolution.

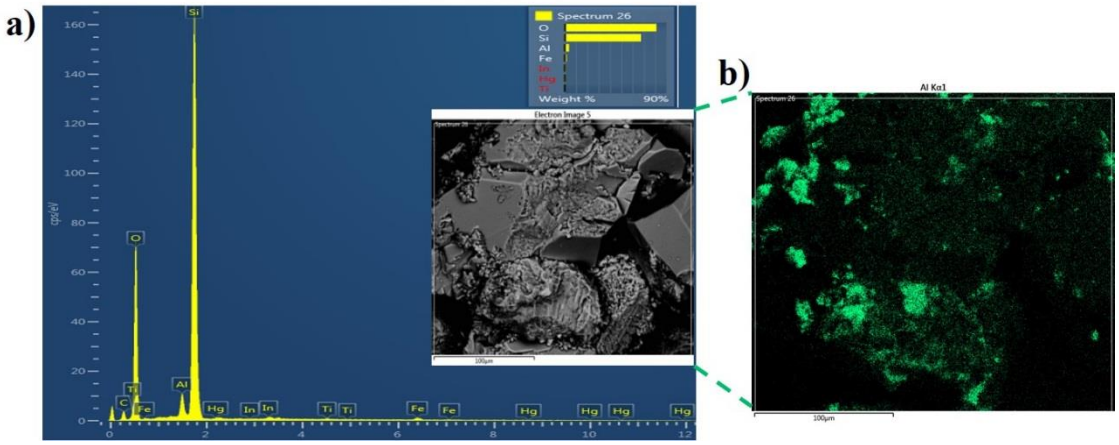

Figure 4-6. (a) Elemental mapping of sandstone using an energy dispersive X-ray spectroscopic, inset is the mapping area; (b) distribution of aluminium components in analysed region.

The surface morphologies of different rock samples were examined by SEM, as shown in Figure 4-5. Big particles with rough surfaces can be found in the SEM images. EDX analysis was done for specific points or interested areas on sample surfaces to detect the elements and mineralogy (Figure 4-6), which demonstrates that Si and O

composed as major elements. In addition, the corresponding EDX micrographs proved the existence of silicate crystals as majority fraction and aluminosilicate mineral as a minor fraction.

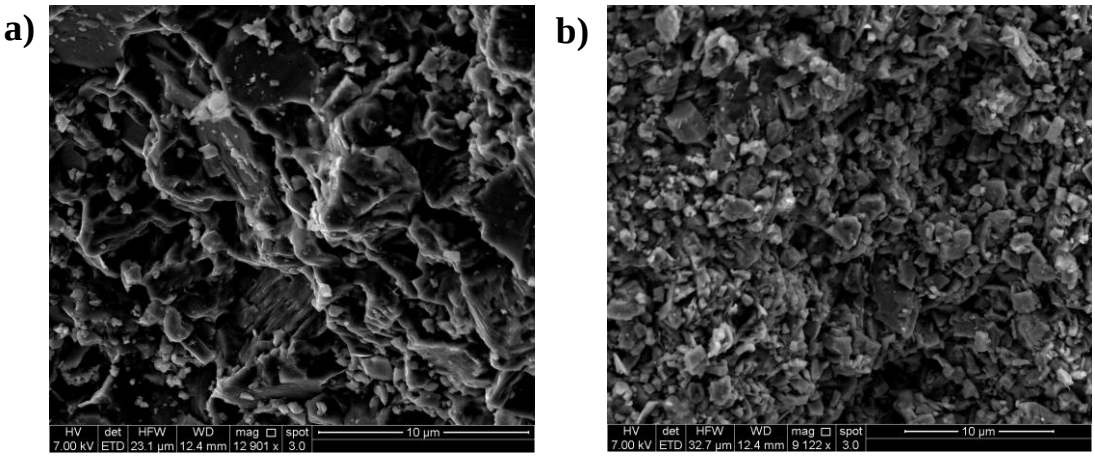

Figure 4-7. SEM photos of (a) black and (b) red limestone.

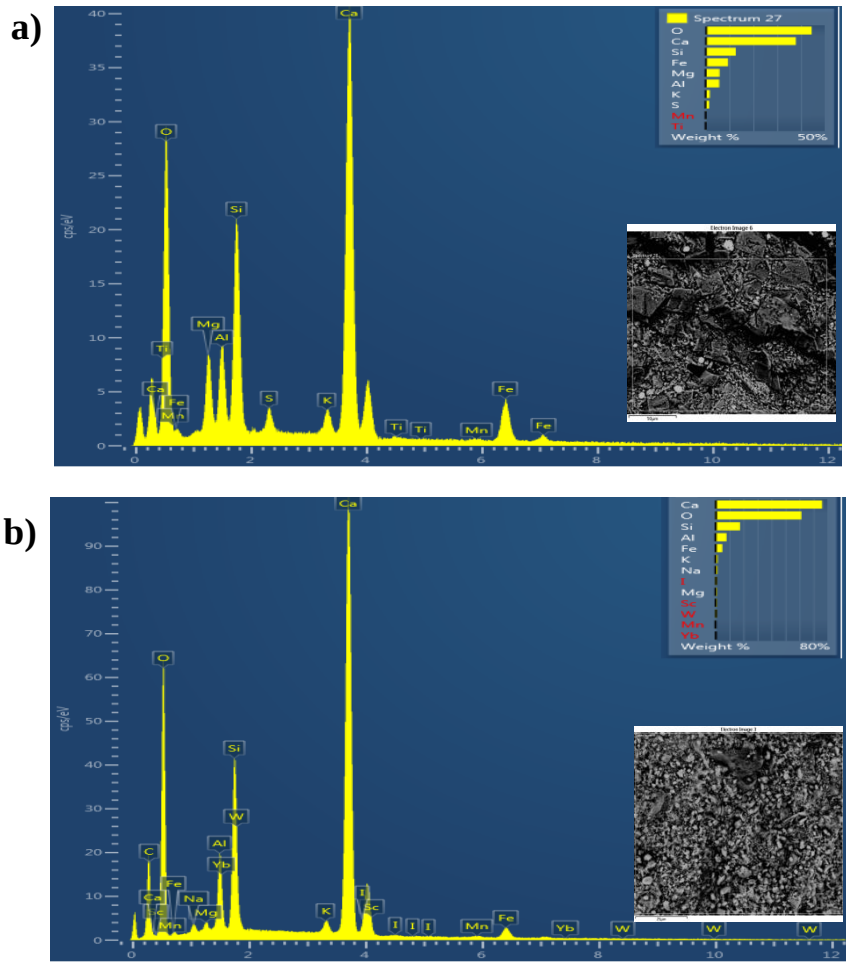

Figure 4-8. Elemental mapping of (a) black and (b) red limestone using an energy dispersive X-ray spectroscopic. The insets are mapping areas.

Limestone is a sedimentary rock, which is composed of a large amount of calcium carbonate mineral with some variable amounts of silica. SEM photos in Figure 4-7 show that the grains of limestone are irregularly shaped and well-crystallized grains are very rare. EDX mapping (Figure 4-8) indicates the existence of manganese and iron in both types of limestone. The black limestone contains higher amount of magnesium oxide mineral, which is the main reason for the black colour. Goethite or hematite are probable the mineralogy of iron in the red limestone as previously investigated by Cai et al. [37]; however the existence of hematite is the reason of red colour in limestone rock. The elemental mapping also verifies the existence of clay minerals (alumina and silica composition) in the limestone rocks.

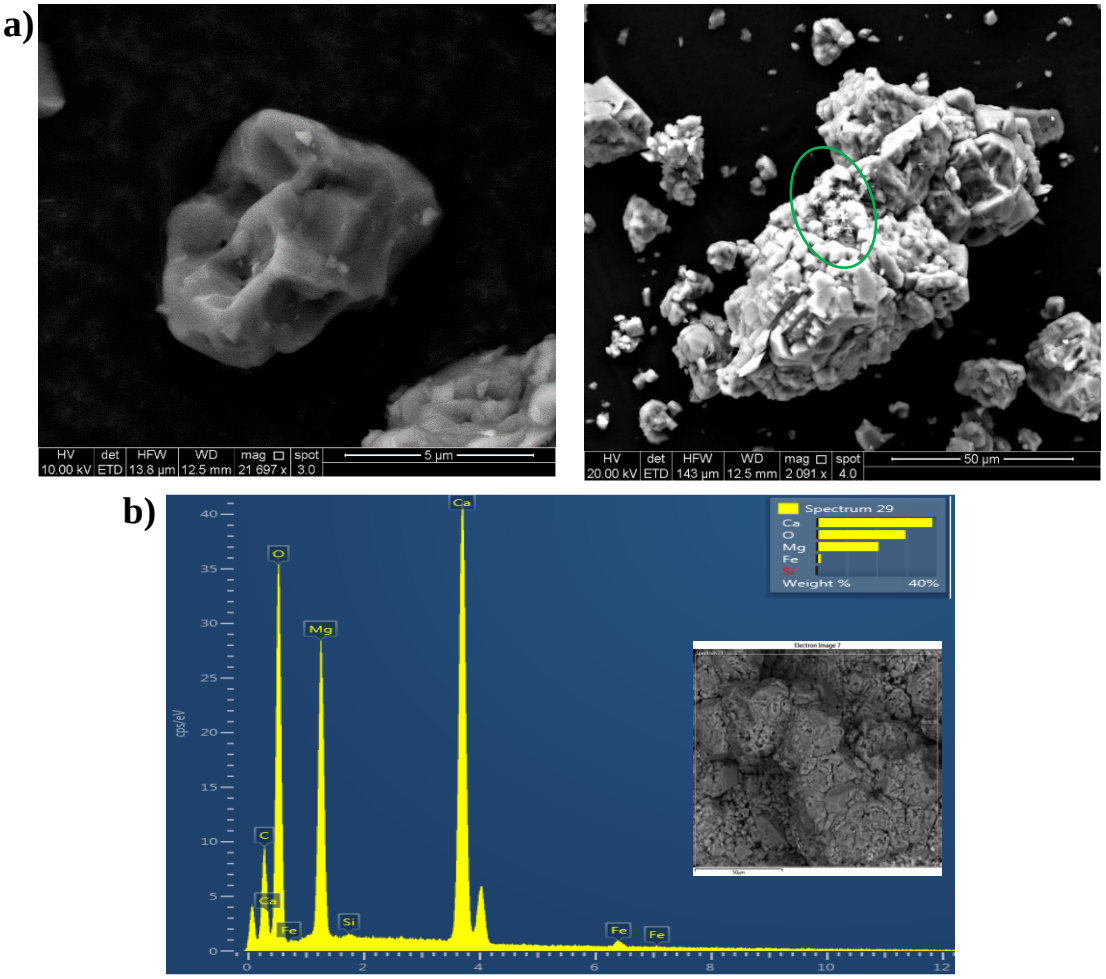

Figure 4-9. (a) SEM photos and (b) Elemental analysis of dolomite using energy dispersive X-ray spectroscopic.

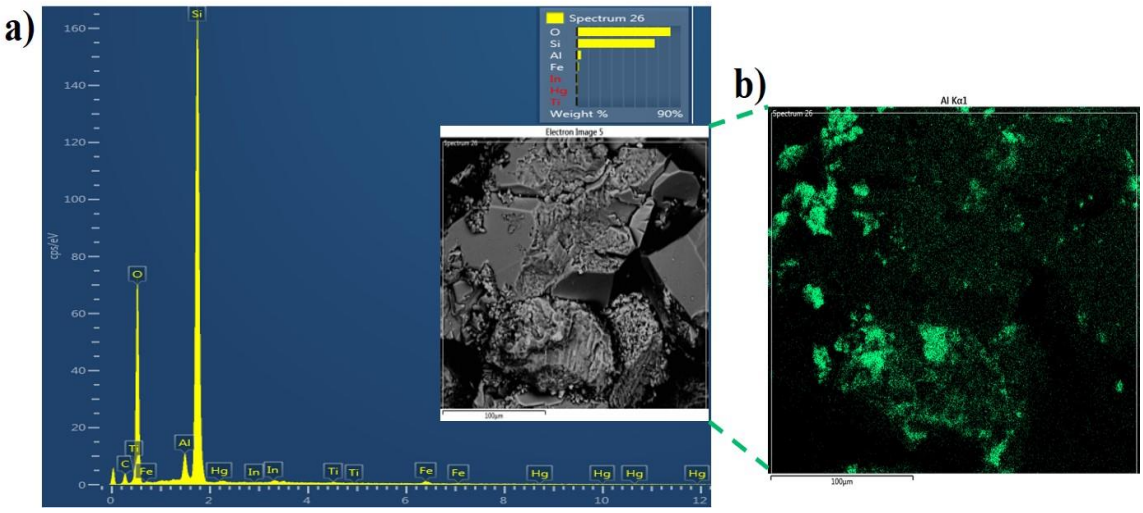

Figure 4-10. (a) SEM photos and (b) Elemental mapping of calcite using energy dispersive X-ray spectroscopic.

According to high-resolution SEM image (18245×) of dolomite (Figure 4-9), the tiny star-like crystals are found on the surface of dolomite. The EDX analysis shows that the composition of star-like crystals is the same with the substrates that appear in different crystal structures. The SEM images of calcite rock show the existence of OOlits structure inside the carbonate rock. Moreover the vein of silica mineral is detected in calcite rock as shown in Figure 4-10.

4.3.2 Roughness analysis non-contact 3D observations and measurements

The roughness of rock samples were observed and analysed contactless by 3D NPFlex, with value listed in Table 4-1. Before measurement, the crushed rock powders which were used as the packing material in NPs-surfactant flooding experiments, were stuck on same plates to form a homogeneous layer. The measurement was done on the surface of rock powder/area randomly selected from the plate. The measure area in both X and Y dimension ranges from 0 to a few millimetres.

Table 4-1. Analytical results of roughness for different rock samples

Parameters	Black limestone	Dolomite	Red limestone	Sandstone	Calcite
S_a (μm)	0.438	0.745	1.216	0.716	0.403
S_q (μm)	2.256	2.869	3.845	2.566	2.086
S_p (μm)	88.204	116.133	119.615	100.097	103.87
S_v (μm)	-63.306	-66.816	-74.942	-80.03	-78.485
S_z (μm)	151.511	182.949	194.557	180.127	182.355

Note: $S_{a,}$ is the arithmetic mean height, indicating the average absolute roughness value z(x,y) in measured area; $S_{q,}$ is root mean squared height, which expresses the root mean squared of rough value z(x,y); S_p, is the maximum peak height. Surface peak is an area above the average level of the surface; $S_{v,}$ is maximum valley height. Surface valley is an area below the average level of the surface; $S_{z,}$ is maximum height.

4.3.3 Specific surface area and surface charge of rock

The average specific surface area of different rocks (250-425 μm) was measured using BET nitrogen adsorption analysis for three repeats. The surface charge of different rocks was obtained using electrophoresis measurements of crushed rock [38]. Rock particles below 45 μm were collected and suspended in de-ionized water. The large particles were sedimented after 1 hour and the remaining suspension was centrifuged at speed of 5000 for 30 minutes. The size of particles in suspension was estimated between 3-4 μm based on the stokes law. The electrophoretic mobility of particles was then measured by using a Malvern Zetasizer at pH ~7, and data is presented in Table 4-2. It is validated that zeta potential measured by this method is quite close to the results from Alotaibi et al. [290], Our results show that all rocks have negative surface charges with magnitude in the sequence: Dolomite (least negative) <calcite<black limestone<red limestone < silica (most negative).

Table 4-2. Main parameters for different rocks.

Rock type	Silica	Black limestone	Red limestone	Dolomite	Calcite
Specific surface area (m^2/g)	0.877 ± 0.001	0.884± 0.003	3.090 ± 0.004	2.540 ± 0.021	1.460± 0.001
Electrophoretic mobility ($\mu m cm V^{-1}s^{-1}$)	-1.58 ± 0.09	-1.07 ± 0.07	-1.14 ± 0.04	-0.83 ± 0.05	-1.00 ± 0.07
Zeta potential (mV)	-20.6	-14.2	-15.2	-11.1	-12.1
Contact angle	20.09±2.5	68.23±0.25	37.88±0.58	29.83±1.5	33.66±2.5

4.3.4 Wettability analysis of rock

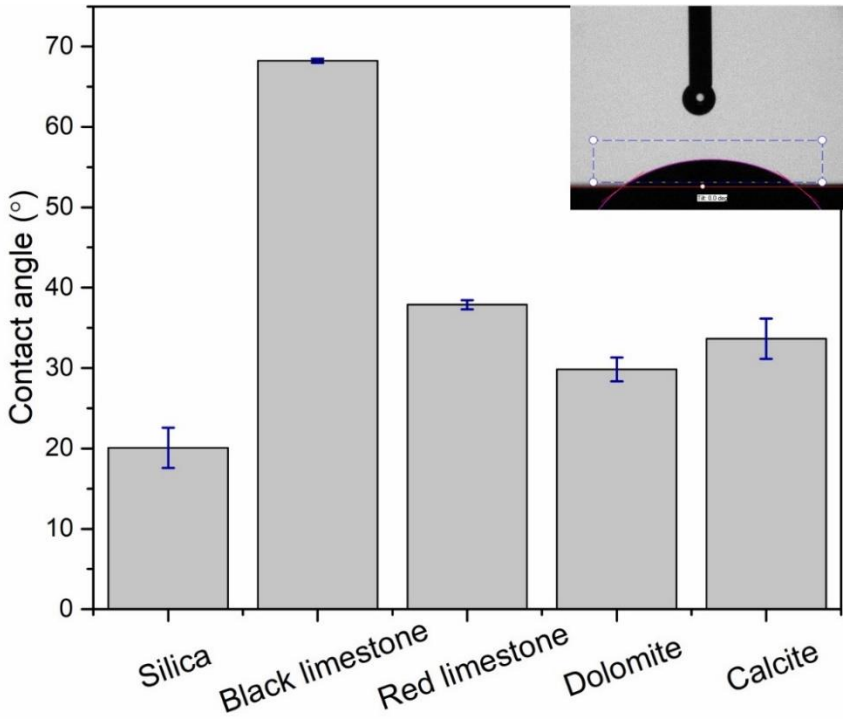

Figure 4-11. Contact angle of brine droplet (4 wt% NaCl) at 22 °C on polished rock surface. The inset is example of droplet photo taken by the optical contact angle meter.

Side images of water drops on polished rock pieces were taken by a high speed camera mounted on the KSV tensiometer. The images of brine drop (at the optimum salinity) sitting on polished substrate were recorded in both fast mode (0.1s interval) for 120 pictures and normal mode (1 s interval) for 240 pictures. The images at steady state

when the contact angle was almost unchanged are shown in Figure 4-11, and the corresponding contact angle values are presented in Table 4-2. According to the results, the black limestone and silica has the lowest and highest degree of water wettability between rocks, respectively.

4.4 Surfactant preparation and characterization

4.4.1 Stability of surfactant solution

Critical micelle concentration (CMC) of XOF-25S was determined by interfacial tension measurement and conductivity method as indicated in Figure 4-12. The conductivity of anionic surfactant solution increases linearly with increasing surfactant concentration until it reaches 2.4×10^{-3} g/mL, beyond which the increased rate of conductivity is slightly reduced. This point on the graph where conductivity changes its slope is identified as the CMC. The CMC for alcohol ethoxylates is equal to 15×10^{-6} g/mL according to the report released by Human & Environmental Risk Assessment (HERA) [[269]].

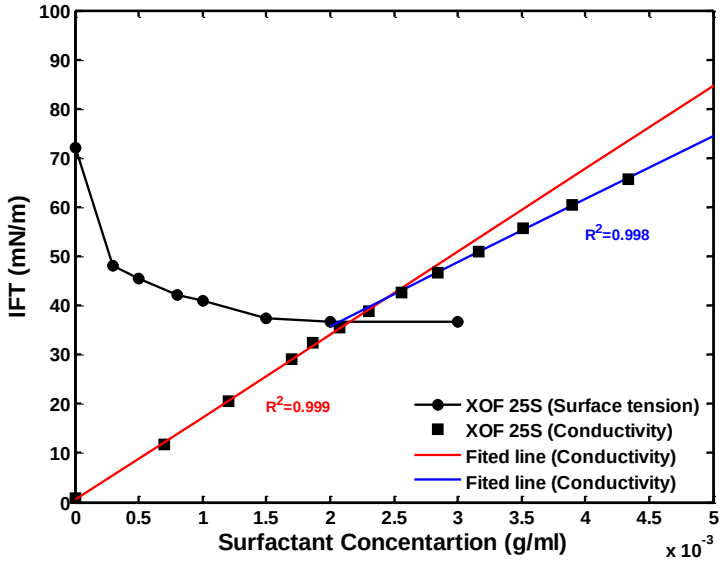

Figure 4-12. Critical micelle concentration (CMC) of XOF-25s.

Generally in ASP/SP flooding the surfactant concentration is in the range of 0.2-1.0 wt%. In this study, a surfactant concentration of 0.3 wt% (combined by 0.15 wt% XOF-

25S and 0.15 wt% EA) was selected as candidate for measuring surfactant adsorption in porous media. As long-term stability are important factors in design of an injectable surfactant slug, it will be necessary to find a suitable composition for formulating single-phase aqueous surfactant solutions at different salinities. Figure 4-13a shows the XOF-25S surfactant solution samples (15 mL, 0.3 wt%) at different salinities. According to Figure 4-13a, the XOF-25S solution presents cloudy state or even not soluble at a salinity higher than 2 wt%. Then, EA surfactant (0.15 wt%) was added as additive to obtain single-phase solutions for XOF-25S surfactant (0.15 wt%) at higher salinities. The non-ionic EA co-surfactant is capable of increasing resistance to high salinity due to the ethylene oxide groups in the structure of EA, which transfers the unsolvable surfactants to be solvable, as shown by the produced clear aqueous solution in Figure 4-13b.

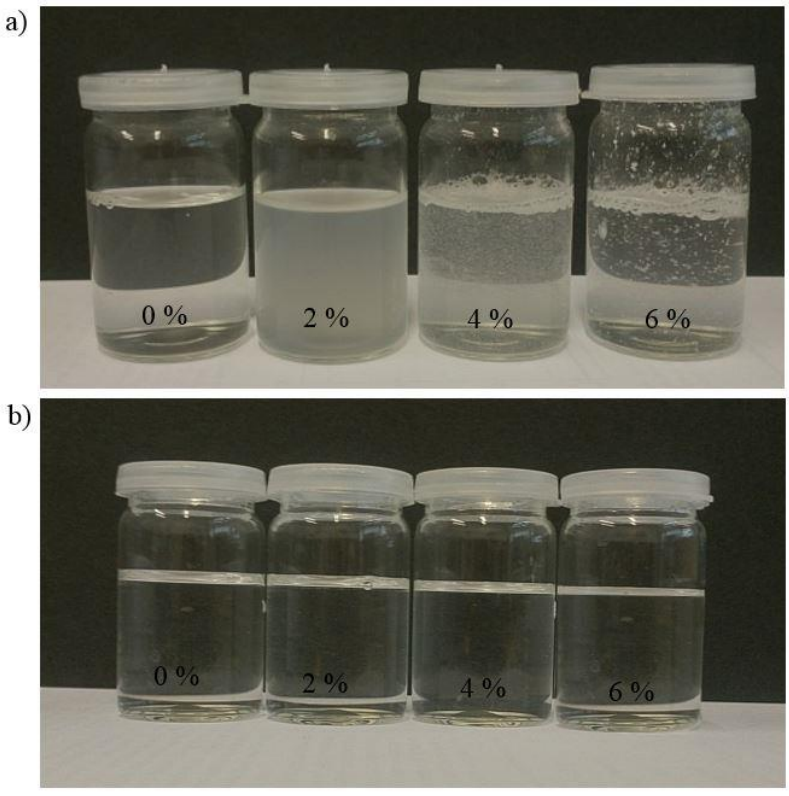

Figure 4-13. (a) XOF-25S surfactant solution at different salinities, (b) blend of XOF-25S and EA surfactant solution with equal weight percentage at different salinities.

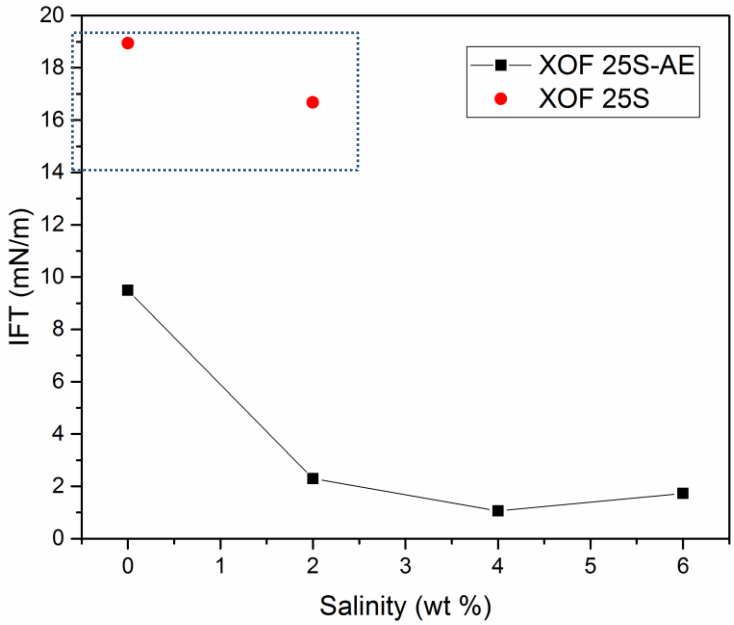

Figure 4-14. Interfacial tension between mineral oil and XOF-25S solution (0 and 2 wt% salinity, because the surfactant was not soluble at salinity higher than 2 wt%, the IFT data for pure XOF-25S solution was not available), and blend of XOF-25S-EA solution with equal weight percentage.

Figure 4-14 illustrates the interfacial tension between mineral oil and XOF-25S solution (0 and 2 wt% salinity), and blend of XOF-25S and EA surfactant with equal weight fraction (0.15 wt%). According to the results, the interfacial tensions of XOF-25S-EA blender are lower than those for XOF-25S microemulsion, due to the synergic effect of these two surfactants on decreasing IFT [291].

4.4.2 Optimum Salinity and blend ratio

Optimum salinity of surfactants solution for their ability to give lowest interfacial tensions in oil-brine systems is important for flooding processes. Optimum salinity is usually obtained by visualizing winsor type III microemulsions in oil-brine. In order to find out how the solution salinity change affects the surfactant functionality, the static glass-pipette tests were performed. N-octane was selected as the oil phase because optimal salinities of surfactants solution against n-octane is nearest to those of the same

surfactants against many crude oils [292]. 1 wt% propyl alcohol as co-solvent was added to samples for better visualization of phase behaviour however this value can be adjusted to commercial compositions. Moreover, it should be noticed that finding clear solutions near optimal conditions in surfactant solution is more applicable when the formulations contain considerable alcohol or other co-solvent.

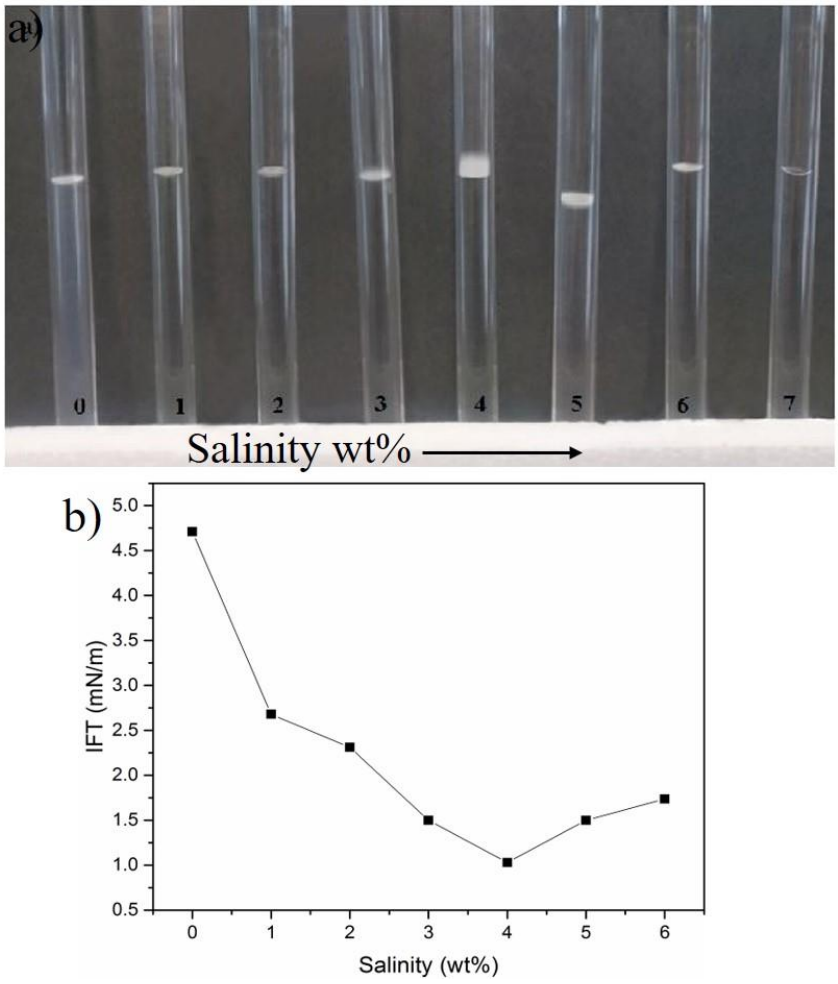

Figure 4-15. (a) Equilibrium phase behaviour of surfactant hybrids of XOF-25S and EA (mass ratio 1:1) solutions with equal volumes of n-octane at 70 °C and various salinity from 0 to 7 wt% NaCl; (b) IFT between mineral oil and surfactant blending solutions at different salinity.

In order to determine optimum salinity, glass sample tubes (pipettes) were filled by 1 mL surfactant solution containing 0.003 g/l of XOF-25S and EA (mass ratio 1:1) at different salinity and 1 mL n-octane. Pipettes were sealed first at the bottom and after

being filled with sample, they were also sealed from the top, followed by 14 days aging in oven at 60 ºC. Each sample was monitored during this period to assess their state after reaching equilibrium condition. Figure 4-15a is a photograph of a salinity scan for surfactant solutions with equal volumes of n-octane at 60 °C. A large middle phase microemulsion indicates an optimal formulation using surfactants. The optimal salinity range in this case is approximately 4 wt%. In the next set of the experiments, the IFT measurements were performed between mineral oil and surfactant solutions at different salinities that has been shown in Figure 4-15b.

Figure 4-16 shows the phase behaviour of solutions at 4 wt% salinity for a surfactant solution blended at different ratios. In this case, the scan includes Winsor I for EA with bluish oil in water microemulsion and Winsor III for blend of XOF-25S and EA while there is not any microemulsion formation in absence of EA. Microemulsions with higher solubilisation parameter were oberserved for sample containing 25% XOF-25S which was an composition for the surfactant blend in the next experiments.

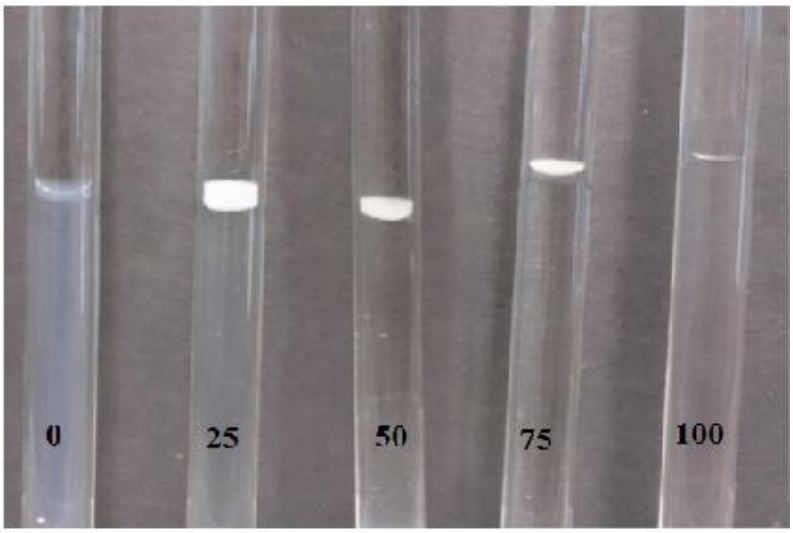

Figure 4-16. Phase behavior of surfactant solutions at 4 wt% salinity for different blend ratio of XOF-25S and EA (wt%).

4.4.3 Determine of surfactant concentration

The number of carbon atom in both surfactant structures is similar. Therefore, Chemical Oxygen Demand (COD) method was used for measuring the surfactant concentration by determining the quantity of oxygen that required to oxidize carbon in surfactant matter in a collecting solution. The reagent concentrations were adjusted so that the method can be applied for samples having a surfactant concentration lower than 0.004 g/mL.

2 mL of sample, 7 mL sulphuric acid (H_2SO_4) and 2.5 mL of potassium dichromate ($K_2Cr_2O_7$) solution (0.250 N) were mixed for 1 hour at 110 ºC in a reflux flask and employed to eliminate loss of sample by volatilization. The flask was then cooled to room temperature, followed by adding 15 mL of distilled water to dilute the solution. Three drops of ferroin indicator was added to the solution and the excess dichromate was titrated with standard ferrous ammonium sulfate ($FeH_8N_2O_8S_2$, $Fe(NH_4)_2(SO_4)_2$ 0.06 N) to the end point [144]. At the end point the colour of solution changed sharply from blue-green to reddish hue.

$$2\ K_2Cr_2O_7 + 8H_2SO_4 \rightarrow 2\ K_2SO_4 + 2\ Cr_2(SO_4)_3 + 8\ H_2O + 3O_2$$

COD of sample, was calculated as follow:

$$\text{COD as mg } O_2\text{/L} = \frac{(A-B)\times N \times 8000}{Vol}$$

where, *A* is volume of ferrous ammonium sulfate (mL) used for titration of the blank solution (without carbon element), *B* is volume of ferrous ammonium sulfate (mL) consumed for sample titration of the sample, *N* is normality of ferrous ammonium sulfate and *Vol* is volume of sample (mL) used for the test.

4.5 Dynamic adsorption experiments

Surfactant mixtures without nanoparticles are injected into the column packed with different rock grains in the cold flooding stage, as shown and described in Section 5.3. All of the effluent samples were collected to measure the surfactant concentration using the COD method.

The dynamic adsorption experiments to exam the NPs/surfactant mixtures in porous matrix packed with a collection of crushed rocks grains as described above were carried out in the cold flooding stage. The parameters for the packing column are described in Table 4-3. Experimental procedures for dynamic nanoparticle breakthrough ability were performed as follows:

- at least 10 PV brine (4 wt% NaCl) was injected through the column packed with crushed rock grains at a flow rate of 2 mL/min in order to make sure that the column was fully saturated and allowed enough time for rock powder depositing.
- 20 mL of surfactant/TiO_2 mixtures was injected into column packed with different porous media at a flow rate of 1 mL/min.
- 20 mL of brine was injected at a flow rate of 1 mL/min as post-flooding

Table 4-3. Parameters for the porous media

Porous media property	Value
Lentgh (cm)	2.6±0.2
Diameter (cm)	2.44
Bulk volume (mL)	12.16±0.94
Pore volume (mL)	4.3±0.3
Porosity (%)	35.4±5.9
Absolute permeability (mD)	22.3±5.2

The effluent liquid flowed through a flow cell placed in UV-Vis spectrophotometer, and was collected at the outlet. The nanoparticle effluent concentration (C) was measured on-line by spectrophotometer operating in 'Kinetic' mode at a wavelength of 450 nm. The breakthrough curves (C/C_0) of nanoparticles were generated by using the NPs' effluent concentration (C) divided by influent concentration (C_0).

Before experiment, calibration curves of adsorption versus NPs concentrations were generated with a known TiO_2 concentration in dispersions (Figure 4-17). The NPs recovery was calculated as a percentage of the effluent collected NPs from both NPs injection and post-brine flooding relative to the total amount of injected nanoparticle. The retention of NPs on solid surface (mg/g rock and mg/m^2 rock) for the coreflooding was then calculated by total injected NPs concentration minus recovered the NPs. Mass balance calculation was performed to evaluate both particles eluted from the column during coreflood and those retained in the column. The calculation showed that the total mass of nanoparticles that emerged from the column together with the retained mass is higher than 95% of the initial mass. Breakthrough curves (BTCs) of TiO_2 nanoparticles that show relative adsorption as a function of PV, are provided in Figure 4-18.

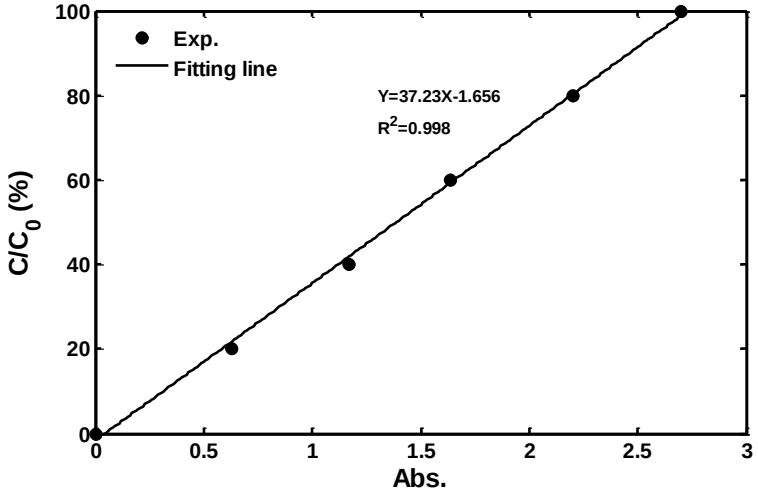

Figure 4-17. Calibration curve for the C/C0 (%) against absorption of TiO2 at 2000 ppm. The wavelength was fixed at 450 nm.

4.6 Results and Discussion

4.6.1 Nanoparticle breakthrough curve

It can be seen from the breakthrough curve in Figure 4-18 that TiO_2 NPs has good migration ability (>85%) in all of the rock types examined. As reviewed in Section 3.5.5, there are several mechanism controlling the particle transport in porous media: sedimentation, interception, straining and diffusion. As the NP size is small, the sedimentation is unlikely to happen due to short residence time of particles in the core and the effect of Brownian motion. Moreover, since the surface charge of all the rock samples was measured as negatively charged, diffusion is also unlikely to play an important role in trapping the particles. Interception is a function of the tortuosity of the porous media and surface roughness of the crushed rock powder [293]. Straining is possible to happen because of the ultra-low narrow pore throat introduced by anomalous shape of rock grain after crushing, and random packing. In those sensitive areas, the relative size of nanoparticle (d_n) and rock grains (d_c) would above the critical ratio of 0.0017.

Therefore, the high breakthrough ability in all rock matrix would be attributed to negligible electrostatic adsorption and occasionally straining. The EDS mapping results for the sample extracted from the column after post injection process, show that small amount of NPs are detected on the surface of rock, verifying the negligible electrostatic adsorption and weak interaction by adsorption/diffusion.

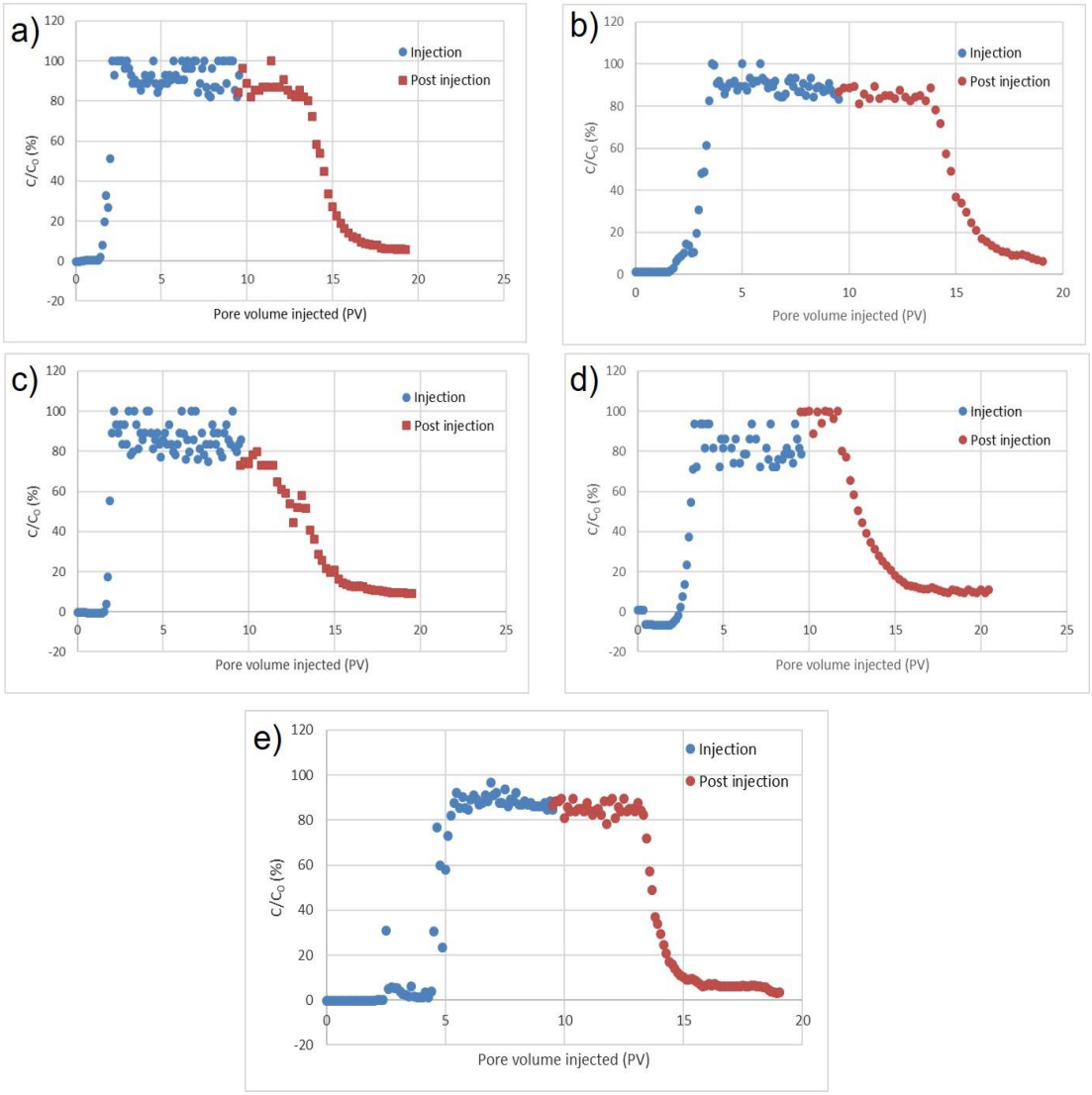

Figure 4-18. TiO_2 nanoparticles breakthrough curves transported through different rocks: (a) silica, (b) black limestone, (c) red limestone, (d) dolomite, (e) Calcite.

4.6.2 Surfactant attachment

Figure 4-19 and Table 4-4 represented weight percentage of nanoparticles which trapped in porous media and those discharged during the flooding and post flooding.

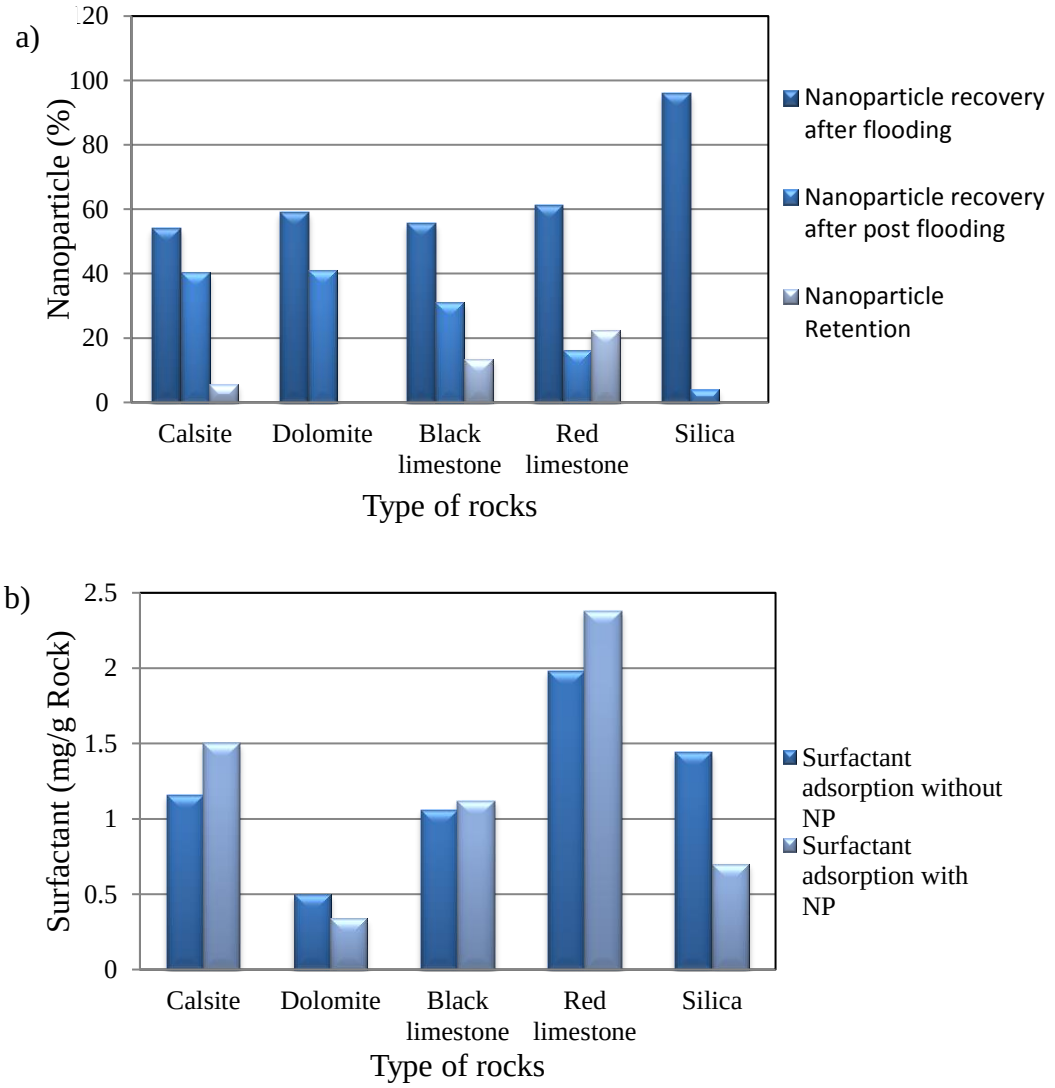

Figure 4-19. (a) weight percentage of trapped NPs in different porous media, and (b) adsorbed surfactant blend with and without NPs at surface of different porous media.

Figure 4-19a indicate that all NPs are discharged from silica and dolomite porous media while limestone rock has a high value of retention rate. Comparing to previous studies, there is some inconsistence on the effect of specific surface area and surface charge of rock on NP retention. Caldelas et al. [30] stated that specific surface area of rock had a linear effect on NP retention, independent of rock lithology. However in this study, the surface area of dolomite rock is relatively high compared to others (Table 4-2) while NPs were completely recovered. In recent research [158, 159, 196, 200, 204, 294], specific surface area is not considered as an important factor for particle retention.

Table 4-4. retention of TiO_2 NPs and adsorption of surfactant in different porous media

Rock type	Calcite	Dolomite	Black limestone	Red limestone	Silica
Surfactant adsorption without nanoparticles (mg/g rock)	1.16	0.5	1.06	1.98	1.44
Surfactant adsorption with nanoparticles (mg/g rock)	1.5	0.34	1.12	2.38	0.71
Surfactant adsorption without nanoparticles (mg/m^2 rock)	0.529	0.131	0.37	0.427	1.094
Nanoparticle retension (wt %)	5.5	0	13.5	22.4	0
Nanoparticle retension (mg/m^2 rock)	0.075	0	0.186	0.145	0

Dunphy Guzman et al. [295] also stated that surface charge of rock was a primary factor on the retention of TiO_2 NPs in porous media. According to Table 4-2, all of those surfaces are negatively charged, even the lowest charge of dolomite has a zeta potential of -10 mV. Therefore, it can deduced that more retention should be expected in dolomite rock compared to other rocks because of the lower electrostatic repulsion between the particle and the grain surface. However the breakthrough curve in Figure 4-18 and retention statistics in Table 4-4 show that electrostatic adsorption is unlikely to play an important role in trapping the particles.

According to our results, it appears that another important factor which have a great effect on retention of particle is the surface roughness. Table 4-1 clearly shows that the surface roughness of a limestone grain is greater compared with dolomite and silica, which cause more retention of NPs. Such an explanation is consistent with other researchers who revealed that irregular dents and bumps of rock surfaces led to more trapped NPs [153, 296].

Surfactant adsorption with and without NPs are shown in Figure 4-19b and Table 2. The highest adsorption of surfactant per unit mass of rock (mg surfactant/g rock) is red lime stone. However based on per unit surface of rock (mg surfactant/m^2 rock), silica

has the highest adsorption rate. All evidence confirms that blend of alkylaryl sulfonates and alcohol ethoxylated incline to adsorb on surfaces containing Si and Al. Si and Al elements (source of silica and clay mineral) are found in all rock samples except the dolomite, which have the least surfactant adsorption. The main proposed mechanism of adsorption surfactant suggests hydrogen bonding between the oxygen in the ethoxy groups of surfactant and the hydroxyl groups of silica on the mineral surface. Figure 4-20 schematically shows the mechanism of ethoxylated surfactant adsorption on surface containing silica. According to the analysis, any specific relation between surfactant attachment with wettability or ability of rock in water adsorption is not found.

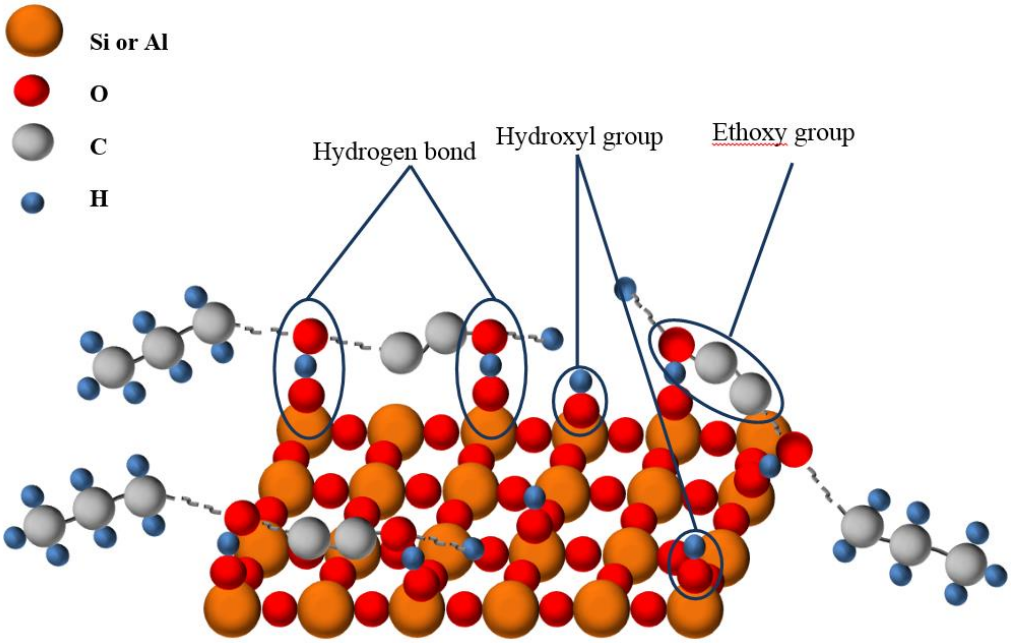

Figure 4-20. Proposed mechanism for ethoxylated surfactant adsorption on rock containing silica.

4.7 Conclusion

Although there is a large amount of literature dealing with nanoparticle transport through porous media, there is still an absence of a comprehensive study about potential and ability of NP as a surfactant carrier for controlled delivery. In this study we focused

on this concept and the main conclusions of the research may be summarized in the following points:

- Blend of 25% XOF-25S as an anionic alkylaryl sulfonates and 75% nonionic alcohol ethoxylated (C12-13/7EO) surfactant at 4% salinity was founded as an stable composition with the lowest IFT. The stability and low IFT of surfactant solution is because of the synergic effect of surfactant mixture at presence NaCl salt.
- Adsorption of surfactant blend in the presence of TiO_2 nanoparticles was proportional with retention of nanoparticles inside column. Therefore the capability of NPs to deliver surfactant blend molecules to oil/water interface is increased when NPs can transport through porous media as much as possible.
- The adsorption of alkylaryl sulfonates and alcohol ethoxylated blend greatly depends on the mineralogy of rock, which was increased at rock surface containing higher amount of silica and alumina. The hydrogen bonding between the oxygen in the ethoxy groups and the hydroxyl groups of silica is suggested as a plausible mechanism for the adsorption of surfactant. Any specific relation between surfactant attachment with wettability or ability of rock in water adsorption was not found.

Chapter 5

Oil/water microemulsion stabilized by in-situ synthesised nanoparticles for enhanced oil recovery

5.1 Introduction

Nanoparticles (NPs) have been investigated to generate and stabilize microemulsions (ME), as reviewed in Section 2.2.3. In spite of those existing applications, it is seldom reported that magnetic NPs, whose behaviour can be controlled by an external magnetic field, were applied as foam/emulsion stabilization agent for EOR application. Although some studies investigated the super- /para- magnetic NPs transporting in porous media and adsorption at o/w interface [19], the focus was on the migration and deposition properties of NPs in rock samples, not for stabilizing emulsions. It is also noteworthy that among all the work published, NPs-stabilized MEs were produced in a two-step method. In this method, nanoparticles were produced first, and then mixed with CO_2 to form CO_2/water emulsions, or o/w, w/o emulsions [297-299]. For the two-step synthesis method, nanoparticles need to be prepared and stored in advance, which inevitably increased cost and produced many agglomerations. *In-situ* synthesis of NPs for emulsification, at the same time improving ME stability, will have important implications / promise for future chemical EOR techniques.

For ME-EOR to work, another essential aspect that needs to be considered is the pressure gradient when ME are migrating in the rocks matrix [73, 300]. Though

extensive work has been conducted on colloidal transport for environmental considerations [196, 277, 294, 301], the transport of ME in porous media in the presence of the oil phase has been scarcely investigated to date, especially when it is stabilized by NPs. From practical considerations, it is preferable to use the ME with lower injection pressure to reduce the pump power required to push displacing fluids and hydrocarbon to production well, and prevent the formation from damaging due to high pressure.

The work in this chapter aims to develop a novel method to produce iron oxide nanoparticle (IONP) *in-situ* in an o/w ME and examine the its potential for enhanced oil recovery. Three tasks are designed, which include, i) design and production of appropriate o/w ME at optimum salinity, ii) *in-situ* production of IONP inside ME prepared at optimized salinity, where IONPs were firstly demonstrated to stabilize ME and iii) core-flooding experiments to assess the performance of bare MEs and NPs-stabilized MEs, in terms of EOR efficiency and pressure drop. The results reveal that MEs stabilized by *in-situ* produced IONPs have great potential in increasing oil recovery efficiency while maintaining an excellent pressure profile.

5.2 Materials preparation and Characterisation

5.2.1 Materials

Analytical grade materials including n-hexane, sodium chloride, sodium hydroxide, Span 80, Sodium dodecyl sulphate (SDS) and propyl alcohol were purchased from Sigma Aldrich and used as received. The iron (III) 2-ethylhexanoate and mineral oil with a measured value of 42.6 mPa·s were obtained from Alfa Aesar and Kerax Ltd. (UK), respectively. The standard glass beads with diameter of 425-600 μm were purchased from Sigma Aldrich. Prior to use, the glass beads were thoroughly cleaned

using a sequential acid wash, water rinse, ultrasonication, and oven-drying procedure [196].

5.2.2 Microemulsion preparation and characterization

A set of ME suspensions were synthesized at various ionic strength ranging from 0 to 10 wt% NaCl. The other compositions of ME were fixed as 4 wt% n-hexane as the oil phase, 4 wt% propyl alcohol as the co-solvent, 4 wt% SDS as the surfactant, and 1% Span 80 as the co-surfactant to achieve an ultra-low interfacial tension between the oil and water phases, $\gamma_{o/w}$, where SDS is not sufficient to achieve due to its single-hydrocarbon-chain structure. The interfacial tension (IFT) between bulk ME and mineral oil, the hydrodynamic size of oil droplet and optimum salinity results were measured and presented in Section 5.4.1. The optimum salinity of ME occurs when the IFT between ME and mineral oil achieves minimum value, which was measured by an optical tensiometer (KSV CAM 200, KSV instruments Ltd., Finland) under an atmospheric environment. One of the advantages of using ME compared to a surfactant solution is that in the ME solution, surfactants can distribute at the interface between oil droplets and the water phase, consequently preventing themselves from adsorbing on the substrate or forming micelles. It is commonly known that at high concentrations above CMC, the surfactant molecules tend to self-assemble and form turbid micelles, which could precipitate on the substrate and reduce the availability of surfactant in the solution.

5.2.3 In-situ synthesis of Iron Oxide NPs in microemulsion

The procedures from Okoli et al. [302] and Sanchez-Dominguez et al. [10, 303] were referred and modified for the synthesis of Iron Oxide nanoparticle (IONP) in o/w MEs. Generally, one type of ME containing the metallic precursor and another one the precipitating agent of reaction are mixed together. Upon mixing, the collision and

coalescence of droplets could allow the originally-separated reactants contact with each other, and thus a chemical reaction is triggered. The surfactant-covered water droplets actually act as a nanoreactor for the formation of nanoparticles. The chemical reaction in the emerged droplet experiences, subsequently, the process of nuclei, growth and finally formation of nanoparticles, after exchange of precursors [10].

The concentration of reactants was pre-determined so that the concentration of final IONP in ME could reach approximately 800, 1600 and 6400 ppm after the reaction. Briefly, iron (III) 2-ethylhexanoate was firstly dissolved in the oil phase and then used to formulate 20 mL ME at different salinities of 0, 5 (optimum salinity as determined in Section 5.4.1) and 8 wt% NaCl. Sodium hydroxide with a stoichiometric value was dissolved in brine with a similar salinity so that the amount of brine for NaOH solution was considered a tenth of ME. NaOH solution as a precursor was added dropwise via a syringe pump (KDS-410-CE, kdScientific, USA) to synthesize IONP in ME. An ultrasound probe (Fisher Scientific Ltd.) operating with an amplitude of 25 out of 100 was used for mixing and performing the proposed reaction in Equation (5-1):

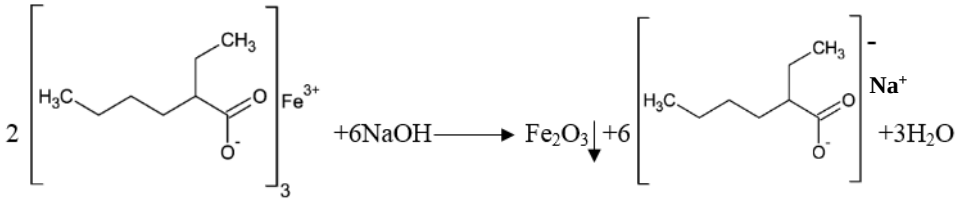

Equation (5-1)

Figure 5-1a shows that the IONPs are successfully synthesized in ME, and they can be drawn towards a magnet (neodymium-samarium cobalt magnet with 18 kg pull force). The long-term stability was checked by unaided eye observation, and results in Figure 5-1b show that ME suspension with 5 wt% NaCl had the best macroscopic stability after 24 h. The morphologies of the synthesized IONPs were examined using a transmission electron microscope (TEM, FEI Tecnai TF20). As shown in Figure 5-2,

the observed IONP mainly consisted of globular morphologies in the order of 5 to 20 nm.

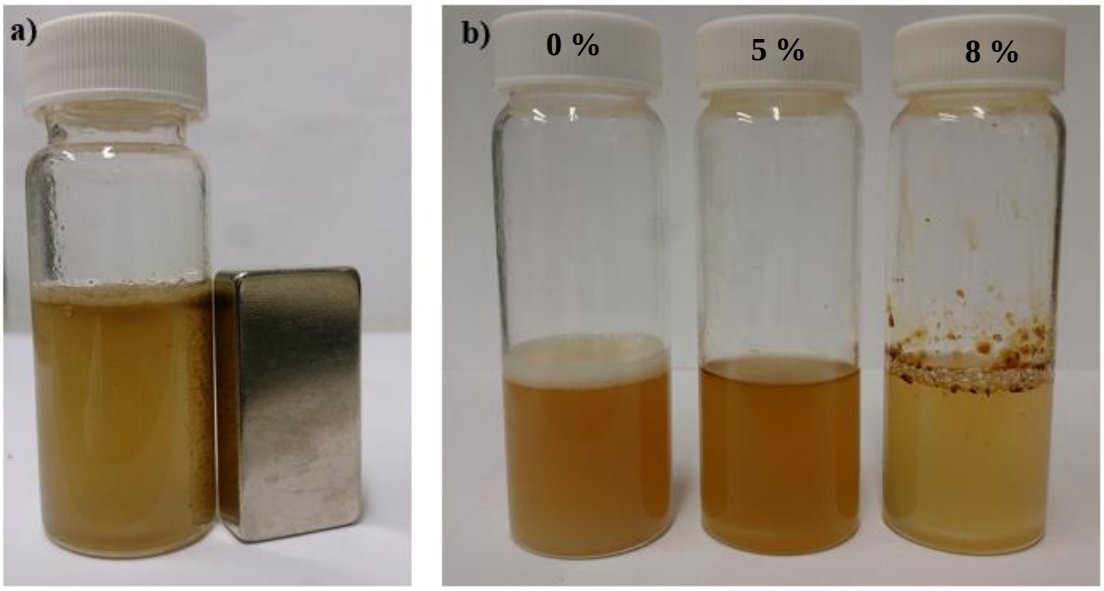

Figure 5-1. iron oxide magnetic nanoparticles inside the O/W ME a) with presence of magnet (neodymium-samarium cobalt magnet with 18 kg pull force), b) Microemulsion containing *in-situ* synthesized Iron Oxide nanoparticle (MEIN) synthesised in different salinity after 24 h.

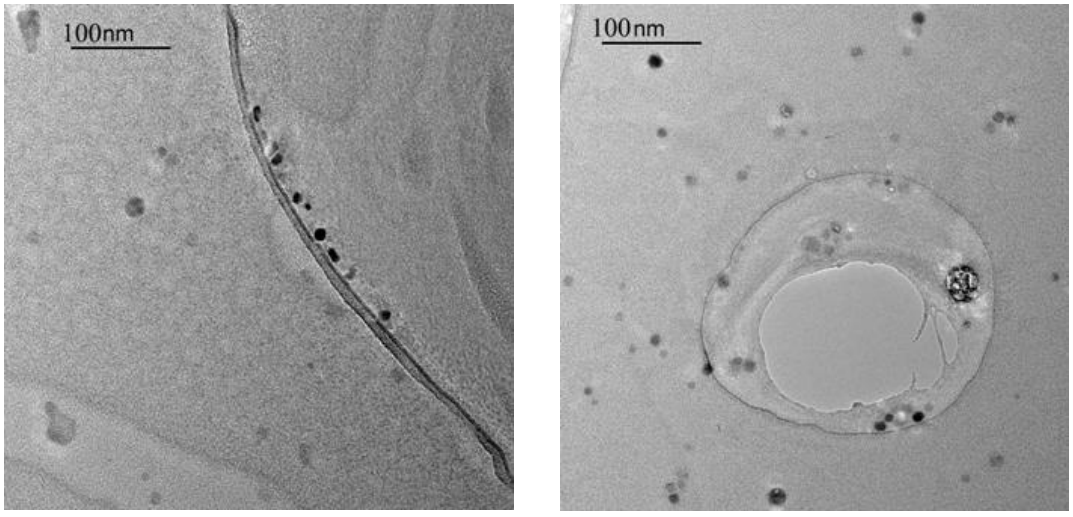

Figure 5-2. TEM photos of iron oxide nanoparticles which were synthesized in ME at optimum salinity.

5.3 Core flooding experiments

5.3.1 Porous medium preparation

Prior to use, glass beads (Sigma Aldrich) with 30-40 mesh size fraction (425-600 μm) were thoroughly cleaned using a sequential acid wash, DI water rinse, and oven-drying according to reference [196].

The dried glass beads were saturated in distilled water, and then deposited into a glass column in 1.5 cm increments with 0.5~1 cm thick of water on the top of borosilicate glass columns (10 cm L × 2.44 i.d., Glass solutions, Blacktrace Holding Ltd., UK). After the formation of a layer of 1.5 cm, vibration was accomplished for 3 minutes using a vortex mixer (Scientific Fisher), with the amplitude of vibration represented by 8 on the vibrating table's dial. The column was kept vertical by one hand. The packing length in column was actually 7 cm due to the reduced to O-ring blocker in two sides. To prevent glass beads from flowing out of column, the inlet and outlet column end blockers were fitted with a single layer of membrane with the pore size of 10 μm (Millipore limited, UK), respectively. The absolute water permeability for glass beads was computed as 98.0 $\pm$ 17.3 mD based on Darcy's law. The porosity or volumetric water content was determined by extracting and oven-drying the glass beads in the already packed glass column. Parameters relating to the column are listed in Table 5-1.

5.3.2 Porosity determination

Before experiments, the packing in glass column was practiced 21 times until achieving a confidence with constant packing . After fully saturated by at least 400 mL distilled water, the weight of saturated glass column was recorded as m_{sc}. Then the dry

weight of glass beads was measured as m_{dg}, after drying 24 hours in oven at 70 °C. The column weight was measured as m_{dc}, thus the pore volume V_p can be calculated as:

$$V_p = \frac{m_{sc} - m_{dc} - m_{dg}}{\rho_w}$$

The average porosity was measured as 38.0%, which was applied for all core flooding experiments.

Table 5-1. Parameters in average value for packed glass beads column from over 20 times practice for packing.

Porous media properties	Value
Length (cm)	7 ±0.3
Diameter (cm)	2.44
Bulk volume (mL)	33.7±1.4
Pore volume (mL)	12.8±0.5
Porosity (%)	38.0±1.6
Absolute permeability (mD)	98.0±17.3

5.3.3 Experiment setup

A core-flooding system was set up to reveal the EOR potential for ME with *in-situ* synthesized IONP. Figure 5-3 shows the integrated experimental instruments and schematic view of the core-flooding setup. A HPLC pump (Series I, Scientific Systems, Inc.), which is equipped with a pulse damper to minimize pulsation for the benefit of downstream instrumentation, was used for injecting brine during coreflooding. A syringe pump (KDS-410-CE, KD Scientific Inc., USA) was applied to inject mineral oil and emulsion/NPs suspension loaded in different syringes in order to avoid overlap contamination. The concentration of NPs in suspension was measured by UV-spectrophotometer (UV 1800, Shimadzu) on-line and real-time (applicable for 0 and 0).

A pressure transducer (150 psi, Omega Engineering Ltd., UK) is installed on the back of rig board to measure the pressure drop when fluids passing through the packed porous media. A borosilicate glass columns (10 cm L × 2.44 i.d., Glass solutions, Blacktrace Holding Ltd., UK) was applied as a core holder in which the porous media was packed. A bypass route connecting the inlet and outlet of the column was applied to remove bubbles in tubing before experiments, as shown in Figure 5-3a. The effluent liquid is collected in a 50 mL graduated cylinder marked in 0.1 mL divisions in order to determine the accumulate oil recovers, as shown in the schematic diagram Figure 5-3b.

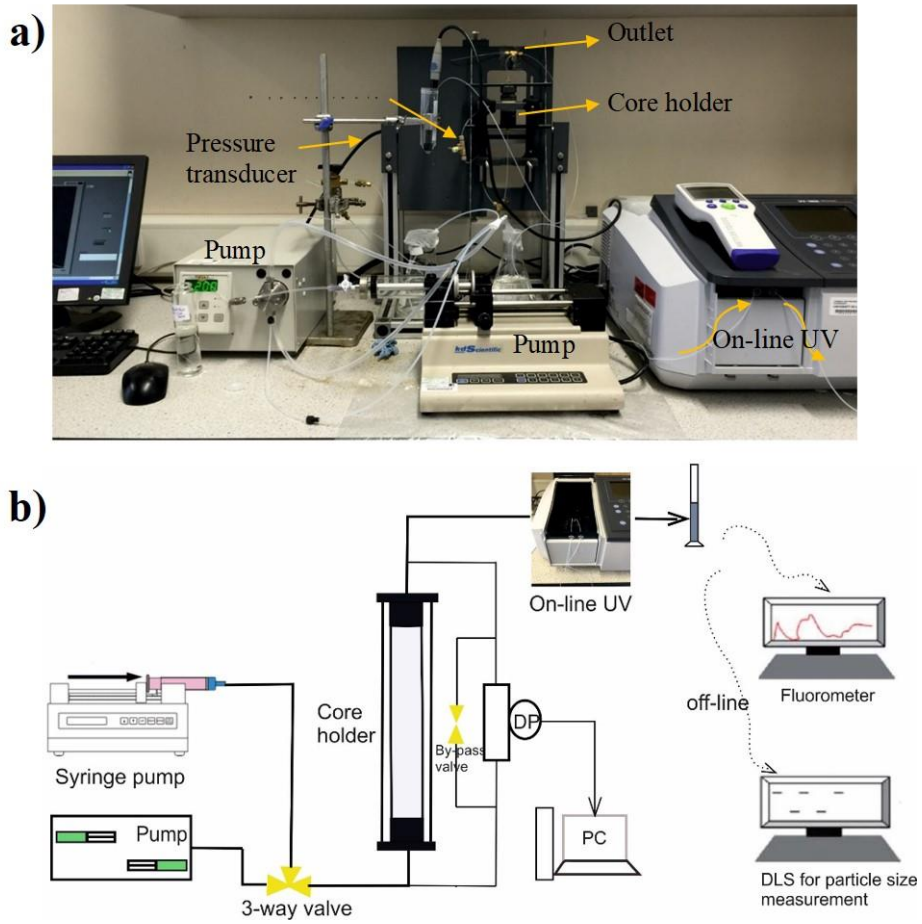

Figure 5-3. (a) Experimental core flooding set-up, and (b) Schematic of the apparatus for laboratory detection and quantitative analysis of CDs in simulated reservoir rock. The concentration of particles was detected on-line by UV-Vis spectrophotometer, running at a wavelength of 310 nm.

5.3.4 Coreflooding procedures

The procedures of coreflooding experiments were accomplished as below:

- Brine saturation by injecting at less 20 PV of brine at optimum salinity (5 wt%) into the glass column at 2 mL /min in order to make sure the column is fully saturated by brine and allow enough time for grains depositing.
- Oil saturation by injecting mineral oil (Keratech 24 MLP, Kerax Limited, UK) at flow rate of 0.5 ml/min until no water coming out, and the original oil in place (OOIP) was determined by the volume of water collected.
- Brine flooding as a secondary oil recovery stage was performed with a fixed flow rate of 0.5 mL/min for 3 PV, and followed by 20 mL (1.6 PV) displacing sample injection at flow rate of 0.5 m/min to simulate EOR process.
- Chasing brine injection at a flow rate of 0.5 mL/min for 20 mL.

5.4 Results and discussion

5.4.1 IFT, emulsion size and optimum salinity of microemulsion

As explained in Section 5.2, the MEs were fabricated under different salinities. The transparency of ME samples containing NaCl at 5 and 7 wt% show the formation of oil core inside the ME, whereas when the amount of NaCl was lower or higher than 5 wt%, the ME was not fully formed. The oil/water phase of ME even experienced segregation with presence of 10 wt% NaCl (Figure 5-4). The reason behind this phenomenon is because the surfactant distribution at o/w interface can be affected by electrolyte present in the aqueous phase, which will be further explained in Figure 5-7. Corresponding to the macroscopic image of transparency shown in Figure 5-4, the IFT results in Figure 5-5 consistently show that with the presence of 5 wt% of NaCl, the IFT between ME and mineral oil was reduced most effectively to the relative low region (<0.01 mN/m)

with a tiny drop hanging on the syringe tip, due to the sufficient formation of ME. By decreasing or increasing the salinity from 5 wt%, the IFT increased for both directions, and when the salinity increase to 10 wt%, the emulsion became unstable and eventually segregate, similarly, the size determined by DLS method in Figure 5-6 also shows the same trend with transparency and IFT. Therefore, the optimum salinity (5%) obtained above was applied to synthesis IONP in ME, and the sample show good stability.

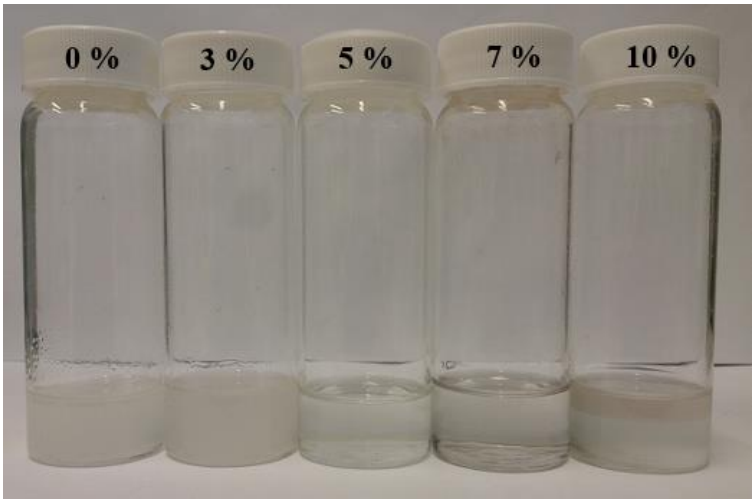

Figure 5-4. Macroscopic image of ME samples containing NaCl from 3 wt% to 10 wt%.

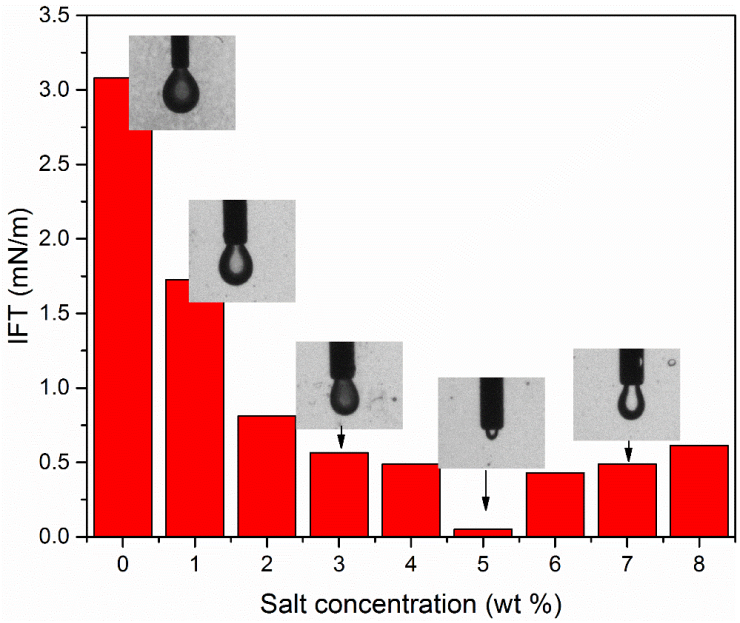

Figure 5-5. The interfacial tension between ME and mineral oil. Insets are images of ME suspension hanging on needle tip. The volume of ME sample capable to hang on the needle tip is changing with the trend of IFT.

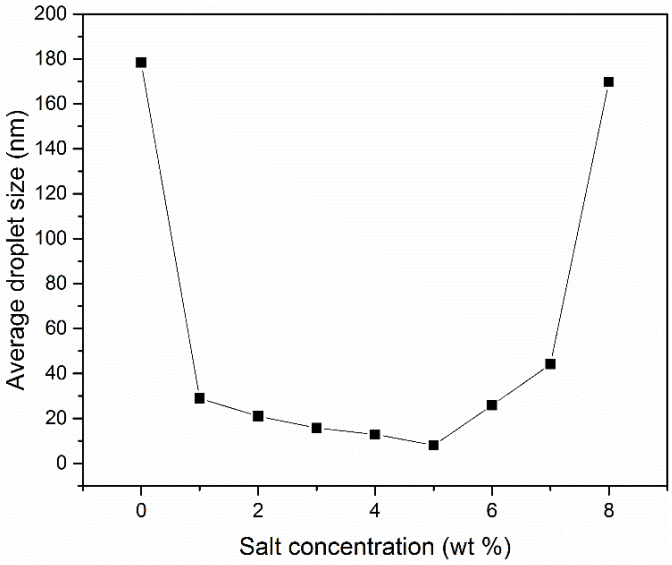

Figure 5-6. Hydrodynamic size of ME samples with different NaCl concentrations.

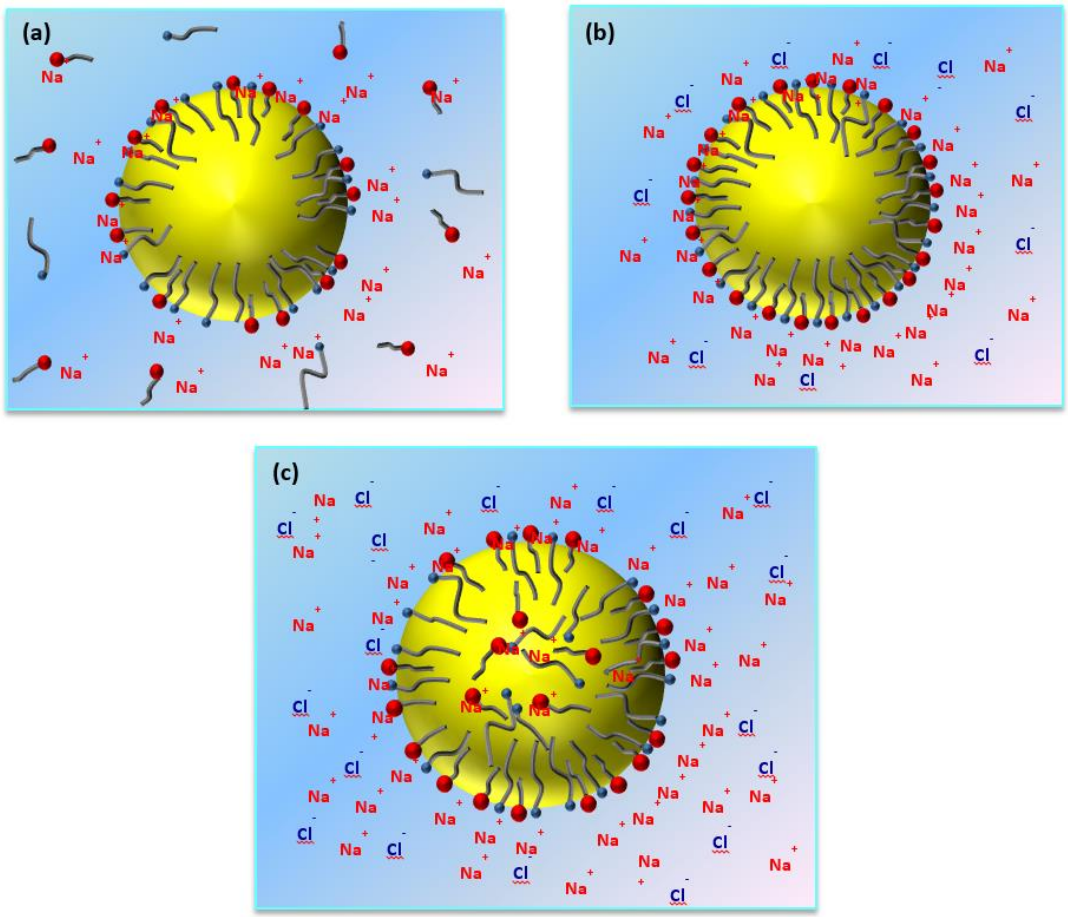

Figure 5-7. Schematic of surfactant distribution at the o/w interface with increasing ionic strength. (a) More surfactant are dispersed in water phase at low saline water ; (b) most surfactant distribute at the interface at proper salinity; (c) at high concentration of salt, the electric double layer was compressed.

Increasing salinity could decrease the mutual solubility between water and surfactant. At lower salinities (e.g. <3 wt %), more surfactant molecules were dispersed in water phase. Therefore, the steric and electrostatic repulsion between oil droplets is too weak to overcome the hydrogen bonds of water molecules. As salinity increased, the solubility of surfactant in water phase is increasingly reduced and most surfactants tend to distribute at the oil/water interface, which leads to the decrease of interfacial tension and formation of oil nanodroplets. At very high salinity values (e.g. 10 wt%), the screening impact of the extra electrolytes compress the electrical double layers around droplets and the O/W phases would be separated (Figure 5-7).

5.4.2 Fluids viscosities

The dynamic viscosities of microemulsion suspension (ME) and microemulsion containing *in-situ* synthesized iron oxide nanoparticle (MEIN) are shown in Figure 5-8. After Fe_2O_3 nanoparticle formed in the emulsion, the viscosity of the ME is influenced markedly by the presence of both the nanoparticle and surfactant. The increase in viscosity due to the adsorbed nanoparticle which may slow down the diffusion of surfactant near the interface [304], and the particle-surfactant network (as proposed in Figure 5-11 in Section 5.5.1) also prevents the coalescence of ME when shear force is applied. Similar reports in terms of emulsion/foam viscosity increase by NPs were reported by several authors. Adsorbed nanoparticles may increase the interfacial viscosity [304-306], which may further slow lamella drainage and stabilize foam. [307, 308] It is also interesting to see that ME with 6400 ppm Fe_2O_3 NPs experienced a dramatic increase in viscosity. This suggests that when optimal amount of nanoparticles and surfactant are employed, they can favour the formation of a strong high-quality emulsion/foam, as found by Prigiobbe et al. [309]

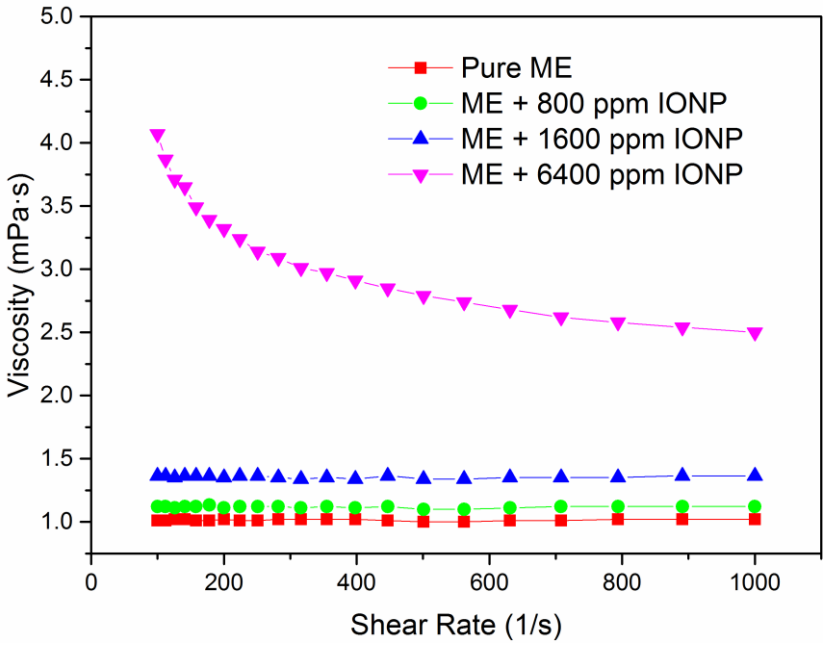

Figure 5-8. Viscosity of ME and MEINs.

5.4.3 Oil displacement experiments

5.4.3.1 Oil recovery efficiency

In order to clarify the effects of nanoparticles, four tertiary flooding experiments were conducted with only ME, and ME with *in-situ* formed IONPs at concentrations varying from 800 to 6400 ppm. As described in the coreflooding procedures, all the effluent materials, including oil, brine and ME suspension, were collected by using a long slim graduated tube marked in 0.1 mL divisions. Due to the density difference, the oil/water phase can be separated instantly and automatically. The cumulative oil recovery efficiency (E_{COR}) is calculated by using the amount of cumulative oil production divided by the OOIP (Original Oil in Place). The EOR efficiency (E_{EOR}) is calculated by using the amount of oil produced in the process of ME/chase-water flooding divided by OOIP.

It can be seen that the cumulative oil recovery efficiencies of brine floodings for different cases are quite close to each other (at around 45%), which means that the tertiary flooding started from a similar residual oil saturation. With an overall oil

recovery efficiency of 59.1% OOIP by the end of tertiary flooding, ME can mobilize 10% more trapped oil (EOR efficiency which is relative to OOIP) after brine flooding, while the presence of nanoparticles in ME further improved the efficiency, depending on the amount of iron nanoparticle contained (Figure 5-9). With the increase of iron oxide nanoparticle concentration, the cumulative oil recovery efficiency was increased from 59.1% to 85.2%, and EOR efficiency was correspondingly increased from 10% to 28.9% (Table 5-2). In addition to a higher oil recovery ability, the pressure drop for MEIN flooding is more stable and lower than that of the ME flooding, which is beneficial for the flow assurance in oil reservoir (Figure 5-10).

Table 5-2. The amount of oil recovered at different stages, for flooding experiments with different displacing fluids

Displacing fluid	E_{COR} after brine flooding, % OOIP	E_{COR} after ME flooding, % OOIP	Ultimate oil recovery efficiency, % OOIP	E_{EOR} by ME, % OOIP	E_{EOR} by Chasing-water, %
ME	42.4	52.4	59.1	10.0	6.7
ME+ 800 Fe_2O_3	48.5	61.9	70.5	13.4	8.7
ME+1600 Fe_2O_3	45.9	61.6	73.1	17.4	9.8
ME+6400 Fe_2O_3	43.4	72.3	85.2	28.9	12.9

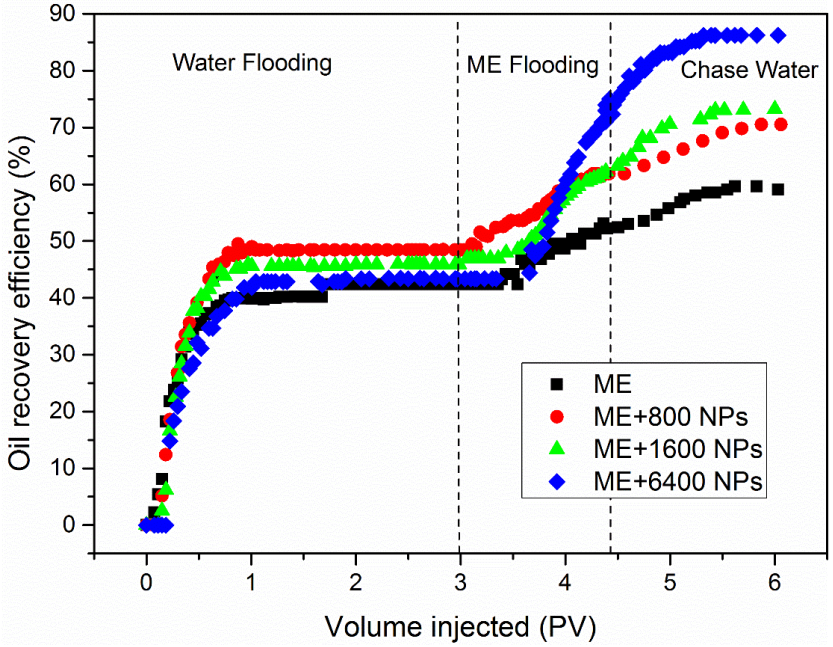

Figure 5-9. Tertiary oil recovery obtained by ME and MEIN.

5.4.3.2 Pressure files during injection

Pressure drop is a necessary consideration for the design of core flooding. A 3.28 psi/m pressure gradient is common for field-scale water flooding, at the frontal velocity generally around 1 ft/day [73]. Therefore, a similar pressure gradient is necessary for the design of chemical flooding at given flow rate in the laboratory. Figure 5-10a shows the differential pressures for the core flooding experiments, by ME and MEIN (with 800 ppm NPs) formulated with the same surfactant concentration. For ME flooding, the pressure at tertiary stage started slightly higher than that in brine flooding stage, but experienced a rapidly increase approximately from 3.5 PV, soaring up over 20 psi by the end of tertiary flooding. This might be attributed to the surfactant release trigged by ME destruction and its retention in porous media. However, after being stabilized by IONP the pressure profile for ME kept lower than 6 psi, which is even lower than the brine flooding stage and showed no tendency to increase, as shown in Figure 5-10b. The reason is because stabilized by nanoparticles, the ME structure is much more stable and there is a persistent existence of particle and surfactant molecules at the interface.

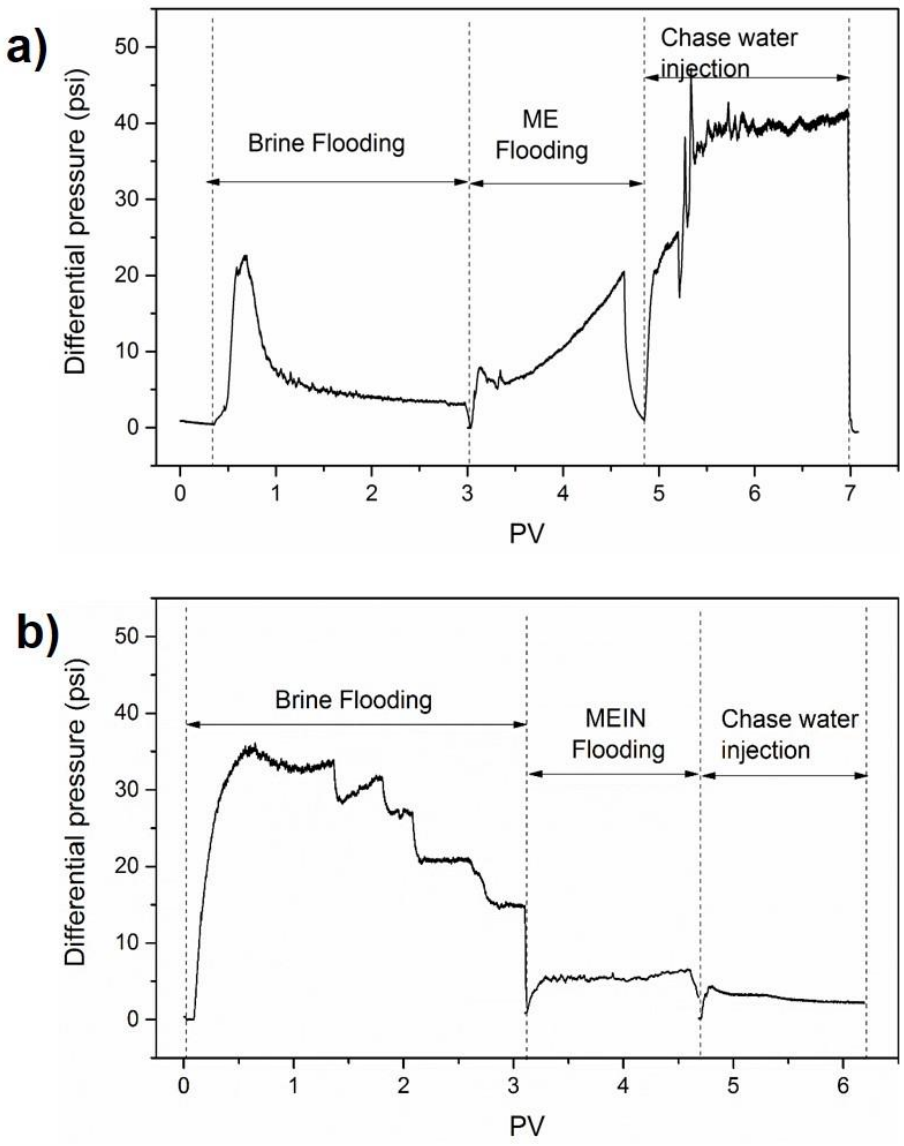

Figure 5-10. The differential pressure for oil displacement (a) ME and (b) MEIN.

Considering the chasing-water injection processes, the pressure for MEIN was still lower than 4.5 psi and gradually declined, while the pressure for ME saw a heavy fluctuation at around 40 psi. It means that during the chasing-water injection process, ME kept being destroyed and released the surfactant previously distributed at the o/w interface, while the MEIN could still keep its texture synergistically stabilized by NPs and surfactant, and prevented the pressure gradient from fluctuating due to surfactant retention in porous media. In addition, because of the electrostatic and steric effect jointly introduced by NPs and surfactant, the ME did not tend to adsorb on the surface of glass beads, or breakup due to the collapse of interface texture (Figure 5-11(c)).

5.5 The mechanism for enhanced oil recovery

5.5.1 Enhanced stability by in-situ formed NPs

Although the nucleation, growth and solubility stages of nanoparticle formation may be dependent on transient dimers, collisions, and coalescence of droplets [310], the reaction itself is believed to happen at the O/W interface since the precursor is dissolved in the continuous aqueous phase [302, 311]. Moreover, particles tend to stay at o/w interface after the synthesis due to the high energy (ΔG) required to detach the particle from the interface as calculated by the equation below (Figure 5-11 (a)). de Oliveira et al. [312] observed that cobalt (II) 2-ethylhexanoate precursor in AOT W/O MEs reside at the oil/water interface. In our case, surfactant has not such a complex network to trap the nanoparticle, but to form the particle-surfactant joint arrangement at the interface and synergistically stabilize the emulsion texture (Figure 5-11 (b)).

There are two main mechanisms that support the synergistic stabilization effect by NPs and surfactant: lamella drainage and hole formation [306]. We now provide a molecular-level discussion about how the *in-situ* synthesized NPs and surfactant synergistically stabilize the ME.

In O/W ME, aqueous lamellae separate oil droplets and prevent the droplet from coalescing, and also separate the oil droplet with glass beads surface. The lamellae depends on a disjoining pressure (Π_d) originated from electrostatic, steric, structural, and additional short range repulsive forces, which counteract the van der Waals attraction between the two film surfaces [222, 306, 313]. In our case, the anionic surfactants (SDS) and the formed NPs will contribute electrostatic repulsion to Π_d (Figure 5-11 (c)), and the NPs may also attribute to Π_d via structural effects that increase the osmotic pressure due to organization of particles in the lamella [314, 315],

and contribute steric repulsion due to the nonionic surfactant Span 80 and nanoparticle flocs 'bridging' the lamellae [316], as shown in Figure 5-11 (d).

ME may be destabilized by coalescence due to hole formation in the aqueous lamellae which separate the oil droplets. Holes appear because of thermal fluctuations that produce spatial and density variations in the film. Lamellae drainage acts to thin the aqueous lamellae, which reduces the work required to open a hole and increases the probability of hole formation. [317, 318] The nanoparticles in the present study are expected to resist bending of the interface to allow oil holes to form in the lamellae. The attachment energy required to move the particle from the equilibrium interface can be calculated by the equation below, [319] in the case of a pure solid particle absorbing at the interface.

$$\Delta G = \pi R^2 \gamma_{o/w} (1 \pm cos\theta)^2$$

Where, R is the particle radius, $\gamma_{o/w}$ is the oil-water interface. In our case, the 5-20 nm particle at the oil-water interface with surfactant lowering IFT of microscopic droplets $\gamma_{o/w}$ to 23-27 mN/m [320], would have an ΔG equals 10^3 to 10^4 kT, depending on θ. It can be expected that with surfactant functionalization, particle would be irreversibly detached from the interface driven by the Brownian motion. This high-level detach melt energy indicates that the emulsion system, stabilized by the nanoparticle is more thermodynamically stable than ME without the particle. The organization of nanoparticles at the interface would provide a barrier to resist interface bending to avoid coalescence (Figure 5-11(e)). Consequently, bending of the interface to expose more nanoparticle to either aqueous or oil phase would be unfavourable.

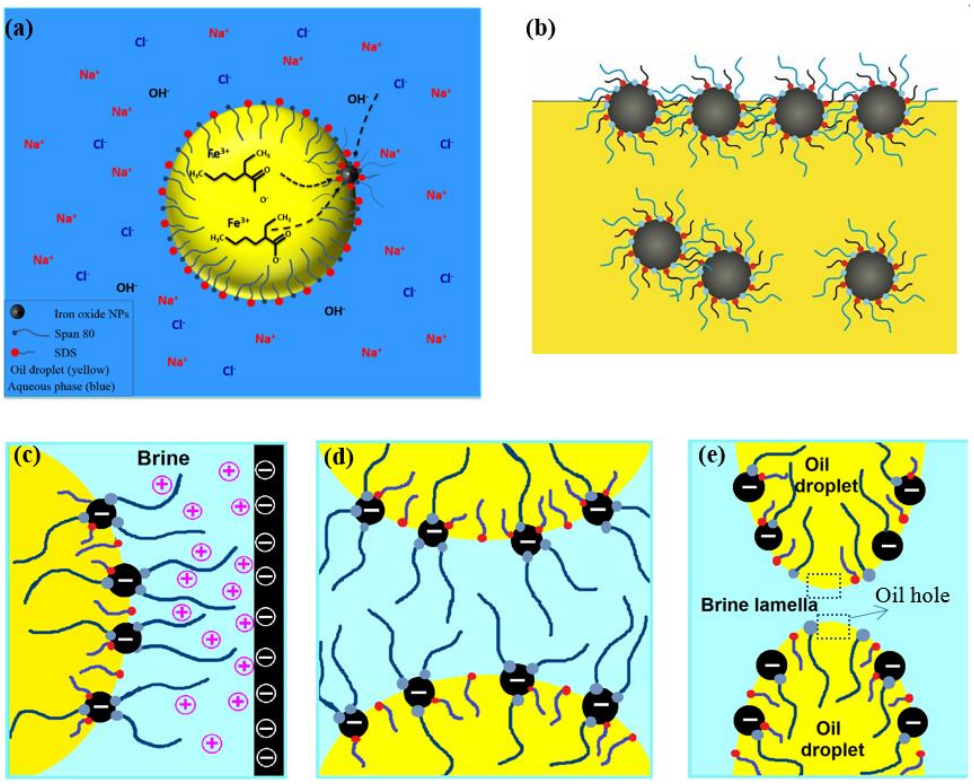

Figure 5-11. (a) chemical reaction for iron oxide nanoparticle synthesis at the oil-water interface； (b) Schematic illustration of particle-surfactant joint arrangement at the interface; (c) electrostatic repulsion between ME thin film (due to the negatively-charged iron oxide NPs and anionic surfactant SDS) and negatively- charged glass beads surface, and steric effect introduced by nonionic surfactant Span 80; (d) electrostatic repulsion and steric effect between MEs thin film to counteract the van der Waals attraction to prevent them from coalescing; (e) Bending the interface to form 'oil hole' is energetically unfavourable because the organization of nanoparticle at the interface would provide a barrier to resist interface bending to avoid coalescence

5.5.2 Preventing the formation of viscous Phase

Several past experimental works have shown that formation of viscous phases such as liquid crystals and viscous macroemulsions in the O/W interface is a challenge for oil recovery using surfactant flooding. Viscous phase is formed when interfacial adsorption of the surfactant molecules is hindered [321]. Screening blend surfactantsis

a common way that is usually used for inhibiting formation of the viscous phase. For instance branched surfactants such as twin-tailed structures are effective to minimize ordering at the O/W interface and prevent the formation of viscous phases [35, 322].

Synthesis of IONP at the interface by local chemical reaction facilitates the uniform distribution of nanoparticles, thus facilitate the attachment of surfactant molecules at the interface. Figure 5-12 shows that the presence of nanoparticles would prevent the formation of a viscous phase at the O/W interface. Therefore, a likely reason for EOR in the presence of nanoparticles in the ME is the improvement of distribution of surfactant molecules at the O/W interface, so as to maintain a very low interfacial tension.

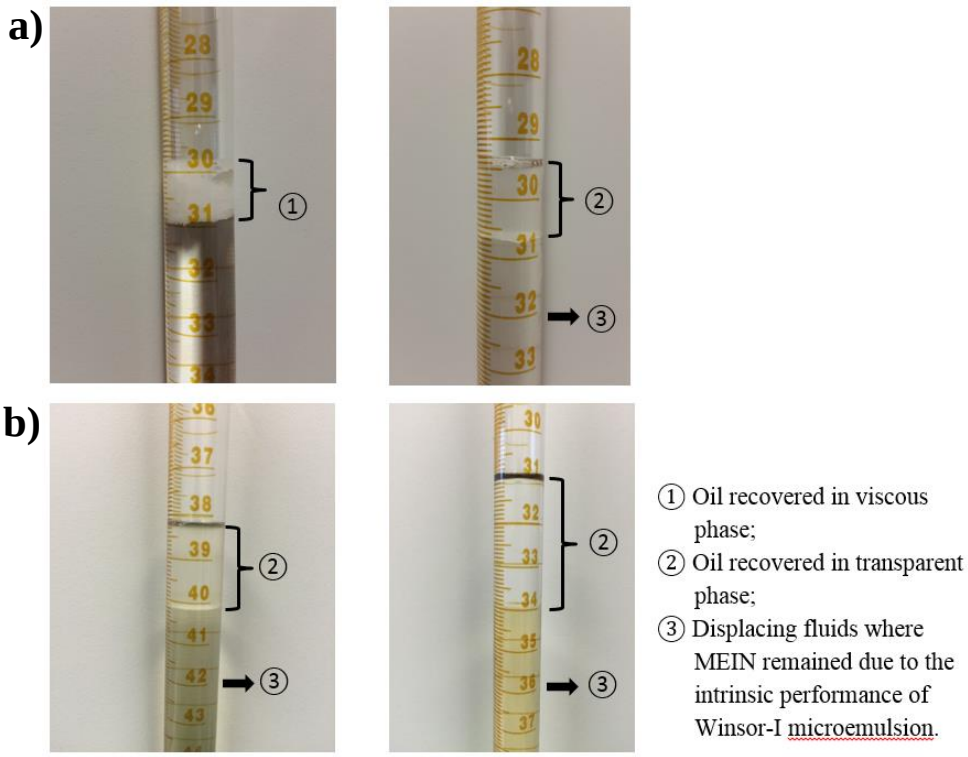

Figure 5-12. The oil recovered at the stage of tertiary flooding displaced by (a) ME, (b) MEIN with 800 ppm IONPs;(c) MEIN with 1600 ppm IONPs; (d) MEIN with 6400 ppm IONPs. The viscous phase formed for ME flooding, whereas the oil remained transparent state for case (b) to (d) where ME was synergistic stabilized by NPs.

5.5.3 Enhancing IFT stability

In terms of the IFT between the bulk ME suspension and oil phase, it has been reported that the surfactant surrounding the ME would raise the chance of chromatographic separation, i.e., adsorption on the pore surface, or preferentially partitioning into the water or oil phase, which could cause IFT variations with possible adverse effects on oil recovery [35]. However, compositions with particles allow the surfactant to be more persistent at the O/W interface, thus preventing surfactant partitioning into water or oil phase and avoid IFT fluctuations. As shown by the dynamic IFT in the range of 0 s to 1000 s in Figure 5-13, the dynamic IFT between the bulk ME drop and mineral oil experienced significant fluctuation from around 580 s to 830 s compared to ME stabilized by NPs. The persistence of molecules at the interface has been shown to be important for emulsification and dispersion [323, 324].

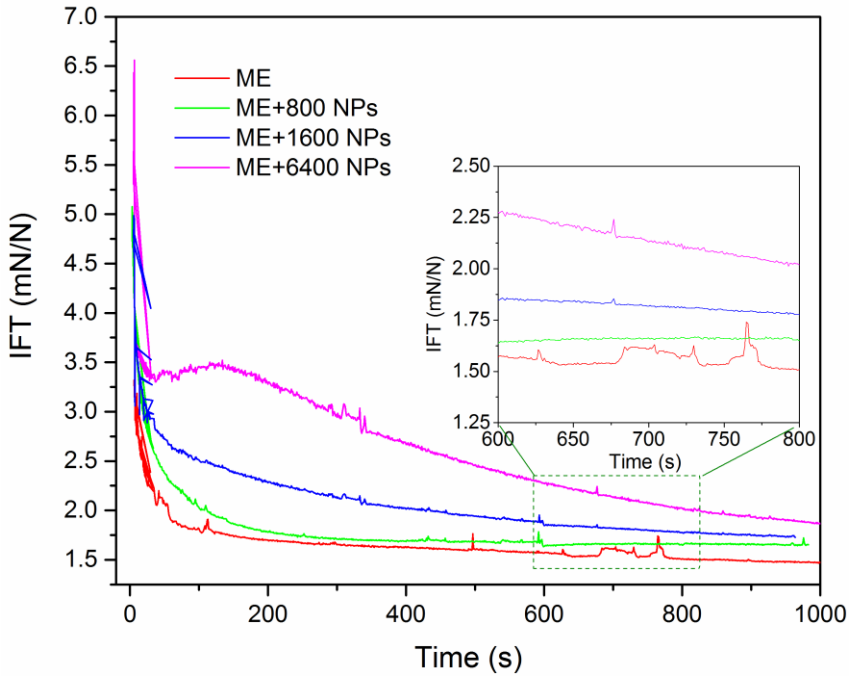

Figure 5-13. Dynamic viscosities between bulk emulsion and mineral from 0 s to 1000 s for the samples applied for enhanced oil recovery, the inset is dynamic amlifying view for the dynamic viscosity changing from 600 s to 800 s.

5.5.4 Increased viscosity for mobility control

Joint arrangements of particle and surfactant at the interface could change the interfacial rheology properties. It is hypothesized here that particle-surfactant mixture could increase interfacial elasticity and cohesiveness over particles or surfactants alone. In effect, interlocking surfactant chains between particles may act as elastic 'springs' in the layer. Also, combined effects could impart significant changes to the interfacial viscosities (essentially the intrinsic hydrodynamic resistance to flow of the layer), much like increases to the bulk viscosity. Given in Figure 5-11 (b) is a possible 'elastic' arrangement of particles and surfactant at an interface [325]. From the viscosity measurement, the formation of IONP increase the viscosity of the ME (Figure 5-8), which is consistent with the report by Prigiobbe et al. [309]. A synergic effect was observed between surfactant and nanoparticles on the gas viscosity, which doubled in the presence of nanoparticles. This relatively high viscosity is beneficial for the mobility control [21, 226].

5.6 Conclusion

The work in this chapter developed a novel method to produce iron oxide nanoparticles (IONPs) *in-situ* in oil-in-water (o/w) MEs to increase their performance in improving oil recovery. The magnetic IONPs were synthesized in o/w ME at the optimum salinity. Core flooding experiments were carried out to evaluate oil recovery ability for MEs containing IONP at different concentrations, and possible reasons for enhanced oil recovery were analyzed. The main conclusions of the research can be summarized in the following points:

- Composite ME synergistically stabilized by surfactant and *in-situ* fabricated IONPs were successfully synthesized at the optimal salinity.

- Coagulating with IONPs allows the surfactant to be more persistently absorbed at the o/w interface, consequently eliminating the variation of IFT and increasing the ME viscosity.
- The synergistic stabilization effect between nanoparticle and surfactant can significantly reduce the pressure gradient and fluctuations during the flooding and post-flooding stages, due to the formation of more stable ME textures.
- Producing IONP can improve the EOR efficiency, and as increasing the concentration of IONP from 0 to 6400 ppm, the tertiary oil recovery efficiency is boosted from 10% to 28.5% relative to OOIP, and the total oil recovery is improved remarkably from 59.1% to 85.2%.
- The oil recovery mechanism is believed mainly due to more stable ME texture synergistically stabilized by NPs and surfactants, avoiding viscous phase formation in flooding process.

Chapter 6

Partially hydrolysed polyacrylamide seeded by nanoparticles for enhanced oil recovery

6.1 Introduction

As reviewed in Section 1.5, there are several problem associated with polymer flooding, especially polymer degradation and viscosity impairment. In this chapter, SiO_2/HPAM nanofluids were prepared by dispersing silica nanoparticles into aqueous HPAM solutions, and their rheological properties were investigated and compared to pure HPAM solutions. The main part of this work was done under high temperature and the effect of important parameters such as nanoparticle loading, temperature, aging time and electrolyte concentration, on the rheological behaviour were investigated. The dynamic viscosity and viscoelastic properties were also checked to clarify the contribution of NPs on the improvement of polymer rheological properties.

6.2 Material preparation and characterization

6.2.1 Material

SiO_2 nanoparticle (12 nm, ≥99.0% in purity) was purchased from Sigma Aldrich Co., LLC. The specific surface area of this kind of particles is 150 m^2/g measured by the BET method, and the corresponding specific weight is 2.4 g/mL. Partially hydrolysed polyacrylamide (HPAM) was purchased from Shandong Tongli Chemical Co. Ltd

China, which has a molecular weight of 5-22 million g/mol and relative density of 1.302 g/mL. Sodium chloride (ACS reagent, ≥99.0% in purity) was obtained from Sigma-Aldrich. All of the chemicals were of analytical reagent (A.R.) grade and used as received without further purification.

The real size and morphology was detected by transmission electron microscope (TEM, FEI Tecnai TF20) as shown in Figure 6-1a. The hydrodynamic particle size distribution in distilled water was measured using a Malvern Nanosizer based on the dynamic light scatting (DLS) method, which shows an average size of 187.5 ±2.851 nm, peaking at 200.8 ±64.85 nm (Figure 2). The zeta potential of the dispersion was measured as -32.0±1.04 mV.

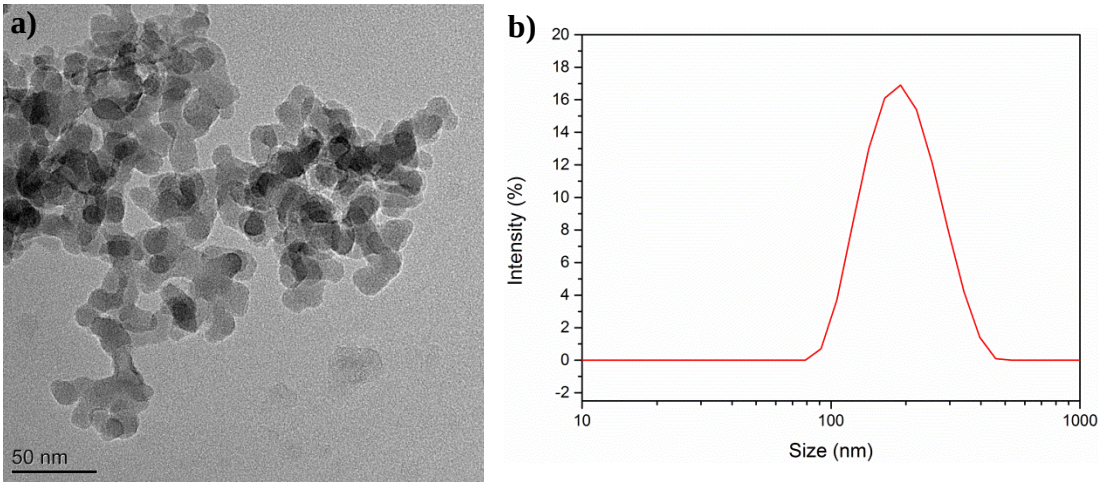

Figure 6-1. Figure 2. (a) TEM image of SiO_2 nanoparticles, and (b) particle size distribution of SiO_2 in distilled water measured by the dynamic light scattering (DLS) method.

6.2.2 Hybrid preparation

SiO_2 NPs at different concentrations (0.0, 0.1, 0.2, 0.4, 0.6, 0.8, 1 wt%) were dispersed in distilled water to form a stable dispersion by ultrasonication via an ultrasonic bath (FB15057, Fisher Scientific) for 20 minutes. Then, HPAM powders were introduced into aqueous SiO_2 suspensions at designed concentrations from 0.01

wt% to 1 wt%. In order to allow enough time for silica NPs contact with polymer, the inorganic/organic mixtures were gently stirred using a magnetic stirrer (SB 162-3, Stuart) at room temperature for one day. Finally NaCl was added to the hybrid solution at different concentrations up to 8 wt%, followed by one- day stirring before rheological tests.

6.2.3 characterization

6.2.3.1 Rheology measurement

The viscosities of these samples were measured by a Physica MCR 301 rheometer (Anton Paar, Austria) equipped with a convection oven and a 'TC30' temperature controller unit, which can stabilize the sample temperature from 0 to +1000 °C with an accuracy of 0.1 °C. A cone-and-plate geometry was selected for the measurement, because the shear rate is uniform across the radius and the gap is pre-set to a certain standard (0.098 mm) determined by the manufacture. The system only requires a small amount of sample (0.7 mL) for each test and is easy to clean. Prior to any measurement, the rheometer was tested with a standard oil and pure water at different temperature to ensure that both the instrument and this particular setup were calibrated, yielding reliable data. The calibration with standard oil (Figure 6-2) was done every 3 months, while the viscosity of pure water at 25 ^{o}C was tested every time before starting the formal measurement, and compared to the standard value of pure water viscosity (0.89 mPa·s) to make sure the accuracy.

The rheological behaviour of samples was determined under both steady and oscillatory shearing conditions to obtain steady and dynamic viscoelastic properties. Dynamic frequency spectra were conducted in the linear viscoelastic regimes, as determined from dynamic stress-sweep measurements. All experiments were conducted under a shear rate controlled mode.

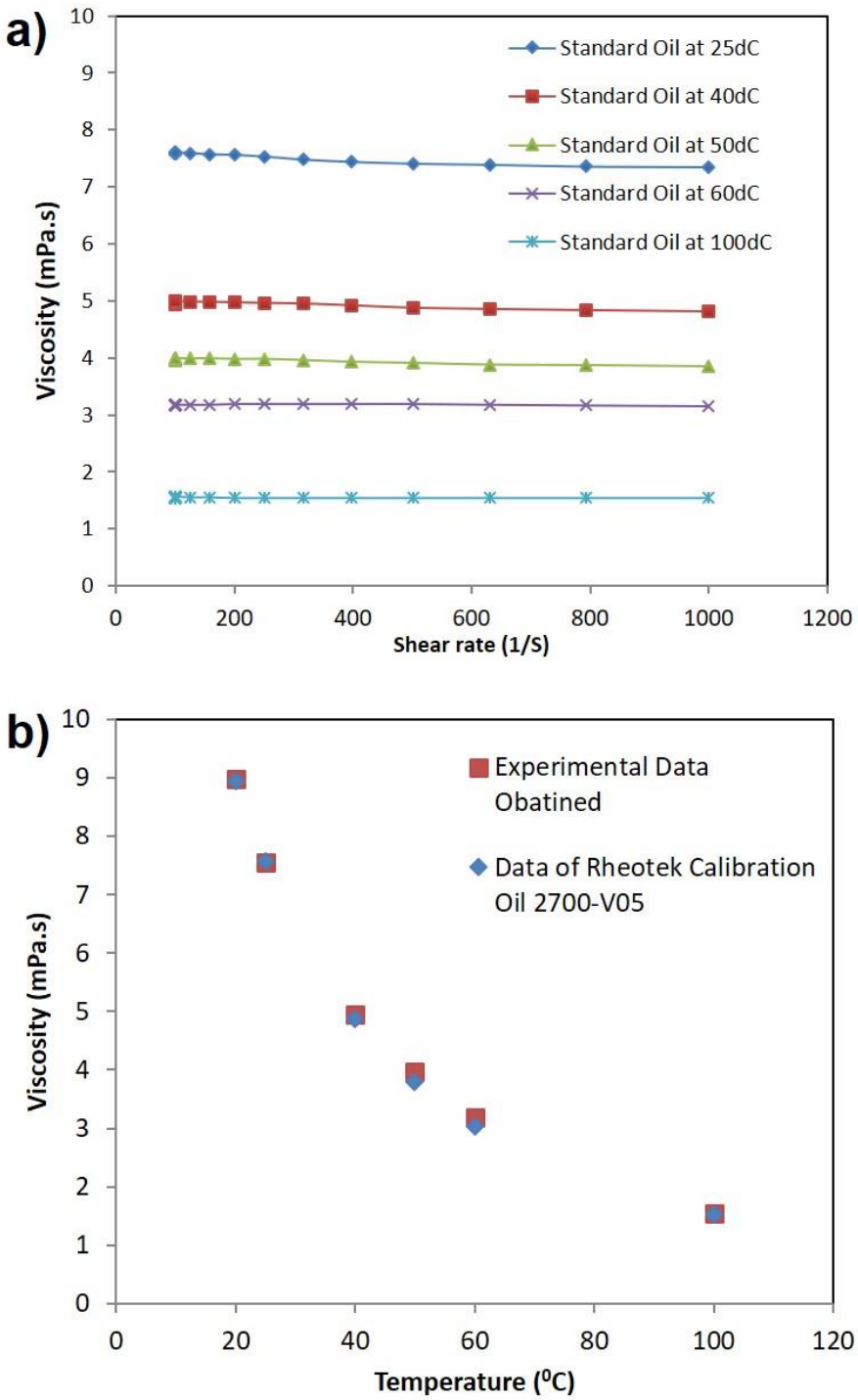

Figure 6-2. Calibrate rheometer using Rheotec Calibration oil 2700-V05. (a) Viscosity, under various temperature, was measured against shear rate changing from 100 to 1000 s^{-1}; (b) Comparison between the measured viscosity (average between 400 s^{-1} to 1000 s^{-1}) with the known viscosity data of Rheotec Calibration Oil. The difference between obtained values were within 3%.

6.2.3.2 Infrared spectroscopy

Infrared spectroscopy (FTIR spectrometer 100, Perkin-Elmer) was used to measure the FTIR spectra of vacuum-dried HPAM and HPAM/silica hybrid samples. The data was collected at a spectral resolution of 4 cm^{-1} within the scanning range of 4000-400 cm^{-1}.

6.2.3.3 Long-term thermal stability

The sample of 0.5 wt% HPAM cross-linked by 0.8 wt% SiO_2 nanoparticle was selected for long-term thermal stability test, while a particle-free sample with the same polymer concentration was selected as the reference. The samples were stored in glass bottles covered by screw-caps with sealed by a sealing tape, and were placed into an oven at 80 °C. The viscosities of those samples were measured at 85 °C at different sampling times spanning 12 days.

6.3 Core flooding experiments

6.3.1 Porous media preparation

As described in Section 4.3, the bulk sandstone were crushed into small grains and sieved into the size ranging from 425 μm to 600 μm. The porous media was prepared by packing crushed grains in a stainless steel cylinder. Because of the irregular shape and wide range of size distribution, it allows a higher/reasonable residual water saturation after being saturated by oil to build up original oil in place (OOIP). A high/reasonable residual water saturation is impossible to acquire for the packed glass beads with single size, because the flowing path is homogeneous and fluids just percolate as a piston face. Only when the flowing path is irregular, can the fluid

penetrate in a finger pattern, due to the unbalance of capillary force at the two sides of the grain. The parameter of the packing are summarized in Table 6-1.

Table 6-1. Parameters for the porous media

Porous media property	Value
Lentgh (cm)	7.1 ±0.3
Diameter (cm)	2.5
Bulk volume (mL)	34.9±1.5
Pore volume (mL)	12.4±0.1
Porosity (%)	35.4±5.9
Absolute permeability (mD)	25.3±4.6

6.3.2 Thermocouple wiring

Three thermocouples are arranged at the both ends and the middle of the stainless steel-made core holder, then they are paralleled twisted together and feed the temperature back to the temperature controller (EZ-ZONE PM Express single loop 16th DIN PID controller, Watlow, USA). One thermocouple is attached at the heating tape and feeding the heater's temperature to the temperature controller. The heating process is controlled by proportional–integral–derivative (PID) control loop.

6.3.3 Setup description and flooding procedure

Figure 6-3a shows the experimental coreflooding set-up. Like the cold stage shown in Section 5.3.3, the piston pump and syringe pump were used for injecting brine and sample, respectively. A stainless steel column with length of 10 cm and diameter of 2.5 cm was manufactured as the core holder in which porous media was loaded to simulate the reservoir. O-rings were mounted to the blockers at two ends to seal the gap between blockers and the inner cylinder wall. Two caps screwed to the end of the core holder are used to compress the blockers and to prevent them from slipping outside at high

pressure, which ensure a solid packing inside the core holder. A stainless tube coil immersed in the water bath powered by the hot plate is applied to preheat the fluids before flowing into the core holder (Figure 6-3b). It has been tested that the pressure can approach as high as 150 psi without leaking for this sort of design.

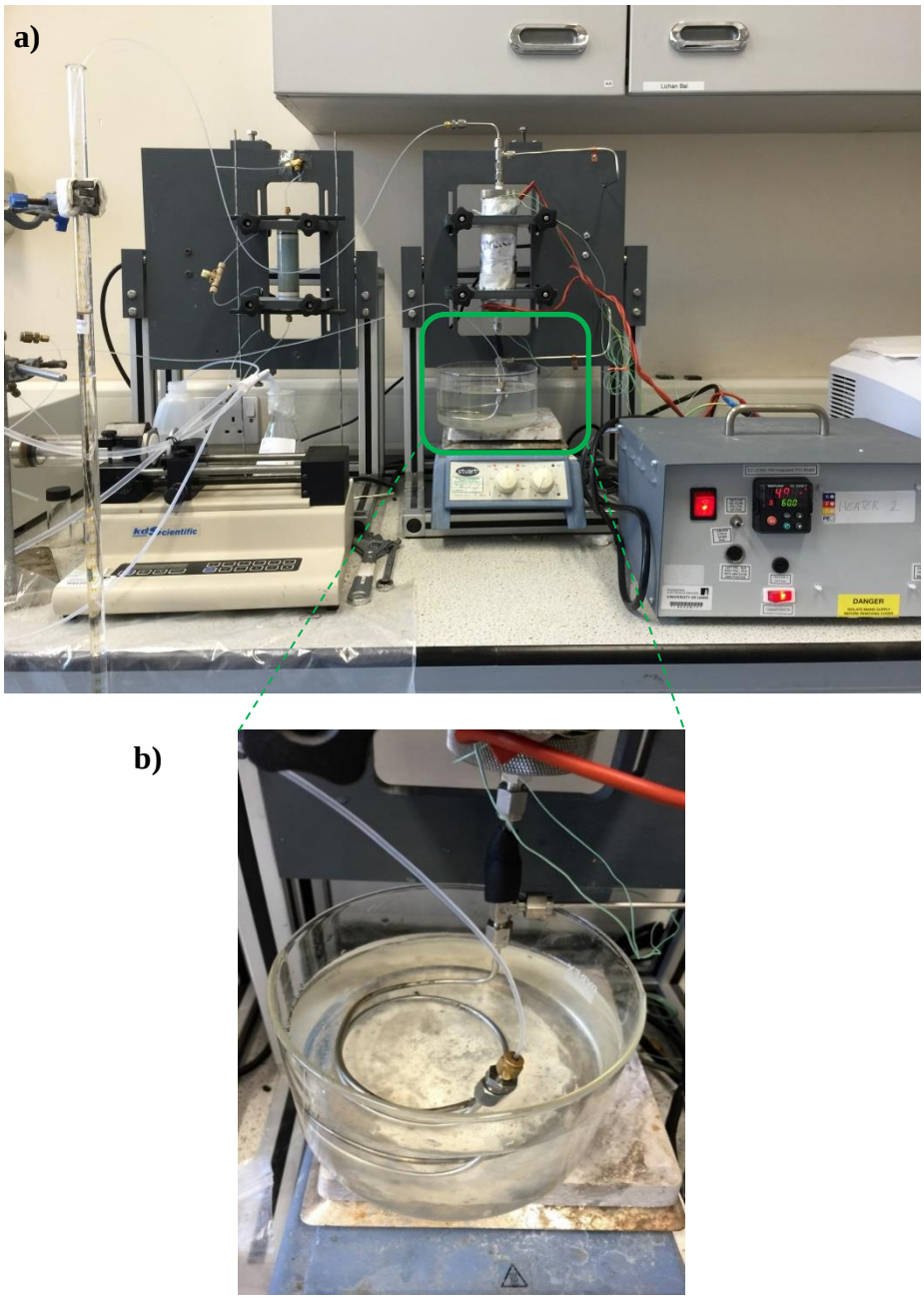

Figure 6-3. a) Cold and Hot core flooding stage. b) pre-heating of injected fluid via water bath heated by hot plate

The effluent sample can be either collected directly in the graduated cylinder or flow pass through the on-line connected UV-spectrophotometer (Shimadzu, UV 1800), with

the purpose to measure the particle concentration and generate particle breakthrough curve (C/C_0). A different pressure transducer (PX409-150DWUV, Omega Engineering Ltd.) running with software from the manufacture is connected to both sides of the core holder to measure the pressure drop during experiments. All column experiments were carried out at 50 ºC. The experiment procedures after packing are described:

- At least 10 PV brine flooding (0.1 M NaCl) at a flow rate of 2 mL /min in order to make sure the column is fully saturated by brine and allows enough time for the deposition of rock powder. In the meantime, turn on the temperature controller to heat up the core holder, and stabilize the temperature of hot plate for pre-heating at 50 ºC.
- Oil injection at a flow rate of 0.5 mL/min, until oil breakthrough.
- Brine injection at a flow rate of 0.5 mL/min, until no more oil coming out.
- Polymer/SiO_2 hybrids flooding at a flow rate of 0.5 mL/min, as tertiary stage.

6.4 Results and discussion

6.4.1 Concentration dependence of hydrolysed polyacrylamide

There is a critical concentration existing for a polymer solution, often called the critical association concentration (CAC), where intra molecules start to self-associate. The CAC values can be obtained by several ways such as light scattering determination and the variations of fluorescence properties when micellisation occurs [326]. In this work, the rheological properties at 25 °C and 85 °C for HPAM solution were studied to determine the CAC at different temperature. Figure 6-4 shows the viscosity of HPAM at 85 ºC under different shear rates. It reveals that when the polymer concentration was lower than 0.1 wt%, the viscosities were almost independent of the shear rate, behaving like Newtonian fluids. While when the concentration was over 0.1 wt%, the viscosities

were gradually reduced with the increase of shear rate, indicating shear-thinning properties.

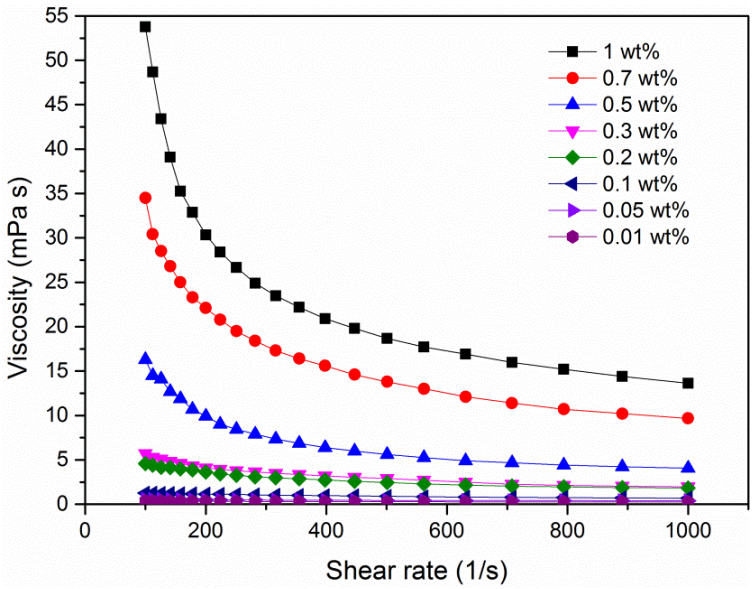

Figure 6-4. The dependence of viscosity for HPAM on shear rate (T= 85 °C).

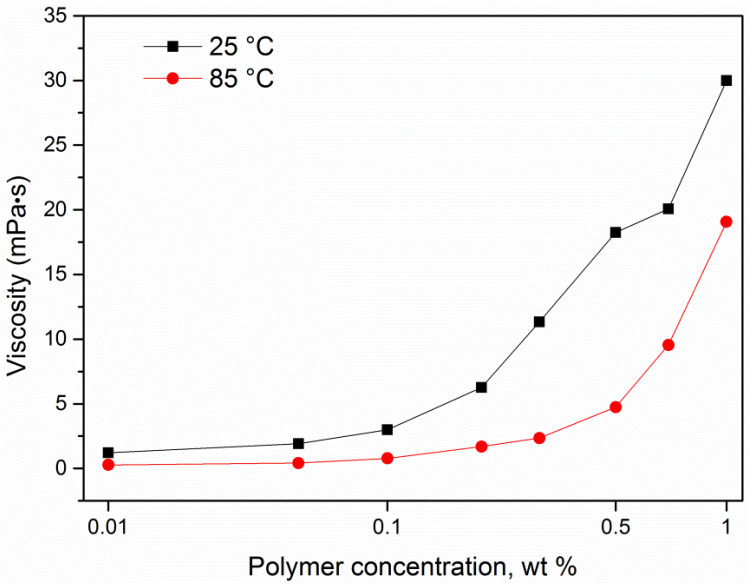

Figure 6-5. Average viscosity for various concentrations of HPAM at 25 °C and 85 °C (shear rate from 500 s^{-1} to 1000 s^{-1})

Figure 6-5 shows the average viscosity at shear rates from 600 s^{-1} to 1000 s^{-1} as a function of the HPAM concentration at 25 °C and 85 °C. The high temperature curve is divided into two parts at a HPAM concentration of ~0.45 wt%. Below that, the viscosity increased slowly with the increase of polymer concentration, but rapid

increase was observed at concentrations of over 0.5 wt%. This trend suggested that 0.5 wt% is the CAC for HPAM at 85 ^{o}C. Similarly, a lower CAC value was observed at 25^{o}C, i.e., ~0.2 wt %.

6.4.2 Effect of nanoparticle loading on the viscosity of HPAM/silica hybrids

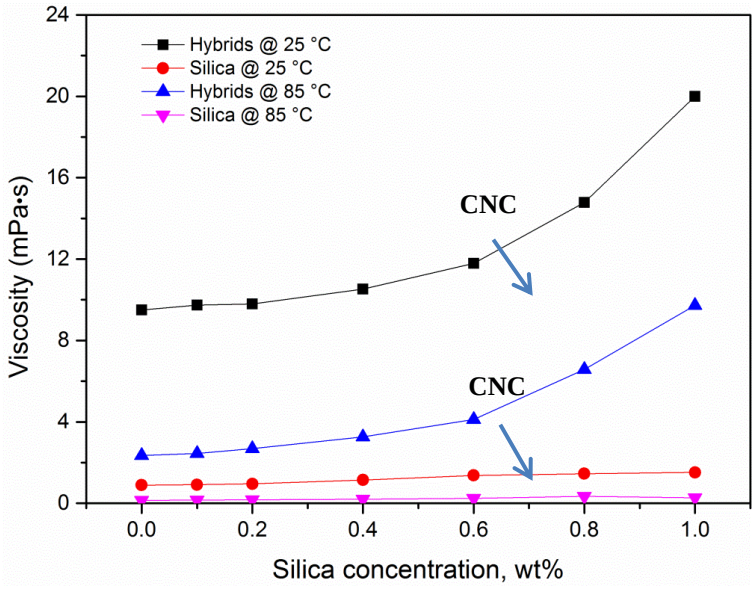

Figure 6-6. Viscosities of 0.5 wt% HPAM with different SiO_2 NP loadings (T= 25 °C and 85 °C, 8 wt% NaCl and shear rate from 500 s^{-1} to 1000 s^{-1}). Under the same condition, the viscosity for pure 0.5 wt% HPAM was measured as 2.9 mPa·s for 85 °C, and 9.1 mPa·s at 25 °C.

In addition to the CAC of HPAM, it is also worthy to examine the effect of NP on the viscosity of hybrids. To do this, 0.5 wt% HPAM solution was chosen as the reference solution in which a series of SiO_2 NPs at different concentrations were added. The same concentrations of SiO_2 NP dispersed in distilled water were also included for comparison. It is clearly from Figure 6-6 that the viscosities of the hybrids were increased with increasing NP concentrations. Similar to the pure HPAM case, a rapid increase in viscosity was observed beyond a certain particle loading, i.e., defined as critical nanoparticle concentration (CNC) here. For 0.5 wt% HPAM solution, the CNC values were found to be around 0.6 wt% in spite of the temperature at 25 °C or 85 °C.

In order to find out the reason why adding SiO_2 NP could increase the viscosity of hybrids, FT-IR spectroscopy was employed to check if there were some potential bonding effects formed between silica and HPAM. For pure SiO_2 samples, only two major peaks at 1064 cm^{-1} and 800 cm^{-1} are found as shown in Figure 6-7a, which corresponds to the Si-O-Si asymmetric stretching vibration and Si-O-Si bending vibration, respectively. Figure 6-7a also shows two peaks at 1078 cm^{-1} and 790 cm^{-1} for HPAM/SiO_2 hybrid sample, where pure HAPM sample does not show these two peaks. These are also due to the Si-O-Si anti-symmetric stretching vibration and Si-O-Si bending vibration, respectively. However, compare with the spectra for SiO_2, these two peaks all show notable shifts. Such results might originate from some combination effects between the SiO_2 NPs and HAPM. For instance, hydrolysable covalent cross-links between SiO_2 and HAPM (Figure 6-7b) might exist in the system.[327]

In addition, anther peak at 920 cm^{-1} was found, which correspond to Si-O-H bending vibration, introduced by the hydroxyl on silica surfaces. Such –OH groups can react with the amide groups, forming hydrogen bonding between the hydrogen from the SiO_2 surface and the oxygen or nitrogen from HPAM (SiO-H·····N-H or SiO-H·····O-$CONH_2$), or between the oxygen from SiO_2 surface and the hydrogen from HPAM (SiO·····HNH-COO-C, as shown in Figure 6-7b. After blended with SiO_2 NPs, the peak area ranging from 3100 to 3800 cm^{-1} for HPAM became broader, which indicates the vibration of –OH, SiO-H and N-H groups. The formed hydrogen bonding might be overlapped in this range. However, no peak appeared in this range for the pure SiO_2 sample. In addition, the possible formation of hydrolysable covalent cross-links between the SiO_2 NPs and HPAM also strengthened their connection and enhanced the viscosity of the hybrids.

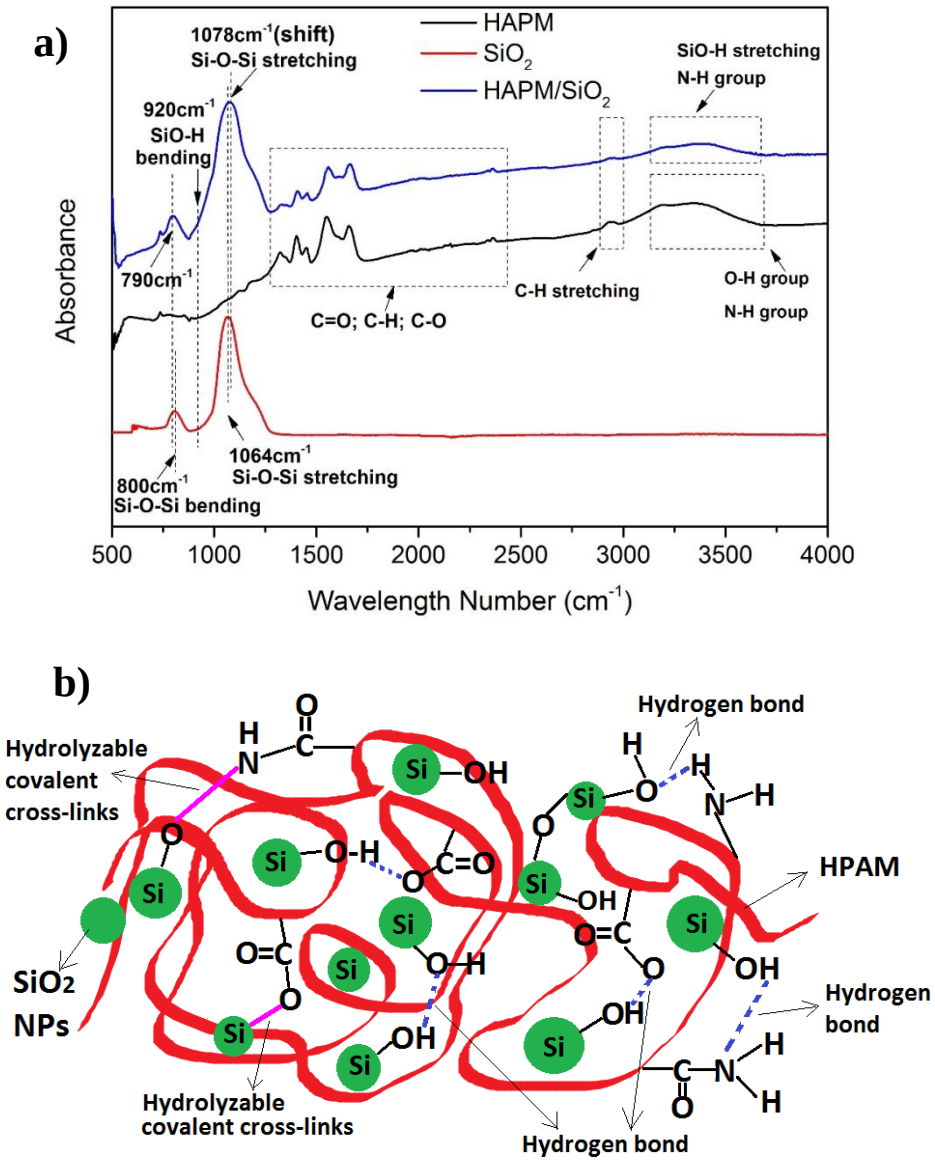

Figure 6-7. (a) FTIR spectra for 0.5 wt% HPAM, 0.5 wt% HPAM/ 0.8 wt% SiO_2 NP hybrid, and SiO_2 NP; (b) Potential interactions between SiO_2 NP and HPAM.

It is assumed that the CNC is related to the adsorption status of SiO_2 NPs onto HPAM, as illustrated in Figure 6-8. When the NP concentration is lower than the CNC value, particles are absorbed onto hydrophobic chain due to the formation of hydrogen bonds between carbonyl groups of HPAM and silanol functions of silica [328]. Consequently there is no free silica nanoparticle in the bulk solution at low particle concentrations. Moreover, when the particle concentration is increased beyond the CNC value, free silica NPs become available, which can bridge between different polymer

chains, preventing them from moving or rotating. This would result in a rapid increase in the viscosity. In addition, free particles may also agglomerate and attach together via Si-O-Si bindings, which further increase the viscosity.

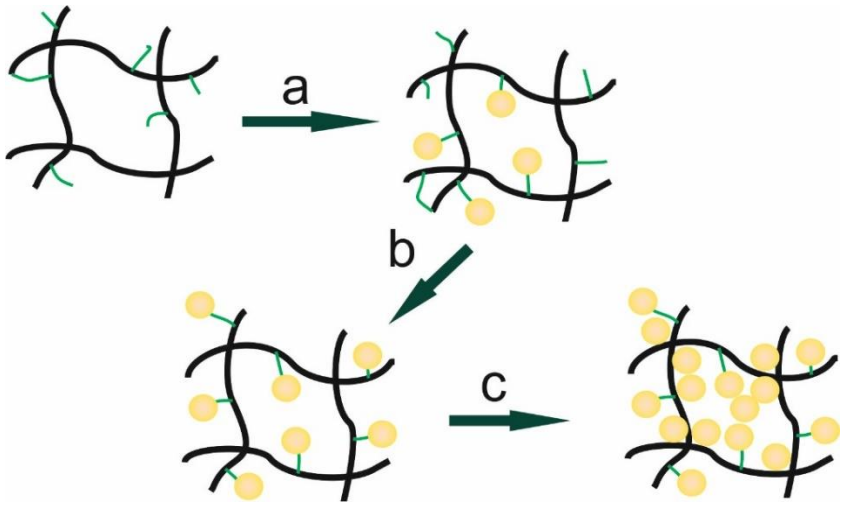

Figure 6-8. Cartoons illustrate the adsorption of SiO_2 nanoparticles onto polymer chains for a given polymer concentration: a): particle increasingly adsorb onto polymer chains via hydrogen bonds; b) saturation is reached (i.e. CNC value) with all the carbonyl groups were attached by SiO_2 nanoparticle; and c) particles accumulate and bridge in the network.

6.4.3 Effect of temperature on viscosity of HPAM/silica hybrids

To investigate the temperature effect, a hybrid sample, i.e., 0.5 wt% HPAM mixed with 0.8 wt% SiO_2, and the corresponding pure polymer and SiO_2 solution were tested (Figure 6-9). It was found that the effective viscosities for all tested samples underwent significant decreases at elevated temperatures. Compared with the pure HPAM solution, the HPAM/SiO_2 hybrids still maintained around threefold higher in viscosity in the whole temperature range studied, albeit with a larger dependence on the temperature. Similar to the analysis above, the presence of silica NPs would crosslink individual polymer molecules to form a solid hybrid network via hydrogen bonding. However the hydrogen bond is sensitive to temperature, hence a large viscosity reduction was

observed for HPAM/SiO_2 hybrids, probably due to the disassociation of the network junctions and the bindings of nanoparticle to the HPAM. For pure HPAM, the increase of temperature would still break down intermolecular hydrophobic associations unavoidably, and hydrolyse the acrylamide group in HPAM into acrylate groups. Both factors would cause the viscosity reduction for HPAM solutions.

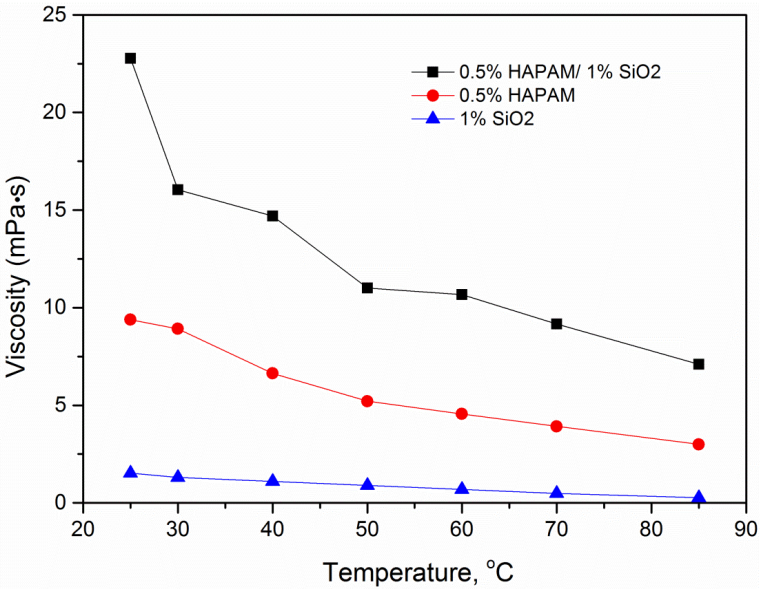

Figure 6-9. Comparison of the temperature effect on effective viscosities at different temperature (8 wt% NaCl and shear rate 500 s^{-1} to 1000 s^{-1})

6.4.4 Long-term thermal stability of HPAM/silica hybrid

In a typical polymer flooding process, polymers have to stay for a long time inside reservoirs, and continuous aging of the polymers would result in a decrease in the effective viscosity and hence a detrimental effect in oil recovery.[329] The remaining viscosity represents a basic benchmark for any polymer to be used in hostile environments. To examine the aging effect, 0.5 wt% HPAM and 0.5 wt% HPAM/0.8 wt% silica NP hybrid in a brine (8 wt% NaCl) were tested at 80 °C, as shown in Figure 6-10. The result clearly shows that the NP /HPAM hybrid had a much better thermal stability. The viscosity impairment was much lower for the hybrid. For example, the HPAM solution viscosity was dropped sharply from 4.8 cP to ~1.5 cP after 12 days'

aging, whereas a slight increase in the effective viscosity was observed for the HPAM/silica hybrid. The increase was peaked after one-day's aging, and started to slightly decline over the following days, yet still with a value higher than the original sample. The effective viscosity was about 5 times higher than the pure HPAM after 12 day's aging. Such a result is quite different to that reported in the literature.[89] The exact mechanism of the aging effect is still unclear but it appears that a gentle heating could promote the formation of binding between silica nanoparticles and polymer chain and an optimum heating duration exists to reach the maximum viscosity. For the sample investigated, one day's aging produced the highest viscosity for HPAM/silica hybrids. Such an aging effect shows an encouraging application prospect for such NP /HPAM hybrids in EOR processes.

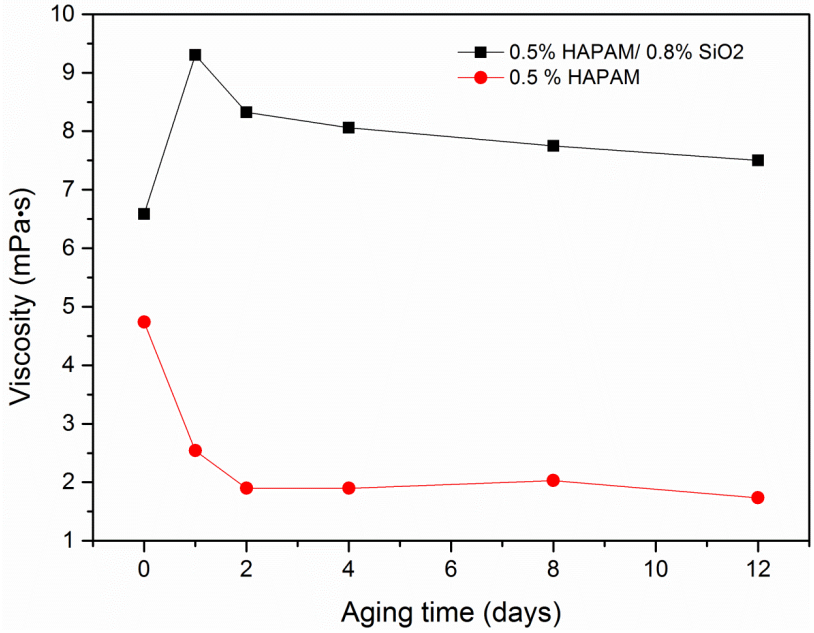

Figure 6-10. Example viscosity changing with the aging time (aging at 80 °C and 8 wt% NaCl).

6.4.5 Effect of electrolyte on viscosity of HPAM/Silica hybrid

Salt tolerance is another consideration for the application of this kind of hybrids. Since HPAM is a polyelectrolyte, the hydrodynamic size and consequently its viscosity

are sensitive to electrolyte concentration. The influences of NaCl on the effective viscosity of silica NPs, HPAM and HPAM/SiO_2 hybrids were examined at 25 $^{\circ}$C and one example is shown in Figure 6-11. Unlike previous results presented, [86, 89] which reported that the effective viscosity of HPAM was either increased or decreased by the addition of NaCl, our work showed a non-monotonic trend. The viscosity was found to significantly increase at low salt concentrations, reaching a peak value, and then started to decline. It is also noted that adding SiO_2 nanoparticle increased the value of peak salt concentration, i.e., it increased from 1.5 wt% to 2 wt% in the presence of nanoparticles. Corresponding to the viscosity data, Figure 6-12 shows that samples with 1.5 wt% and 2 wt% NaCl also have the best stability. It is believed that the initial increase in viscosity was associated with increased inter-molecular interactions. With the increase of NaCl concentration, the polarity of the solvent increased correspondingly, which contributed to reinforced intermolecular associations of the hydrophobic groups, leading to higher viscosities. As the intermolecular associations prevail over the electrostatic screening, the viscosity of aqueous HPAM solutions increased, as also observed by two refs.[90, 330] However the addition of Na^+ also screened the negative charges (carboxyl groups), and resulted in a reduction in the electrostatic repulsion within polymer chains. Consequently the conformational transition of the polymer from a stretched state to a shrinkable state would decrease the hydraulic radius of the chain and the degree of polymer chain entanglement, responsible for the reduction of viscosity of polymer solution. Clearly the salt concentration affects the viscosity significantly, hence the EOR effect. Careful selection of materials that could push the peak viscosity values towards high salt concentration will be of high value, which is currently under investigation.

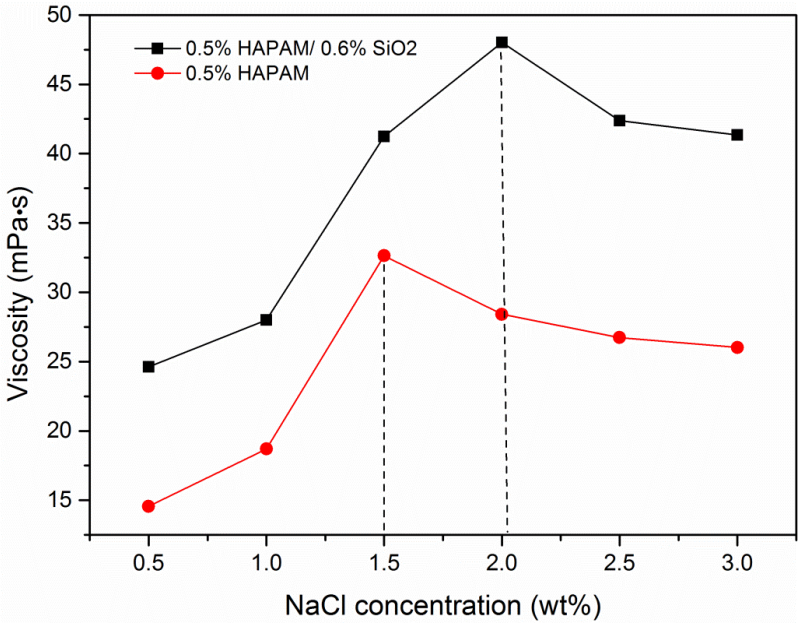

Figure 6-11.Example influence of ionic strength on average viscosity (T= 25 ºC and shear rate from 500 S^{-1} to 1000 S^{-1})

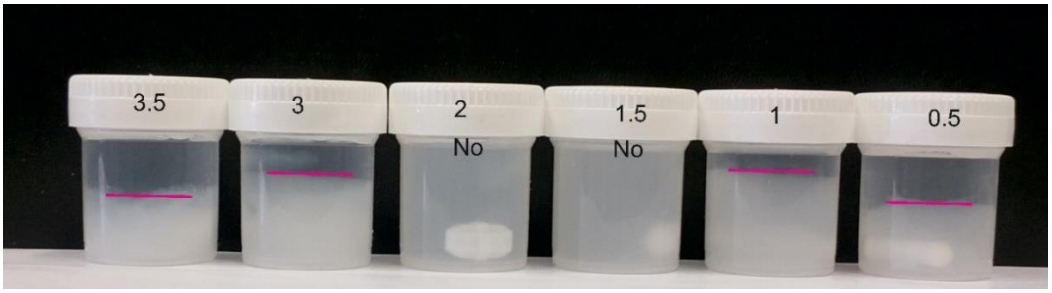

Figure 6-12. Phase separation after storing in the room temperature for 2 months for sample prepared with salinity ranging from 0.5 wt% to 3.5 wt%.

6.4.6 Viscoelastic properties with various nanoparticle loading

The viscoelastic properties for polymer solutions are used broadly to gain understanding into the molecular structure and deformation of polymers, and play a crucial role in the oil recovery process.[87, 331-333] The oscillatory test were performed for both HPAM/silica hybrid and pure HPAM solutions, and the storage modulus (G'), loss modulus (G''), damping factor (tan δ) and complex viscosity (η^*) are

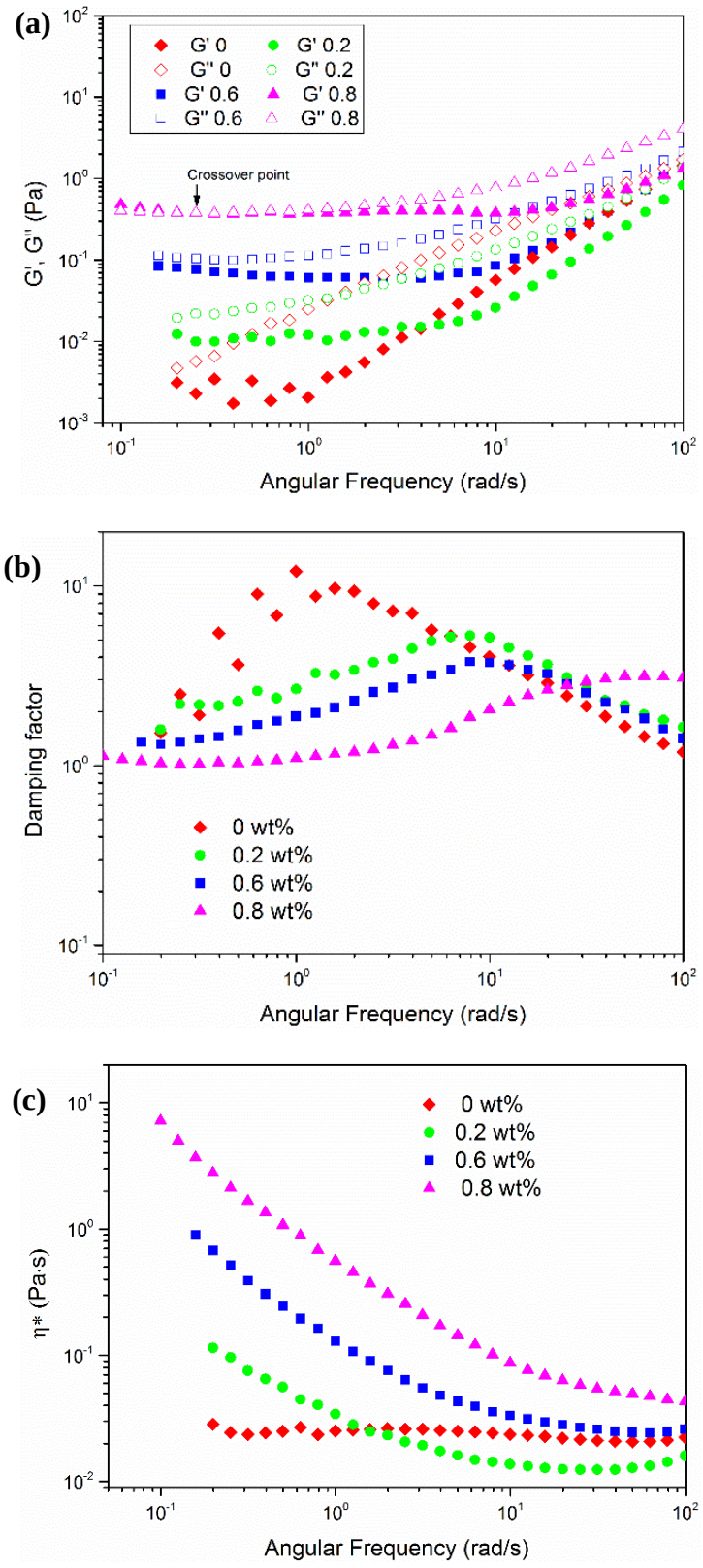

Figure 6-13. (a) Storage modulus (G') and loss modulus (G''), (b) damping factor (tan δ), (c) complex viscosity (η^*) as function of angular frequency (ω) for HPAM/silica hybrids, with SiO_2 loading from 0 wt% to 0.8 wt% (8 wt% NaCl, T = 85 °C).

plotted as a function of angular frequency (ω) in a high salinity solution (8 wt% NaCl) at 85 ^{o}C. The results show that the solutions of both pure HPAM and HPAM/silica hybrids were elastically dominated (tan δ <1) over the investigated frequency range, and became more elastic as the NP concentration increased (Figure 6-13b). When the particle loading was increased from 0 wt% to 0.8 wt%, G' and G'' both increased (Figure 6-13a). From the shape of G' and η^* (Figure 6-13 a &c), it can be concluded that pure polymer (i.e., 0 wt% SiO_2) had a long-term relaxation time due to none or insufficient network structure and links between macromolecules. However the ones with silica NPs showed almost no relaxation time due to the formation of stable 3D-network structure cross-linked by SiO_2 NPs. Although the salinity and temperature were very high, the HPAM/silica hybrid still provided strong interactions between the cyclic components of HPAM and NP surfaces, as such the HPAM structure was strengthened, yielding large hybrid elasticities.

6.4.7 Enhanced oil recovery efficiency

In order to clarify the effects of nanoparticles, four tertiary flooding experiments were conducted with brine (8 wt% NaCl), 0.5 wt% HPAM, 0.5 wt% HPAM with 0.2 wt% and 0.6 wt% SiO_2. As described in the coreflooding procedures, all the effluent materials, including oil, brine and polymer solution, were collected by using a long slim graduated tube marked in 0.1 mL divisions. Due to the density difference, the oil/aqueous phase can be separated instantly and automatically. The cumulative oil recovery efficiency (E_{COR}) is calculated by using the amount of cumulative oil production divided by the OOIP (Original Oil in Place). The increased oil recovery efficiency (E_{IOR}) is calculated by using the amount of oil produced in the process of polymer flooding divided by the oil left in porous media by the end of the brine flooding.

Table 6-2. Oil recovery efficiency for HPAM/SiO_2 hybrids.

Solution	Viscosity (mPa·s)	OOIP (mL)	Oil recovery by brine (mL)	Final Oil recovery amount (mL)	Increased efficiency E_{IOR} (%)	Final E_{COR} efficiency (%)
Brine (base line)	0.934	11.4	6.4	6.6	4.0	56.2
0.5% HPAM	5.207	11.2	6.5	7.4	19.1	65.8
0.5%HPAM/ 0.2%NPs	6.035	10.9	6.2	7.4	25.5	68.3
0.5%HPAM/ 0.6%NPs	8.726	11.2	6.4	7.8	29.2	69.6

It can be seen that the cumulative oil recovery efficiencies of brine floodings for different cases are quite close to each other (at ~56% at 50 °C), which means that the tertiary flooding started from the similar residual oil saturation. With an overall oil recovery efficiency of 65.8% OOIP by the end of tertiary flooding, 0.5 wt% HPAM can mobilize nearly 20% more trapped oil (increased oil recovery efficiency, which refers to the amount of oil recovered by polymer tertiary flooding, relative to the oil unrecovered when the brine flooding is finished), while the presence of NPs in HPAM further improved the efficiency, depending on the amount of SiO_2 NPs contained (Table 6-2). With the increase of silica nanoparticle concentration, the cumulative oil recovery efficiency was increased from 65.8 to 69.6%, but not significantly. The enhanced oil recovery is regarded as the viscosity increase at 50 °C with presence of SiO_2 nanoparticle.

6.5 Conclusion

This work examined the rheological properties of aqueous HAPM/SiO_2 hybrids under different salinities, temperature and aging time. The hybrid of silica nanoparticles

was found to improve significantly the rheological properties of HPAM especially under high temperature and high salinities. More specifically,

- There was a critical SiO_2 nanoparticle concentration existing for a given amount of HPAM. When NP concentration is higher than this critical value, free silica NPs would bridge among different polymer chains, leading to a sharp increase in the effective viscosity.
- The FT-IR spectra data confirmed that the formation of hydrogen bonds between the carbonyl groups in HPAM and the silanol functionalities on the surface of silica nanoparticles, which attributed to the improved rheological performance.
- The use of nanoparticles significantly improved the thermal stability of HPAM over a 12-day test, i.e. the effective viscosity was ~5 times higher at 0.8 wt% nanoparticle loading.
- The inclusion of silica nanoparticles improved HPAM's salt tolerance, and the viscosity peaked at 1.5 wt% and 2 wt% of salt concentration for HPAM and HPAM/NP hybrids respectively.
- The viscoelastic test verified a high level of cross-linking formed by SiO_2 nanoparticle and, and the hybrids were elastic dominant at temperature up to 85 °C and salinity up to 8 wt% NaCl.
- Enhanced oil recovery experiments at 50 °C show that adding nanoparticles could increase the final accumulate oil recovery efficiency from 65.8% for 0.5 wt% HPAM to 69.6% for 0.5wt% HPAM/0.6wt% SiO_2 hybrids.

Chapter 7

Carbon nanoparticle migration in porous media

7.1 Introduction

In the present study, carbon dots (CDs) at around 5 nm were synthesised by a hydrothermal method using xylose as precursor. The CDs were well-characterized and a good stability at high ionic strength was verified by checking the stability via measuring the UV adsorption and luminescent intensity. Their luminescent property allows them to be detected easily even in several ppb. Their transport and retention properties were also studied in packed bed at different concentration, ionic strength and substrate, and a tracer-like breakthrough ability was found. As this sort of CDs are derived from reliable, non-toxic and low-cost resource and most importantly no need to be separated from crude oil, it makes them attractive as potential novel tracer for oil reservoir characterization.

7.2 Material and experimental methods

7.2.1 Synthesis of CNPs

First, 0.2 g of D-(+)-xylose ($C_5H_{10}O_5$) were dissolved in 20 mL of DI-water; then, the solution was transferred into a Teflon-lined, stainless steel autoclave. After being heated at 200 °C for 6 h and then cooled to room temperature, the obtained solution was centrifuged at 10000 r/min for 30 minutes to get the solid black carbon particles

precipitated. Afterward, the supernatant containing fluorescent CDs was filtered using standard syringe filters Figure 7-1. The obtained solution was then characterized and used for further column transport test.

7.2.2 Characterizations

A transmission electron microscope (TEM, FEI Tecnai TF20) operating at 200 kV was used to characterize the size and morphology of CDs. From the obtained high-resolution TEM images, CD size was measured and analysed using Image-J software. The UV-Vis absorption spectra of CDs were measured by PerkinElmer Lambda LS 35 UV/Vis spectrometer. The fluorescence spectra of CDs were recorded by using the fluorescence spectrometer (LS 55, PerkinElmer) performed with a slit width of 10 nm both for excitation and emission. The excitation wavelength was increased from 300 nm to 460 nm in 20 nm increments. An infrared spectrometer (FTIR spectrometer 100, Perkin-Elmer) was used to measure the FTIR spectra of the freeze-dried CDs, collecting data at a spectral resolution of 4 cm^{-1}. The Raman spectra were recorded using a Raman spectrometer at an excitation wavelength of 633 nm. The zeta potential of CDs in DI-water was analysed via a Zetasizer (Zetasizer Nano ZS, Malvern Instruments Ltd).

As shown in Figure 7-1a, CDs were facilely prepared by one-step hydrothermal carbonization of D-(+)-xylose, one abundant and renewable precursor present in most biomass and agricultural waste materials. The obtained CDs were first measured by UV/Vis spectrometer and fluorescence spectrometer to check whether they absorbed UV-Vis light and whether they were fluorescent (Figure 7-1b). The UV/Vis absorbance spectra demonstrates their strong absorption in the UV region of 200-350 nm, displaying two obvious peaks at 228 nm and 278 nm corresponding to the $\pi-\pi^*$ transitions associated with C=C bonds and $n-\pi^*$ transitions related to hydroxyl groups, respectively [334, 335]. From the fluorescence spectra, the excitation-dependent

emission behaviour of the CDs can be clearly observed, where the emission peaks shifted to higher wavelengths when the excitation wavelengths increased from 300 nm to 460 nm. The maximum emission intensity is obtained with an excitation at 360 nm. It shall be noted that all the emission peaks were centred in the visible region of 450-550 nm.

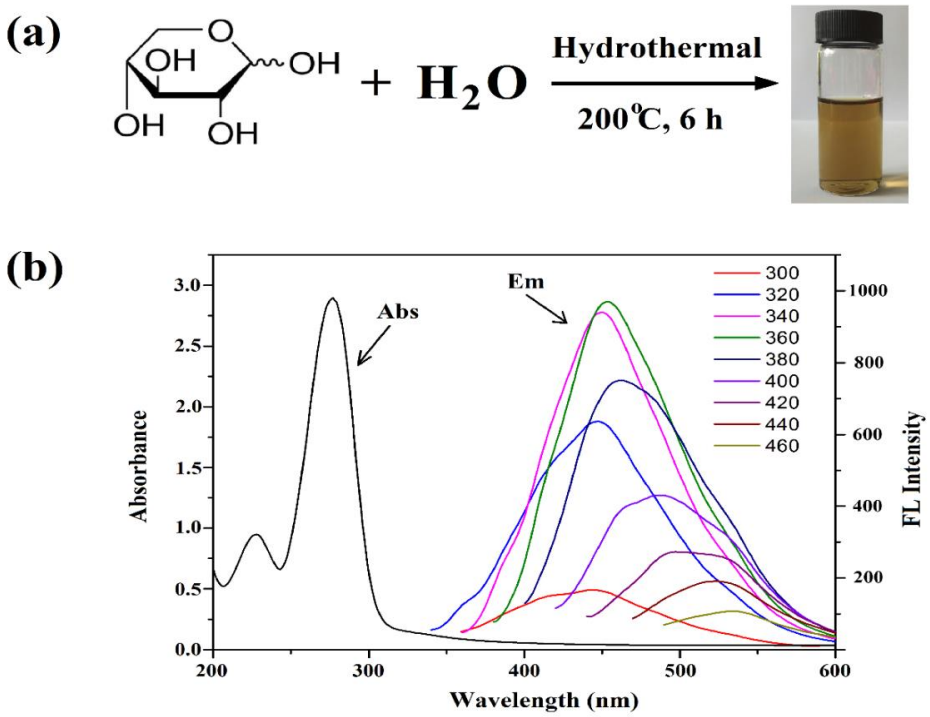

Figure 7-1. (a) Scheme of one-pot synthesis of CDs from xylose; (b) UV-vis absorbance and fluorescence emission spectra of the obtained CDs.

The TEM micrographs of the CDs are given in Figure 2 (a). Some black dots are clearly observed, in which the CDs are well-dispersed, with similar average particle sizes of approximately 5 nm. The high-resolution TEM images show that the CDs exhibits identical lattice fringes with a spacing of 0.24 nm determined using ImageJ software, indicating their graphitic crystalline structure. Raman spectra of the CDs (Figure 7-2C) reveals a D band at 1353 cm^{-1} and a G band at 1585 cm^{-1}. Such result further confirms the graphitic structures of the CDs [336]. Fourier transform infrared (FTIR) spectra in Figure 7-2D reveals that there are abundant hydrophilic groups

including O−H (3600-3100 cm^{-1}, 1191 cm^{-1}) and C−O (1080 cm^{-1}) on the surfaces of CDs, thereby ensuring the good solubility in water. In addition, the O−H vibration band at ~ 3350 cm^{-1} is broad and integrated, which indicates multiple structures of hydroxyl groups on the CD surfaces and consequently resulted in a high polarity and hydrophilicity [336].

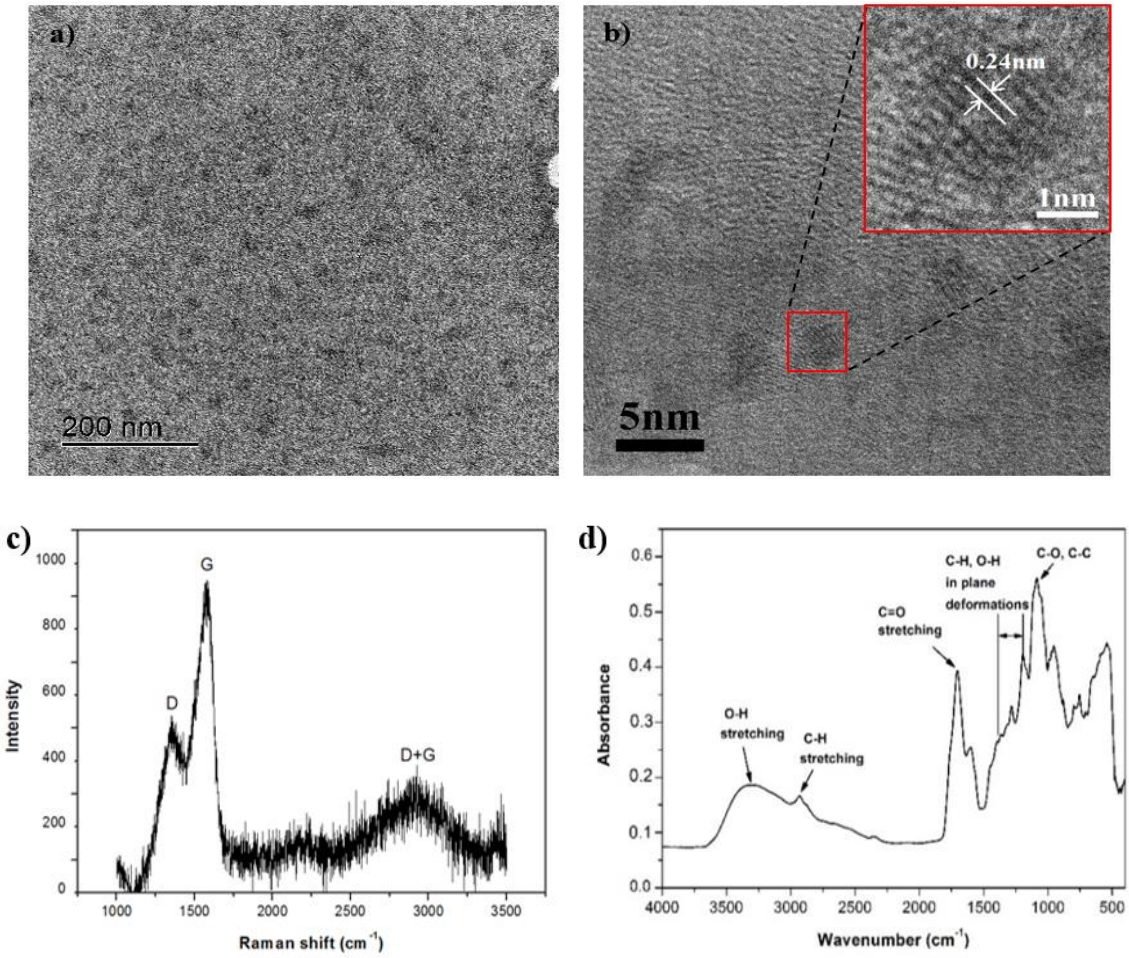

Figure 7-2. (a) TEM images, (b) TEM image with possible Lattice stripes, (c) Raman spectra and (d) FTIR spectra of the CQDs.

7.2.3 Design of simulated porous media

Prior to use, the glass beads (Sigma Aldrich) with 30-40 mesh size fraction (425-600 µm) were thoroughly cleaned using a sequential acid wash, DI water rinse, and oven-drying according to the Ref. [196]. In order to get packed glass columns with constant permeability and porosity, a progression of increasingly rigorous procedures was

utilized. Firstly the dried glass beads was saturated in distilled water, and then deposited into glass column in 1.5 cm increments with 0.5~1 cm thick of water on the top of glass beads. After the formation of a layer of 1.5 cm, vibration was accomplished for 3 minutes using a vortex mixer (Scientific Fisher), with the amplitude represented by 8 on the vibrating table's dial. Thecolumn was kept vertical by hand. The packing length in column was actually 7 cm. To prevent glass beads flowing out of column, the inlet and column end blocker were fitted with a single layer of membrane with the pore size of 10 μm (Millipore limited, UK). The absolute water permeability for glass beads was computed as 97 $\pm$ 10 mD based on Darcy's law. The porosity or volumetric water content was determined by extracting the water-saturated glass beads from packed glass column, and then measuring the amount of water by oven-drying.

7.2.4 Nanoparticle migration study

The cold flooding system, shown in Section 5.3.3, was applied for the core flooding experiments. A total of eight experiments were conducted in pre-saturated packed glass columns to evaluate the transport and retention properties of CDs. Brine containing $CaCl_2$ at different concentration was introduced into the column by piston pump in an up-flow mode at a Darcy velocity of 11.2 m/d, for at least 20 pore volumes (PV). Before injected into column, the pH of this salinity water was adjusted to 7 $\pm$ 0.5 by using low concentration of HCl and NaOH solution. After complete saturation of the column with brine, 3 PV of nanoparticle suspension was introduced into the column with syringe pump at a Darcy velocity of 2.8 m/d, which was followed by the injection of 3 PV of particle-free solution at the same flow rate as post-washing process. This flow rate corresponds to a pore-water velocity of 2.56 m/d, representing a column residence time of 0.25 h. The Reynolds number (Re) was equal to 0.0186, which is several orders-of-magnitude below the limit of laminar flow in packed beds (Re <10).

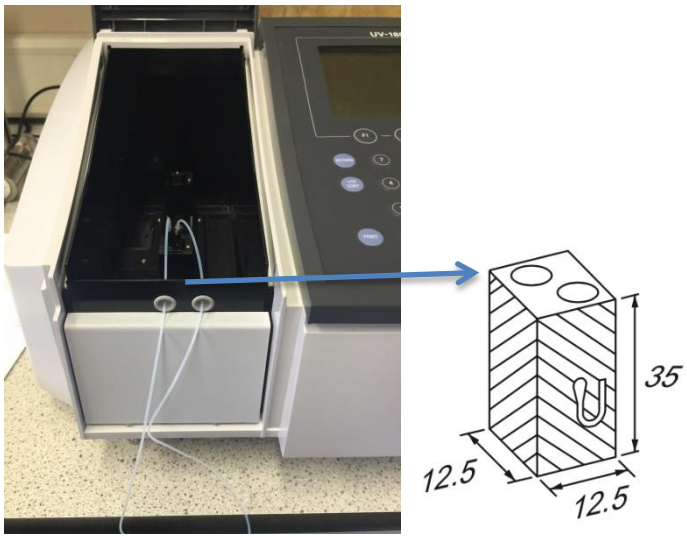

Figure 7-3. Flow cell connection for on-line NPs concentration detection

Table 7-1. Experimental conditions of CDs transport studies conducted in water-saturated glass column packed with either 30-40 mesh glass beads (G) or limestone (L1)

Column	v_p^a (m/d)	V_P^b (mL)	$\emptyset^c$(%)	C_0^d (ppm)	PW^e(PV)	IS^f（mM CaCl2 or API）	MB^f(%)
G1	2.56	12.8±0.18	38.02	10.61	3.0	1	98.75
G2	2.56	12.8±0.18	38.02	24.78	3.0	1	102.5
G3	2.56	12.8±0.18	38.02	8.77	3.0	10	96.85
G4	2.56	12.8±0.18	38.02	9.64	3.0	100	97.5
G5	2.56	12.8±0.18	38.02	8.89	3.0	200	96.06
G6	2.56	12.8±0.18	38.02	12.05	3.0	API	100
L1	2.56	12.8±0.18	38.02	10.36	3.0	API	98.75

[a] Pore water velocity; [b] Pore volume; [c] Porosity; [d] influent concentration; [e] volume of fluids injected; [f] ionic strength; [f] mass balance of nanoparticle

The column outlet was connected with a flow cell inserted into UV-vis spectrophotometer operating at wavelength of 310 nm, by which the effluent particle concentration was monitored real-time (Figure 7-3). After each transport experiment, the column was dissected into seven increments with 1 cm thickness, and the retained NPs were extracted by addition of 10 grams of DI water, followed by ultrasonication for 20 min (Fisher Scientific Ltd.). Experimental conditions for the eight column studies were summarized in Table 7-1.

7.3 Stability and migration ability of carbon dots (CDs)

7.3.1 Stability of CDs in brine

The adsorption stability of CD in API brine was determined using UV-Vis spectrophotometer operating at wavelength of 278 nm, while the luminescent stability was checked by exposing the same sample for a duration of 220 minutes, which was long enough for the injection experiment (Figure 7-4a). The loss of absorbance is less than 4% and the normalized fluorescence intensity only see a slightly reduction to 0.99, which verifying the reliability of using these two methods to quantity the concentration of NPs. A series of samples were diluted by API brine from an original one of 5 ppm, and the absorbance were measured at 278 nm where the absorbance peak appears. The results show that the accuracy is good enough even for diluted sample with concentration as low as 50 ppb (Figure 7-4b)

Table 7-2. Mass balance for injection experiments.

	Influent Conc. (ppm)	Substr-ate	pH	Total NPs injected (mg)	NPs out in NF (mg)	NPs left in column after NF (mg)	Erro-r,%	NPs out in Post-flushing (mg)	NPs left in column after Post-flushing (mg)	Retained percentage after post-flushing, (%)
G1	10.61	GB	6.5	0.4245	0.2562	0.163	1.25	0.141	0.0218	5.2
G2	24.78	GB	6.7	0.992	0.6387	0.3781	-2.5	0.3525	0.0256	2.6
G3	8.77	GB	6.5	0.3507	0.2014	0.1383	3.15	0.1257	0.0126	3.6
G4	9.64	GB	6.9	0.3855	0.2304	0.1454	2.5	0.1452	0.00026	0.1
G5	8.89	GB	7.2	0.3557	0.2030	0.1387	3.94	0.1257	0.0131	3.7
G6	12.05	GB	7.4	0.3915	0.2223	0.1692	0	0.1672	0.00197	0.5
L1	10.36	Calcium	6.8	0.4144	0.1248	0.2844	1.25	0.1278	0.1566	

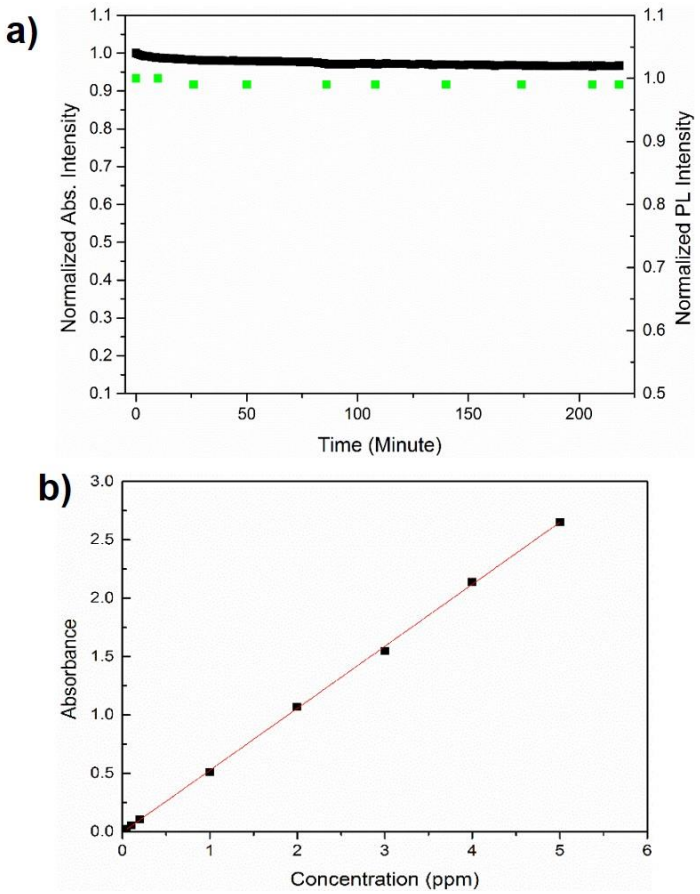

Figure 7-4. (a) Absorbance and fluorescent intensity for CD dispersed in API brine; (b) Absorbance for CD at different concentration from 5 ppm to 50 ppb.

7.3.2 The influence of concentration

Two effluent breakthrough curves (BTCs) for CDs transport through water-saturated columns packed with glass beads are shown in Figure 7-5. More than 2-fold increase (from 10.61 to 24.68 ppm) in the concentration of CDs suspensions containing 1.0 mM $CaCl_2$ as a background electrolyte were injected to the glass beads porous matrixes. For both concentrations, the yielded BTCs was almost symmetrical and sharply increased to maximum value in injection process and experienced a sharp decline to relative concentration (C/C_0) approaching zero during post-washing process, which is obviously different with the break-through performance of presently reported NPs [196, 294]. Regardless of the big difference on concentrations, both of low and high concentration achieved nearly 100% after 1.6 PV injection. Extraction of the retained CDs from glass

column show that there is 1 PV of particle-containing solution left in the pore space after CDs injection. Upon the reintroduction of CDs-free water as post-washing process

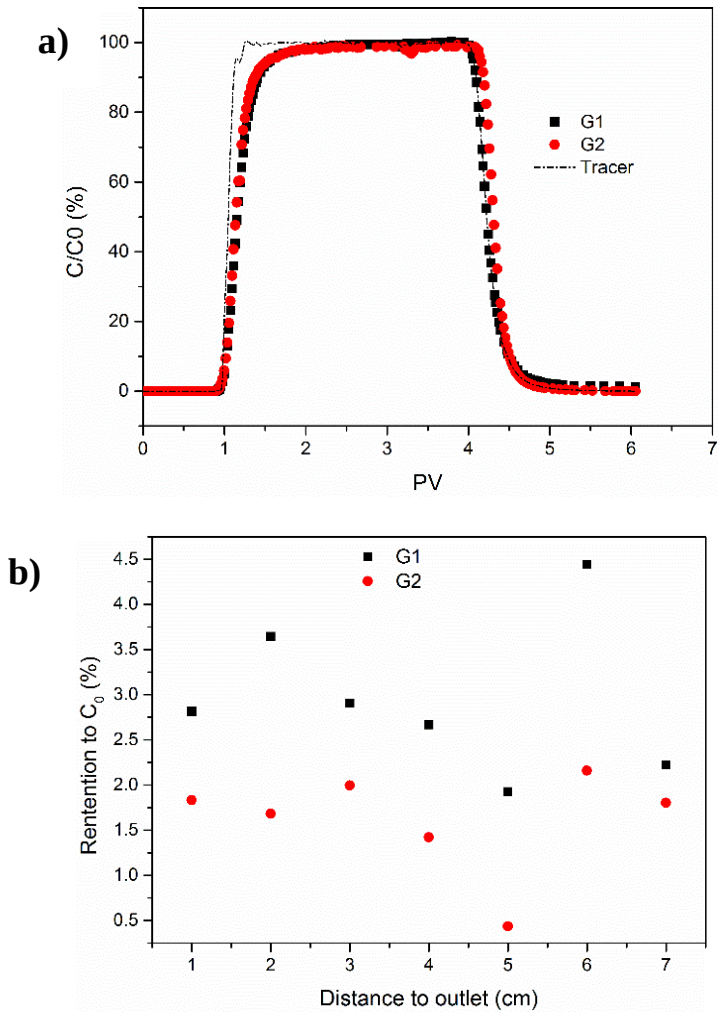

Figure 7-5. Measured (a) breakthrough curves, and (b) retention profiles for xylose-CDs at two distinct concentrations.

from 3 PV, the effluent relative concentration appeared as 100% from 3 to 4 PV. The sharp reduction in relative concentration observed in the distal portion of the BTCs indicates that retained CDs were not released from the surface of glass beads or the CDs was irreversibly retained in the column. Mass balance in Table 7-2 shows that for concentration both at 10.61 ppm and 24.68 ppm there are only 5.2% and 2.6% of particle relative to total injection, irreversibly retained in column, respectively. Higher

concentration has a lower relative retention ratio, which was consistent with the findings in Ref.[294] for SiO_2 NPs.

7.3.3 The influence of ionic strength

In the next phase of research, the transport and deposition properties of CDs have been studied with an electrolyte background ranging from 1 mM to 200 mM $CaCl_2$, and then increased to API standard brine containing 1.6 M NaCl and 0.2 M $CaCl_2$ [104]. The concentration of CDs was fixed at around 10.05±1.23 ppm. For all of the ionic strength, CDs appeared in the column effluent after injecting 1 PV of suspension, followed by sharp approaching to the plateau concentration at ca. 1.5 PV. From Figure 7-6, it can be also seen that increasing the ionic strength does not yield a discernible change in the shape of BTCs as well as the maximum breakthrough ability. The CDs always show a near-tracer breakthrough behaviour regardless of the ionic strength. The retention mass of CDs at different ionic strength in Figure 7-6b show that, after post-flushed with particle-free salinity water, only 0.1% to 5.2% of CDs is retained in glass column relative to the total mass of injection. A short tailing effect in Figure 7-6a also show that the CDs have a slight adhesive effects on the surface of glass beads and little particle was released from the solid surface via post-flushing. More importantly, the retention mass seems unrelated to ionic strength, which is controversy to most of previous studies [153, 243, 337, 338].

Most current theoretical description of NP retention and transport is limited to classical clean bed filtration theory (CFT), supplemented by Derjaguin-Landau-Verwey-Overbeek (DLVO) theory. For instance, Li et al. found that the effective collision efficiency was more than 1 order of magnitude larger than the value predicted by the DLVO theory. Conventional DLVO theory uses approximate expressions, i.e., Derjaguin approximation [339], to represent electric double layer interaction. The

assumptions under which the approximations hold [340], i.e., $h \ll \gamma_N$ (i.e., separation distance is much less than NPs' radius) and $\kappa h \gg 1$ (i.e., separation distance is much larger than the Debye length), however, may not be applicable to small NPs. Because NPs, especially those with sizes < ~30 nm, may have unique properties (e.g., large specific surface area, exponentially increased surface atoms, and high interfacial reactivity) [341] or are smaller than the thickness of electrical double layer [342]. The applicability of the DLVO theory for describing their agglomeration, retention, and transport behavior of small particles should be re-visited [343].

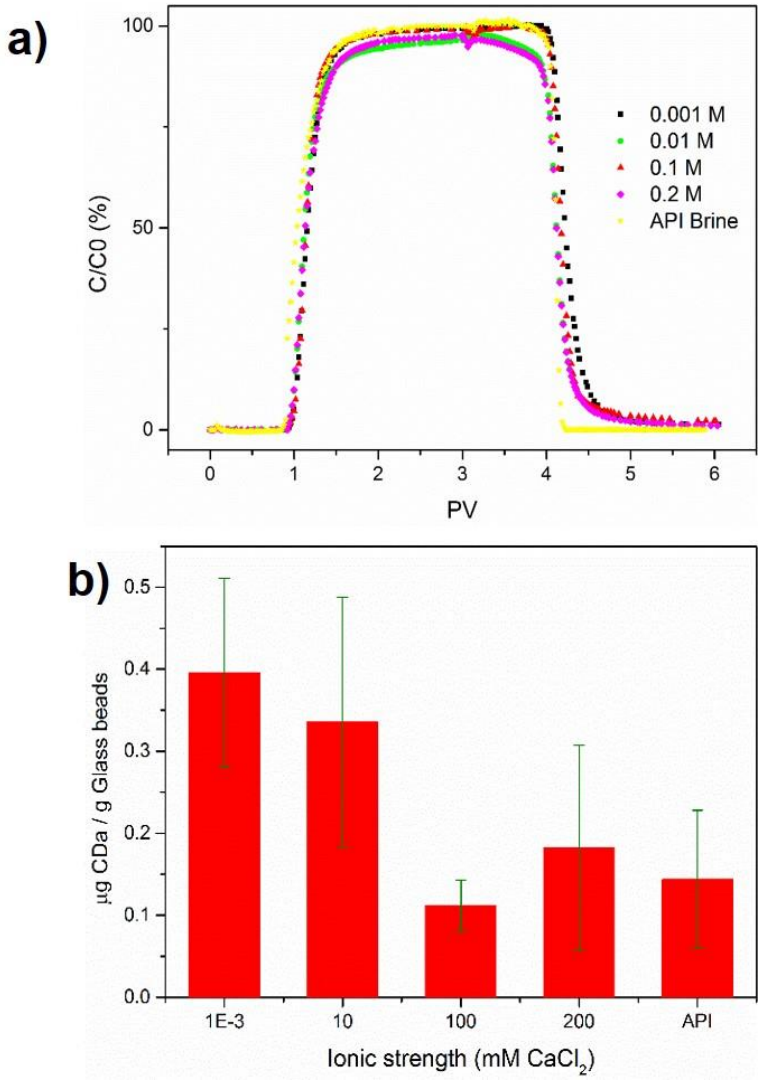

Figure 7-6. (a) Breakthrough of CDs synthesised from xylose in glass beads-packed column at room temperature with ionic strength ranging from 1 mM $CaCl_2$ to the standard of API brine, (b) Retention mass of CDs after post-flushing with brine.

The confocal laser scanning microscopy (CLSM) pictures of extracted glass beads from the packed column directly show a situation that CDs homogeneously distribute as a particle cloud in the aqueous phase, instead of sticking on the surface of glass beads (Figure 7-8 group A). While after washing with distilled water, no luminescent particle is observed and the picture of glass beads becomes dark under confocal microscopy.

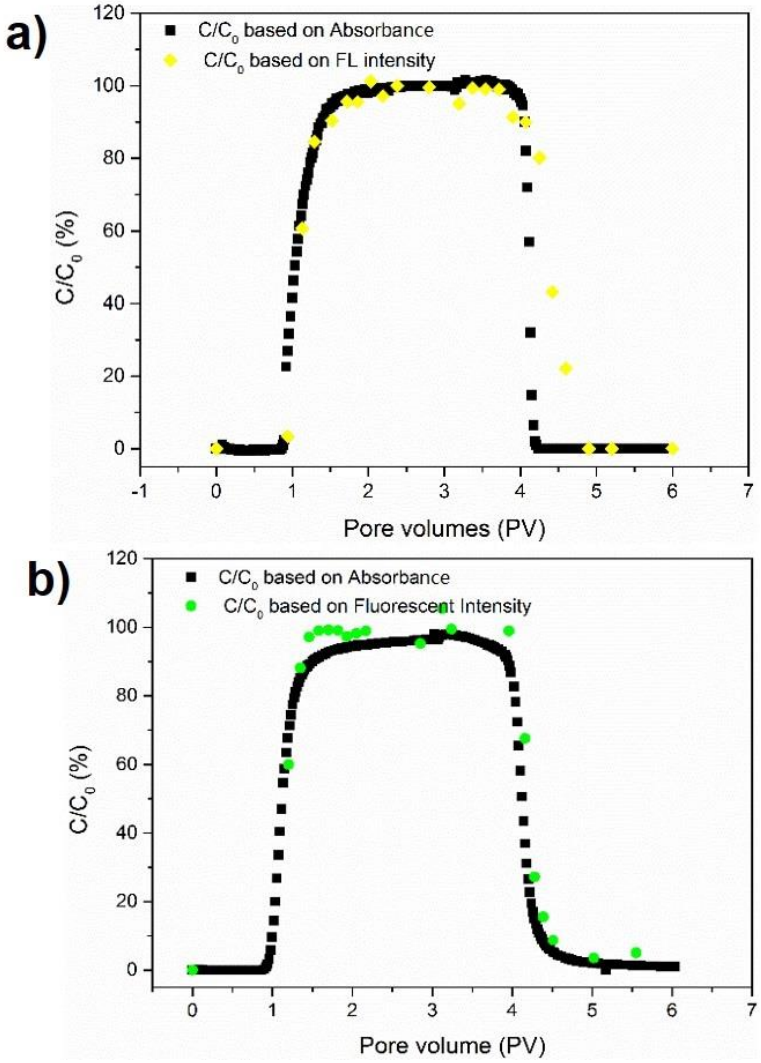

Figure 7-7. Breakthrough curves generated from the concentration on-line measured by UV-Vis spectrophotometer, and off-line measured by fluorescence meter. (a) for G6 in API brine, (b) for G3 in 0.01 M $CaCl_2$.

Eleven effluent samples were collected for both injection and post-injection processes, in two groups of transport experiments selected for the luminescent test, namely the experiments at ionic strength of 10 mM $CaCl_2$ and API brine. The

fluorescence intensity was measured under excitation of 360 nm UV light, and fluorescent intensity for each sample was defined as an average value from 442 nm to 452 nm. As can be seen from Figure 7-7, the off-line BTCs acquired based on the luminescent intensity is perfectly consistent with the BTCs acquired from on-line UV determination. The luminescent BTCs even delineate the tailing effect in Figure 7-7a at ionic strength of API brine, which was detected by UV spectrometer. It is also should be mentioned that the measurement of fluorescence was usually done after 2 weeks of storage, but the intensity is still retain strong enough to clarify the low concentration, regardless that the CDs were soaking in high salinity water.

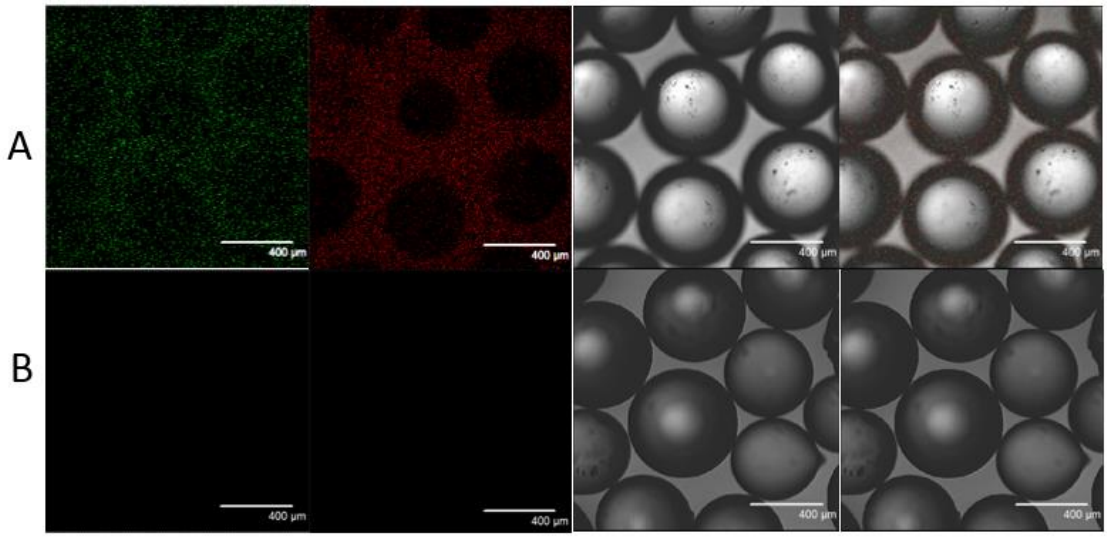

Figure 7-8. CLSM images of Glass Beads incubation together with CDs after washing four times with distilled water, group (A) original glass beads extracted from column; (B) glass beads washed.

7.3.4 The influence of substrate

For a limestone column, the substrate yields a discernible change in the shape of CDs BTCs (Figure 7-9), compared to the BTCs in glass beads column (G6). Even the particle breakthrough also occurs at ca. 1 PV, a 3 PV pulse of CDs is just approaching a maximum relative effluent concentration of 64.4%, with a tendency to rise if continuing with injection. The larger applied volume of CDs (3 PV vs 1.5 PV) required to reach a

plateau effluent concentration indicates that calcium carbonate possesses a greater capacity to retain CDs relative to glass beads. Mass balance calculation in Table 7-2 shows that 37.8% of CDs is retained in calcium carbonate column after the injection of particle-free solution. The long tailing effect also shows that particle is reversely adhered on the surface of calcite rock grains.

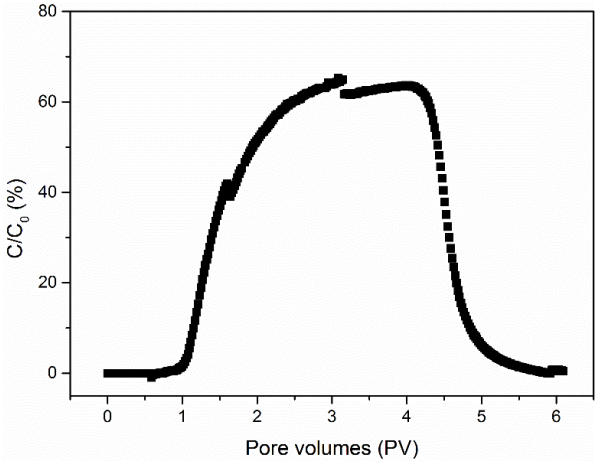

Figure 7-9. Breakthrough of xylose-CDs in calcite-packed column at room temperature.

After transport experiments, pieces of limestone were extracted from the column and washed with distilled water 4 times. A significant difference in colour of the calcium carbonate rocks is clearly observed from the optical images in Figure 7-10. Before incubation with CDs, the rocks are off-white but become into black brown colour after soaking in aqueous CDs solution even washed with DI-water four times, which indicates that blown CDs are firmly attached on the surfaces of the rocks. The colour of grinded powders is in good accordance with that of rock grains. In order to further confirm the successfully adhesion of the CDs, CLSM was used to characterize the rock pieces after washing. Bright fluorescent images of CDs irradiated by laser of 488 nm and 561 nm were obtained in Figure 7-10. The overlay image reveals these CDs were located on the surface of the rock. Such phenomenon is induced by the electrical forces between the negatively charged CDs and positively charged rocks.

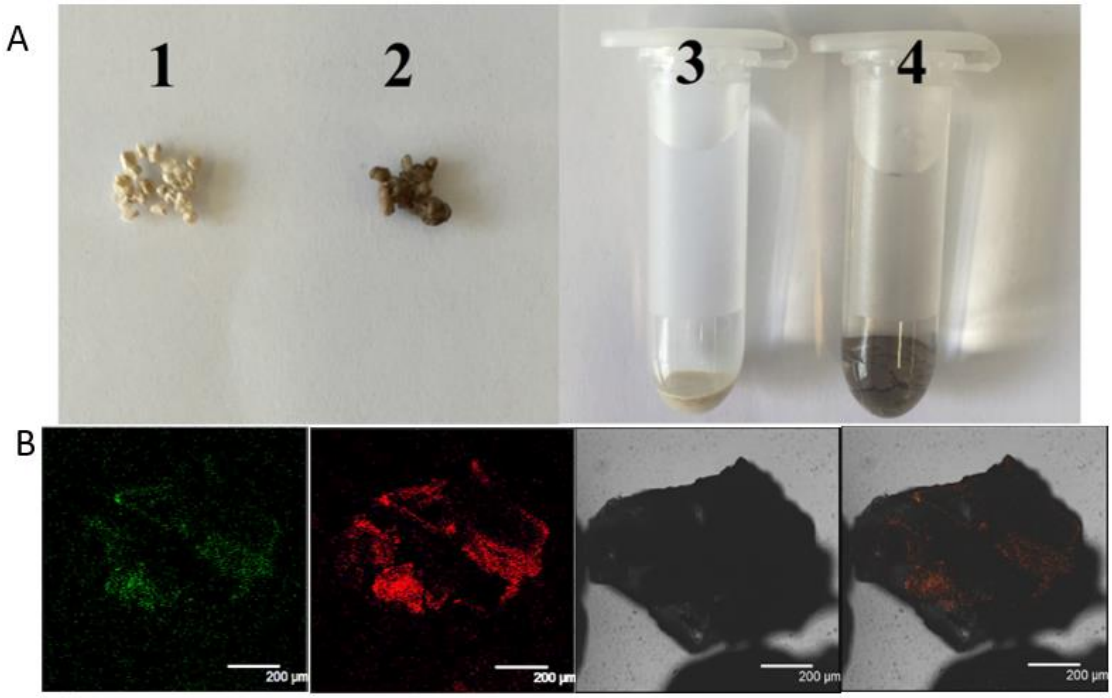

Figure 7-10. (a) Optical photos of calcite rock pieces (1) original, and (2) after incubation together with xylose-CDs. (3, 4) crushed grain of the rock pieces. (b) CLSM images of calcite rock pieces incubation together with xylose-CDs after washing with distilled water

7.4 Oil saturation detection in sandstone cores

Based on the testing data above, the CDs were regarded as good candidates for hydrocarbon detection due to their thermal stability, efficient mobility in subsurface environment and luminescent property. Thus CDs were used as agent to detect the oil saturation in sandstone core.

7.4.1 Experiment procedure

The key points of this experiment were how to obtain the core sample with different oil saturation. As it is well known, it is difficult to further reduce the residual oil saturation (s_{or}) after brine breakthrough in the secondary water flooding process. This suggest that by injecting well-calculated amount of oil at higher flow rate, the oil

saturation can be controlled under the value of residual oil saturation (S_{or}) at the brine breakthrough point in brine flooding. The flow rate of nanofluid injection should be lower than injecting oil, in case the oil would be displaced out and the oil saturation is changed during the process of CDs dispersion injection. The experiment procedures are conducted as below, and the experiment conditions are listed in Table 7-3:

- Saturated the core with brine (0.1 M NaCl)
- Injected pre-determined volume of oil into core;
- Flooded the core with brine at a higher flow rate of 1 mL/min for 2 PV to simulate the secondary flooding procedure, and collected oil recovered during this process.
- Injected CD dispersion into the core at a lower flow rate of 0.5 mL/h, and collect the effluent sample every 3 min.

Table 7-3. Experiment condition by injecting CQDs into the sandstone core.

Core No.	Oil injected, mL	Oil collected, mL	OOIP, mL	OOIP relative to pore volume, %	Particle concentration, ppm	Flow rate
SZ2	0	0	0	0	20	1
ET2	2.3	0	2.3	17.2	20	0.89
SZ8	5	0	5	37.3	20	0.78
SZ4	7.8	1.8	6	44.6	20	0.67

7.4.2 Experiment results

Figure 7-11 shows the breakthrough curves influenced by different oil saturation degrees. As the oil saturation increases, the BTC is shifting towards left, and breakthrough time is bring forward from ~ 1PV at 0% oil saturation to 0.67 PV at 44.6% (relative to pore volume),. However, the maximum breakthrough abilities show little difference and can approach above 95% after 3 PV. Figure 7-12 provides the fitting

relationship between the oil saturation and the breakthrough time, which would be used for predict the amount of oil content according to the breakthrough time.

Similar to the analysis in Section 3.5.5, the transport of CDs is confined in the aqueous phase, because it is a kind of water-wet particle. The early breakthrough for the transport of CDs would occur in the presence of oil (as shown in Figure 3-27) because the NPs are confined to be transported in the water phase that initially occupies only a fraction of the pore volume, resulting in an early break through. By contrast, in the absence of an oil phase the nanofluids have the entire pore volume to travel through during the entire injection process. The breakthrough is consequently delayed until about 1 PV or slightly less than 1 PV, assuming the displacing fluid is moving in a piston front. It can be derived that a different oil saturation would correspond to a different break through time.

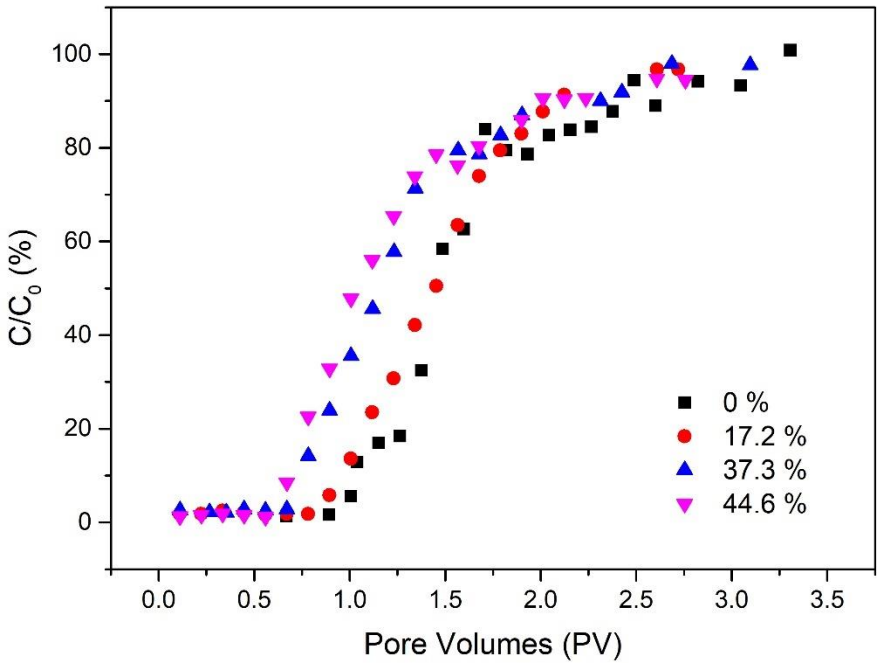

Figure 7-11. Breakthrough curve changing with injection time, when injecting CD suspension at 0.5 mL/min into sandstone core.

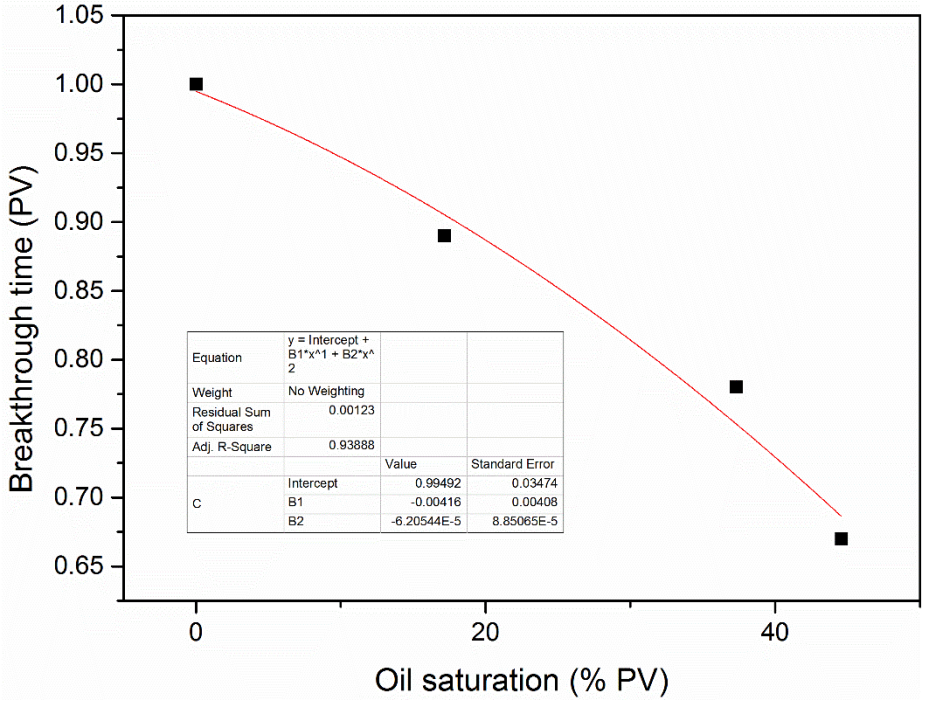

Figure 7-12. the CD breakthrough time (during injection) changing as a function of oil saturation (percentage relative to pore volume)

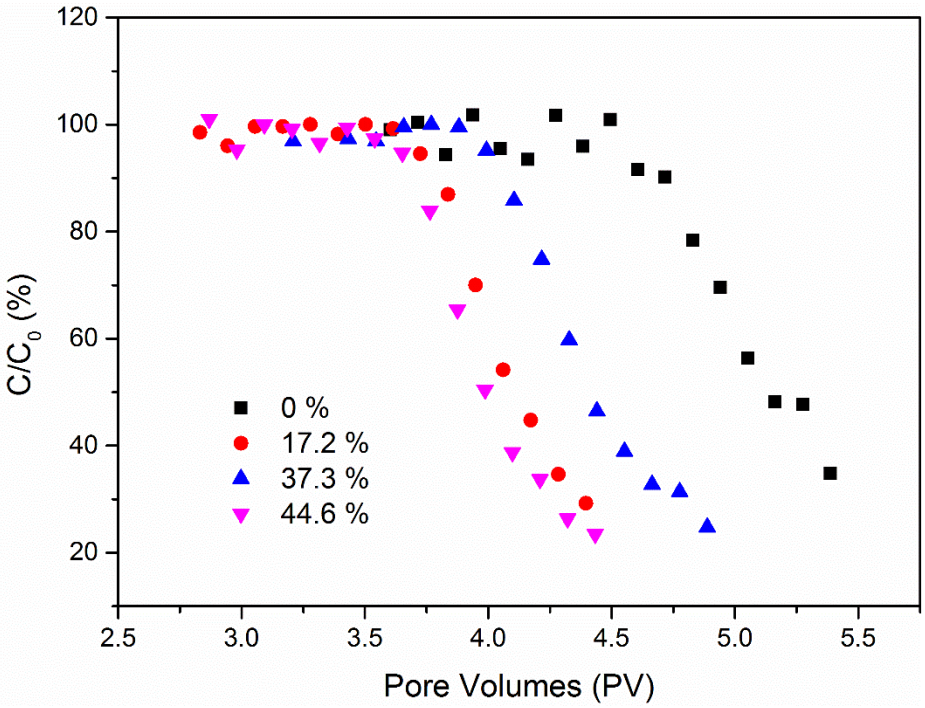

Figure 7-13. Breakthrough curve changing with injection time, when injecting particle-free brine at 0.5 mL/min as post-flooding process (the process is following injection process and started from 3 PV, thus the x-axis starts from 2.5 instead of zero).

Post-flushing with brine in Figure 7-13 shows that, a longer time is needed to flush out the CD retained in the core. When the oil saturation is at 0%, the concentration starts to decrease from 1 PV during the post-flooding process, while increasing the oil saturation to 44.6%, the starting time of lowering particle concentration is brought forward to 0.89, 0.78 and 0.67 PV. Those time points are coincide with the injection process.

7.5 Conclusion

Extracting practically-unsalable information for the subsurface hydrocarbon reservoir seems cannot be sufficiently met by currently intrusion or detection methods. Even currently applied tracers are not good enough to address this challenge. Derived from a low-cost precursor, carbon dots (CDs) may provide a promising solution to locate and map the petroleum reservoir, due to their excellent migration ability in porous media, easy-detected luminescent property, and reservoir-friendly existence. Our results reveal that:

- Xylose-CDs showed a good stability in high ionic strength, in terms of size, long-time absorption and fluorescent intensity, due to multi high-polarity functional group on their surface.
- According to the breakthrough curves, xylose-CDs showed a tracer-like transport properties in packed glass beads regardless of concentration and ionic strength. The retention files showed that less than 5.6% of particle was stuck in the glass beads column.
- The CLSM pictures showed remarkable difference for particle attachment on the surface of glass beads and calcite rock.

- There is a good consistence between the UV-Vis (On-line) and CLSM (off-line) on generating break-through curves, which means the CD concentration can be more easily detected by UV-Vis.
- CD can be used to detect the oil saturation in sandstone reservoir, because its breakthrough time changes with the oil saturation. Moreover, a relationship between the breakthrough time and OOIP has been found, for a particular case at the core scale.

Chapter 8

Conclusion and future work

8.1 Conclusions

The aim of this thesis was to explore how emerging nanotechnology can be used to address the challenges that conventional EOR are facing. Through a series of experiments, it has been tested that the NPs can be used to assist the traditional chemical flooding via several ways: i) NP can be used as additive in formation brine to improve the efficiency of secondary flooding; ii) nanoparticle can behavier like surfactant/polymer carriers to reduce their retention in porous media, and potentially for targeted delivery of chemicals; iii) NP can be *in-situ* formulated and absorbed at the oil/water interface in a microemuslion system, leading to more stable emulsion texture and higher oil recovery efficiency as increasing NPs concentration; iv) nanoparticle can be used as cross linker, to reinforce the thermal stability, salt tolerance and viscoelastic properties of HPAM commonly used for chemical flooding; v) special designed nanoparticle, like CQDs, can be used as oil reservoir sensor to obtain information where traditional characterization methods are not effective.

The main conclusions drawn via the experimental investigations are summarized as below:

1) Nanoparticle-assisted water flooding

- Stabilized by Tri-sodium citrate dehydrate (SCD), TiO_2 NPs was found to have non-

negligible influences on the effective properties of brine when used in relatively low concentration;

- At breakthrough point, addition NPs mobilizes more oil than plain synthetic brine which achieved only 30.3% of OOIP. Small NPs concentrations provided higher enhancement of oil production, with a 20 ppm concentration providing an enhancement of 39.8% of OOIP compared to a value of 31.8% for 500 ppm. However, when considering the total cumulative recovery, the best performance is achieved by 10 ppm nanofluid, with a total oil recovery of 43.75% of OOIP, representing a 44.39% increase on the plain water-flooding scenario.
- When considering the post-breakthrough oil production, the better performance was achieved by larger concentrations of nanoparticles, which was partially attributed to a log-jamming effect.
- The wettability study shows that the water-wet Berea sandstone used in this work became progressively more water-wet by saturation with fluids with increasing concentrations of nanoparticles. The possible mechanisms for the enhanced oil recovery due to nanoparticles suggested that while the exact causes are unknown at present, the EOR effect in our experiments occurs through a combination of mobility ratio modification, rock wettability modification and log-jamming effect.

2) nanoparticle as surfactant carrier

- Blend of 25% XOF-25S as an anionic alkylaryl sulfonates and 75% nonionic alcohol ethoxylated (C12-13/7EO) surfactant at 4% salinity was found as an stable composition with the lowest IFT. The stability and low IFT of surfactant solution is because of the synergic effect of surfactant mixture at presence NaCl salt.

- Adsorption of surfactant blend in the presence of TiO2 nanoparticles was proportional with retention of nanoparticles inside column. Therefore to reduce the surfactant retention in porous media, the nanoparticles should have a good mobility .
- The adsorption of surfactant blend can be increased at rock surface containing higher amount of silica and alumina. The hydrogen bonding between the oxygen in the ethoxy groups and the hydroxyl groups of silica is suggested as a plausible mechanism for the adsorption of surfactant.

3) nanoparticle-assisted microemulsion flooding

- IONPs was in-situ fabricated in the o/w microemulsion at optimum salinity;
- Coagulating with NPs enable the surfactant to be more persistently absorbed at the o/w interface, leading to reduced variation of IFT and increased emulsion viscosity.
- Reduced differential pressures in EOR experiments indicate that joint arrangement of nanoparticle and surfactant at o/w interface results in a stronger and more stable emulsion system, which can reduce the possible blocking induced by surface adsorption.
- The EOR efficiency was improved as increasing the the concentration of IO NP from 0 to 6400 ppm.

4) nanoparticle-assisted polymer flooding

- The hybrid of silica nanoparticles improved significantly the rheological properties of HPAM especially under thermal treatment and high salinities.
- The formation of hydrogen bonds between the carbonyl groups in HPAM and the silanol functionalities on the surface of silica nanoparticles attributed to the improved performance of polymer.

- Viscoelastic test verified the high cross-link formed by incorporating SiO_2 nanoparticle and, the hybrids are elastic dominant under 85 °C and high salinity of 8 wt% NaCl.
- Flooding experiments at 50 ^oC in porous media packed with crushed sandstone show that the EOR efficiency was improve from 56.2% for brine flooding to 69.6% for 0.5% HPAM / 0.6%NPs hybrids.

5) nanoparticle migration in porous media

- The concentration of TiO2 NPs trapped in the core after flooding increased with the increase of particle concentrations. Some of these nanoparticles could be removed from the core by subsequent flooding with plain synthetic brine, while some crossed into the oil phase, lowering its viscosity marginally.
- The migration of TiO2 and CQDs was heavily influence by the presence of oil phase. When particle is water wet, earlier breakthrough usually corresponds to higher oil saturation.

6) Nanoparticle for reservoir characterization

- CQD can be used to detect the oil saturation in sandstone reservoir, because its breakthrough time changes with the oil saturation. A method to detect OOIP in saturated sandstone core is demonstration in chapter 7.

8.2 Future work

There is great potential to extend the current study and build upon the knowledge within this area. Such points are discussed below.

- Develop more advanced flooding system, which can generate high pressure and high temperature in the pore space;

- More focused experiments on nanoparticle as surfactant carrier in reservoir rock, starting from sandstone. Investigate how to further reduce the surfactant retention by nanoparticle; Further clarify the relationship among subsurface properties, surfactant absorption, and particle migration behaviour.
- Encapsulate the surfactant/polymer in nano-capsule, emulsion or porous particle, Controlled release when being delivered to interested area, contacting with oil phase or stimulated by external stimuli.
- In-situ synthesis the emulsion stabilized by nanoparticle in porous media for EOR purpose.
- Try different nanoparticle to hybrids with polymer.
- Producing the nanoparticle/polymer hybrids in one step and check their viscoelastic properties.
- Particle migration behaviour with the influence of oil phase, the presence of surfactant/polymer, and modify clean bed filtration theory to fit with experiment results.
- Explore novel ways to apply quantum dots as reservoir sensor.

List of References

1. Administration, U.S.E.I., *International Energy Outlook 2017.* 2017. https://www.eia.gov/outlooks/ieo/.
2. Muggeridge, A., et al., *Recovery rates, enhanced oil recovery and technological limits.* Philos Trans A Math Phys Eng Sci, 2012. **A372**: p. 20120320.
3. *Schlumberger Ltd., Oilfield Glossary- Oil recovery, http://www.glossary.oilfield.slb.com/Terms/p/primary_recovery.aspx, access on 09 November 2017.*
4. Ahmed, T., *Reservoir Engineering Handbook (4th Edition)*. 2010, Oxford, UK: Elsevier.
5. *PetroWiki, Waterflooding, http://petrowiki.org/Waterflooding, access on 09 November 2017.*
6. Zhao, D.W., J. Wang, and I.D. Gates, *Thermal recovery strategies for thin heavy oil reservoirs.* Fuel, 2014. **117**: p. 431-441.
7. *Petro Industry News, What is the Difference between Primary, Secondary & Enhanced Recovery for Oil Extraction?. https://www.petro-online.com/news/fuel-for-thought/13/breaking-news/what-is-the-difference-between-primary-secondary-amp-enhanced-recovery-for-oil-extraction/31405, access on 09 November 2017.*
8. Olajire, A.A., *Review of ASP EOR (alkaline surfactant polymer enhanced oil recovery) technology in the petroleum industry: Prospects and challenges.* Energy, 2014. **77**: p. 963-982.
9. Gurgel, A., et al., *A review on chemical flooding methods applied in enhanced oil recovery.* Brazilian Journal of Petroleum and Gas, 2008. **2**: p. 83-95.
10. Talebian, S.H., et al., *Foam assisted CO2-EOR: A review of concept, challenges, and future prospects.* Journal of Petroleum Science and Engineering, 2014. **120**: p. 202-215.
11. NETL, *Carbon dioxide enhanced oil recovery: untapped domestic energy supply and long term carbon storage solution, https://www.netl.doe.gov/file%20library/research/oil-gas/CO2_EOR_Primer.pdf, access on 8 January 2018.*
12. *U.S. Department of Energy, Enhanced Oil Recovery, https://energy.gov/fe/science-innovation/oil-gas-research/enhanced-oil-recovery, access on 30 October 2018.*
13. Guo, K., H. Li, and Z. Yu, *In-situ heavy and extra-heavy oil recovery: A review.* Fuel, 2016. **185**: p. 886-902.
14. *Swift Technical Solutions LLc., Thermal Injection, http://www.swiftts.com/Thermal_Injuction.html, access on 12 November 2018.*
15. Schramm, L.L., *Surfactants: Fundamentals and Applications in the Petroleum Industry*. 2010: Cambridge University Press.
16. Jeirani, Z., et al., *Pre-prepared Microemulsion Flooding in Enhanced Oil Recovery: A Review.* Petroleum Science and Technology, 2014. **32**(2): p. 180-193.
17. Guo, J., et al., *Synthesis of temperature-resistant and salt-tolerant surfactant SDB-7 and its performance evaluation for Tahe Oilfield flooding (China).* Petroleum Science, 2014. **11**(4): p. 584-589.

18. CURBELO, F.D.S., et al., *Oil recovery by ionic surfactant and sweep efficiency study in sandstones.* Brazilian Journal of Petroleum and Gas, 2008. **2**(1): p. 9-16.
19. Zargartalebi, M., R. Kharrat, and N. Barati, *Enhancement of surfactant flooding performance by the use of silica nanoparticles.* Fuel, 2015. **143**: p. 21-27.
20. ShamsiJazeyi, H., R. Verduzco, and G.J. Hirasaki, *Reducing adsorption of anionic surfactant for enhanced oil recovery: Part I. Competitive adsorption mechanism.* Colloids and Surfaces A: Physicochemical and Engineering Aspects, 2014. **453**: p. 162-167.
21. Raffa, P., A.A. Broekhuis, and F. Picchioni, *Polymeric surfactants for enhanced oil recovery: A review.* Journal of Petroleum Science and Engineering, 2016. **145**: p. 723-733.
22. Bera, A., et al., *Adsorption of surfactants on sand surface in enhanced oil recovery: Isotherms, kinetics and thermodynamic studies.* Applied Surface Science, 2013. **284**: p. 87-99.
23. Hosseinzade Khanamiri, H., et al., *EOR by Low Salinity Water and Surfactant at Low Concentration: Impact of Injection and in Situ Brine Composition.* Energy & Fuels, 2016. **30**(4): p. 2705-2713.
24. Spildo, K., et al., *A strategy for low cost, effective surfactant injection.* Journal of Petroleum Science and Engineering, 2014. **117**: p. 8-14.
25. Bakhitov, G.G., V.G. Ogandzhanyants, and A.M. Polishchuk, *Experimental investigation into the influence of polymer additives in water on the relative permeabilities of porous media.* Fluid Dynamics, 1981. **15**(4): p. 611-615.
26. Nilsson, S., A. Stavland, and H.C. Jonsbraten, *Mechanistic Study of Disproportionate Permeability Reduction*, in *SPE/DOE Improved Oil Recovery Symposium*. 1998, Society of Petroleum Engineers: Tulsa, Oklahoma.
27. Liang, J.-T. and R.S. Seright, *Further Investigations of Why Gels Reduce Water Permeability More Than Oil Permeability.* SPE Production & Facilities, 2013. **12**(04): p. 225-230.
28. Mennella, A., et al., *Pore-scale Mechanism for Selective Permeability Reduction by Polymer Injection*, in *SPE/DOE Improved Oil Recovery Symposium*. 1998, Society of Petroleum Engineers: Tulsa, Oklahoma.
29. Wei, B., L. Romero-Zerón, and D. Rodrigue, *Oil displacement mechanisms of viscoelastic polymers in enhanced oil recovery (EOR): a review.* Journal of Petroleum Exploration and Production Technology, 2013. **4**(2): p. 113-121.
30. Ramakrishnan, T.S. and D.T. Wasan, *A Model for Interfacial Activity of Acidic Crude Oil/Caustic Systems for Alkaline Flooding.* Society of Petroleum Engineers Journal, 2013. **23**(04): p. 602-612.
31. deZabala, E.F., et al., *A Chemical Theory for Linear Alkaline Flooding.* Society of Petroleum Engineers Journal, 2013. **22**(02): p. 245-258.
32. Wang, B., et al., *The effects of oil displacement agents on the stability of water produced from ASP (alkaline/surfactant/polymer) flooding.* Colloids and Surfaces A: Physicochemical and Engineering Aspects, 2011. **379**(1-3): p. 121-126.
33. Wang, Y., F. Zhao, and B. Bai, *Optimized Surfactant IFT and Polymer Viscosity for Surfactant-Polymer Flooding in Heterogeneous Formations*,

in *SPE Improved Oil Recovery Symposium*. 2010, Society of Petroleum Engineers: Tulsa, Oklahoma, USA.
34. Wang, J., et al., *Understanding of the Fluid Flow Mechanism in Porous Media of EOR by ASP Flooding from Physical Modeling*, in *International Petroleum Technology Conference*. 2007, International Petroleum Technology Conference: Dubai, U.A.E.
35. Hirasaki, G., C.A. Miller, and M. Puerto, *Recent Advances in Surfactant EOR.* SPE Journal, 2011. **16**(04): p. 889-907.
36. Liu, S., et al., *Alkaline/Surfactant/Polymer Processes: Wide Range of Conditions for Good Recovery.* SPE Journal, 2010. **15**(02): p. 282-293.
37. Al-Sahhaf, T., A. Suttar Ahmed, and A. Elkamel, *Producing Ultralow Interfacial Tension at the Oil/Water Interface.* Petroleum Science and Technology, 2002. **20**(7-8): p. 773-788.
38. Gao, S., H. Li, and H. Li, *Laboratory Investigation Of Combination Of Alkaline-Surfactant-Polymer For Daqing EOR.* SPE Reservoir Engineering, 1995. **10**(03): p. 194-197.
39. Martin, F.D., J.C. Oxley, and H. Lim, *Enhanced Recovery of a "J" Sand Crude Oil With a Combination of Surfactant and Alkaline Chemicals*, in *SPE Annual Technical Conference and Exhibition*. 1985, Society of Petroleum Engineers: Las Vegas, Nevada.
40. Zerkalov, G., *Polymer Flooding for Enhanced Oil Recovery,* http://large.stanford.edu/courses/2015/ph240/zerkalov1/. 2015.
41. Ligthelm, D.J., et al., *Novel Waterflooding Strategy By Manipulation Of Injection Brine Composition*, in *EUROPEC/EAGE Conference and Exhibition*. 2013, Society of Petroleum Engineers: Amsterdam, The Netherlands.
42. Gupta, R., et al., *Enhanced Waterflood for Carbonate Reservoirs - Impact of Injection Water Composition*, in *SPE Middle East Oil and Gas Show and Conference*. 2011, Society of Petroleum Engineers: Manama, Bahrain.
43. Lager, A., et al., *LoSal Enhanced Oil Recovery: Evidence of Enhanced Oil Recovery at the Reservoir Scale*, in *SPE Symposium on Improved Oil Recovery*. 2008, Society of Petroleum Engineers: Tulsa, Oklahoma, USA.
44. Yousef, A.A., S.H. Al-Salehsalah, and M.S. Al-Jawfi, *New Recovery Method for Carbonate Reservoirs through Tuning the Injection Water Salinity: Smart WaterFlooding*, in *SPE EUROPEC/EAGE Annual Conference and Exhibition*. 2011, Society of Petroleum Engineers: Vienna, Austria.
45. Kilybay, A., B. Ghosh, and N. Chacko Thomas, *A Review on the Progress of Ion-Engineered Water Flooding.* Journal of Petroleum Engineering, 2017. **2017**: p. 1-9.
46. William, C.L. and J.P. Gary, *Standard handbook of petroleum & natural gas engineering* 2nd ed. 2005, Burlington, MA: Elsevier Inc.
47. Smalley, P.C., et al., *Reservoir Technical Limits: A Framework for Maximizing Recovery From Oil Fields.* SPE Reservoir Evaluation & Engineering, 2009. **12**(04): p. 610-629.
48. Houseworth, J.E., *Sensitivity of Large-Scale Water/Oil Displacement Behavior to Fine-Scale Permeability Heterogeneity and Relative Permeabilities*, in *SPE Annual Technical Conference and Exhibition*. 1991, Society of Petroleum Engineers: Dallas, Texas.

49. Araktingi, U.G. and F.M. Orr Jr, *Viscous Fingering in Heterogeneous Porous Media.* SPE Advanced Technology Series, 1993. **1**(01): p. 71-80.
50. Homsy, G., *Viscous Fingering In Porous Media.* Annual Review of Fluid Mechanics, 1987. **19**(1): p. 271-311.
51. Waggoner, J.R., J.L. Castillo, and L.W. Lake, *Simulation of EOR Processes in Stochastically Generated Permeable Media.* SPE Formation Evaluation, 1992. **7**(02): p. 173-180.
52. Kumar, M., et al., *High-Mobility-Ratio Waterflood Performance Prediction: Challenges and New Insights.* SPE Reservoir Evaluation & Engineering, 2013. **11**(01): p. 186-196.
53. Rosen, M.J., et al., *Ultralow interfacial tension for enhanced oil recovery at very low surfactant concentrations.* Langmuir, 2005. **21**(9): p. 3749-56.
54. Hirasaki, G.J., et al., *Wettability Evaluation During Restored-State Core Analysis*, in *SPE Annual Technical Conference and Exhibition*. 1990, Society of Petroleum Engineers: New Orleans, Louisiana.
55. E., U.J., *EOR in chalk: optimization oil recovery with modified seawater*, in *Faculty of Science and Technology*. 2011, University of Stavanger. p. 55.
56. Akin, S. and S. Bagci, *A laboratory study of single-well steam-assisted gravity drainage process.* Journal of Petroleum Science and Engineering, 2001. **32**(1): p. 23-33.
57. Ashrafi, M., Y. Souraki, and O. Torsaeter, *Numerical Simulation Study of Field Scale SAGD and ES-SAGD Processes Investigating the Effect of Relative Permeabilities.* Energy and Environment Research, 2013. **3**(1).
58. Tiab, D. and E.C. Donaldson, *Petrophysics: Theory and Practice of Measuring Reservoir Rock and Fluid Transport Properties*. 3rd ed., Oxford, UK: Elsevier Inc.
59. Alvarado, V. and E. Manrique, *Enhanced Oil Recovery: An Update Review.* Energies, 2010. **3**(9): p. 1529-1575.
60. Nasr-El-Din, H.A., B.F. Hawkins, and K.A. Green, *Recovery of residual oil using the alkali/surfactant/polymer process: effect of alkali concentration.* Journal of Petroleum Science and Engineering, 1992. **6**(4): p. 381-401.
61. Jeirani, Z., et al., *Formulation, optimization and application of triglyceride microemulsion in enhanced oil recovery.* Industrial Crops and Products, 2013. **43**: p. 6-14.
62. Levitt, D. and G.A. Pope, *Selection and Screening of Polymers for Enhanced-Oil Recovery*, in *SPE Symposium on Improved Oil Recovery*. 2008, Society of Petroleum Engineers: Tulsa, Oklahoma, USA.
63. Nagy, R., et al., *Selection Method of Surfactants for Chemical Enhanced Oil Recovery.* Advances in Chemical Engineering and Science, 2015. **05**(02): p. 121-128.
64. J., R.M. and K.J. T., *Surfactants and Interfacial Phenomena*. 4th ed. 2012, New Jersey: John Wiley & Sons, Inc.
65. Wyatt, K., M.J. Pitts, and H. Surkalo, *Economics of Field Proven Chemical Flooding Technologies*, in *SPE Symposium on Improved Oil Recovery*. 2008, Society of Petroleum Engineers: Tulsa, Oklahoma, USA.
66. Sheng, J., *Modern Chemical Enhanced Oil Recovery: Theory and Practice*. 2010, Burlington, MA: Gulf Professional Publishing. 648.

67. Alhassawi, H. and L. Romero-Zerón, *New Surfactant Delivery System for Controlling Surfactant Adsorption onto Solid Surfaces. Part I: Static Adsorption Tests.* The Canadian Journal of Chemical Engineering, 2015. **93**(7): p. 1188-1193.
68. Fjelde, I., T. Austad, and J. Milter, *Adsorption VII. Dynamic adsorption of a dual surfactant system onto reservoir cores at seawater salinities.* Journal of Petroleum Science and Engineering, 1995. **13**(3-4): p. 193-201.
69. Bourrel, M. and C. Chambu, *The Rules for Achieving High Solubilization of Brine and Oil by Amphiphilic Molecules.* Society of Petroleum Engineers Journal, 1983. **23**(02): p. 327-338.
70. Healy, R.N., R.L. Reed, and D.G. Stenmark, *Multiphase Microemulsion Systems.* Society of Petroleum Engineers Journal, 1976. **16**(03): p. 147-160.
71. Wu, B., et al., *Alcohol-free diphenyl oxide disulfonate middle-phase microemulsion systems.* Journal of Surfactants and Detergents, 2000. **3**(4): p. 465-474.
72. Anderson, D.R., et al., *Interfacial Tension and Phase Behavior in Surfactant-Brine-Oil Systems*, in *SPE Improved Oil Recovery Symposium*. 1976, Society of Petroleum Engineers: Tulsa, Oklahoma.
73. Flaaten, A., et al., *A Systematic Laboratory Approach to Low-Cost, High-Performance Chemical Flooding.* SPE Reservoir Evaluation & Engineering, 2008. **12**(05): p. 713-723.
74. Bera, A., et al., *Interfacial tension and phase behavior of surfactant-brine–oil system.* Colloids and Surfaces A: Physicochemical and Engineering Aspects, 2011. **383**(1-3): p. 114-119.
75. Clark, S.R., M.J. Pitts, and S.M. Smith, *Design and Application of an Alkaline-Surfactant-Polymer Recovery System to the West Kiehl Field.* SPE Advanced Technology Series, 1988. **1**(01): p. 172-179.
76. Nelson, R.C., et al., *Cosurfactant-Enhanced Alkaline Flooding*, in *SPE Enhanced Oil Recovery Symposium*. 1984, Society of Petroleum Engineers: Tulsa, Oklahoma.
77. Zhang, R. and P. Somasundaran, *Advances in adsorption of surfactants and their mixtures at solid/solution interfaces.* Adv Colloid Interface Sci, 2006. **123-126**: p. 213-29.
78. Koopal, L.K., E.M. Lee, and M.R. Böhmer, *Adsorption of Cationic and Anionic Surfactants on Charged Metal Oxide Surfaces.* Journal of Colloid and Interface Science, 1995. **170**(1): p. 85-97.
79. Somasundaran, P. and D.W. Fuerstenau, *Mechanisms of Alkyl Sulfonate Adsorption at the Alumina-Water Interface1.* The Journal of Physical Chemistry, 1966. **70**(1): p. 90-96.
80. Paria, S. and K.C. Khilar, *A review on experimental studies of surfactant adsorption at the hydrophilic solid-water interface.* Adv Colloid Interface Sci, 2004. **110**(3): p. 75-95.
81. Somasundaran, P., E. Fu, and X. Qun, *Coadsorption of anionic and nonionic surfactant mixtures at the alumina water interface.* Langmuir, 1992. **8**(4): p. 1065-1069.
82. Liu, S., et al., *Favorable Attributes of Alkaline-Surfactant-Polymer Flooding.* SPE Journal, 2008. **13**(01): p. 5-16.

83. Ko, K.M., et al., *Surfactant flooding characteristics of dodecyl alkyl sulfate for enhanced oil recovery.* Journal of Industrial and Engineering Chemistry, 2014. **20**(1): p. 228-233.
84. Zitha, P.L.J., K.G.S. van Os, and K.F.J. Denys, *Adsorption of Linear Flexible Polymers During Laminar Flow Through Porous Media*, in *SPE/DOE Improved Oil Recovery Symposium*. 2013, Society of Petroleum Engineers: Tulsa, Oklahoma.
85. Park, H., J. Han, and W. Sung, *Effect of polymer concentration on the polymer adsorption-induced permeability reduction in low permeability reservoirs.* Energy, 2015. **84**: p. 666-671.
86. Jung, J.C., et al., *Rheology and polymer flooding characteristics of partially hydrolyzed polyacrylamide for enhanced heavy oil recovery.* Journal of Applied Polymer Science, 2013. **127**(6): p. 4833-4839.
87. Spildo, K. and E.I.O. Sae, *Effect of Charge Distribution on the Viscosity and Viscoelastic Properties of Partially Hydrolyzed Polyacrylamide.* Energy & Fuels, 2015. **29**(9): p. 5609-5617.
88. Ma, K., *Transport of Surfactant and Foam in Porous Media for Enhanced Oil Recovery Processes*, in *Department of Chemical and Biomolecular Engineering*. 2013, RICE UNIVERSITY: HOUSTON, TEXAS. p. 222.
89. Zhu, D.W., et al., *Enhancing Rheological Properties of Hydrophobically Associative Polyacrylamide Aqueous Solutions by Hybriding with Silica Nanoparticles.* Journal of Applied Polymer Science, 2014. **131**(19): p. 40876.
90. Lu, H., et al., *Retention Behaviors of Hydrophobically Associating Polyacrylamide Prepared via Inverse Microemulsion Polymerization Through Porous Media.* Journal of Macromolecular Science, Part A, 2010. **47**(6): p. 602-607.
91. Karnanda, W., et al., *Effect of temperature, pressure, salinity, and surfactant concentration on IFT for surfactant flooding optimization.* Arabian Journal of Geosciences, 2012. **6**(9): p. 3535-3544.
92. Negin, C., S. Ali, and Q. Xie, *Most common surfactants employed in chemical enhanced oil recovery.* Petroleum, 2017. **3**(2): p. 197-211.
93. Lages, S., et al., *Formation of Ca2+-Induced Intermediate Necklace Structures of Polyacrylate Chains.* Macromolecules, 2009. **42**(12): p. 4288-4299.
94. Sinn, C.G., R. Dimova, and M. Antonietti, *Isothermal Titration Calorimetry of the Polyelectrolyte/Water Interaction and Binding of Ca2+: Effects Determining the Quality of Polymeric Scale Inhibitors.* Macromolecules, 2004. **37**(9): p. 3444-3450.
95. Xue, Z., et al., *Effect of Grafted Copolymer Composition on Iron Oxide Nanoparticle Stability and Transport in Porous Media at High Salinity.* Energy & Fuels, 2014. **28**(6): p. 3655-3665.
96. Wang, W., Y.Z. Liu, and Y.G. Gu, *Application of a novel polymer system in chemical enhanced oil recovery (EOR).* Colloid and Polymer Science, 2003. **281**(11): p. 1046-1054.
97. Mothe, C.G., et al., *Thermal and rheological study of polysaccharides for enhanced oil recovery.* Journal of Thermal Analysis and Calorimetry, 2006. **85**(1): p. 31-36.
98. Seright, R.S., et al., *Stability of Partially Hydrolyzed Polyacrylamides at Elevated Temperatures in the Absence of Divalent Cations.* SPE Journal, 2010. **15**(2): p. 341-348.

99. Zhu, D., et al., *Laboratory Study on the Potential EOR Use of HPAM/VES Hybrid in High-Temperature and High-Salinity Oil Reservoirs.* Journal of Chemistry, 2013. **2013**: p. 1-8.
100. Erdlac, J.R.J., et al. *Ongoing Resource Assessment of Geothermal Energy from Sedimentary Basins in Texas*. in *PROCEEDINGS of Thirty-Second Workshop on Geothermal Reservoir Engineering*. 2007. Stanford University, Stanford, California.
101. Yahya, G.O., et al., *Preparation and viscosity behavior of hydrophobically modified poly(vinyl alcohol) (PVA).* Journal of Applied Polymer Science, 1995. **57**(3): p. 343-352.
102. Kopperud, H.M., F.K. Hansen, and B. Nyström, *Effect of surfactant and temperature on the rheological properties of aqueous solutions of unmodified and hydrophobically modified polyacrylamide.* Macromolecular Chemistry and Physics, 1998. **199**(11): p. 2385-2394.
103. Shaikh, S., et al., *Synthesis and solution properties of poly(acrylamide-styrene) block copolymers with high hydrophobic content.* Polymer Engineering & Science, 1999. **39**(10): p. 1962-1968.
104. Bagaria, H.G., et al., *Iron oxide nanoparticles grafted with sulfonated copolymers are stable in concentrated brine at elevated temperatures and weakly adsorb on silica.* ACS Appl Mater Interfaces, 2013. **5**(8): p. 3329-39.
105. CL McCormick, T Nonaka, and C. Johnson, *Water-soluble copolymers: 27. Synthesis and aqueous solution behaviour of associative acrylamideN-alkylacrylamide copolymers.* Polymer, 1988. **29**(4): p. 731-739.
106. Sabhapondit, A., A. Borthakur, and I. Haque, *Characterization of acrylamide polymers for enhanced oil recovery.* Journal of Applied Polymer Science, 2003. **87**(12): p. 1869–1878.
107. Samanta, A., et al., *Effects of Alkali, Salts, and Surfactant on Rheological Behavior of Partially Hydrolyzed Polyacrylamide Solutions.* Journal of Chemical and Engineering Data, 2010. **55**(10): p. 4315-4322.
108. J. François, et al., *Aqueous solutions of acrylamide-acrylic acid copolymers: stability in the presence of alkalinoearth cations.* Polymer, 1997. **38**(25): p. 6115–6127.
109. Zhu, D., et al., *Aqueous Hybrids of Silica Nanoparticles and Hydrophobically Associating Hydrolyzed Polyacrylamide Used for EOR in High-Temperature and High-Salinity Reservoirs.* Energies, 2014. **7**(6): p. 3858-3871.
110. Moradi-Araghi, A., D.H. Cleveland, and I.J. Westerman, *Development and Evaluation of EOR Polymers Suitable for Hostile Environments: II-Copolymers of Acrylamide and Sodium AMPS*, in *SPE International Symposium on Oilfield Chemistry*. 1987, Society of Petroleum Engineers: San Antonio, Texas
111. Skauge, T., K. Spildo, and A. Skauge, *Nano-sized Particles For EOR* in *SPE Improved Oil Recovery Symposium*. 2010, Society of Petroleum Engineers: Tulsa, USA.
112. Bayat, A.E., et al., *Impact of Metal Oxide Nanoparticles on Enhanced Oil Recovery from Limestone Media at Several Temperatures.* Energy & Fuels, 2014. **28**(10): p. 6255-6266.
113. Ayatollahi, S. and M.M. Zerafat, *Nanotechnology-Assisted EOR Techniques: New Solutions to Old Challenges*, in *SPE International*

Oilfield Nanotechnology Conference and Exhibition. 2012, Society of Petroleum Engineers: Noordwijk, The Netherlands.
114. Brinkman, H.C., *The Viscosity of Concentrated Suspensions and Solutions.* The Journal of Chemical Physics, 1952. **20**(4): p. 571.
115. Bobbo, S., et al., *Viscosity of water based SWCNH and TiO2 nanofluids.* Experimental Thermal and Fluid Science, 2012. **36**: p. 65-71.
116. Chen, H., et al., *Rheological behaviour of ethylene glycol based titania nanofluids.* Chemical Physics Letters, 2007. **444**(4-6): p. 333-337.
117. Roustaei, A., S. Saffarzadeh, and M. Mohammadi, *An evaluation of modified silica nanoparticles' efficiency in enhancing oil recovery of light and intermediate oil reservoirs.* Egyptian Journal of Petroleum, 2013. **22**(3): p. 427-433.
118. Li, S., L. Hendraningrat, and O. Torsater, *Improved Oil Recovery by Hydrophilic Silica Nanoparticles Suspension: 2-Phase Flow Experimental Studies*, in *International Petroleum Technology Conference*. 2013: Beijing, China.
119. Suresh, S., *Studies on the dielectric properties of CdS nanoparticles.* Applied Nanoscience, 2013. **4**(3): p. 325-329.
120. Parvazdavani, M., M. Masihi, and M.H. Ghazanfari, *Monitoring the influence of dispersed nano-particles on oil–water relative permeability hysteresis.* Journal of Petroleum Science and Engineering, 2014. **124**: p. 222-231.
121. Karimi, A., et al., *Wettability Alteration in Carbonates using Zirconium Oxide Nanofluids: EOR Implications.* Energy & Fuels, 2012. **26**(2): p. 1028-1036.
122. Hwang, C.C., et al., *Highly stable carbon nanoparticles designed for downhole hydrocarbon detection.* Energy & Environmental Science, 2012. **5**(8): p. 8304-8309.
123. Hwang, C.C., et al., *Carbon-based nanoreporters designed for subsurface hydrogen sulfide detection.* ACS Appl Mater Interfaces, 2014. **6**(10): p. 7652-7658.
124. *2B1stconsulting, EOR, https://www.2b1stconsulting.com/eor/, cited on 29 October 2017.*
125. *John Ullo Consultant (Schlumberger)/AEC, Advanced Energy Consortium, https://www.nist.gov/sites/default/files/documents/cnst/Ullo-NIST_03_01_2011_Final.pdf, cited on 1 November 2018.*
126. Alaskar, M., *In-Situ Multifunctional Nanosensors for Fractured Reservoir Characterization*, in *Department of Energy Resources Engineering*. 2013, STANFORD UNIVERSITY: Stanford, California. p. 295.
127. Ehtesabi, H., et al., *Enhanced Heavy Oil Recovery in Sandstone Cores Using TiO2Nanofluids.* Energy & Fuels, 2014. **28**(1): p. 423-430.
128. Singh, R. and K.K. Mohanty, *Synergy between Nanoparticles and Surfactants in Stabilizing Foams for Oil Recovery.* Energy & Fuels, 2014. **29**(2): p. 467-479.
129. Pei, H.H., et al., *Investigation of Nanoparticle and Surfactant Stabilized Emulsion to Enhance Oil Recovery in Waterflooded Heavy Oil Reservoirs* in *SPE Canada Heavy Oil Technical Conference*. 2015, Society of Petroleum Engineers: Calgary, Alberta, .

130. Hassani, S.S., et al., *The effect of nanoparticles on the heat transfer properties of drilling fluids.* Journal of Petroleum Science and Engineering, 2016. **146**: p. 183-190.
131. Abdo, J. and M.D. Haneef, *Clay nanoparticles modified drilling fluids for drilling of deep hydrocarbon wells.* Applied Clay Science, 2013. **86**: p. 76-82.
132. Li, M.C., et al., *Cellulose Nanoparticles as Modifiers for Rheology and Fluid Loss in Bentonite Water-based Fluids.* Acs Applied Materials & Interfaces, 2015. **7**(8): p. 5006-5016.
133. Vryzas, Z., et al., *A Comprehensive Approach for the Development of New Magnetite Nanoparticles Giving Smart Drilling Fluids with Superior Properties for HP/HT Applications*, in *International Petroleum Technology Conference*. 2016, International Petroleum Technology Conference: Bangkok, Thailand.
134. Suleimanov, B.A., F.S. Ismailov, and E.F. Veliyev, *Nanofluid for enhanced oil recovery.* Journal of Petroleum Science and Engineering, 2011. **78**(2): p. 431-437.
135. Hendraningrat, L., S. Li, and O. Torsæter, *A coreflood investigation of nanofluid enhanced oil recovery.* Journal of Petroleum Science and Engineering, 2013. **111**: p. 128-138.
136. Ehtesabi, H., M.M. Ahadian, and V. Taghikhani, *Enhanced Heavy Oil Recovery Using TiO2Nanoparticles: Investigation of Deposition during Transport in Core Plug.* Energy & Fuels, 2015. **29**(1): p. 1-8.
137. Safari, M., *Variations in Wettability Caused by Nanoparticles.* Petroleum Science and Technology, 2014. **32**(12): p. 1505-1511.
138. Maghzi, A., et al., *Monitoring wettability alteration by silica nanoparticles during water flooding to heavy oils in five-spot systems: A pore-level investigation.* Experimental Thermal and Fluid Science, 2012. **40**: p. 168-176.
139. Haroun, M.R., et al., *Smart Nano-EOR Process for Abu Dhabi Carbonate Reservoirs*, in *Abu Dhabi International Petroleum Conference and Exhibition*. 2012, Society of Petroleum Engineers: Abu Dhabi, UAE.
140. Luo, D., et al., *Nanofluid of graphene-based amphiphilic Janus nanosheets for tertiary or enhanced oil recovery: High performance at low concentration.* Proc Natl Acad Sci U S A, 2016. **113**(28): p. 7711-6.
141. Reppert, T.R., et al., *Second Ripley Surfactant Flood Pilot Test*, in *SPE/DOE Enhanced Oil Recovery Symposium*. 1990, Society of Petroleum Engineers: Tulsa, Oklahoma.
142. Curbelo, F.D.S., et al., *Adsorption of nonionic surfactants in sandstones.* Colloids and Surfaces A: Physicochemical and Engineering Aspects, 2007. **293**(1-3): p. 1-4.
143. Puerto, M.C., et al., *Effects of Hardness and Cosurfactant on Phase Behavior of Alcohol-Free Alkyl Propoxylated Sulfate Systems.* SPE Journal, 2015. **20**(05): p. 1145-1153.
144. *COD Method 410: Chemical Oxygen Demand (Titrimetric, Mid-Level), http://www.envexp.com/technical/method-downloads/cod-method-410, access on 06 February 2018.*
145. *Huntsman Corporation, Technical Bulletin: Products for Enhanced Oil Recovery, http://www.huntsman.com/performance_products/Media%20Library/a_MC348531CFA3EA9A2E040EBCD2B6B7B06/Home_MC348531CFA8*

BA9A2E040EBCD2B6B7B06/Energy%20%20%20Resources_MC348531D0031A9A2E040EBCD2B6B7B06/Oilfield%20chemicals_MC348531D0299A9A2E040EBCD2B6B7B06/files/Products%20for%20Enhanced%20Oil%20Recovery.pdf, access on 18 December 2017.

146. Guo, S., et al., *A nanoparticulate pre-chemosensitizer for efficacious chemotherapy of multidrug resistant breast cancer.* Sci Rep, 2016. **6**: p. 21459.
147. Tarangelo, A. and S.J. Dixon, *Nanomedicine: An iron age for cancer therapy.* Nat Nanotechnol, 2016. **11**(11): p. 921-922.
148. Gao, H., et al., *In Situ Synthesis of Fluorescent Carbon Dots/Polyelectrolyte Nanocomposite Microcapsules with Reduced Permeability and Ultrasound Sensitivity.* ACS Nano, 2016. **10**(10): p. 9608-9615.
149. Gao, H., D.S. Wen, and G.B. Sukhorukov, *Composite silica nanoparticle/polyelectrolyte microcapsules with reduced permeability and enhanced ultrasound sensitivity.* Journal of Materials Chemistry B, 2015. **3**(9): p. 1888-1897.
150. Neves Libório De Avila, J., et al., *Polystyrene nanoparticles as surfactant carriers for enhanced oil recovery.* Journal of Applied Polymer Science, 2016. **133**(32).
151. Yu, H., et al., *Transport and retention of aqueous dispersions of superparamagnetic nanoparticles in sandstone.* Journal of Petroleum Science and Engineering, 2014. **116**: p. 115-123.
152. Jian, G., et al., *Static Adsorption of an Ethoxylated Nonionic Surfactant on Carbonate Minerals.* Langmuir, 2016. **32**(40): p. 10244-10252.
153. Esfandyari Bayat, A., et al., *TiO(2) nanoparticle transport and retention through saturated limestone porous media under various ionic strength conditions.* Chemosphere, 2015. **134**: p. 7-15.
154. Caldelas, F.M., et al., *Factors Governing Distance of Nanoparticle Propagation in Porous Media*, in *SPE Production and Operations Symposium*. 2013, Society of Petroleum Engineers: Oklahoma City, Oklahoma, USA.
155. Lau, H.C., M. Yu, and Q.P. Nguyen, *Nanotechnology for Oilfield Applications: Challenges and Impact*, in *Abu Dhabi International Petroleum Exhibition & Conference*. 2016, Society of Petroleum Engineers: Abu Dhabi, UAE.
156. Fan, W., et al., *Effects of surfactants on graphene oxide nanoparticles transport in saturated porous media.* J Environ Sci (China), 2015. **35**: p. 12-19.
157. Wang, Y.G., et al., *Enhanced Mobility of Fullerene (C-60) Nanoparticles in the Presence of Stabilizing Agents.* Environmental Science & Technology, 2012. **46**(21): p. 11761-11769.
158. Wang, Y.G., et al., *Effect of surface coating composition on quantum dot mobility in porous media.* Journal of Nanoparticle Research, 2013. **15**(8): p. 16.
159. Wang, Y.G., et al., *Influence of Residual Polymer on Nanoparticle Deposition in Porous Media.* Environmental Science & Technology, 2014. **48**(18): p. 10664-10671.
160. Taghavy, A., et al., *Mathematical Modeling of the Transport and Dissolution of Citrate-Stabilized Silver Nanoparticles in Porous Media.* Environmental Science & Technology, 2013. **47**(15): p. 8499-8507.

161. Bera, A., et al., *Screening of microemulsion properties for application in enhanced oil recovery.* Fuel, 2014. **121**: p. 198-207.
162. Binks, B.P. and A. Rocher, *Effects of temperature on water-in-oil emulsions stabilised solely by wax microparticles.* J Colloid Interface Sci, 2009. **335**(1): p. 94-104.
163. Winsor, P.A., *Solvent properties of amphiphilic compounds*. 1954, London: Butterworths Scientific Publ. Ltd.
164. Bellocq, A.M., et al., *Microemulsions.* Advances in Colloid and Interface Science, 1984. **20**(3-4): p. 167-272.
165. Zhang, T., et al., *Foams and Emulsions Stabilized With Nanoparticles for Potential Conformance Control Applications*, in *SPE International Symposium on Oilfield Chemistry*. 2009, Society of Petroleum Engineers: The Woodlands. Texas
166. Sun, Q., et al., *Utilization of Surfactant-Stabilized Foam for Enhanced Oil Recovery by Adding Nanoparticles.* Energy & Fuels, 2014. **28**(4): p. 2384-2394.
167. Zhang, T., et al., *Nanoparticle-Stabilized Emulsions for Applications in Enhanced Oil Recovery*, in *SPE Improved Oil Recovery Symposium*. 2010, Society of Petroleum Engineers: Tulsa, Oklahoma, USA.
168. Zaid, H.M., N. Yahya, and N.R.A. Latiff, *The Effect of Nanoparticles Crystallite Size on the Recovery Efficiency in Dielectric Nanofluid Flooding.* Journal of Nano Research, 2013. **21**: p. 103-108.
169. Esmaeilzadeh, P., et al., *Effect of ZrO2 nanoparticles on the interfacial behavior of surfactant solutions at air–water and n-heptane–water interfaces.* Fluid Phase Equilibria, 2014. **361**: p. 289-295.
170. Aroonsri, A., et al., *Conditions for Generating Nanoparticle-Stabilized CO2 Foams in Fracture and Matrix Flow.* 2013.
171. Nguyen, P., H. Fadaei, and D. Sinton, *Pore-Scale Assessment of Nanoparticle-Stabilized CO2Foam for Enhanced Oil Recovery.* Energy & Fuels, 2014. **28**(10): p. 6221-6227.
172. Yang, L. and K. Du, *Investigations of Surface Tension of Binary Nanofluids.* Advanced Materials Research, 2011. **347-353**: p. 786-790.
173. Wever, D.A.Z., F. Picchioni, and A.A. Broekhuis, *Polymers for enhanced oil recovery: A paradigm for structure-property relationship in aqueous solution.* Progress in Polymer Science, 2011. **36**(11): p. 1558-1628.
174. Wu, Y., et al., *Development of new polymers with better performance under conditions of high temperature and high salinity*, in *SPE EOR Conference at Oil and Gas West Asia*. 2012, Society of Petroleum Engineers: Muscat, Oman.
175. Sang, G., et al., *Biodegradation for hydrolyzed polyacrylamide in the anaerobic baffled reactor combined aeration tank.* Ecological Engineering, 2015. **84**: p. 121-127.
176. Li, H., et al., *Novel polymer aids for low-grade oil sand ore processing.* The Canadian Journal of Chemical Engineering, 2008. **86**(2): p. 168-176.
177. Gao, C., *Viscosity of partially hydrolyzed polyacrylamide under shearing and heat.* Journal of Petroleum Exploration and Production Technology, 2013. **3**(3): p. 203-206.
178. Zhang, L., et al., *Mechanism Study of the Cross-Linking Reaction of Hydrolyzed Polyacrylamide/Ac3Cr in Formation Water.* Energy & Fuels, 2015. **29**(8): p. 4701-4710.

179. Maitin, B.K., *Performance Analysis of Several Polyacrylamide Floods in North German Oil Fields*, in *SPE/DOE Enhanced Oil Recovery Symposium*. 1992: Tulsa, Oklahoma.
180. Sohn, W.O., B.K. Maitin, and V. Hartwig, *Preconditioning Concepts in Polymer Flooding in High-Salinity Reservoirs: Laboratory Investigations and Case Histories.* SPE Reservoir Engineering, 1990. **5**(04): p. 503-507.
181. Zhong, C.R., H. Zhang, and L.M. Feng, *Solution behavior and associating structures of a salt-tolerant tetra-polymer containing an allyl-capped macromonomer.* Journal of Polymer Research, 2014. **21**(12): p. 604.
182. Zhao, T., et al., *Synthesis of Polyacrylamide with Superb Salt-Thickening Performance.* Industrial & Engineering Chemistry Research, 2015. **54**(43): p. 10568-10574.
183. Chen, G., et al., *An Attenuated Total Reflection FT-IR Spectroscopic Study of Polyamide 6/Clay Nanocomposite Fibers.* Macromolecular Rapid Communications, 2004. **25**(11): p. 1121-1124.
184. Tjong, S.C., *Structural and mechanical properties of polymer nanocomposites.* Materials Science and Engineering: R: Reports, 2006. **53**(3-4): p. 173-197.
185. Okay, O. and W. Oppermann, *Polyacrylamide-clay nanocomposite hydrogels: Rheological and light scattering characterization.* Macromolecules, 2007. **40**(9): p. 3378-3387.
186. Liu, J., G. Chen, and J. Yang, *Preparation and characterization of poly(vinyl chloride)/layered double hydroxide nanocomposites with enhanced thermal stability.* Polymer, 2008. **49**(18): p. 3923-3927.
187. Fu, P.J., et al., *Preparation, stability and rheology of polyacrylamide/pristine layered double hydroxide nanocomposites.* Journal of Materials Chemistry, 2010. **20**(19): p. 3869-3876.
188. Hu, Z. and G. Chen, *Novel nanocomposite hydrogels consisting of layered double hydroxide with ultrahigh tensibility and hierarchical porous structure at low inorganic content.* Adv Mater, 2014. **26**(34): p. 5950-5956.
189. Zhang, L., T. Tao, and C. Li, *Formation of polymer/carbon nanotubes nano-hybrid shish–kebab via non-isothermal crystallization.* Polymer, 2009. **50**(15): p. 3835-3840.
190. Fan, J.C., et al., *Mechanically strong graphene oxide/sodium alginate/polyacrylamide nanocomposite hydrogel with improved dye adsorption capacity.* Journal of Materials Chemistry A, 2013. **1**(25): p. 7433-7443.
191. Liu, J., et al., *Self-healing in tough graphene oxide composite hydrogels.* Macromol Rapid Commun, 2013. **34**(12): p. 1002-1007.
192. Bhardwaj, P., et al., *Nanosize Polyacrylamide/SiO2 Composites by Inverse Microemulsion Polymerization.* International Journal of Polymeric Materials, 2008. **57**(4): p. 404-416.
193. Parizad, A. and K. Shahbazi, *Experimental investigation of the effects of SnO2 nanoparticles and KCl salt on a water base drilling fluid properties.* Canadian Journal of Chemical Engineering, 2016. **94**(10): p. 1924-1938.
194. Kennedy, J.R.M., K.E. Kent, and J.R. Brown, *Rheology of dispersions of xanthan gum, locust bean gum and mixed biopolymer gel with silicon dioxide nanoparticles.* Materials Science & Engineering C-Materials for Biological Applications, 2015. **48**: p. 347-353.

195. Maghzi, A., et al., *The impact of silica nanoparticles on the performance of polymer solution in presence of salts in polymer flooding for heavy oil recovery.* Fuel, 2014. **123**: p. 123-132.
196. Wang, Y., et al., *Transport and retention of nanoscale C60 aggregates in water-saturated porous media.* Environ Sci Technol, 2008. **42**(10): p. 3588-3594.
197. Berlin, J.M., et al., *Engineered nanoparticles for hydrocarbon detection in oil-field rocks.* Energy & Environmental Science, 2011. **4**(2): p. 505-509.
198. Feriancikova, L. and S. Xu, *Deposition and remobilization of graphene oxide within saturated sand packs.* J Hazard Mater, 2012. **235-236**: p. 194-200.
199. Sun, Y., et al., *Transport, retention, and size perturbation of graphene oxide in saturated porous media: effects of input concentration and grain size.* Water Res, 2015. **68**: p. 24-33.
200. Li, Y., et al., *Investigation of the transport and deposition of fullerene (C60) nanoparticles in quartz sands under varying flow conditions.* Environ Sci Technol, 2008. **42**(19): p. 7174-7180.
201. Wang, X., et al., *Cotransport of multi-walled carbon nanotubes and titanium dioxide nanoparticles in saturated porous media.* Environ Pollut, 2014. **195**: p. 31-38.
202. Wang, Y., et al., *Transport behavior of functionalized multi-wall carbon nanotubes in water-saturated quartz sand as a function of tube length.* Water Res, 2012. **46**(14): p. 4521-4531.
203. Tian, Y., et al., *Deposition and transport of functionalized carbon nanotubes in water-saturated sand columns.* J Hazard Mater, 2012. **213-214**: p. 265-72.
204. Wang, Y., et al., *Influence of residual polymer on nanoparticle deposition in porous media.* Environ Sci Technol, 2014. **48**(18): p. 10664-10671.
205. Kini, G.C., et al., *Salt- and temperature-stable quantum dot nanoparticles for porous media flow.* Colloids and Surfaces A: Physicochemical and Engineering Aspects, 2014. **443**: p. 492-500.
206. Wasan, D.T. and A.D. Nikolov, *Spreading of nanofluids on solids.* Nature, 2003. **423**: p. 156-159.
207. Nikolov, A. and D. Wasan, *Wetting-dewetting films: the role of structural forces.* Adv Colloid Interface Sci, 2014. **206**: p. 207-221.
208. Shahrabad, A., et al., *Experimental investigation of HLP nanofluid potential to enhanced oil recovery.pdf*, in *SPE International Oil Field Nanotechnology Conference*. 2012: Noordwijk, Netherlands.
209. Hendraningrat, L., L. Shidong, and S.a.O. Torsater, *A Glass micromodel experimental study of hydrophilic nanoparticles retention for eor project*, in *SPE Russian Oil & Gas Exploration & Production Technical Conference and Exhibition* 2015: Moscow, Russia.
210. El-Diasty, A.I. and A.M. Aly, *Understanding the Mechanism of Nanoparticles Applications in Enhanced Oil Recovery*, in *SPE North Africa Technical Conference and Exhibition*. 2015, Society of Petroleum Engineers: Cairo, Egypt
211. Wen, D., *On the role of structural disjoining pressure to boiling heat transfer with thermal nanofluids.* Journal of Nanoparticle Research, 2008. **10**(7): p. 1129-1140.

212. Giraldo, J., et al., *Wettability Alteration of Sandstone Cores by Alumina-Based Nanofluids.* Energy & Fuels, 2013. **27**(7): p. 3659-3665.
213. Onyekonwu, M.O. and N.A. Ogolo, *Investigating the use of nanoparticles in enhanced oil recovery*, in *Nigeria Annual International Conference and Exhibition*. 2010, Society of Petroleum Engineers: Tinapa - Calabar, Nigeria.
214. Al-Anssari, S., et al., *Wettability alteration of oil-wet carbonate by silica nanofluid.* J Colloid Interface Sci, 2016. **461**: p. 435-442.
215. Vafaei, S., et al., *Effect of nanoparticles on sessile droplet contact angle.* Nanotechnology, 2006. **17**(10): p. 2523-2527.
216. Kim, S.J., et al., *Surface wettability change during pool boiling of nanofluids and its effect on critical heat flux.* International Journal of Heat and Mass Transfer, 2007. **50**(19-20): p. 4105-4116.
217. KIM, S.J., et al., *Study of pool boiling and critical heat flux enhancement in nanofluids.* Bulletin of the Polish Academy of Sciences-Technical Sciences, 2007. **55**: p. 211-216.
218. Sethumadhavan, G.N., A.D. Nikolov, and D.T. Wasan, *Stability of Liquid Films Containing Monodisperse Colloidal Particles.* J Colloid Interface Sci, 2001. **240**(1): p. 105-112.
219. Kondiparty, K., et al., *Wetting and spreading of nanofluids on solid surfaces driven by the structural disjoining pressure: statics analysis and experiments.* Langmuir, 2011. **27**(7): p. 3324-3335.
220. Chengara, A., et al., *Spreading of nanofluids driven by the structural disjoining pressure gradient.* J Colloid Interface Sci, 2004. **280**(1): p. 192-201.
221. Kondiparty, K., et al., *Dynamic spreading of nanofluids on solids. Part I: experimental.* Langmuir, 2012. **28**(41): p. 14618-14623.
222. Wasan, D., A. Nikolov, and K. Kondiparty, *The wetting and spreading of nanofluids on solids: Role of the structural disjoining pressure.* Current Opinion in Colloid & Interface Science, 2011. **16**(4): p. 344-349.
223. Zhang, H., A. Nikolov, and D. Wasan, *Dewetting film dynamics inside a capillary using a micellar nanofluid.* Langmuir, 2014. **30**(31): p. 9430-9435.
224. Hendraningrat, L. and O. Torsæter, *Metal oxide-based nanoparticles: revealing their potential to enhance oil recovery in different wettability systems.* Applied Nanoscience, 2014. **5**(2): p. 181-199.
225. Bai, Y., et al., *Experimental Study on Ethanolamine/Surfactant Flooding for Enhanced Oil Recovery.* Energy & Fuels, 2014. **28**(3): p. 1829-1837.
226. ShamsiJazeyi, H., et al., *Polymer-Coated Nanoparticles for Enhanced Oil Recovery.* Journal of Applied Polymer Science, 2014. **131**(15): p. 40576.
227. Hendraningrat, L., S.D. Li, and O. Torster, *A coreflood investigation of nanofluid enhanced oil recovery.* Journal of Petroleum Science and Engineering, 2013. **111**: p. 128-138.
228. Alomair, O.A., K.M. Matar, and Y.H. Alsaeed, *Nanofluids Application for Heavy Oil Recovery*, in *SPE Asia Pacific Oil & Gas Conference and Exhibition*. 2014, Society of Petroleum Engineers: Adelaide, Australia.
229. Abu Tarboush, B.J. and M.M. Husein, *Adsorption of asphaltenes from heavy oil onto in situ prepared NiO nanoparticles.* J Colloid Interface Sci, 2012. **378**(1): p. 64-69.

230. Kazemzadeh, Y., et al., *Behavior of Asphaltene Adsorption onto the Metal Oxide Nanoparticle Surface and Its Effect on Heavy Oil Recovery.* Industrial & Engineering Chemistry Research, 2015. **54**(1): p. 233-239.
231. Shokrlu, Y.H. and T. Babadagli, *Transportation and Interaction of Nano and Micro Size Metal Particles Injected to Improve Thermal Recovery of Heavy-Oil*, in *SPE Annual Technical Conference and Exhibition*. 2011, Society of Petroleum Engineers: Denver, Colorado, USA.
232. Revil, A. and P.W.J. Glover, *Theory of ionic-surface electrical conduction in porous media.* Physical Review B, 1997. **55**(3): p. 1757-1773.
233. Revil, A. and P.W.J. Glover, *Nature of surface electrical conductivity in natural sands, sandstones, and clays.* Geophysical Research Letters, 1998. **25**(5): p. 691-694.
234. GLOVER, P.W.J., *Geophysical Properties of the Near Surface Earth: Electrical Properties*, in *Treatise on Geophysics*, G. Schubert, Editor. 2015, Elsevier: Oxford. p. 89-137.
235. Vajjha, R.S. and D.K. Das, *A review and analysis on influence of temperature and concentration of nanofluids on thermophysical properties, heat transfer and pumping power.* International Journal of Heat and Mass Transfer, 2012. **55**(15-16): p. 4063-4078.
236. Caputo, G., et al., *Reversible Wettability Changes in Colloidal TiO2 Nanorod Thin-Film Coatings under Selective UV Laser Irradiation.* Journal of Physical Chemistry C, 2008. **112**: p. 701-714.
237. Nasiri, A., et al., *Effect of dispersion method on thermal conductivity and stability of nanofluid.* Experimental Thermal and Fluid Science, 2011. **35**(4): p. 717-723.
238. Fazeli, S.A., et al., *Experimental and numerical investigation of heat transfer in a miniature heat sink utilizing silica nanofluid.* Superlattices and Microstructures, 2012. **51**(2): p. 247-264.
239. Baghbanzadeh, M., et al., *Investigating the rheological properties of nanofluids of water/hybrid nanostructure of spherical silica/MWCNT.* Thermochimica Acta, 2014. **578**: p. 53-58.
240. Metin, C.O., et al., *Stability of aqueous silica nanoparticle dispersions.* Journal of Nanoparticle Research, 2011. **13**(2): p. 839-850.
241. Agarwal, D.K., A. Vaidyanathan, and S. Sunil Kumar, *Synthesis and characterization of kerosene–alumina nanofluids.* Applied Thermal Engineering, 2013. **60**(1-2): p. 275-284.
242. French, R.A., et al., *Influence of ionic strength, pH, and cation valence on aggregation kinetics of titanium dioxide nanoparticles.* Environ Sci Technol, 2009. **43**(5): p. 1354-1359.
243. Solovitch, N., et al., *Concurrent aggregation and deposition of TiO2 nanoparticles in a sandy porous media.* Environ Sci Technol, 2010. **44**(13): p. 4897-902.
244. Bouhaik, I.S., et al., *Influence of surface conductivity on the apparent zeta potential of TiO2 nanoparticles: Application to the modeling of their aggregation kinetics.* Journal of Colloid and Interface Science, 2013. **406**: p. 75-85.
245. Bagaria, H.G., et al., *Iron Oxide Nanoparticles Grafted with Sulfonated Copolymers are Stable in Concentrated Brine at Elevated Temperatures and Weakly Adsorb on Silica.* ACS Applied Materials & Interfaces, 2013. **5**(8): p. 3329-3339.

246. Wen, D., et al., *Review of nanofluids for heat transfer applications.* Particuology, 2009. **7**(2): p. 141-150.
247. Ghadimi, A., R. Saidur, and H.S.C. Metselaar, *A review of nanofluid stability properties and characterization in stationary conditions.* International Journal of Heat and Mass Transfer, 2011. **54**(17-18): p. 4051-4068.
248. Hwang, Y.J., et al., *Investigation on characteristics of thermal conductivity enhancement of nanofluids.* Current Applied Physics, 2006. **6**: p. 1068-1071.
249. Hwang, Y., et al., *Stability and thermal conductivity characteristics of nanofluids.* Thermochimica, 2007. **455**.
250. Jiang, L., L. Gao, and J. Sun, *Production of aqueous colloidal dispersions of carbon nanotubes.* Journal of Colloid and Interface Science, 2003. **260**(1): p. 89-94.
251. Ayatollahi, S. and M.M. Zerafat, *Nanotechnology-Assisted EOR Techniques: New Solutions to Old Challenges.* 2013.
252. Ersenkal, D.A., et al., *Impact of dilution on the transport of poly(acrylic acid) supported magnetite nanoparticles in porous media.* Journal of Contaminant Hydrology, 2011. **126**(3-4): p. 248-257.
253. Kim, H.-J., et al., *Effect of kaolinite, silica fines and pH on transport of polymer-modified zero valent iron nano-particles in heterogeneous porous media.* Journal of Colloid and Interface Science, 2012. **370**(1): p. 1-10.
254. Ranka, M., P. Brown, and T.A. Hatton, *Responsive Stabilization of Nanoparticles for Extreme Salinity and High-Temperature Reservoir Applications.* ACS Appl Mater Interfaces, 2015. **7**(35): p. 19651-8.
255. Sabbagh, I. and M. Delsanti, *Solubility of highly charged anionic polyelectrolytes in presence of multivalent cations: Specific interaction effect.* The European Physical Journal E - Soft Matter, 2000. **1**(1): p. 75-86.
256. Hwang, Y., et al., *Production and dispersion stability of nanoparticles in nanofluids.* Powder Technology, 2008. **186**.
257. Zhang, X., H. Gu, and M. Fujii, *Effective thermal conductivity and thermal diffusivity of nanofluids containing spherical and cylindrical nanoparticles.* Experimental Thermal and Fluid Science, 2007. **31**(6): p. 593-599.
258. TREIBER, L.E., et al., *A Laboratory Evaluation of the Nettability of Fifty Oil-Producing Reservoirs.* SOCIETY OF PETROLEUM ENGINEERS JOURNAL, 1972. **253**: p. 531-540.
259. Wang, X.-j., D.-s. Zhu, and S. yang, *Investigation of pH and SDBS on enhancement of thermal conductivity in nanofluids.* Chemical Physics Letters, 2009. **470**.
260. Zhu, D., et al., *Dispersion behavior and thermal conductivity characteristics of Al2O3–H2O nanofluids.* Current Applied Physics, 2009. **9**: p. 131-139.
261. LotfizadehDehkordi, B., et al., *Investigation of viscosity and thermal conductivity of alumina nanofluids with addition of SDBS.* Heat Mass Transfer, 2013.
262. Esmaeilzadeh, P., et al., *Effect of ZrO2 nanoparticles on the interfacial behavior of surfactant solutions at air–water and n-heptane–water interfaces.* Fluid Phase Equilibria, 2014. **361**.

263. Kole, M. and T.K. Dey, *Viscosity of alumina nanoparticles dispersed in car engine coolant.* Experimental Thermal and Fluid Science, 2010. **34**: p. 677-683.
264. Kole, M. and T.K. Dey, *Thermal conductivity and viscosity of Al2O3 nanofluid based on car engine coolant.* J. Phys. D: Appl. Phys., 2010. **43**.
265. Maghzi, A., et al., *An Experimental Investigation of Silica Nanoparticles Effect on the Rheological Behavior of Polyacrylamide Solution to Enhance Heavy Oil Recovery.* Petroleum Science and Technology, 2013. **31**(5).
266. Amraei, A., Z. Fakhroueian, and A. Bahramian, *Influence of new SiO2 Nanofluids on Surface Wettability and Interfacial Tension Behaviour between Oil-Water Interface in EOR Processes.* Journal of Nano Research, 2014. **26**.
267. Alagic, E., et al., *Effect of crude oil ageing on low salinity and low salinity surfactant flooding.* Journal of Petroleum Science and Engineering, 2011. **78**(2): p. 220-227.
268. Lasfargues, M., *Nitrate based High Temperature Nano-Heat-Transfer-Fluids: Formulation & Characterisation*. 2014, University of Leeds. p. 78.
269. *Technex, Capture the fastest wetting phenomena and experience the most precise drop shape analysis, http://www.technex.nl/news/37/64/Capture-the-fastest-wetting-phenomena-and-experience-the-most-precise-drop-shape-analysis. Access on 1 February 2018.*
270. *Károly Havancsák, High-Resolution Scanning Electron Microscopy, http://www.technoorg.hu/news-and-events/articles/high-resolution-scanning-electron-microscopy-1/, Technoorg Linda Co. Ltd., access 5 January 2017.*
271. Zhulina, E.B., O.V. Borisov, and V.A. Priamitsyn, *Theory of Steric Stabilization of Colloid Dispersions by Grafted Polymers.* Journal of Colloid and Interface Science, 1990. **137**(2): p. 495-511.
272. Fritz, G., et al., *Electrosteric Stabilization of Colloidal Dispersions.* Langmuir, 2002. **18**(16): p. 6381-6390.
273. Glover, P.W.J. and N. Dery, *Streaming potential coupling coefficient of quartz glass bead packs: Dependence on grain diameter, pore size, and pore throat radius.* Geophysics, 2010. **75**(6): p. F225-F241.
274. Pieranski, P., *Two-Dimensional Interfacial Colloidal Crystals.* Physical Review Letters, 1980. **45**(7): p. 569-572.
275. Du, K., et al., *Adsorption energy of nano- and microparticles at liquid-liquid interfaces.* Langmuir, 2010. **26**(15): p. 12518-12522.
276. Du, K., J.A. Liddle, and A.J. Berglund, *Three-dimensional real-time tracking of nanoparticles at an oil-water interface.* Langmuir, 2012. **28**(25): p. 9181-9188.
277. Shani, C., N. Weisbrod, and A. Yakirevich, *Colloid transport through saturated sand columns: Influence of physical and chemical surface properties on deposition.* Colloids and Surfaces A: Physicochemical and Engineering Aspects, 2008. **316**(1-3): p. 142-150.
278. Vinogradov, J. and M.D. Jackson, *Zeta potential in intact natural sandstones at elevated temperatures.* Geophysical Research Letters, 2015. **42**: p. 6287-6294.

279. Walker, E., P.W.J. Glover, and J. Ruel, *A transient method for measuring the DC streaming potential coefficient of porous and fractured rocks.* Journal of Geophysical Research-Solid Earth, 2014. **119**(2): p. 957-970.
280. WALKER, E., P.W.J. GLOVER, and N. EARDLEY, *Measurements and modeling of the streaming and zeta potential of porous rocks.* Geophysical Journal International, 2015. **In press**.
281. Becker, M.D., et al., *A multi-constituent site blocking model for nanoparticle and stabilizing agent transport in porous media.* Environ. Sci.: Nano, 2015. **2**(2): p. 155-166.
282. Glover, P.W.J., *A generalized Archie's law for n phases.* Geophysics, 2010. **75**(6): p. E247-E265.
283. Shahrabadi, A., et al., *Experimental Investigation of HLP Nanofluid Potential to Enhance Oil Recovery: A Mechanistic Approach* in *SPE International Oilfield Nanotechnology Conference and Exhibition*. 2012, Society of Petroleum Engineers: Noordwijk, The Netherlands
284. Jeong, S.-W., *Evaluation of the use of capillary numbers for quantifying the removal of DNAPL trapped in a porous medium by surfactant and surfactant foam floods.* Journal of Colloid and Interface Science, 2005. **282**: p. 181-187.
285. Hu, Z., et al., *Nanoparticle-Assisted Water-Flooding in Berea Sandstones.* Energy & Fuels, 2016. **30**(4): p. 2791-2804.
286. Cheraghian, G., et al., *An experimental investigation of the enhanced oil recovery and improved performance of drilling fluids using titanium dioxide and fumed silica nanoparticles.* Journal Of Nanostructure in Chemistry, 2013. **3**(78): p. 1-9.
287. Karapati, S., et al., *Eco-efficient TiO2 modification for air pollutants oxidation.* Applied Catalysis B: Environmental, 2015. **176-177**: p. 578-585.
288. Potapova, E., et al., *In-situ spectroscopic study of surfactant adsorption onto hematite from binary mixtures and the effect of inorganic ions.* Surface and Interface Analysis, 2014. **46**(10-11): p. 1110-1114.
289. Liu, Y., et al., *LiFePO4nanoparticles growth with preferential (010) face modulated by Tween-80.* RSC Adv., 2015. **5**(13): p. 9745-9751.
290. Alotaibi, M.B., H.A. Nasr-El-Din, and J.J. Fletcher, *Electrokinetics of Limestone and Dolomite Rock Particles.* SPE Reservoir Evaluation & Engineering, 2011. **14**(05): p. 594-603.
291. Athas, J.C., et al., *An effective dispersant for oil spills based on food-grade amphiphiles.* Langmuir, 2014. **30**(31): p. 9285-94.
292. Nelson, R.C., *The Effect of Live Crude on Phase Behavior and Oil-Recovery Efficiency of Surfactant Flooding Systems.* Society of Petroleum Engineers Journal, 1983. **23**(03): p. 501-510.
293. Rottman, J.J., *Fundamentals and Application of Porous Media Filtration for The Removal of Nanoparticles From Industrial Wastewater*. 2013, UNIVERSITY OF ARIZONA. p. 159.
294. Wang, C., et al., *Retention and transport of silica nanoparticles in saturated porous media: effect of concentration and particle size.* Environ Sci Technol, 2012. **46**(13): p. 7151-7158.
295. Dunphy Guzman, K.A., M.P. Finnegan, and J.F. Banfield, *Influence of Surface Potential on Aggregation and Transport of Titania Nanoparticles.* Environmental Science & Technology, 2006. **40**(24): p. 7688-7693.

296. Bradford, S.A. and S. Torkzaban, *Colloid Transport and Retention in Unsaturated Porous Media: A Review of Interface-, Collector-, and Pore-Scale Processes and Models.* Vadose Zone Journal, 2008. **7**(2): p. 667.
297. Gupta, A., et al., *Nanoemulsions: formation, properties and applications.* Soft Matter, 2016. **12**(11): p. 2826-41.
298. Gupta, A., et al., *Controlling and predicting droplet size of nanoemulsions: scaling relations with experimental validation.* Soft Matter, 2016. **12**(5): p. 1452-8.
299. Binks, B.P. and J.A. Rodrigues, *Enhanced stabilization of emulsions due to surfactant-induced nanoparticle flocculation.* Langmuir, 2007. **23**(14): p. 7436-9.
300. Flaaten, A.K., *An Integrated Approach to Chemical EOR Opportunity Valuation: Technical, Economic, and Risk Considerations for Project Development Scenarios and Final Decision*. 2012, The University of Texas at Austin.
301. Yoon, J.S., J.T. Germaine, and P.J. Culligan, *Visualization of particle behavior within a porous medium: Mechanisms for particle filtration and retardation during downward transport.* Water Resources Research, 2006. **42**(6): p. W06417.
302. Okoli, C., et al., *Comparison and functionalization study of microemulsion-prepared magnetic iron oxide nanoparticles.* Langmuir, 2012. **28**(22): p. 8479-85.
303. *https://www.nist.gov/sites/default/files/documents/cnst/Ullo-NIST_03_01_2011_Final.pdf, access on 1 February 2018.*
304. Murray, B.S., et al., *Stabilization of foams and emulsions by mixtures of surface active food-grade particles and proteins.* Food Hydrocolloids, 2011. **25**(4): p. 627-638.
305. Lishchuk, S.V. and I. Halliday, *Effective surface viscosities of a particle-laden fluid interface.* Phys Rev E Stat Nonlin Soft Matter Phys, 2009. **80**(1 Pt 2): p. 016306.
306. Worthen, A.J., et al., *Carbon dioxide-in-water foams stabilized with nanoparticles and surfactant acting in synergy.* AIChE Journal, 2013. **59**(9): p. 3490-3501.
307. Wijmans, C.M. and E. Dickinson, *Simulation of Interfacial Shear and Dilatational Rheology of an Adsorbed Protein Monolayer Modeled as a Network of Spherical Particles.* Langmuir, 1998. **14**(25): p. 7278-7286.
308. Kabalnov, A. and H. Wennerström, *Macroemulsion Stability: The Oriented Wedge Theory Revisited.* Langmuir, 1996. **12**(2): p. 276-292.
309. Prigiobbe, V., et al., *Transport of Nanoparticle-Stabilized CO2-Foam in Porous Media.* Transport in Porous Media, 2015. **111**(1): p. 265-285.
310. Destree, C. and J.B. Nagy, *Mechanism of formation of inorganic and organic nanoparticles from microemulsions.* Advances in Colloid and Interface Science, 2006. **123**: p. 353-367.
311. Nourafkan, E., et al., *Synthesis of stable iron oxide nanoparticle dispersions in high ionic media.* Journal of Industrial and Engineering Chemistry, 2017. **50**: p. 57-71.
312. de Oliveira, R.J., et al., *Photoreactive surfactants: a facile and clean route to oxide and metal nanoparticles in reverse micelles.* Langmuir, 2011. **27**(15): p. 9277-84.
313. Adkins, S.S., et al., *Morphology and stability of CO2-in-water foams with nonionic hydrocarbon surfactants.* Langmuir, 2010. **26**(8): p. 5335-48.

314. Wasan, D. and A. Nikolov, *Thin liquid films containing micelles or nanoparticles.* Current Opinion in Colloid & Interface Science, 2008. **13**(3): p. 128-133.
315. Langevin, D., *Influence of interfacial rheology on foam and emulsion properties.* Advances in Colloid and Interface Science, 2000. **88**(1-2): p. 209-222.
316. Binks, B.P., M. Kirkland, and J.A. Rodrigues, *Origin of stabilisation of aqueous foams in nanoparticle–surfactant mixtures.* Soft Matter, 2008. **4**(12): p. 2373.
317. Vrij, A. and J.T.G. Overbeek, *Rupture of thin liquid films due to spontaneous fluctuations in thickness.* Journal of the American Chemical Society, 1968. **90**(12): p. 3074-3078.
318. Babak, V.G. and M.-J. Stébé, *Highly Concentrated Emulsions: Physicochemical Principles of Formulation.* Journal of Dispersion Science and Technology, 2002. **23**(1-3): p. 1-22.
319. Binks, B.P. and S.O. Lumsdon, *Influence of Particle Wettability on the Type and Stability of Surfactant-Free Emulsions†.* Langmuir, 2000. **16**(23): p. 8622-8631.
320. Martinez, H., et al., *The intrinsic interfacial structure of ionic surfactant monolayers at water-oil and water-vapour interfaces.* Proceedings of the Royal Society A: Mathematical, Physical and Engineering Sciences, 2011. **467**(2131): p. 1939-1958.
321. Fanun, M., *Microemulsions: Properties and Applications*, ed. M. Fanun. 2008: CRC Press.
322. Barnes, J.R., et al., *Controlled Hydrophobe Branching To Match Surfactant To Crude Composition For Chemical EOR*, in *SPE Improved Oil Recovery Symposium*. 2012, Society of Petroleum Engineers: Tulsa, Oklahoma, USA.
323. Boyd, J., C. Parkinson, and P. Sherman, *Factors affecting emulsion stability, and the HLB concept.* Journal of Colloid and Interface Science, 1972. **41**(2): p. 359-370.
324. Riehm, D.A. and A.V. McCormick, *The role of dispersants' dynamic interfacial tension in effective crude oil spill dispersion.* Mar Pollut Bull, 2014. **84**(1-2): p. 155-63.
325. Hunter, T.N., et al., *The role of particles in stabilising foams and emulsions.* Adv Colloid Interface Sci, 2008. **137**(2): p. 57-81.
326. Grassl, B., et al., *Poly(ethylene oxide)- and poly (acrylamide)-based water-soluble associative polymers: synthesis, characterisation, properties in solution.* Polymer International, 2006. **55**(10): p. 1169-1176.
327. Gao, H., et al., *Bifunctional ultraviolet/ultrasound responsive composite TiO2/polyelectrolyte microcapsules.* Nanoscale, 2016. **8**(9): p. 5170-80.
328. Haraguchi, K., T. Takehisa, and S. Fan, *Effects of Clay Content on the Properties of Nanocomposite Hydrogels Composed of Poly(N-isopropylacrylamide) and Clay.* Macromolecules, 2002. **35**(27): p. 10162-10171.
329. Pospisil, J., et al., *Degradation and aging of polymer blends - I. Thermomechanical and thermal degradation.* Polymer Degradation and Stability, 1999. **65**(3): p. 405-414.
330. Feng, Y., et al., *Hydrophobically associating polyacrylamides and their partially hydrolyzed derivatives prepared by post-modification. 2.*

Properties of non-hydrolyzed polymers in pure water and brine. Polymer, 2005. **46**(22): p. 9283-9295.
331. Mitchell, J., et al., *Viscoelastic polymer flows and elastic turbulence in three-dimensional porous structures.* Soft Matter, 2016. **12**(2): p. 460-468.
332. Wei, B., *Flow Characteristics of Three Enhanced Oil Recovery Polymers in Porous Media.* Journal of Applied Polymer Science, 2015. **132**(10): p. 7.
333. Zhang, L.J. and X.A. Yue, *Mechanism for Viscoelastic Polymer Solution Percolating through Porous Media.* Journal of Hydrodynamics, 2007. **19**(2): p. 241-248.
334. Mewada, A., et al., *Non-blinking dendritic crystals from C-dot solution.* Carbon letters, 2015. **16**(3): p. 211-214.
335. Yang, X., et al., *Novel and green synthesis of high-fluorescent carbon dots originated from honey for sensing and imaging.* Biosensors and Bioelectronics, 2014. **60**: p. 292-298.
336. Ding, H., et al., *Full-Color Light-Emitting Carbon Dots with a Surface-State-Controlled Luminescence Mechanism.* ACS Nano, 2016. **10**(1): p. 484-91.
337. Petosa, A.R., et al., *Aggregation and deposition of engineered nanomaterials in aquatic environments: role of physicochemical interactions.* Environ Sci Technol, 2010. **44**(17): p. 6532-49.
338. Tiraferri, A., T. Tosco, and R. Sethi, *Transport and retention of microparticles in packed sand columns at low and intermediate ionic strengths: experiments and mathematical modeling.* Environmental Earth Sciences, 2010. **63**(4): p. 847-859.
339. Hogg, R., T.W. Healy, and D.W. Fuerstenau, *Mutual coagulation of colloidal dispersions.* Transactions of the Faraday Society, 1966. **62**: p. 1638.
340. Elimelech, M., et al., *Particle Deposition & Aggregation : Measurement, Modelling and Simulation*. 1995.
341. Auffan, M., et al., *Towards a definition of inorganic nanoparticles from an environmental, health and safety perspective.* Nat Nanotechnol, 2009. **4**(10): p. 634-41.
342. Kallay, N. and S. Zalac, *Stability of nanodispersions: a model for kinetics of aggregation of nanoparticles.* J Colloid Interface Sci, 2002. **253**(1): p. 70-6.
343. He, Y.T., J. Wan, and T. Tokunaga, *Kinetic stability of hematite nanoparticles: the effect of particle sizes.* Journal of Nanoparticle Research, 2007. **10**(2): p. 321-332.